

**DYNAMIC ECCENTRIC RESPONSE
OF A CIRCULAR FOOTING ON A SAND STRATUM
BY PHYSICAL MODELING**

by

DAN W. CHANDLER

B.S., Physics, Michigan State University

2004

A thesis submitted to the
Faculty of the Graduate School of the
University of Colorado in partial fulfillment
of the requirements for the degree of
Master of Science
Department of Mechanical Engineering

2010

This thesis entitled:
Dynamic Eccentric Response of a Circular Footing on a Sand Stratum
by Physical Modeling
written by Dan Chandler
has been approved for the Department of Mechanical Engineering

Ronald Y. S. Pak

H. Jerry Qi

Richard Regueiro

Date_____

The final copy of this thesis has been examined by the signatories, and we find that both the content and the form meet acceptable presentation standards of scholarly work in the above mentioned discipline.

Chandler, Dan W. (M.S., Mechanical Engineering)

Dynamic Eccentric Response of a Circular Footing on a Sand Stratum by Physical Modeling

Thesis directed by Professor Ronald Y. S. Pak

Due to the stress dependent nature of the material properties of soil, it can be difficult to find a comprehensive approximate method that captures all features of the response of a structure or foundation under dynamic loading. For this reason, a fundamental problem in soil-structure interaction was investigated, both experimentally by means of centrifuge modeling, and computationally using boundary element methods. The problem consisted of a circular surface foundation resting on a soil stratum, subjected to random loading applied at a vertically eccentric location on the upper surface of the footing. The experimental data was compared with computational results for two soil material models: A soil with an equivalent homogeneous shear modulus, and a two-zone soil model that more directly accounts for the stress dependence of the soil's material properties. The two-zone model represents the far-field using a shear modulus that has square root dependence with depth, and a local homogeneous zone directly underneath the footing. Computational and experimental results were also compared with a previous study involving square footings on a soil stratum, having contact pressures equal to the circular footings in this report.

ACKNOWLEDGEMENTS

I would like to thank Professor Ronald Y. S. Pak, my advisor for this project. His direction and insight were essential. I could not have completed this thesis without his persistence, patience, and encouragement.

I am indebted to Drs. Mahdi Souhdkhah and Jeramy Ashlock for the knowledge passed down, both from themselves and their predecessors. The work of Jacob Mitchell was also an essential contribution to the computational analysis presented in this study.

CONTENTS

CHAPTER

1	INTRODUCTION	1
2	EXPERIMENT OVERVIEW	3
2.1	Centrifuge Modeling	3
2.2	Experimental Targets	5
2.3	The Soil Sample and Container	7
2.4	Cylindrical Footing Models	10
2.5	Frequency Domain Analysis	14
3	PRELIMINARY TESTING	18
3.1	Testing at 1g	18
3.2	Loading Type and Excitation Level	18
3.3	Order of Centrifuge tests as a Function of g-level	21
3.4	Quality of Soil-footing Contact	30
4	EXPERIMENTAL RESULTS AND ANALYSIS	34
4.1	Typical Response Features	34
4.2	Typical Measured Accelerances	38
4.3	Footing Response Comparison	60
4.4	Repeatability	63
5	MEASURED RESPONSE COMPARISON OF CIRCULAR AND SQUARE FOOTINGS	68
5.1	Footing Properties	68
5.2	Comparison	69
6	COMPUTATIONAL MODELING	81
6.1	Boundary Element Method	81
6.2	The Two-zone Model	81
6.3	Material Properties	85
6.4	Impedance Functions	87
6.5	Impedance Comparison: Circle vs. Square	94
6.6	Theoretical Accelerance Functions	102
6.7	Theoretical Accelerance Behavior	105
7	SYNTHESIS OF DATA AND THEORY	116
7.1	Equivalent Homogeneous Shear Modulus	116
7.2	Calibrating the Two-zone Continuum Model	127
7.3	Homogeneous Shear Modulus vs. the Two-zone Model	137

8	CONCLUSIONS	147
	BIBLIOGRAPHY	148
	APPENDIX	151

TABLES

Table

2.1	Scaling relations for centrifuge modeling.....	3
2.2	Circular footing properties without attachments.....	11
2.3	Instrumentation mount-points for footing C1	12
2.4	Instrumentation mount-points for footing C2	12
2.5	Instrumentation mount-points for footing C3	12
2.6	Load cell and accelerometer inertial properties	13
2.7	Circular footing properties with attachments.....	13
2.8	Prototype footing properties with g-level	14
4.1	Rocking peak frequencies for C1, C2, and C3.....	62
4.2	Testing dates	63
5.1	Footing properties: square (B1) vs. circle (C1)	68
5.2	Footing properties: square (B2) vs. circle (C2)	69
5.3	Footing properties: square (B3) vs. circle (C3)	69
5.4	Circle and square, UH and LH coordinates	69
6.1	Material properties used in BEASSI.....	86
6.2	Reference shear modulus by g-level	88
6.3	Effect of inclusion depth on static impedance	93
6.4	Effect of inclusion stiffness on static impedance.....	93
7.1	Static impedance (homogeneous) comparison between the circle and square	118
7.2	Contact Pressures for Prototype Footings.....	119
7.3	Homogeneous shear modulus comparison: fitting the vertical or horizontal response	125
7.4	Error measure weighting schemes	129

FIGURES

Figure

2.1	CU 440 g-ton centrifuge schematic	4
2.2	CU 440 g-ton centrifuge picture	4
2.3	Planar motion of footings	6
2.4	Separate loading tests.....	6
2.5	Combined loading tests.....	7
2.6	Footing C2 with instrumentations, placed on the soil.....	7
2.7	Footing C2 with the excitation system.....	7
2.8	Duxéal layer	10
2.9	Instrumentation mount-point numbering scheme	11
2.10	Footings C1, C2, and C3.....	14
2.11	Measurement location names.....	16
3.1	Effects of excitation level on accelerance magnitudes	20
3.2	Sample 1g load cell time history for footing C2.....	20
3.3	Another sample 1g load cell time history for footing C2	20
3.4	Preliminary g-level order	21
3.5	Free-field response, spin-up vs. spin-down	22
3.6	Footing C3 LH, spin-up vs. spin-down.....	23
3.7	Footing C3 LH, spin-up vs. spin-down, 33g.....	24
3.8	Footing C3 UH, spin-up vs. spin-down, 33g	24
3.9	Footing C3 VC, spin-up vs. spin-down, 33g	24
3.10	g-level order	27
3.11	Footing C1 intermediate 1g tests	28
3.12	Footing C1 intermediate 33g tests, LH/VE	28
3.13	Footing C3 intermediate 33g tests, LH/VE	29
3.14	Footing C3 intermediate 33g tests, UH/VE	29
3.15	Footing C3 intermediate 33g tests, VC/VE	30
3.16	Initial placement tests	32
3.17	Response after light tamping around footing	32
3.18	Effects of light tamping and roughened soil-footing interface	33
3.19	Close-up on the peak region in Figure 3.18.....	33
4.1	Footing C3 LH/VE data at 33g.....	35
4.2	Footing C3 UH/VE data at 33g.....	35
4.3	Footing C3 horizontal data at 33g.....	35

4.4	Footing C3 VC/VE data at 33g.....	35
4.5	Footing C3 horizontal rocking peak 33g	37
4.6	Footing C3 second horizontal peak at 33g.....	37
4.7	Footing C3 second horizontal peak magnitude, close-up at 33g	37
4.8	Footing C3 LH/VE data, 33g – 66g.....	38
4.9	Footing C3 LH/VE data rocking peak, 33g – 66g	38
4.10	Footing C3 LH/VE data second peak, 33g – 66g	39
4.11	Footing C3 UH/VE data, 33g – 66g	39
4.12	Footing C3 UH/VE data rocking peak, 33g – 66g	39
4.13	Footing C3 UH/VE data second peak, 33g – 66g	39
4.14	Footing C3 VC/VE data, 33g – 66g	40
4.15	Footing C3 VC/VE data peak, 33g – 66g	40
4.16	Footing C3 LH/VE 3D plot, rocking peak, 1g – 66g	40
4.17	Footing C3 UH/VE 3D plot, rocking peak, 1g – 66g	40
4.18	Footing C3 VC/VE 3D plot, 1g – 66g	42
4.19	Footing C3 VC/VE 3D plot, peak, 1g – 66g	42
4.20	Footing C3 LH/VE, prototype scale	43
4.21	Footing C3 LH/VE second peak, prototype scale	43
4.22	Footing C3 LH/VE rocking peak prototype scale	45
4.23	Footing C3 UH/VE, prototype scale	45
4.24	Footing C3 UH/VE second peak, prototype scale	45
4.25	Footing C3 UH/VE rocking peak prototype scale	45
4.26	Footing C3 VC/VE, prototype scale	46
4.27	Footing C3 VC/VE peak, prototype scale	46
4.28	Footing C2 vs. C3, accelerance magnitudes	46
4.29	Footing C2 LH/VE data, 33g – 66g.....	46
4.30	Footing C2 LH/VE data second peak, 33g – 66g	48
4.31	Footing C2 LH/VE data rocking peak, 33g – 66g	49
4.32	Footing C2 UH/VE data, 33g – 66g	49
4.33	Footing C2 UH/VE data second peak, 33g – 66g	49
4.34	Footing C2 UH/VE data rocking peak, 33g – 66g	49
4.35	Footing C2 VC/VE data, 33g – 66g	50
4.36	Footing C2 VC/VE data peak, 33g – 66g	50
4.37	Footing C2 intermediate 1g tests	50
4.38	Footing C2 LH/VE data second peak, 3D plot.....	50
4.39	Footing C2 UH/VE data second peak, 3D plot	51
4.40	Footing C2 LH/VE, prototype scale	51

4.41	Footing C2 LH/VE rocking peak, prototype scale	52
4.42	Footing C2 UH/VE, prototype scale	53
4.43	Footing C2 UH/VE rocking peak, prototype scale	53
4.44	Footing C2 VC/VE, prototype scale	54
4.45	Footing C1 LH/VE data, 33g – 66g	54
4.46	Footing C1 LH/VE data second peak, 33g – 66g	54
4.47	Footing C1 LH/VE data rocking peak, 33g – 66g	55
4.48	Footing C1 UH/VE data, 33g – 66g	55
4.49	Footing C1 UH/VE data rocking peak, 33g – 66g	56
4.50	Footing C1 VC/VE data, 33g – 66g	57
4.51	Footing C1 LH/VE, prototype scale	57
4.52	Footing C1 UH/VE, prototype scale	58
4.53	Footing C1 VC/VE, prototype scale	59
4.54	Footing data comparison, LH/VE	59
4.55	Footing data comparison, LH/VE second peak	59
4.56	Footing data comparison, UH/VE rocking peak	60
4.57	Footing data comparison, UH/VE second peak	60
4.58	Footing data comparison, VC/VE peak	61
4.59	Footing data comparison, VC/VE	61
4.60	Footing C3 LH/VE, data consistency	61
4.61	Footing C3 LH/VE second peak, data consistency	61
4.62	Footing C3 UH/VE, data consistency	64
4.63	Footing C3 VC/VE, data consistency	64
4.64	Footing C2 LH/VE, data consistency	64
4.65	Footing C2 LH/VE second peak, data consistency	64
4.66	Footing C2 UH/VE, data consistency	65
4.67	Footing C2 UH/VE second peak, data consistency	65
4.68	Footing C2 VC/VE, data consistency	65
4.69	Footing C1 LH/VE, data consistency	65
4.70	Footing C1 LH/VE second peak, data consistency	66
4.71	Footing C1 UH/VE, data consistency	66
4.72	Footing C1 UH/VE second peak, data consistency	66
4.73	Footing C1 VC/VE, data consistency	67
5.1	Circle (C1) vs. square (B1), LH/VE data	67
5.2	Circle (C1) vs. square (B1), LH/VE data, second peak	67
5.3	Circle (C1) vs. square (B1), UH/VE data	71
5.4	Circle (C1) vs. square (B1), VC/VE data, peak	71

5.5	Circle (C1) vs. square (B1), VC/VE data	71
5.6	Circle (C2) vs. square (B2), LH/VE data	71
5.7	Circle (C2) vs. square (B2), LH/VE data, second peak	72
5.8	Circle (C2) vs. square (B2), UH/VE data	73
5.9	Circle (C2) vs. square (B2), VC/VE data	73
5.10	Circle (C3) vs. square (B3), LH/VE data	73
5.11	Circle (C3) vs. square (B3), LH/VE data, second peak	73
5.12	Circle (C3) vs. square (B3), UH/VE data	74
5.13	Circle (C3) vs. square (B3), LH/VE data, peak	74
5.14	Circle (C3) vs. square (B3), UC/VE data	74
5.15	Circle (C3) vs. square (B3), VC/VE data	74
5.16	C1 and B1 LH/VE accelerance magnitudes by g-level	75
5.17	C1 and B1 UH/VE accelerance magnitudes by g-level	76
5.18	C1 and B1 VC/VE accelerance magnitudes by g-level	76
5.19	C2 and B2 LH/VE accelerance magnitudes by g-level	77
5.20	C2 and B2 UH/VE accelerance magnitudes by g-level	77
5.21	C2 and B2 VC/VE accelerance magnitudes by g-level	78
5.22	C3 and B3 LH/VE accelerance magnitudes by g-level	78
5.23	C3 and B3 UH/VE accelerance magnitudes by g-level	79
5.24	C3 and B3 VC/VE accelerance magnitudes by g-level	80
6.1	Full mesh for BEASSI input.....	82
6.2	Side view of mesh.....	82
6.3	Stiffened-zone mesh, $h_f/a = 2.5$	83
6.4	Stiffened-zone mesh side view, $h_f/a = 2.5$	83
6.5	Stiffened-zone mesh, $h_f/a = 3.0$	83
6.6	Stiffened-zone mesh side view, $h_f/a = 3.0$	83
6.7	Stiffened-zone mesh, $h_f/a = 3.5$	84
6.8	Stiffened-zone mesh side-view, $h_f/a = 3.5$	84
6.9	Stiffened-zone mesh, $h_f/a = 4.0$	84
6.10	Stiffened-zone mesh side view, $h_f/a = 4.0$	84
6.11	BEM domains	86
6.12	Dimensionless impedances, $h_f/a = 3.0$	90
6.13	Dimensionless impedances, $h_f/a = 3.5$	91
6.14	Dimensionless impedances, $h_f/a = 4.0$	92
6.15	Equivalent square vs. circle, dimensionless impedances, vertical term.....	96
6.16	Equivalent square vs. circle, dimensionless impedances, horizontal term	98
6.17	Equivalent square vs. circle, dimensionless impedances, coupling term	99

6.18	Equivalent square vs. circle, dimensionless impedances, rocking term	100
6.19	Free body diagram of footing	101
6.20	C1 circle vs. equivalent square, LH/VE theory	102
6.21	C1 circle vs. equivalent square, UH/VE theory	106
6.22	C1 circle vs. equivalent square, VC/VE theory	106
6.23	Footing C1 LH/VE rocking peak, $h_f/a = 3.0$	107
6.24	Footing C1 LH/VE second peak, $h_f/a = 3.0$	108
6.25	Footing C1 UH/VE rocking peak, $h_f/a = 3.0$	108
6.26	Footing C1 UH/VE second peak, $h_f/a = 3.0$	108
6.27	Footing C1 UH/VE, $h_f/a = 3.0$	108
6.28	Footing C1 VC/VE, $h_f/a = 3.0$	109
6.29	Footing C2 LH/VE rocking peak, $h_f/a = 3.5$	109
6.30	Footing C2 LH/VE second peak, $h_f/a = 3.5$	109
6.31	Footing C2 UH/VE rocking peak, $h_f/a = 3.5$	109
6.32	Footing C2 UH/VE second peak, $h_f/a = 3.5$	110
6.33	Footing C2 UH/VE, $h_f/a = 3.5$	110
6.34	Footing C2 VC/VE rocking peak, $h_f/a = 3.5$	110
6.35	Footing C3 LH/VE rocking peak, $h_f/a = 4.0$	111
6.36	Footing C3 LH/VE second, $h_f/a = 4.0$	111
6.37	Footing C3 UH/VE rocking peak, $h_f/a = 4.0$	111
6.38	Footing C3 UH/VE second peak, $h_f/a = 4.0$	111
6.39	Footing C3 UH/VE, $h_f/a = 4.0$	112
6.40	Footing C3 VC/VE, $h_f/a = 4.0$	112
6.41	Footing C2 LH/VE rocking peak, $G_f/G_{tip} = 2.0$	112
6.42	Footing C2 LH/VE second peak, $G_f/G_{tip} = 2.0$	114
6.43	Footing C2 UH/VE rocking peak, $G_f/G_{tip} = 2.0$	114
6.44	Footing C2 UH/VE second peak, $G_f/G_{tip} = 2.0$	114
6.45	Footing C2 UH/VE, $G_f/G_{tip} = 2.0$	114
6.46	Footing C2 VC/VE, $G_f/G_{tip} = 2.0$	115
7.1	Dimensionless impedances for a stratum with homogeneous shear modulus	117
7.2	Footing C1, G_{eq-hom} horiz. match, LH/VE	120
7.3	Footing C1, G_{eq-hom} horiz. match, UH/VE	120
7.4	Footing C1, G_{eq-hom} horiz. match, VC/VE	120
7.5	Footing C1, G_{eq-hom} vert. match, VC/VE	120
7.6	Footing C1, G_{eq-hom} vert. match, LH/VE	121
7.7	Footing C1, G_{eq-hom} vert. match, UH/VE	121
7.8	Footing C2, G_{eq-hom} horiz. match, LH/VE	121

7.9	Footing C2, G_{eq-hom} horiz. match, UH/VE rocking peak	121
7.10	Footing C2, G_{eq-hom} horiz. match, LH/VE rocking peak	122
7.11	Footing C2, G_{eq-hom} horiz. match, VC/VE	122
7.12	Footing C2, G_{eq-hom} vert. match, VC/VE	122
7.13	Footing C2, G_{eq-hom} vert. match, LH/VE	122
7.14	Footing C2, G_{eq-hom} vert. match, LH/VE rocking peak	123
7.15	Footing C2, G_{eq-hom} vert. match, UH/VE rocking peak	123
7.16	Footing C3, G_{eq-hom} horiz. match, LH/VE	123
7.17	Footing C3, G_{eq-hom} horiz. match, UH/VE rocking peak	123
7.18	Footing C3, G_{eq-hom} horiz. match, VC/VE	124
7.19	Footing C3, G_{eq-hom} vert. match, VC/VE	124
7.20	Footing C3, G_{eq-hom} vert. match, LH/VE	124
7.21	Footing C3, G_{eq-hom} vert. match, UH/VE rocking peak	124
7.22	Footing C2, G_{eq-hom} horiz. match with equivalent square, VC/VE	126
7.23	Footing C3, G_{eq-hom} horiz. match with equivalent square, VC/VE	126
7.24	Footing C3 fit error summary	129
7.25	Footing C3 fit error summary, 3D map	130
7.26	Footing C1 two-zone vs. 33g data: LH/VE, $h_f/a = 3.0$	131
7.27	Footing C1 two-zone vs. 33g data: UH/VE, $h_f/a = 3.0$	131
7.28	Footing C1 two-zone vs. 33g data: UH/VE rocking peak, $h_f/a = 3.0$	131
7.29	Footing C1 two-zone vs. 33g data: VC/VE, $h_f/a = 3.0$	131
7.30	Footing C1 two-zone vs. 66g data: LH/VE, $h_f/a = 3.0$	132
7.31	Footing C1 two-zone vs. 66g data: UH/VE, $h_f/a = 3.0$	132
7.32	Footing C1 two-zone vs. 66g data: UH/VE rocking peak, $h_f/a = 3.0$	132
7.33	Footing C1 two-zone vs. 66g data: VC/VE, $h_f/a = 3.0$	132
7.34	Footing C2 two-zone vs. 33g data: LH/VE, $h_f/a = 3.5$	133
7.35	Footing C2 two-zone vs. 33g data: UH/VE rocking peak, $h_f/a = 3.5$	133
7.36	Footing C2 two-zone vs. 33g data: VC/VE, $h_f/a = 3.5$	133
7.37	Footing C2 two-zone vs. 66g data: LH/VE, $h_f/a = 3.5$	133
7.38	Footing C3 two-zone vs. 33g data: LH/VE, $h_f/a = 4.0$	134
7.39	Footing C3 two-zone vs. 33g data: UH/VE, $h_f/a = 4.0$	134
7.40	Footing C3 two-zone vs. 33g data: UH/VE rocking peak, $h_f/a = 4.0$	134
7.41	Footing C3 two-zone vs. 33g data: VC/VE, $h_f/a = 4.0$	134
7.42	Footing C3 two-zone vs. 66g data: LH/VE, $h_f/a = 4.0$	135
7.43	Footing C3 two-zone vs. 66g data: UH/VE, $h_f/a = 4.0$	135
7.44	Footing C3 two-zone vs. 66g data: VC/VE, $h_f/a = 4.0$	135
7.45	Fit results by error weight scheme	136

7.46	Fit results by g-level, using scheme w	136
7.47	Footing C1, two-zone w vs. G_{eq-hom} horiz., LH/VE	138
7.48	Footing C1, two-zone w vs. G_{eq-hom} horiz., UH/VE	138
7.49	Footing C1, two-zone w vs. G_{eq-hom} horiz., VC/VE	139
7.50	Footing C2, two-zone w vs. G_{eq-hom} horiz., LH/VE rocking peak	139
7.51	Footing C2, two-zone w vs. G_{eq-hom} horiz., LH/VE	139
7.52	Footing C2, two-zone w vs. G_{eq-hom} horiz., UH/VE, rocking peak	139
7.53	Footing C2, two-zone w vs. G_{eq-hom} horiz., UH/VE, entire rocking peak	140
7.54	Footing C2, two-zone w vs. G_{eq-hom} horiz., VC/VE	140
7.55	Footing C3, two-zone w vs. G_{eq-hom} horiz., LH/VE	140
7.56	Footing C3, two-zone w vs. G_{eq-hom} horiz., LH/VE rocking peak	140
7.57	Footing C3, two-zone w vs. G_{eq-hom} horiz., UH/VE rocking peak	141
7.58	Footing C3, two-zone w vs. G_{eq-hom} horiz., VC/VE	141
7.59	Footing C2, two-zone w vs. G_{eq-hom} vert., VC/VE	144
7.60	Footing C2, two-zone w vs. G_{eq-hom} vert., UH/VE entire rocking peak	144
7.61	Footing C2, two-zone w vs. G_{eq-hom} vert., LH/VE	144
7.62	Footing C2, two-zone w vs. G_{eq-hom} vert., UH/VE rocking peak.....	144
7.63	Footing C3, two-zone w vs. G_{eq-hom} vert., VC/VE	145
7.64	Footing C3, two-zone w vs. G_{eq-hom} vert., UH/VE	145
7.65	Footing C3, two-zone w vs. G_{eq-hom} vert., LH/VE rocking peak	145
7.66	Footing C3, two-zone w vs. G_{eq-hom} vert., UH/VE rocking peak.....	145

Chapter 1

Introduction

Dynamic soil-structure interaction (SSI) is a subject that is inherently complicated in the context of both geotechnical and structural engineering disciplines. Even without the consideration of a superstructure, such problems are not only three-dimensional in nature but also unbounded. For intense loading, one also has to deal with the well-known nonlinear and hysteretic behavior of soils. Since the pioneering work of Reissner and Sagoci (1944), many analytical solutions for the forced vibration of a footing sitting on soil are based on the homogeneous half-space model (e.g., Bycroft (1956), Robertson (1966), Gladwell (1968), Luco and Westmann 1971, Pak and Gobert (1991)). Intended to address foundation response in the stress-strain regime where linearization is legitimate, many of these solutions have been found to fall short in dealing with real soils, especially for sand. In a number of experimental field studies for instance, significant discrepancies between theory and experiment were found in both response magnitude and modal characteristics (e.g. Crouse and Hushmand 1989, Crouse et al. 1990, Fry 1963, Gazetas and Stokoe 1991, Lin and Jennings 1984, Novak and Beredugo 1972, Stokoe and Richart Jr. 1974, Wong et al. 1977), even under specially-prepared uniformity conditions for the soil (e.g. Erden 1974). As noted in Pak et al. (2008), these difficulties can be attributed to the fact that the shear modulus of most soils depends on the effective-stress state of the soil, may it be sand or clay (e.g., see Hardin and Drnevich, 1972). Specifically, they have shown that the approach of using a ‘homogenized’ or ‘representative’ shear modulus cannot simultaneously predict horizontal, vertical, and rocking motions of a foundation without a set of *Impedance Modification Factors (I.M.F.)* (see Pak and Ashlock 2000).

Aimed to resolve this class of difficult problems beyond the empirical level, some notable progress has been made both theoretically and experimentally by Pak et al. (2008, 2010). As a novel mechanics idea with practical engineering resolution for the sandy soil problem, for instance,

the concept of a dual-zone continuum representation of the soil for a deep soil medium was presented in Pak and Ashlock (2010a). Going beyond the experimental results for a deep soil medium in Pak et al. (2010b), a new experimental database was generated by Soudkhah (2010) for a case of square footings resting on a shallow stratum. In this M.S. thesis, the foregoing investigation was further extended to the case of circular foundations. Specifically, multiple series of physical simulations of a circular surface foundation resting on a soil stratum under forced vertically eccentric excitation were performed utilizing the 400 g-ton geotechnical centrifuge at the University of Colorado. Apart from the direct physical insights that the data provides, the experimental data proves to be useful as a reference against which the validity of dynamic SSI theories can be assessed physically. Of particular interest is the performance of the classical homogeneous-modulus model versus the dual-zone continuum soil representation in the stratum configuration. In terms of various transfer functions in the frequency domain, the theoretical solutions and experimental database for circular foundations are also compared with the results of Soudkhah (2010) for square footings on a stratum under similar loading conditions.

In this thesis, the coverage is divided in four main groups. Chapters 2 and 3 are concerned with the experiment design and test methodology. Chapters 4 and 5 contain the key experimental data and their direct interpretations. Chapter 6 focuses on the computational modeling and the characteristic features of past and new continuum dynamic SSI solutions. Chapter 7 provides a rigorous comparison of the performance of the theoretical solutions with the measured data and Chapter 8 contains the conclusions.

Chapter 2

Experiment Overview

2.1 Centrifuge Modeling

As mentioned in the Introduction, a series of dynamic soil-foundation interaction experiments was conducted by means of centrifuge scaled modeling. For fundamental investigations, centrifuge modeling has many advantages over full scale or field testing. Generally, such testing is much less expensive as well as more configurable and controllable, and tests can be repeated or modified readily. One of the primary advantages to centrifuge modeling is that a large array of data can be collected for many length scales with the same setup simply by changing the g-level. Length and other physical properties scale according to Table 2.1. The 440 g-ton centrifuge at the University of Colorado Boulder used in this study is shown in Figures 2.1 and 2.2.

Quantity	Prototype	Model at n-g
Length	1	$1/n$
Area	1	$1/n^2$
Volume	1	$1/n^3$
Mass Density	1	1
Mass	1	$1/n^3$
Strain	1	1
Displacement	1	$1/n$
Velocity	1	1
Acceleration	1	n
Energy Density	1	1
Energy	1	$1/n^3$
Stress	1	1
Force	1	$1/n^2$
Time (viscous flow)	1	1
Time (dynamic)	1	$1/n$
Time (seepage)	1	$1/n^2$

Table 2.1: Scaling relations for centrifuge modeling at the nth g-level.

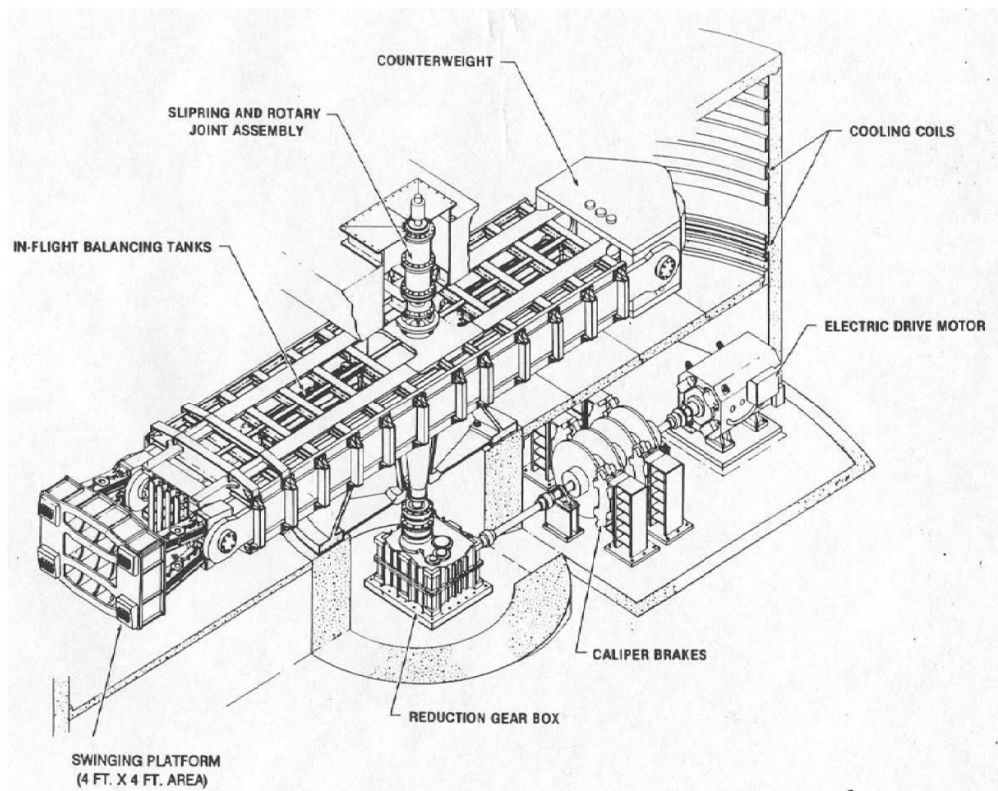


Figure 2.1: Schematic of the large 400 g-ton centrifuge at the University of Colorado Boulder.



Figure 2.2: Picture of the 400 g-ton centrifuge at CU Boulder.

These factors can be derived from the governing differential equations of physics or by using dimensional analysis. Depending on the physical phenomena of interest and the form of the governing equations, there can be different possible scale factors for time. As dry soil is used in all series, the dynamic time relation is most relevant.

It is important to remember that when converting to the prototype, one must extrapolate the length dimension of all components of the system such as the soil's grain size. For this reason, a fine, manufactured silica sand as in Gillmor (1999) and Ashlock (2000) was used in the study to minimize this effect. 'Modeling of models tests' were conducted in the aforementioned studies. It involved testing different size models of the same prototype and the results were found to be consistent, by which one can conclude that the effects of soil grain-size scaling were insignificant for the chosen experimental configurations in the centrifuge tests.

2.2 Experimental Targets

The models in the SSI experiments were cylindrical footings. Such a choice allows the fundamental dynamic SSI behavior to be more easily identified, and makes for a simpler comparison with canonical analytical solutions. Focused on the regime of small strain and elastic deformation of the soil as in Pak et al. (2010), dynamic tests were performed to solicit the dynamic foundation-soil system characteristics in planar vertical-horizontal-rocking motions (see Figure 2.3). Two types of dynamic load test formats as depicted in Figures 2.4 a and b can be used to characterize the fundamental characteristics of the system. The method in Figure 2.4a is the conventional one: apply a dynamic load first in a vertical-centric (VC) location and follow it by applying at a horizontal-centric (HC) location. The second approach is to employ a vertical-eccentric (VE) load configuration (see Pak et al. 2010 and Figure 2.5) which can provoke vertical-horizontal-rocking motion in a hybrid form. For its efficiency as discussed in Pak et al. (2010), the latter method is employed in this investigation.

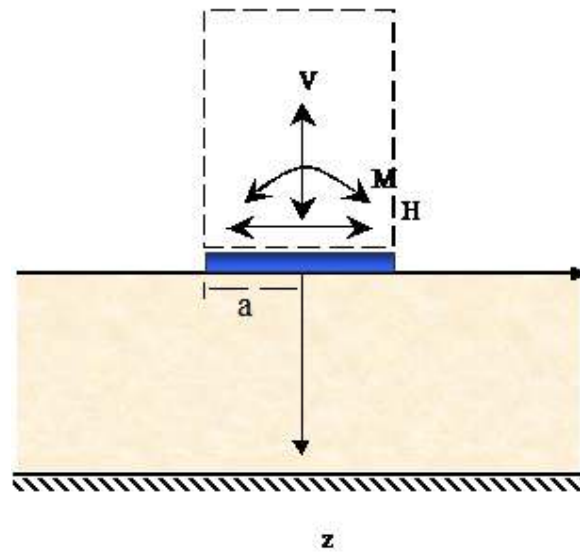


Figure 2.3: Planar motion of footings. Three degrees of freedom: vertical, horizontal, and in-plane rotation.

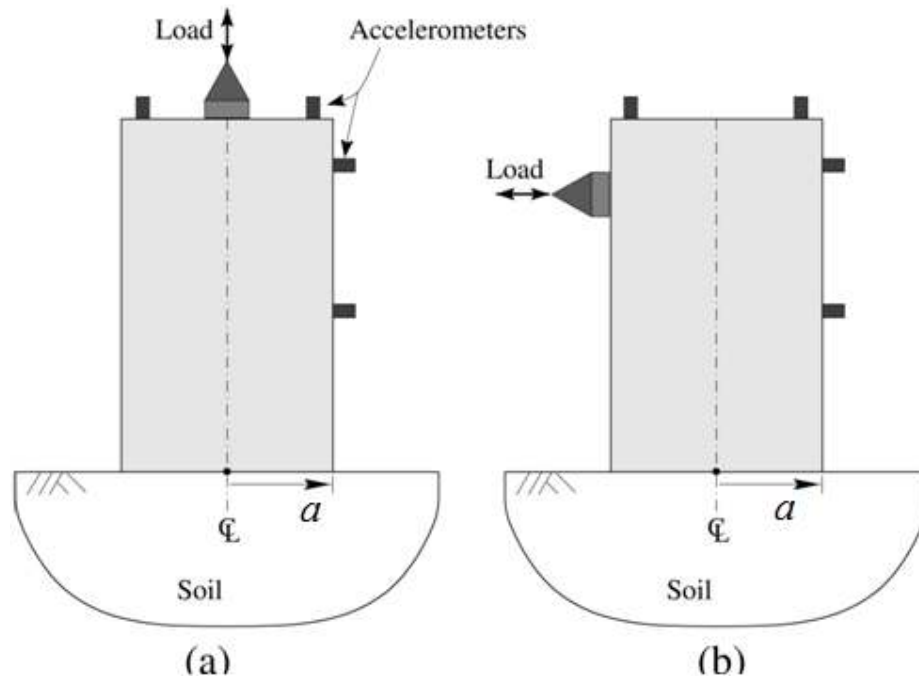


Figure 2.4: Conventional horizontal-l and vertical-centric testing configurations.

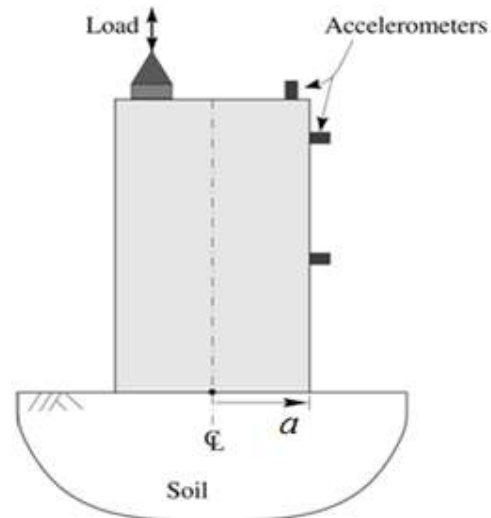


Figure 2.5: Vertical-eccentric (VE) loading configuration to excite vertical-horizontal-rocking motion of foundation-soil system



Figure 2.6: Footing C2 with instrumentations placed on the soil. The excitation system is moved back for a clearer picture.



Figure 2.7 Footing C2 with the excitation system in place for a VE test.

2.3 Soil Sample and Container

Using the method of pluviation, the soil sample was created using a bucket-funnel-hose assembly to rain soil from a specified height to obtain the desired density. The raining height (1.15 m) directly affects the momentum of particles as they impact the sample, resulting in a particular density of the soil model. The direction of the flow was controlled by suspending the raining device from a mobile crane in combination with a flexible hose attached to the bottom of the funnel.

Although this method was much slower than the hopper used by Ashlock (2006), it allowed for more precise control over the raining apparatus, thus a more uniform sample. The resulting density of 1739 kg/m^3 closely matched the soil sample conditions prepared by Ashlock (2006) and Soudkhah (2010) which were between 1720 kg/m^3 and 1730 kg/m^3 . In the funnel method, the desired density was achieved by raining from a distance of 1.15 m, measured from the end of the hose to the top of the sample surface. The raining height was reset to this value after each pass over the sample, while flow was stopped using a rubber stopper at the end of the hose during adjustment. Once the stopper was removed to resume raining, uniform flow was allowed to return before making additional passes over the sample. The raining apparatus was calibrated by making a soil sample in a smaller aluminum container of known mass and volume. Weight measurements were taken and the raining height was adjusted accordingly.

Once the soil raining was completed, the soil surface was graded by passing a widthwise oriented metal straight edge along the length of the container. The edge was held at a fixed depth by hanging it from a steel bar resting on top of the container walls via two long studs. After several passes, excess sand was removed from the container using a vacuum cleaner. This process was repeated until the desired sample height of seven inches was achieved.

The maximum dry density of the F-75 silica sand used in these tests was determined by the U.S. Bureau of Reclamation to be 1781 kg/m^3 (Ashlock, 2006). The soil sample in the container was prepared to 86% of relative density or 98% of its maximum density. With the high density, the increased gravity experienced by the sand on the centrifuge would have minimal influence on the density of the soil. Furthermore, if a surface region were to be damaged accidentally, the sand in the affected area could be removed with a shop vacuum and soil could be re-rained and prepared to the same high density by compaction.

As was discussed in Soudkhah (2010), dynamic centrifuge experiments on a finite soil model should be cognizant of unwanted wave reflections from the container walls during testing. Following the procedure in Guzina (1992), a viscous oil-base putty called Duxseal (also known as

Duct Seal) was installed as vertical wall panels as a means to absorb, though imperfectly, waves that should radiate to infinity in an unbounded domain . This approach was also utilized by Ashlock (2006) and Soudkhah (2010). The vertical Duxseal wall lining was supported by a grid of horizontal steel slats on wood wall panels. A thin layer of plastic wrap was further used to separate the Duxeal from the soil to avoid contamination of the soil and Duxeal (see Figure 2.8). Accelerometers are installed on the base-plate to provide measurement options at the bottom of the soil layer. The eye hooks on the aluminum plate are equipped only for installation of the plate, and are removed before preparation of the soil sample. Underneath the plate are four rubber pads, allowing the setup to optionally function as a shake table for seismic vibration type tests.

The container itself was a 1700 lb rectangular box of steel construction. The rectangular shape was again chosen to minimize wave reflections from the boundary. It was found by Lenke et al. (1991) that a circular container tends to concentrate reflected waves at the center. Also for this reason the model footings were placed at a slightly off-center location for testing.



Figure 2.8: Duxéal layer around the vertical container walls.

2.4 Cylindrical Model Footings

A total of three circular-based footings of different heights were made for this investigation using high strength aluminum. Labeled C1, C2, and C3 respectively, they were designed to achieve contact pressures equal to the square footings B13, B23, and B33 employed in Soudkhah (2010) and Ashlock (2006). Their shop drawings with full dimensions are included in the Appendix. The key properties of each footing are summarized in table Table 2.2.

Footing	C1	C2	C3
Base Radius [m]	0.02975	0.02975	0.02975
Height [m]	0.0450	0.0900	0.1375
Contact Area [m ²]	0.00278	0.00278	0.00278
Mass M [kg]	0.3526	0.7084	1.0801
1g Average Contact Pressure [kPa]	1.244	2.500	3.811
Mass Mom. Inertia J_y [kg m ²]	0.00013728	0.00063444	0.0019466
Centroid: x_c [mm]	0	0	0
Centroid: y_c [mm]	0	0	0
Centroid: z_c [mm]	22.46	44.96	68.68

Table 2.2: Circular footing properties without attachments.

Because of the circular geometry, it was necessary to machine small recessed flat surfaces on the side of each footing for instrumentation mounting. The mount location numbering scheme is shown as an example in Figure 2.9. The instrumentation mount locations are summarized for each footing in Tables 2.3 – 2.5. Instrumentation properties are summarized in Table 2.6.

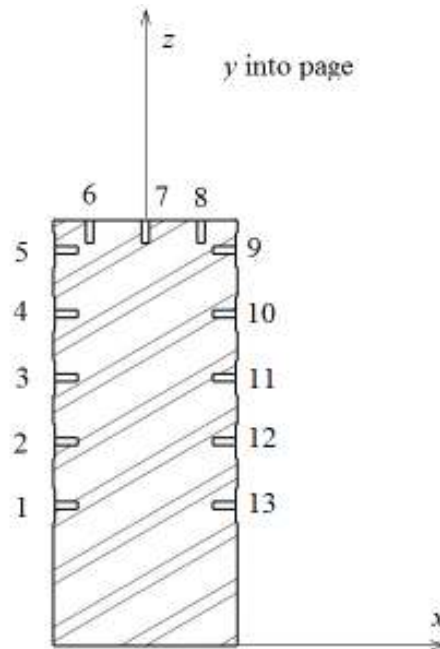


Figure 2.9: Instrumentation mount-points for the largest model foundation, C3. Numbering scheme is similar for footings C1 and C2.

Footing C1: Hole	x [mm]	z [mm]
1	-29.225	15.000
2	-29.225	25.000
3	-29.225	35.000
4 (Load Cell)	-18.000	45.000
5 (VC Accelerometer)	0	45.000
6	18.000	45.000
7 (UH Accelerometer)	29.225	35.000
8	29.225	25.000
9 (LH Accelerometer)	29.225	15.000

Table 2.3: Possible mount-point for instrumentations on footing C1. Actual holes used were specified at the same locations as for the corresponding square footing B13. Total footing height is 45.000 mm, so holes 4, 5, and 6 are on the top surface of the footing.

Footing C2: Hole	x [mm]	z [mm]
1	-29.225	20.000
2	-29.225	40.000
3	-29.225	60.000
4	-29.225	80.000
5 (Load Cell)	-18.000	90.000
6 (VC Accelerometer)	0.000	90.000
7	18.000	90.000
8	29.225	80.000
9 (UH Accelerometer)	29.225	60.000
10	29.225	40.000
11 (LH Accelerometer)	29.225	20.000

Table 2.4: Possible mount points for instrumentations on footing C2. Actual holes used were specified at the same locations for the corresponding square footing, B23. Total footing height is 90.000 mm, so holes 5, 6, and 7 are on the top surface of the footing.

Footing C3: Hole	x [mm]	z [mm]
1	-29.225	45.380
2	-29.225	66.000
3	-29.225	86.630
4	-29.225	107.250
5	-29.225	127.880
6 (Load Cell)	-18.000	137.500
7 (VC Accelerometer)	0.000	137.500
8	18.000	137.500
9	29.225	127.880
10 (UH Accelerometer)	29.225	107.250
11	29.225	86.630
12 (LH Accelerometer)	29.225	66.000
13	29.225	45.380

Table 2.5: Possible mount points for instrumentations on footing C3. Actual holes used were specified at the same locations for the corresponding square footing, B33. Total footing height is 137.500 mm, so holes 6, 7, and 8 are on the top surface of the footing.

Property	Load Cell	Accelerometer
Mass [g]	12.06	2.50
Centroid: x_c [mm]	0.00	0.00
Centroid: y_c [mm]	0.00	0.00
Centroid: z_c [mm]	8.00	5.70
J_x [kg m ²]	3.3265×10^{-7}	4.4192×10^{-8}
J_y [kg m ²]	3.3265×10^{-7}	4.4192×10^{-8}
J_z [kg m ²]	1.5075×10^{-7}	2.1399×10^{-8}

Table 2.6: Summary of Kistler 9001A Load Cell and PCB accelerometers. The accelerometers were hand-picked by PCB specifically for low cross-sensitivity.

With attachments installed in the locations specified by Tables 2.3 – 2.5, the modified centroidal location, mass, and mass moment of inertia values are indicated in Table 2.7. The three footing radii scale with g-level as described in Table 2.8.

Footing	C1	C2	C3
Mass M [kg]	0.37216	0.72796	1.09966
Mass Mom. Inertia J_y [kg m ²]	0.000160974	0.000687434	0.00204597
Centroid: x_c [mm]	-0.1141	-0.0583	-0.0386
Centroid: y_c [mm]	0	0	0
Centroid: z_c [mm]	23.67	46.11	69.73

Table 2.7: Properties of circular footings with attachments installed in the locations described in Tables 2.3 – 2.5.



Figure 2.10: The three circular footings used for testing.

g-level	a_{proto} [m]	p_{proto} [kPa] (C1, C2, C3)	h_{proto} [m] (C1, C2, C3)
1	0.02975	1.2, 2.5, 3.8	0.0450, 0.090, 0.1375
22	0.65450	27.4, 55.0, 83.9	0.9900, 1.9800, 3.0250
33	0.98175	41.1, 82.5, 125.8	1.4850, 2.9700, 4.5375
44	1.30900	54.7, 110.0, 167.7	1.9800, 3.9600, 6.0500
55	1.63625	68.4, 137.5, 209.6	2.4750, 4.9500, 7.5625
66	1.96350	82.1, 165.0, 251.6	2.9700, 5.9400, 9.0750

Table 2.8: Footing prototype radius and height vs. g-level.

2.5 Frequency-Domain Analysis

The vertical-eccentric dynamic tests were conducted by applying random-impact type loading directly to the load cell. Measurements from the accelerometers and load cell were collected simultaneously and converted to the frequency domain via the fast Fourier transform (FFT) algorithm given below (2.1), where capitol X denotes the transformed quantity. Time domain measurements were also recorded in each data file.

$$X(f_k) = \Delta t \sum_{n=0}^{N-1} x_n e^{-i2\pi kn/N}, \quad k = 0, 1, 2, \dots, N-1 \quad (2.1)$$

$$x(t_n) = \frac{1}{N\Delta t} \sum_{k=0}^{N-1} X_k e^{i2\pi kn/N}, \quad n = 0, 1, 2, \dots, N-1 \quad (2.2)$$

For a detailed description of the signal processing and data acquisition system refer to Ashlock (2006) and Soudkhah (2010). The measurements at each location were used to construct frequency response functions (FRF) intended to provide quantitative insights into the motion of the footing. Specifically, these functions represent the acceleration at each accelerometer location per excitation force measured by the load cell. Termed ‘accelerances,’ the transfer functions were theoretically the Fourier transform of the acceleration measurements at each location divided by the Fourier transform of the corresponding force data. Generally, at least three non-collinear accelerance functions were obtained in each test. Accelerances were computed using multiple time windows and averaging. Twenty averages were used for the majority of tests so as to reduce the contribution of random noise without artificially smoothing the data. This can be verified by the repeatability of tests as will be demonstrated in the next section. In Figure 2.11, the notations are defined for vertical-eccentric (VE), vertical-centric (VC), upper horizontal (UH), and lower horizontal (LH) directions. The transfer functions are referred to as VC/VE, UH/VE, and LH/VE, etc.

Units of the acceleration functions are mass^{-1} and can be determined from the acceleration definition using the FFT algorithm given in equation (2.1).

$$A(f) = \frac{\mathcal{F}\{a(t)[m/s^2]\}}{\mathcal{F}\{f(t)[kg\ m/s^2]\}} \quad (2.3)$$

The acceleration units can be written in a few ways as shown in equations (2) through (4):

$$A(f)[units] \rightarrow \left[\frac{\frac{m}{s^2} s}{kg \frac{m}{s^2} s} \right] \quad (2.4)$$

$$A(f)[units] \rightarrow \left[\frac{\frac{m}{s^2}}{kg \frac{m}{s^2}} \right] = \left[\frac{m}{N} \right] \quad (2.5)$$

$$A(f)[units] \rightarrow \left[\frac{1}{kg} \right] \quad (2.6)$$

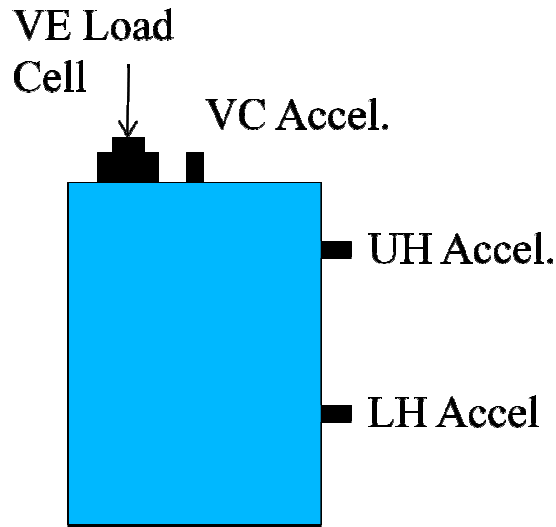


Figure 2.11: Notation for measurement and loading locations on footing.

The form in (2.5) is the most meaningful because it conveys the most transparent physical meaning of the acceleration transfer function which is effectively the ratio of acceleration to force in complex notation. Henceforth, the acceleration functions will be denoted according to the location/direction of the acceleration and force excitation as indicated in Figure 2.11. Specifically, there are four locations of interest: Vertical-concentric, vertical-eccentric, upper-horizontal, and lower-horizontal.

Each transfer function will be referred to in terms of the acceleration and force measurement locations with a prefix (which denotes the acceleration measurement location) and suffix (which denote the excitation location). For example, the accelerance $A_{VC/VE}$ is the ratio of the accelerometer response at the vertical-centric location due to a force excitation at the vertical-eccentric location at the top of the footing.

Chapter 3

Preliminary Testing

3.1 Testing at 1g

To ensure the highest quality of results, many preparations were made at 1g before performing the dynamic centrifuge tests. Testing at 1g is a useful way to develop physical insights prior to centrifuge experiments. For example, centrifuge testing is generally limited by the availability of the facility, whereas 1g tests can be conducted in common laboratory setting. An extensive period of 1g testing was therefore pursued prior to centrifuge testing to further the understanding of the dynamic soil-structure configurations employed and possible issues. Results from testing at 1g are also often useful as a material response reference for centrifuge testing with multiple spin cycles.

3.2 Loading Type and Excitation Level

For the dynamic tests of interest, it was vital to first determine the optimal excitation level and loading type for collecting data. Minimal excitation amplitude is desired in order to obtain responses in the benchmark small-strain levels, but the input must be large enough to overcome noise and produce motion that is measurable within the precision range of the instrumentation. Exciter input is also closely tied to the proximity or contact condition between the exciter bolt and load cell button. By minimizing the contact duration through the use of impact loading in this study, effects on the system that might arise from an exciter's internal dynamics can be minimized and omitted from analytical modeling. Use of impact loading also helps to minimize any cyclic frictional contact effects between the exciter and load cell button during testing.

Multiple 1g test series were conducted using a Siglab Analyzer with a Matlab based user interface. This system is described in detail in Ashlock (2000, 2006). The data collected is in the

same form as in centrifuge testing which has a National Instrument –Labview system which was programmed to emulate and enhance the Siglab setup. The minimum excitation input using Siglab ranged between 0.03 V and 0.05 V, with the gain on the amplifier set to three. This corresponds to maximum impacts ranging between 0.5-1.0 N, and an RMS loading of about 0.03 N. Impacts were made to be sparse whose control must be delicately handled especially for small loading. These levels of loading were found to be sufficient for all footings, but anything lower generally did not produce usable data. Higher excitation yields a stronger and clearer response but may invoke soil's nonlinearity. Typical load cell time histories and impact distributions employed in 1g tests are shown in Figures 3.2 or 3.3. Larger and sharper horizontal transfer function peaks have been observed with impacts that were spread out more sparsely. It should also be noted that a similar but cleaner response can be attained by applying slightly higher excitation ($F_{RMS} > 0.3N$); however the response should be closely monitored for changes in resonance peak locations and magnitudes, as well as asymptotes with proper judgment by the operator. In general, the lowest possible excitation should be applied on the first test in order to define a benchmark. If the excitation is increased beyond a certain level, it has been observed that the first horizontal peak of the acceleration-to-force transfer function will shift towards lower frequencies. In Figure 3.1 for instance, the plot shows a band of responses at different excitation levels where the force level is indicated in Newtons and exciter input voltage in Volts. All three accelerances can be seen to shift to lower frequencies at higher excitation. Note that high excitation increases the VC/VE peak magnitude but it decreases the horizontal accelerance magnitude. Once such shifts occur, even if the excitation is then lowered, the original low excitation response cannot always be recovered due to the modification of the soil-foundation contact.

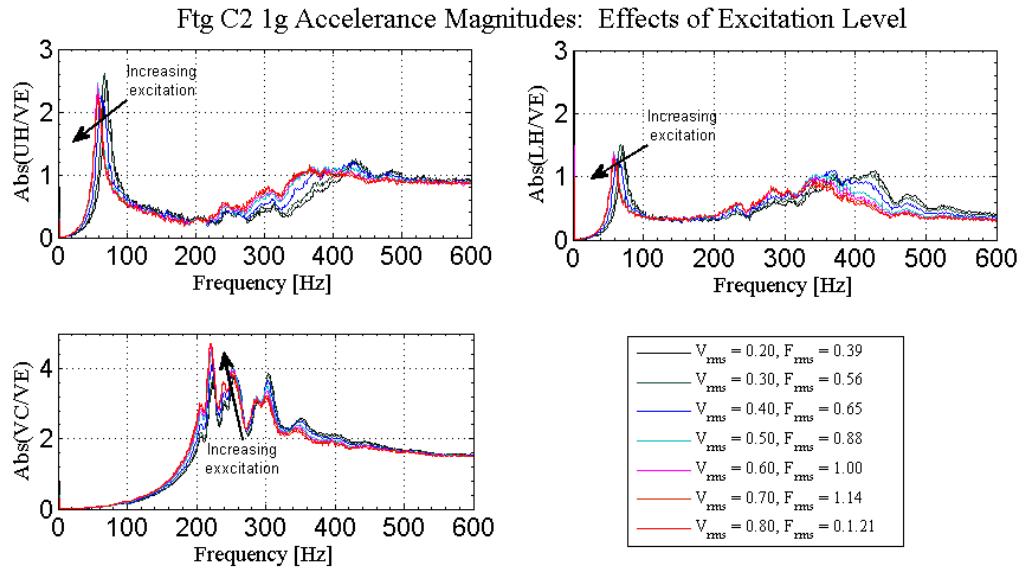


Figure 3.1: Model scale accelerance magnitudes plotted at 1g for footing C2.

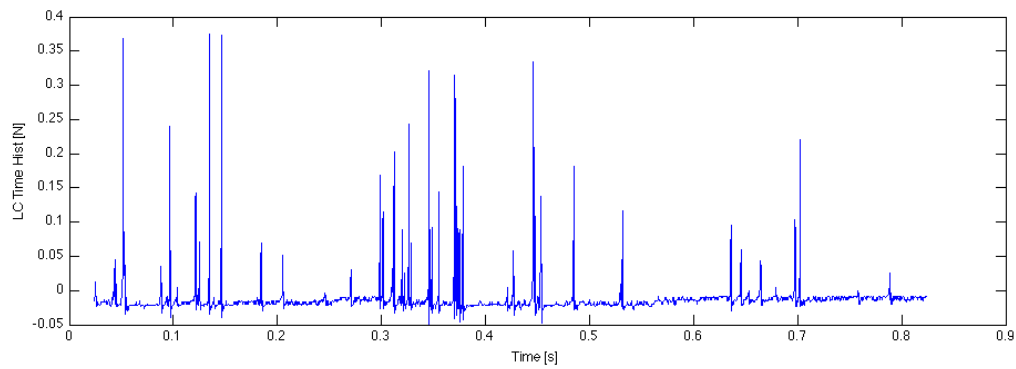


Figure 3.2: Sample 1g load cell time history for footing C2.

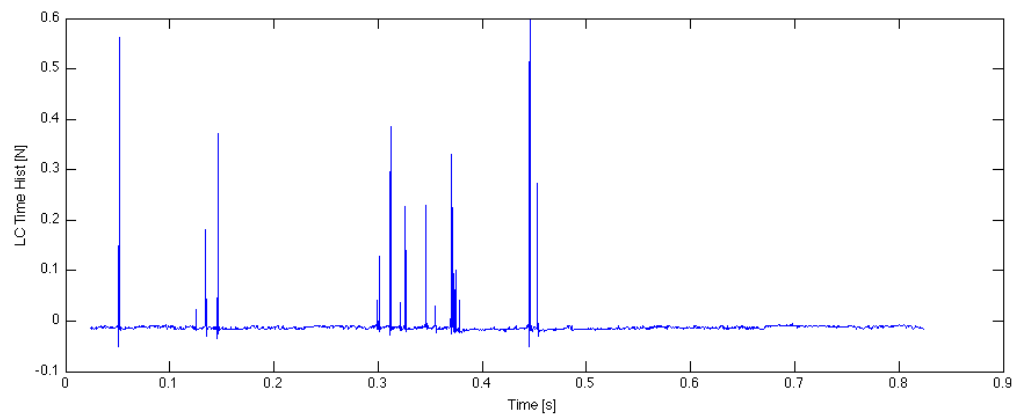


Figure 3.3: Sample 1g load cell time history for footing C2.

3.3 Order of Centrifuge tests as a Function of g-level

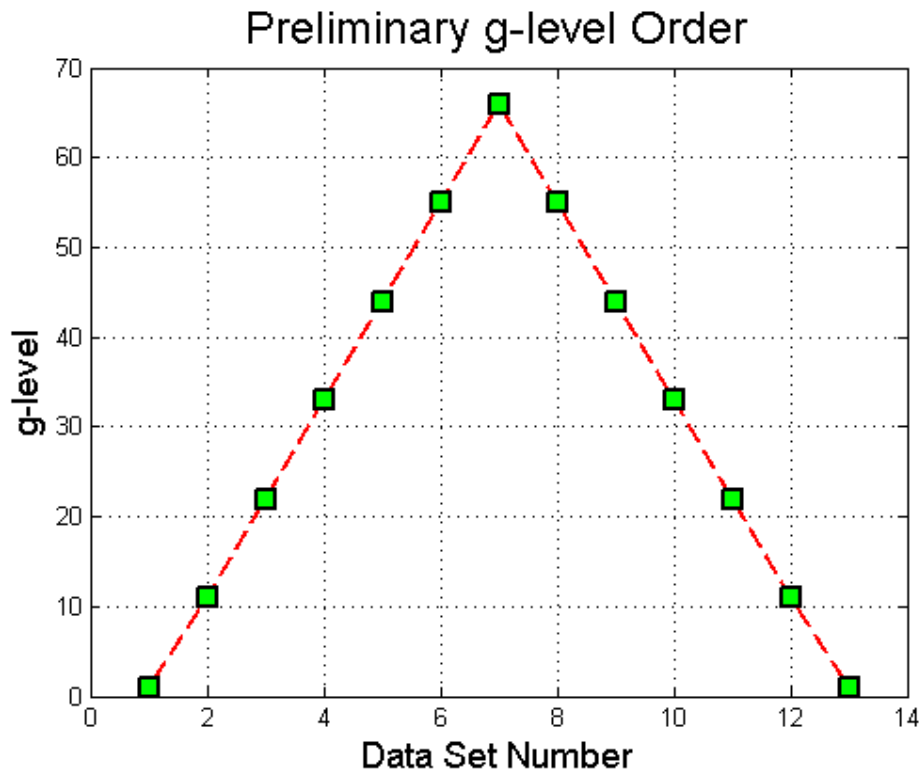


Figure 3.4: g-level order used in previous centrifuge tests conducted with the same and similar container setups. One preliminary set of circular footing data was also collected using this g-level order.

In previous square-footing VE tests, some differences between the spin-up and spin-down responses in test sequences in the form of Figure 3.4 in a single spin-cycle were noted. On spin-down, the transfer functions tend to shift towards lower frequencies in comparison to spin-up. This phenomenon was also found in this investigation to some extent despite using low excitation in circular footing tests (Figure 3.6). Such a behavior is likely caused by the stress created and then trapped in the soil-container system when it has been exposed to high g-forces during spin up. With such conditions, it is not unreasonable to expect a slightly higher soil shear modulus and therefore a stiffer response. This slight stiffening effect has been observed consistently in previous free-field seismic excitation tests (Figure 3.5) as well. In the figure, the accelerances are transfer functions that relate the horizontal motion measured by a central embedded accelerometer on the soil surface

(TCH), to a parallel accelerometer installed underneath the soil in the center of the aluminum base plate (BCH). The base plate is subjected to a horizontal impact loading in the direction of the aforementioned accelerometers to simulate a seismic type excitation (Soudkhah 2010). The plot is labeled as “Forced Free-field Seismic Accelerance” to differentiate it from the unforced ambient tests that were also conducted. The transfer function termed “seismic accelerance” here is dimensionless, as opposed to the acceleration per unit force transfer functions in forced vibration which is the focus of this thesis. One can see that the system exhibits a slightly stiffer response on spin-down (blue) when compared with spin-up (red). While minor, this is believed to be a result of the inelasticity of the soil and the higher residual lateral stress in the soil in the spin-down cycle, and is analogous to the effect of over-consolidation in soil mechanics (see Craig 1995).

Freefield Accelerance: Spin Up (red) Vs. Spin Down (blue)

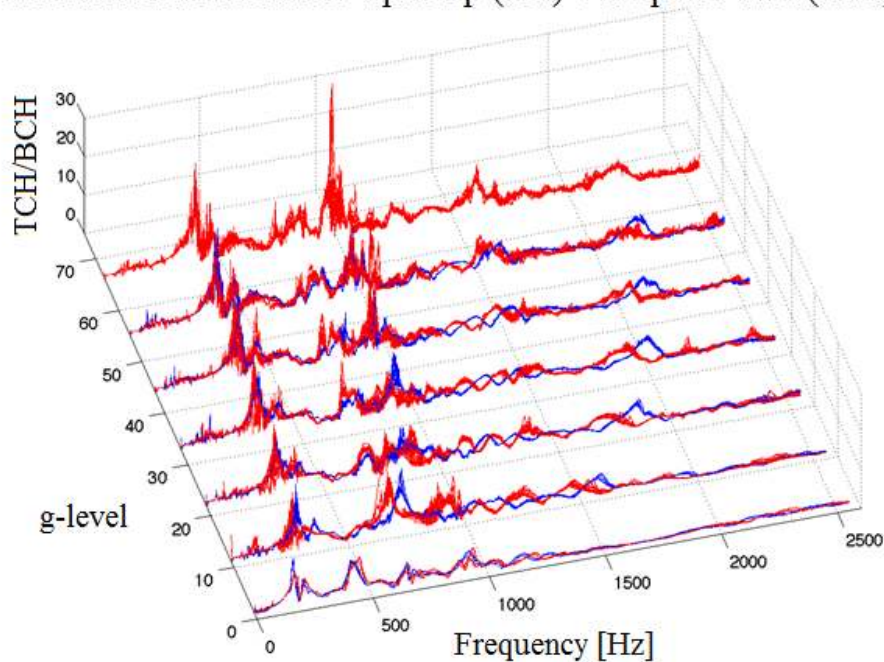


Figure 3.5: Free-field seismic accelerances of the centrifuge soil model at multiple g-levels.

Illustrating the same effects, the results in Figure 3.6 obtained using carefully applied minimal force excitation on Footing C3 show that there is an observable shift of the resonance peak toward lower frequencies on spin -down, notable at lower g-levels. Close-up views of the 33g tests are shown in

Figures 3.7-3.9. Figure 3.6 is a close-up view of the LH/VE accelerance curves taken from Figure 3.6 and highlights the differences between spin-up and spin-down. The rms value of the load cell time history is given on the plot to indicate excitation level. The shift in peak frequency is clear in this picture. In Figure 3.7, a close-up of the UH/VE accelerance curves taken from Figure 3.6 is given to highlight similar differences between spin-up and spin-down. The softer horizontal response during spin-down is observable here. In Figure 3.8, VC/VE accelerance curves taken from Figure 3.6 to highlight the differences between spin-up and spin-down. In contrast to the horizontal accelerances, a frequency shift is not clearly observable in the VC/VE plot.

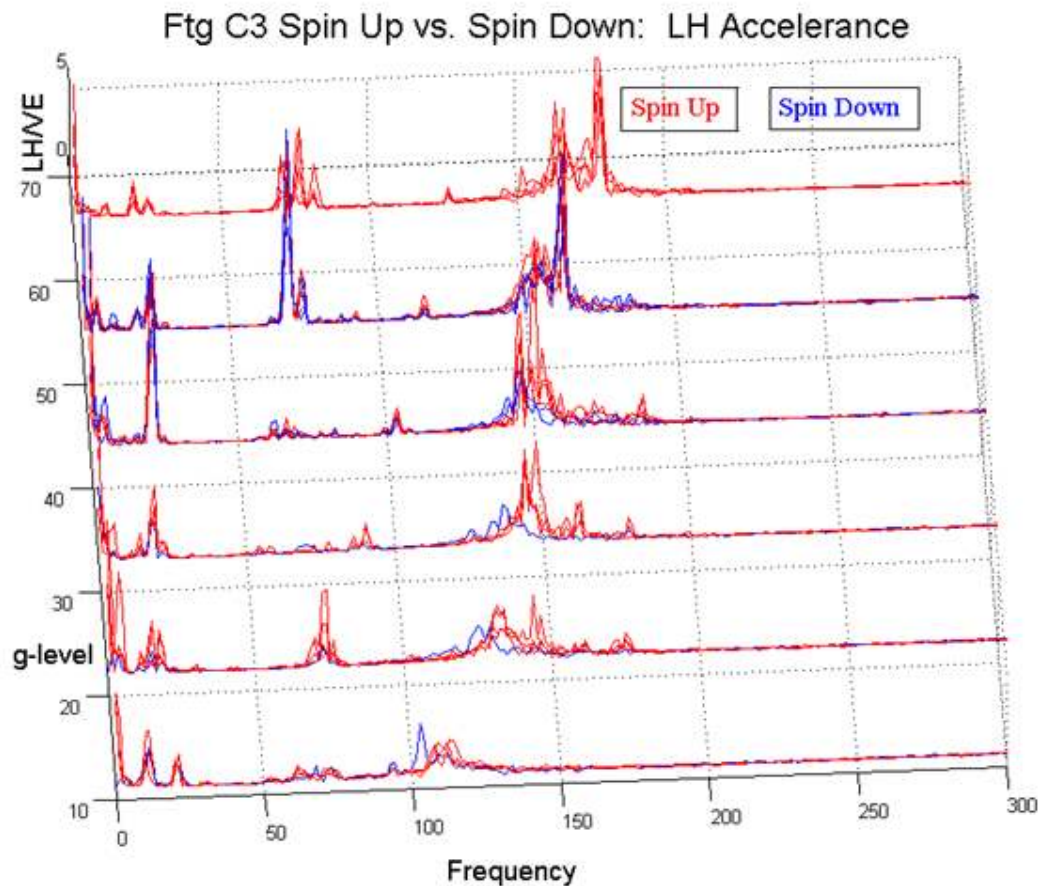


Figure 3.6: Spin-up vs spin-down LH/VE accelerances plotted for footing C3 at multiple g-levels

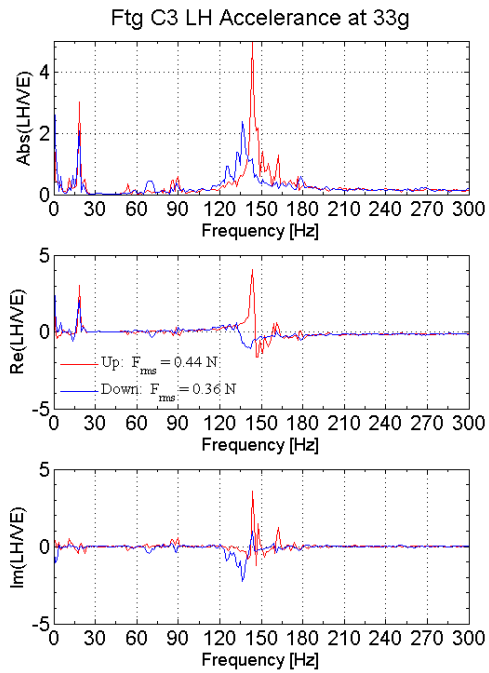


Figure 3.7: LH/VE acceleration curves taken from Figure 3.6 to highlight the differences between spin-up and spin-down.

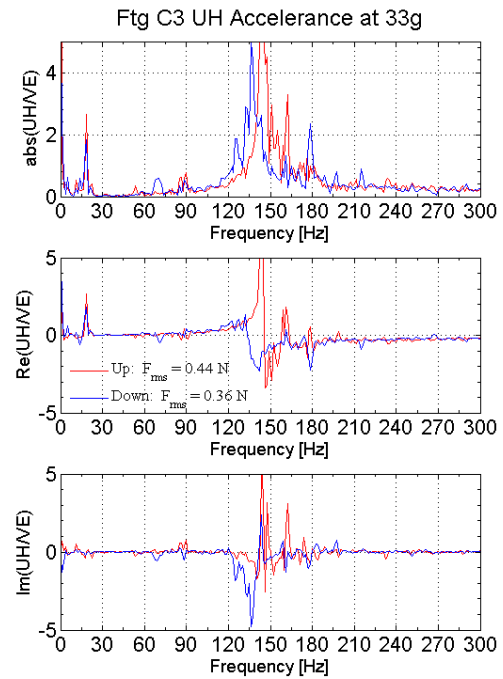


Figure 3.8: UH/VE acceleration curves taken from Figure 3.6 to highlight the differences between spin-up and spin-down.

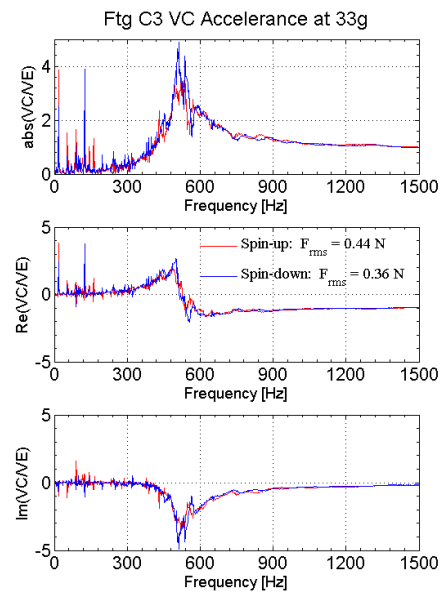


Figure 3.9: VC/VE acceleration curves taken from Figure 3.6 to highlight the differences between

spin-up and spin-down.

Figures 3.5 to 3.9 bring forth questions about which data set to use in comparisons with theoretical predictions or other data, along with a significant band of uncertainty regarding the location of certain features in the frequency domain. To resolve the issue and as an improvement to the experimental procedure, the experimental centrifuge test plan illustrated in Figure 3.10, while more laborious, was pursued. Such a test sequence was found to minimize both the cumulative over-stress effect on the soil (Figure 3.5) as well as the softening observed in Figure 3.6. A useful feature of using this g-level order of testing is the database of 1g tests, as well as the option of repeating tests at other g-levels can be employed to check the consistency. The intermediate 1-g tests served well as a gage of the degree of change in the experimental mode condition between g-levels as a result of the variation of footing-soil contact, embedment, or residual stress in the soil-duxseal system. While it is not always possible to determine the exact source of disagreements in 1g control tests, the model setup can always be re-set or repaired for a new series of tests, and the control tests provide an error measure for the data that has already been collected. Figures 3.11 and 3.12 show some typical intermediate tests conducted for the smallest footing (C1).

It was also important to closely monitor excitation levels in the new testing procedure. For example, comparing Figures 3.6 and 3.1 indicates that perhaps high excitation was applied at some point and produced the observed discrepancy in the spin-up vs. spin-down comparison (Figure 3.6). To overcome the ambient vibration effects at higher g-levels, it was sometimes necessary to apply higher excitation. In turn, the soil is stiffer under the increased stress and can sustain higher force inputs while remaining in the elastic region. Thus, “higher” excitation in this context refers to an excitation level that is high relative to the increased stiffness of the system, meaning that it has the possibility of damaging the soil in the footing region. The intermediate tests can reveal the presence of these effects.

To maintain low levels of force input, the effects of high g-levels on the exciter’s internal assembly also had to be considered. The exciter bolt is supported by a set of internal flexural

springs of the exciter with brackets limiting the extent of travel. At higher g-levels, the bolt can be pulled down by its increased weight, reducing the load cell clearance as a result. If the force is high enough, the bolt can make contact with the load cell and eventually end up resting on the button. At even higher g-levels, the load may be sufficient to push the footing into the soil and disturb the contact condition. As a remedy, negative DC was applied to the excitation system at higher g-levels to pull the exciter bolt away from the footing setup. Continuous load cell measurements were used as verification that the exciter was indeed not making contact. Accidental high force contact was avoided during testing by slowly bridging the gap between the load cell and exciter using continuously increasing DC and an AC input that was barely measureable. Once contact was established, the user could adjust the excitation levels as necessary. Utilizing these considerations along with the g-level order (Figure 3.10) allowed for a greater level of data consistency and reproducibility, as demonstrated by Figure 3.12 through Figure 3.15 (compare with Figures 3.7 – 3.9).

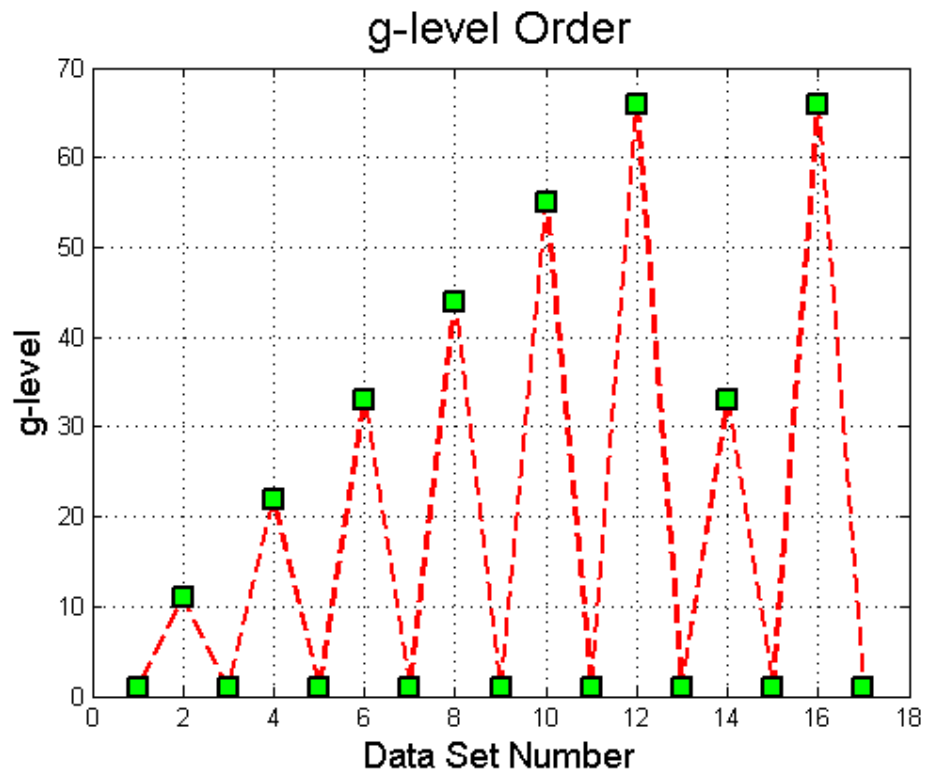


Figure 3.10: The modified test sequence to minimize stiffening/softening effects observed in Figures 3.5 and 3.6 in spin-up versus spin-down.

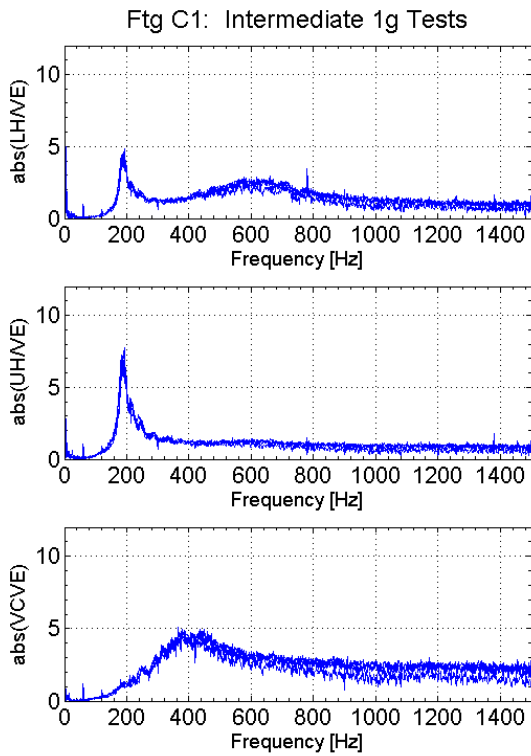


Figure 3.11: Footing C1 accelerance magnitudes for intermediate 1g tests, indicating data consistency.

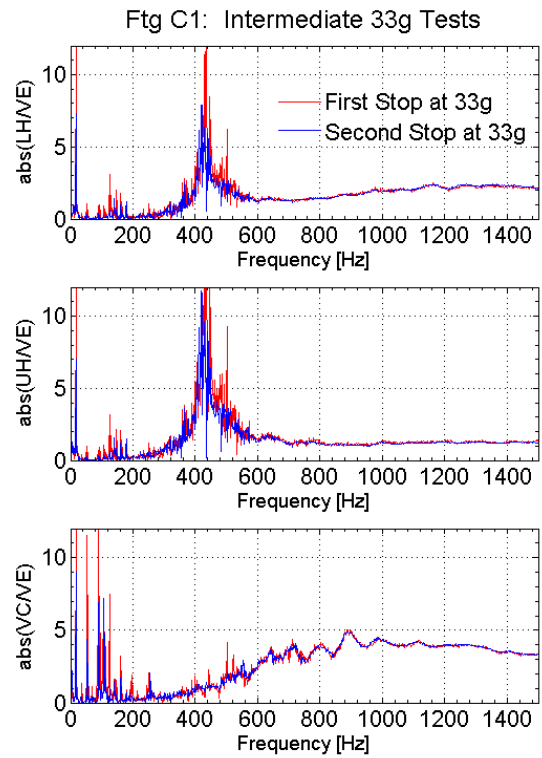


Figure 3.12: Footing C1 accelerance magnitudes for the first and last 33g test using the g-level order given in Figure 3.10.

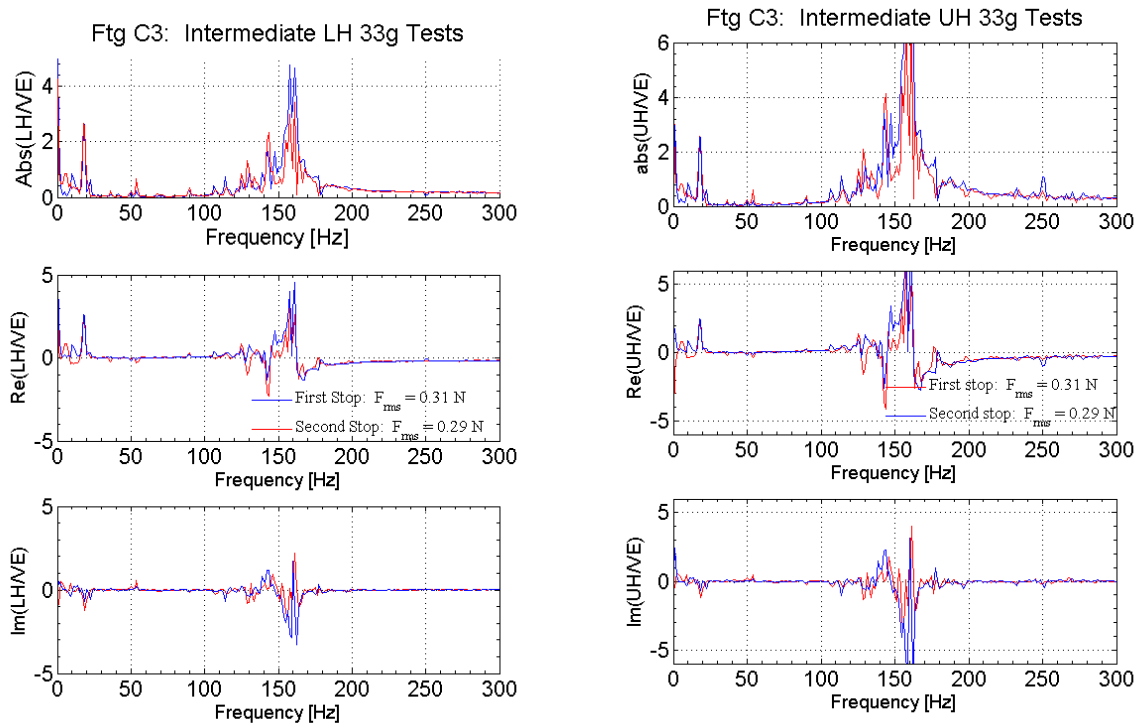


Figure 3.13: Footing C3 LH/VE accelerance plot comparing the first and second stop at 33g (see Figure 3.10 for testing order).

Figure 3.14: Footing C3 UH/VE intermediate 33g test using the g-level order from Figure 3.10.

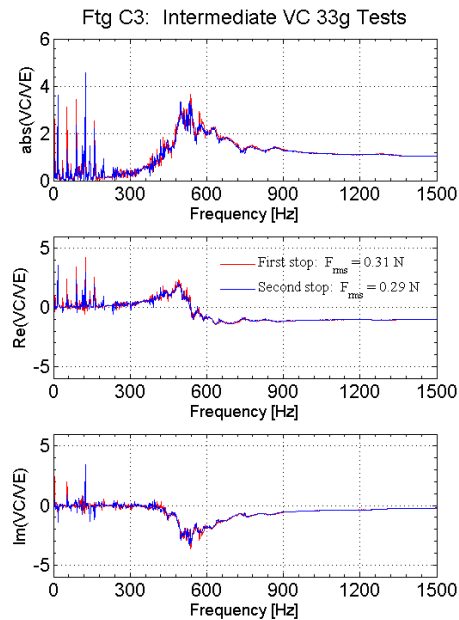


Figure 3.15: Footing C3 VC/VE 33g accelerance comparison using the g-level order described in Figure 3.10.

3.4 Quality of Soil-Footing Contact

With similar concerns in full-scale, the quality of soil-footing contact is often one of the reasons for the sensitivity to excitation level as depicted in Figure 3.1. Because the soil used was a dry cohesionless sand, it can easily be permanently displaced by the leading edge of the footing when undergoing rocking type motions if a high enough excitation is applied. Additionally, if during the placement, the footing is not lowered onto the sample in a direction that is normal to the soil surface, the possibility of non-uniform contact and depression of the soil sample may arise. Furthermore, non-uniform contact can also occur if the soil surface does not match the flat underside of the footing during placement. As a countermeasure, after each placement the soil in the footing region was lightly tamped using a smooth piece of aluminum to fill any small gaps that may have resulted from the footing placement.

In another attempt to improve the contact and aid in preserving the compacted soil condition, a single layer of coarse sand was superglued to the bottom of footing C2 for an additional series of 1g tests. Soil grains that passed through a #10 sieve and were retained by a #12 sieve were used on the basis that they were large compared to the silica sand grains but small on the scale of the footing and container. This relative coarseness of the soil was chosen in hopes that it would help prevent the soil from moving laterally, out from under the footing.

The effects of the local light tamping and the coarse grain (gravel) soil-footing interface are highlighted in Figures 3.16 – 3.19 depicting a series of 1g tests. The major effect of the gravel interface was an increase in the VC/VE peak magnitude (Figures 3.16 and 3.17). Horizontal peak frequencies were considered equal within the level of precision garnered by the variation of measurements from test to test. This effect of increasing VC/VE peak magnitude is similar to the phenomenon observed with increasing excitation (Figure 3.1). The gravel interface was also more damaging to the soil and required additional time for repairs when removing and replacing the

footing on the sample. Because there seemed to be no added benefit of the gravel interface, it was not used further in the centrifuge tests. The effects of a rough interface could be more important in the torsional loading.

The light tamping procedure was utilized for all data presented in this report unless otherwise noted. The effects of the procedure were an increase in horizontal peak frequency and a decrease in VC/VE peak magnitude. For the particular data shown in Figures 3.16 and 3.17, this frequency shift amounted to 4 Hz (5%) for the smooth interface and 9 Hz (11%) for the gravel interface tests. The largest difference in Figure 3.9 is in the VC/VE transfer function peak magnitude. Figure 3.10 shows the data for both a smooth and gravel soil-footing interface with some tamping to improve the contact at the edge of the foundation. In both cases the first horizontal peak is shifted higher by the tamping procedure (see Figure 3.16). As in Figure 3.16 the VC/VE acceleration peak magnitude is higher for the gravel interface. Figure 3.11 is a direct comparison of the results in Figures 3.16 and 3.17. One can see that the difference appears to be largest for the VC/VE peak magnitude. Figure 3.12 is the same as Figure 3.18 but plotted at a scale highlighting the peak regions. The light tamping in the footing region shifts the horizontal peaks to a slightly higher frequency (85 Hz vs 81 for the smooth interface, 87 vs 78 for the gravel interface).

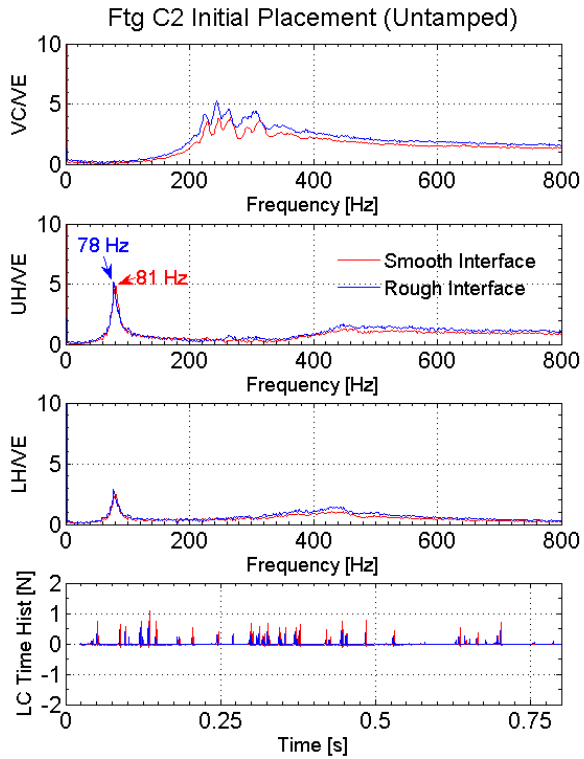


Figure 3.16: $1g$ accelerances of footing C2, showing the effects of a roughened soil-footing interface on the response.

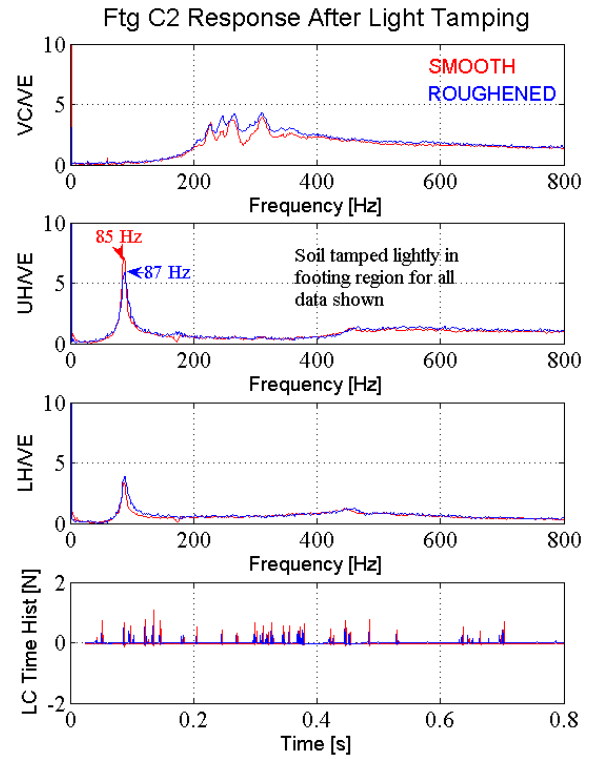


Figure 3.17: Footing C2 accelerance magnitudes plotted to show the effects of light tamping of the soil in the footing region in an attempt to improve the contact condition.

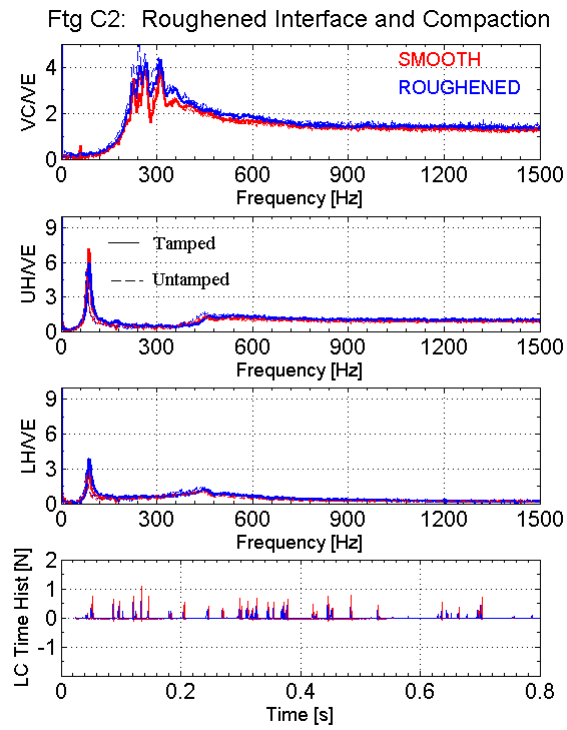


Figure 3.18: Comparison of Model C2's response on tamped and untamped soils.

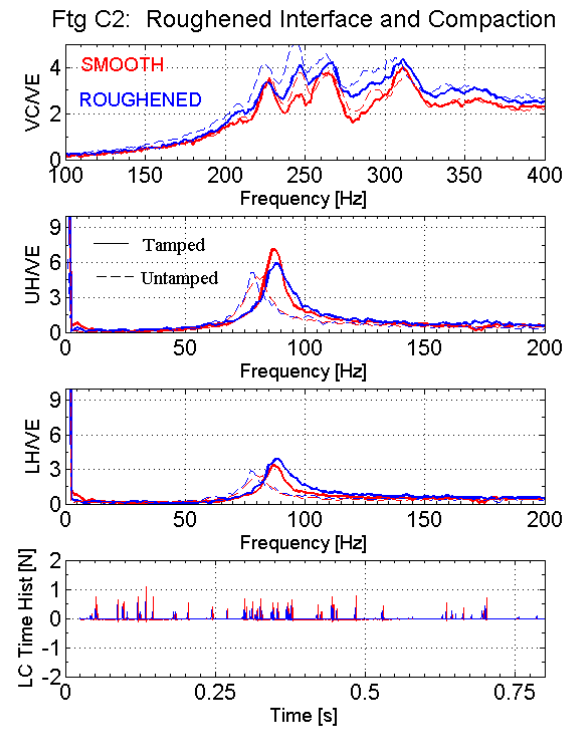


Figure 3.19: Close-up of Figure 3.18 but plotted at a scale highlighting the peak regions

Chapter 4

Experimental Results and Analysis

4.1 Typical Response Features

In this chapter, the results from extensive centrifuge testing of all three footing models are presented. There are major trends in the data sets that can easily identified, with respect to prominent response features and g-level. Plotted in this section are the LH, UH, and VC acceleration-per-unit-force transfer functions for each footing at a number of g-levels. Results in model scale will be discussed to directly interpret the results. To provide practical insight into the corresponding full-scale problems, model data will also be converted to prototype length scale according to centrifuge scaling relationships. A comparison with theory currently in use in engineering analysis will also be made in the prototype scale to shed further light on the challenge of this class of dynamic soil-structure interaction problems.

To begin, Fig. 4.1-4.3 is a set of typical transfer functions for footing C3 at 33g in model scale. One can see that the features of the upper horizontal (UH) and lower horizontal (LH) accelerances in Fig. 4.1 and 4.2 are similar, a comparison of which is shown in Fig. 4.3. The VC/VE accelerance typified by Figure 4.4 is described by a wide gentle peak containing many smaller peaks; it eventually reaches an asymptote which is inversely proportional to the mass of the footing. Specifically, in high frequencies, the magnitude of the transfer function approaches a value of 0.9 kg^{-1} , close to the $1/m$ value for footing C3 (0.923 kg^{-1}). This asymptotic behavior can be shown theoretically (Ashlock 2006), and observed in the measured VC/VE accelerance (see Figure 4.4). The smaller peaks may vary depending on footing placement quality and excitation level.

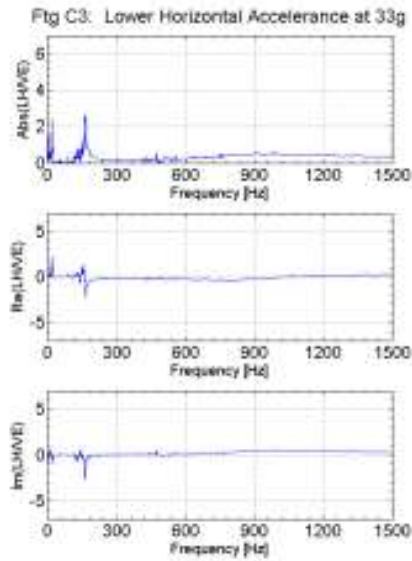


Figure 4.1: Footing C3 LH/VE accelerance recorded at 33g on the centrifuge.

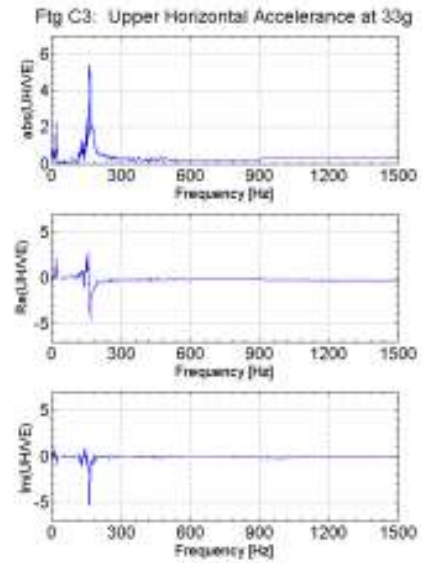


Figure 4.2: Footing C3 UH/VE accelerance recorded at 33g on the centrifuge.

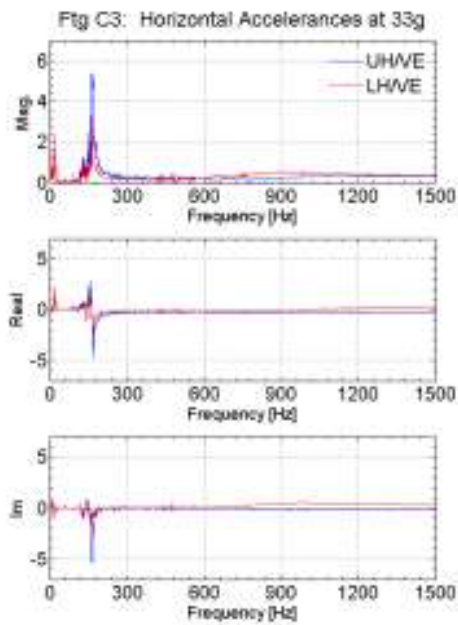


Figure 4.3: UH//VE and LH/VE 33g accelerances plotted for footing C3.

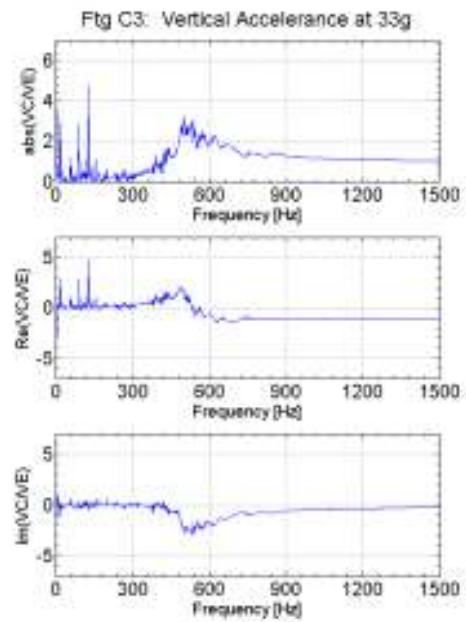


Figure 4.4: Footing C3 VC/VE accelerance recorded at 33g on the centrifuge.

Shown as a close-up of the UH/VE and LH/VE responses in Figure 4.5, two main features that characterize both the upper and lower horizontal accelerances are a sharp peak at low frequency (between 100 and 200 Hz) followed by a soft smooth peak spread over the higher frequency range. As one would expect, the first peak frequencies of the UH/VE and LH/VE accelerances agree but differ in both width and magnitude, with the larger measurements recorded by the upper accelerometer. Notice also that the real and imaginary parts of the upper and lower horizontal accelerances have the same sign in the first peak region. Both of these observations support past observations (e.g., Ashlock 2006) that this lowest resonant frequency corresponds to a ‘rocking’ mode. This is consistent with the assumptions of small deformation and the no-slip frictional contact condition at the soil interface, which gives significant resistance to horizontal motion in the contact region and leaves the footing more free to move at the upper accelerometer location by comparison. The second peak’s magnitude however is much lower in comparison with the first peak in both UH and LH accelerances. Furthermore, comparing the UH and LH responses, the second peak is much more prominent in the LH/VE accelerance of footing C3 (see the close-ups in Figures 4.6 and 4.7). Looking at the upper and lower horizontal measurements in their real and imaginary parts, one can see that the signs are now opposite. These observations signify that the second peak is associated with motions in opposite directions at the two points on the vertical plane. This is indicative of a higher-order vibration mode in a dynamic system. The asymptotic values at high frequency of the horizontal transfer functions depend on footing’s mass, mass moment of inertia, and instrumentation locations, as observed in Ashlock (2006).

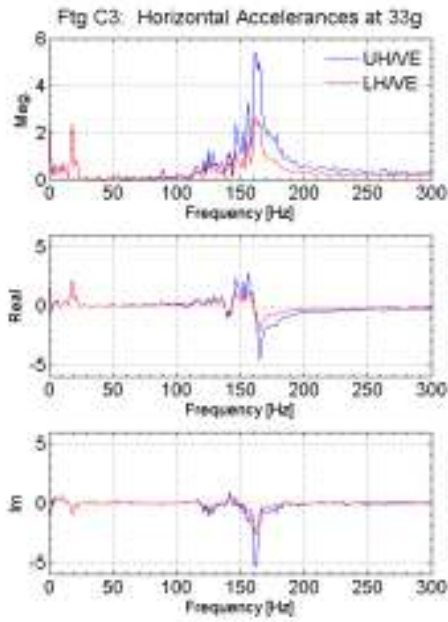


Figure 4.5: Close-up around first peak horizontal accelerances of Footing C3 at 33g.

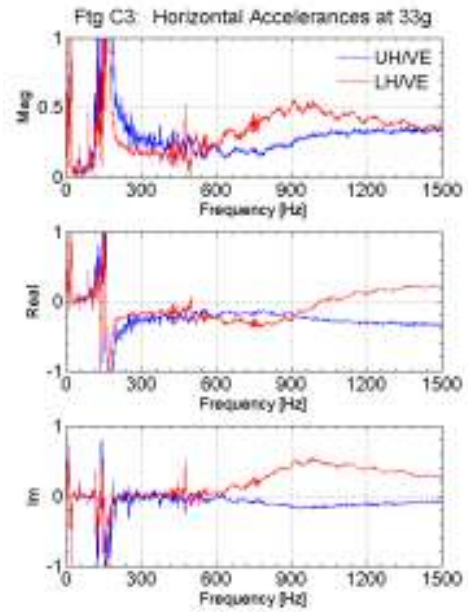


Figure 4.6: Close-up around the second horizontal peak in UH/VE and LH/VE accelerances.

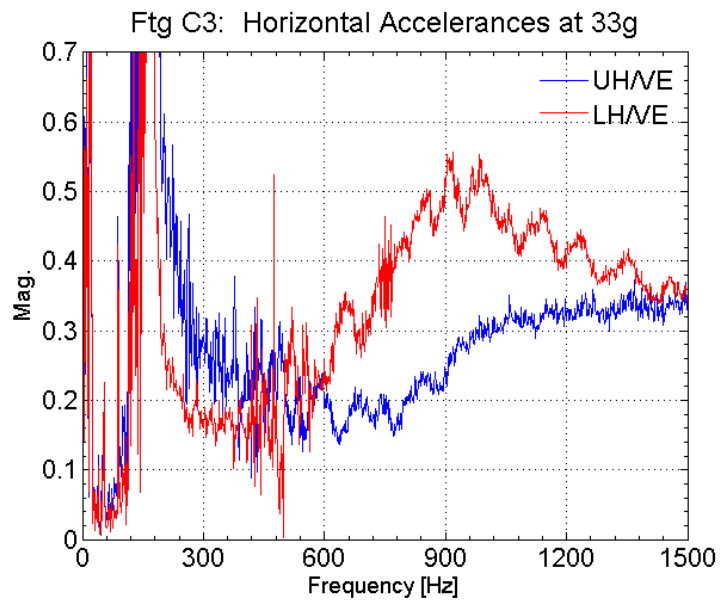


Figure 4.7: Close-ups for second peak in horizontal acceleration magnitudes of Footing C3 at 33g.

4.2 Typical Measured Accelerances

Next, we consider each measured transfer function in relation to g-level as shown in Figures 4.10 – 4.21. As the g-level is increased, the effective weight of the entire system, as well as the stress in the soil, Duxeal, and rubber will increase. According to experimental studies such as those of Hardin and Drnevich (1972), the soil shear modulus G is approximately dependent on the square root of the mean stress σ_{mean} as in

$$G_{HD} [psi] = 1230 \frac{(2.973 - e)^2}{(1 + e)} (OCR)^K \sigma_{mean}^{1/2} \quad (4.1)$$

where e is the void ratio and OCR is the over-consolidation ratio of the soil. As a result, the soil shear modulus is expected to increase with g-level. While the footing mass is not affected by the g-level, the resonant frequencies will likely increase due to the stiffening of the soil in enhanced gravity. The consequences of such effects can be observed in Figures 4.8 – 4.19 where all transfer functions for Footing C3 are shown. They generally all shift towards higher frequencies with increasing g-level. In Fig. 4.9 which is close-up of Fig. 4.6 near the first resonant frequency for example, the shift of features toward higher frequencies with increasing g-level is observable even though the peaks are somewhat jagged. Looking at close-up in Figure 4.8 around the mild second peak of the horizontal accelerance, one can confirm the same trend even though it doesn't have the sharpness of the first peak. Note that the second peak magnitude shown in these data sets does not change significantly with respect to g-level. Analogous observations can be made about the UH/VE accelerances in Fig. 4.11-4.14. Figure 4.9 is a close-up on the peak region of the vertical VC/VE transfer function. With increasing g-level, the peak is clearly shifting to higher frequencies.

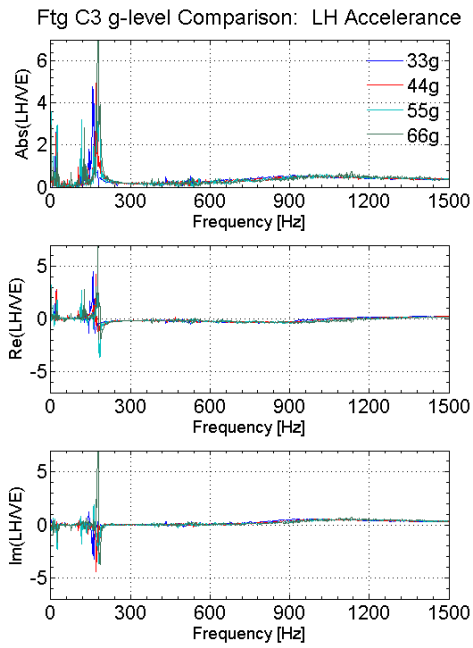


Figure 4.10: Overview of VC, UH and LH accelerances for footing C3 at 33, 44, 55 and 66g.

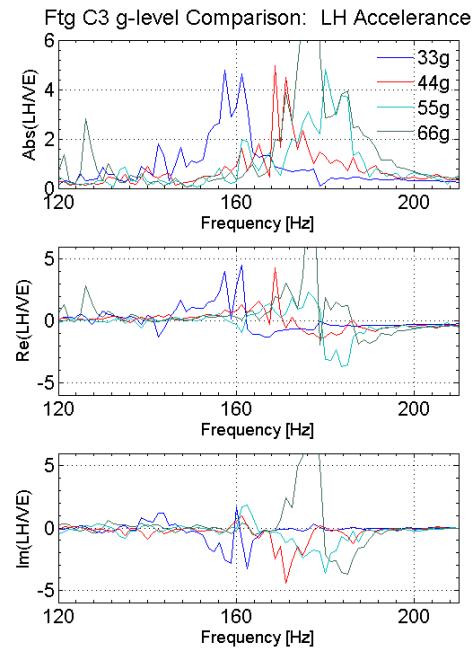


Figure 4.11: Close-up of VC, UH and LH accelerances for footing C3 at 33, 44, 55 and 66g near first resonance of LH/VE response.

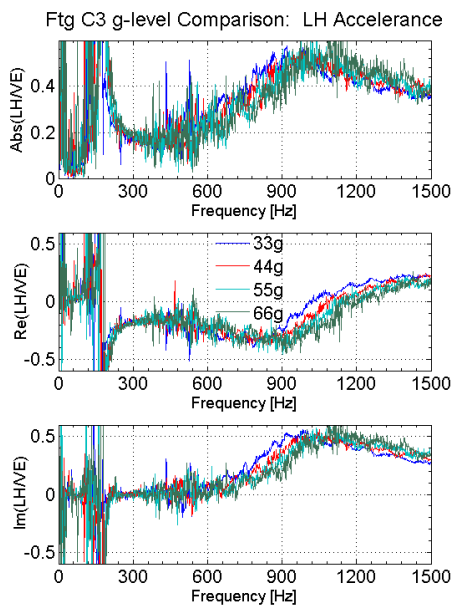


Figure 4.12: Close-up of VC, UH and LH accelerances for footing C3 at 33, 44, 55 and 66g near second resonance of LH/VE response.

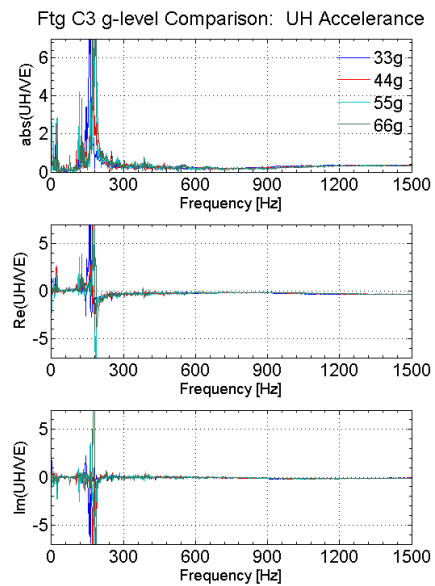


Figure 4.13: Overview plots of the UH/VE acceleration for footing C3 at 33, 44, 55 and 66g

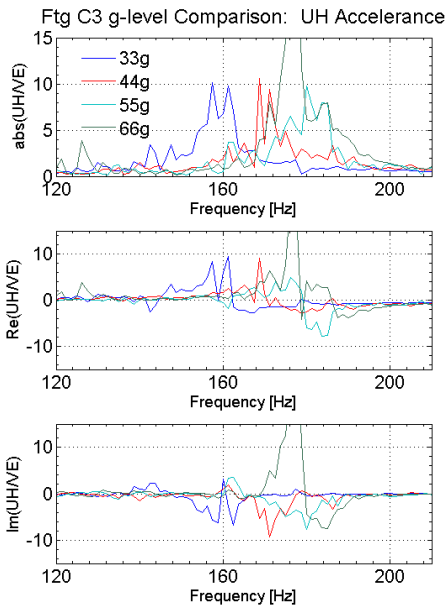


Figure 4.14: Close-up of VC, UH and LH accelerances for footing C3 at 33, 44, 55 and 66g near first resonant frequency range.

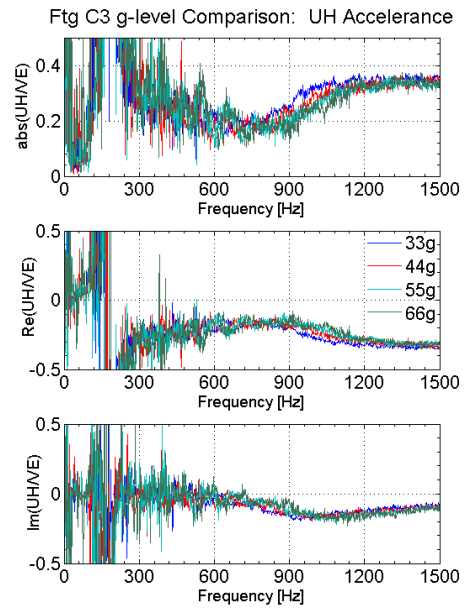


Figure 4.15: Close-up for the UH/VE transfer function for footing C3 at 33, 44, 55 and 66g near second peak.

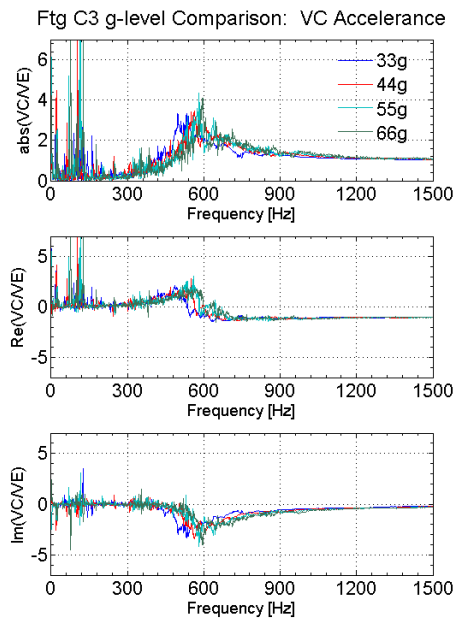


Figure 4.16: VC/VE accelerances for footing C3 at 33, 44, 55 and 66g.

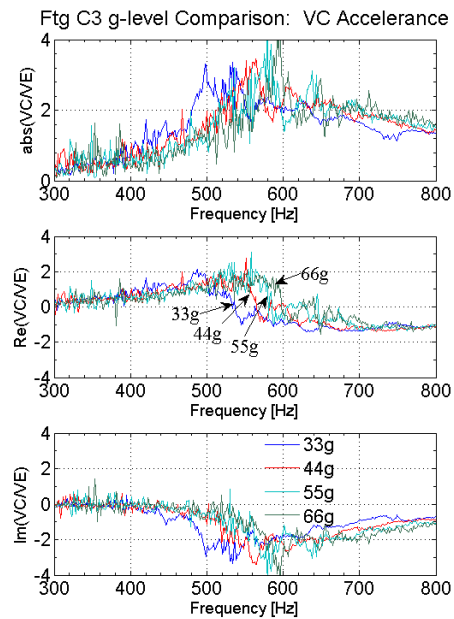


Figure 4.17: A close-up on the peak region of the VC/VE accelerances for footing C3 at 33, 44, 55 and 66g.

Plotting the results in the close-ups (e.g. Figure 4.15) sometimes appears cluttered but it allows for a direct comparison of transfer functions by g-level on the same scale. The stiffer response trend with increased g-level is quite clear when comparing 33g, 44g, and 55g results, but not as clear in the horizontal peak when comparing 55g and 66g. As previously mentioned, the soil shear modulus increases with the square root of the mean stress (Equation 4.1). On the centrifuge, this correlates to the square root of g-level. Consequently, the predicted increase in shear modulus grows smaller as g-level is linearly increased. This explains the smaller frequency shift between 55g and 66g when compared with 33g and 44g for example.

The first sharp horizontal peak's magnitude can be seen to be somewhat variable between g-levels, and even when comparing tests conducted at the same g-level. This is not so in the case of the milder vertical peak, second horizontal peak, or either asymptotic value. Each of the latter aforementioned features remains more or less constant in magnitude throughout the test series. These are useful observations to remember when comparing the results with theoretical predictions. Because of the nature of the soil, electrical noise and ambient vibrations from the centrifuge, there are unavoidable variations at each g-level and accelerances may vary in clarity. As previously mentioned, the first horizontal peak magnitude is sensitive to these effects, and has sometimes been observed to split or exhibit spikes in correlation with g-level, excitation amplitude, or footing placement. This can be seen to a certain degree in the plots, where sometimes spikes within the first peak have equal or contrasting magnitudes (Figure 4.12). The peak can also appear "chopped-off" in some data sets. To see the underlying trends more easily, the foregoing accelerance data are plotted three-dimensionally in Figure 4.16 – 4.19 versus both frequency and g-level. In Figure 4.16 for example, one can see how the peak is split at times with the largest portion sometimes residing in different respective locations in each g-level. Despite this somewhat lack of clarity, it is straightforward to observe the frequency shift in the accelerances. While the visualization is affected by viewing angle, the 3D method of presentation complements well the 2D plots which are

useful for quantitative comparisons.

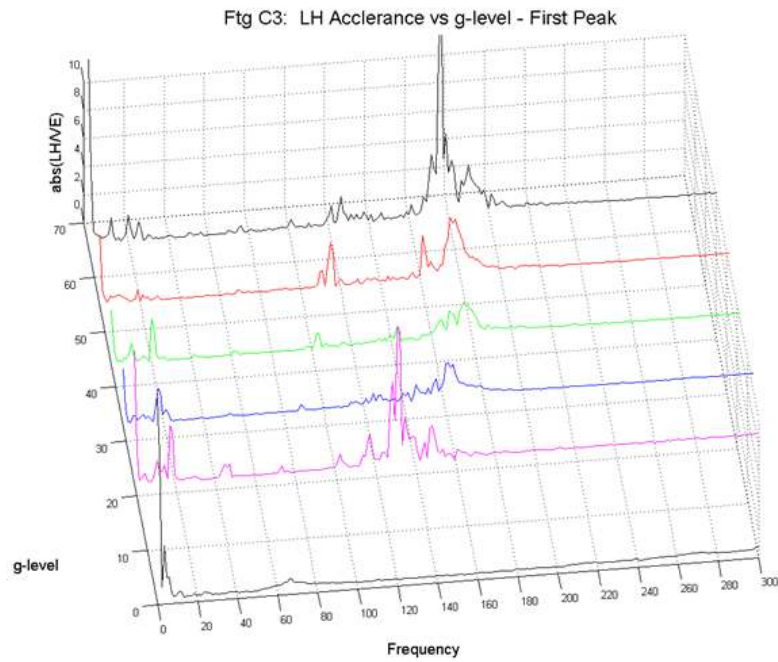


Figure 4.18: Close-up of LH/VE accelerance near first peak for footing C3 at 1, 22, 33, 44, 55 and 66g.

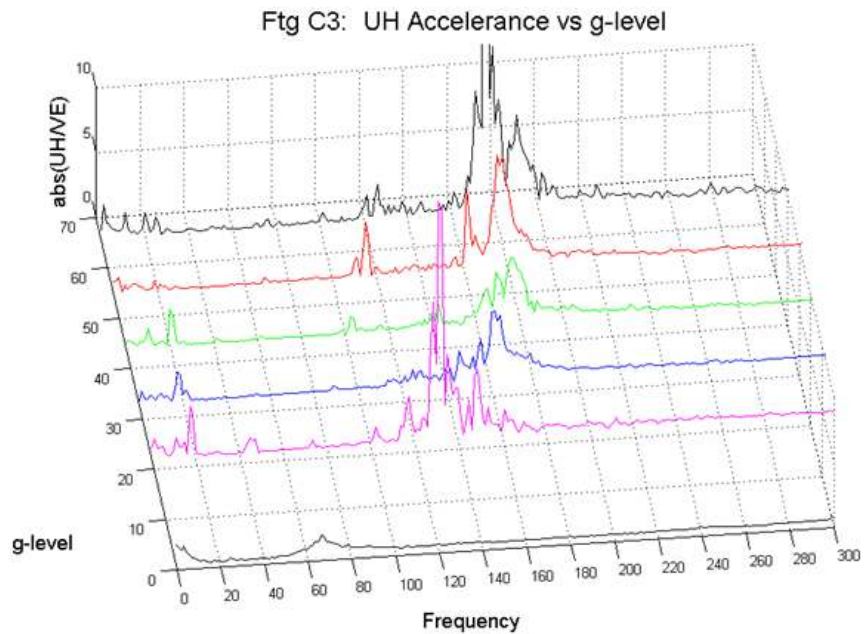


Figure 4.19: Close-up of UH/VE accelerances near first peak for footing C3 at 1, 22, 33, 44, 55 and 66g.

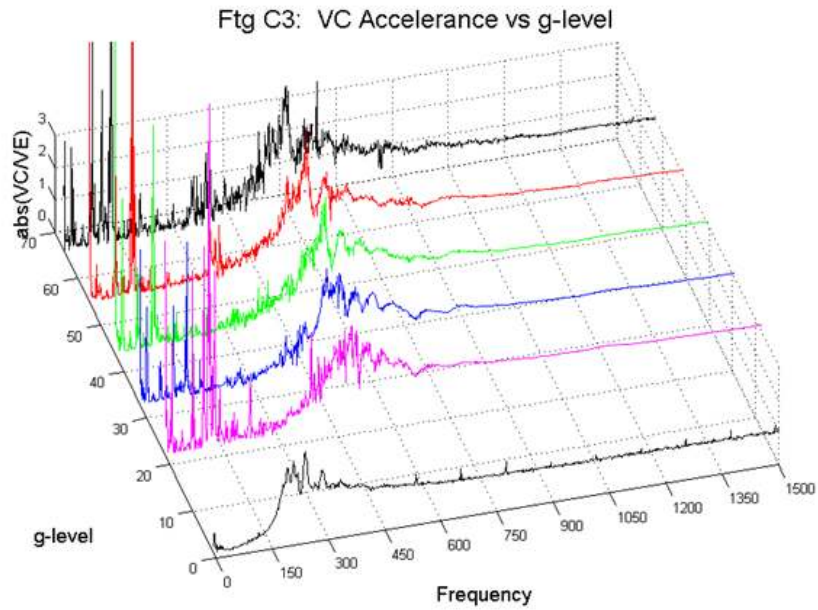


Figure 4.20: VC/VE accelerance for footing C3 at 1,22, 33, 44, 55 and 66g.

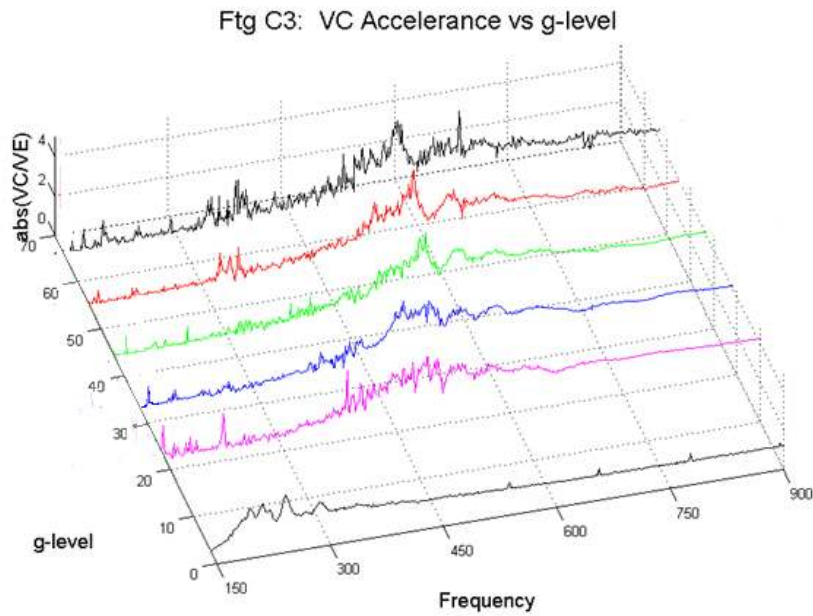


Figure 4.21: Close-up of VC/VE accelerance near first peak for footing C3 at 22, 33, 44, 55 and 66g.

For a clearer understanding by engineering practice, it is also meaningful to present the data in prototype scale. As with model scale, accelerances are in units of mass^{-1} and frequency is time^{-1}

(dynamic). The proper scaling relations for centrifuge tests are listed in Table 2.1 of Chapter 2. Referring to the table, the measured acceleration and frequency data must be multiplied by factors of n^{-3} and n^{-1} respectively. Accelerance units for plotted prototype data are $k t^{-1}$ (kilotonne⁻¹, same as Gg^{-1}). An equivalent acceleration per force unit would be $(mm/s^2)/kN$. Length scales directly with g-level, so a footing at the nth g-level will correspond to one with a radius that is n times larger than that of the model. Consider Figures 4.20 – 4.27 with this information in mind. As the scale factors are applied to the entire data set directly, electrical noise and ambient vibrations from the centrifuge (under 100 Hz for example) will be scaled as well. Units for all prototype scale plots are $(mm/s^2)/kN$, which are equivalent to Gg^{-1} . The radii, contact pressure, height, and correspondence with g-level for each prototype footing can be found in Table 2.8. Radii are also listed on the plots.

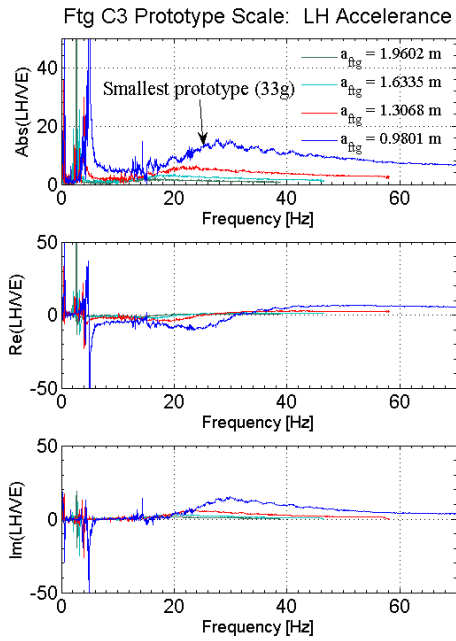


Figure 4.22: LH/VE acceleration for footing C3 at prototype scale.

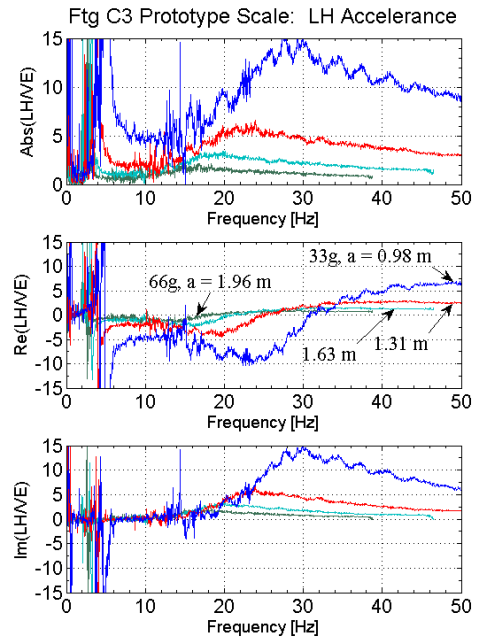


Figure 4.23: Second peak in the LH/VE acceleration of footing C3 at prototype scale.

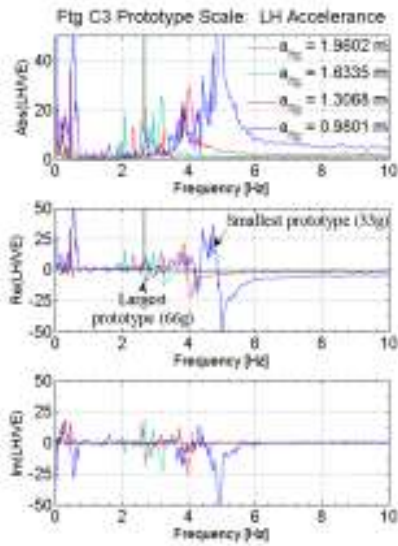


Figure 4.24: The first peak in the LH/VE acceleration of footing C3 at prototype scale.

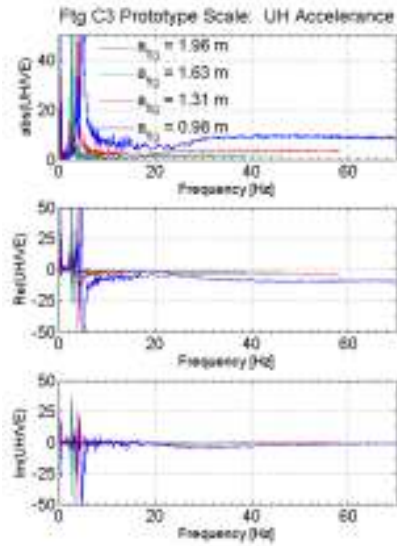


Figure 4.25: UH/VE acceleration for footing C3 at prototype scale.

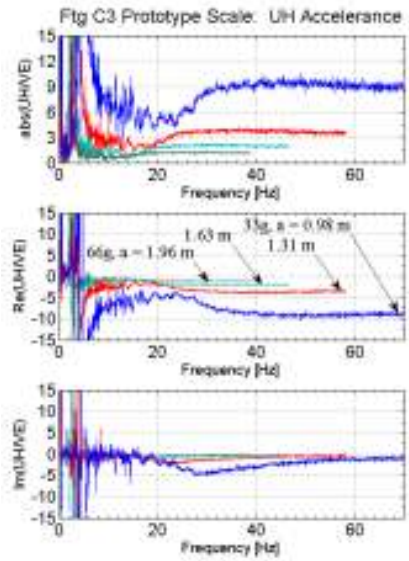


Figure 4.26: The second peak and asymptote of the UH/VE acceleration of footing C3 at prototype scale.

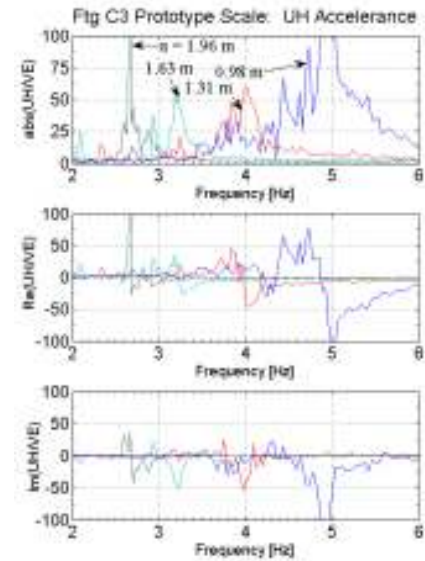


Figure 4.27: Close-up on the first peak region of the UH/VE acceleration of footing C3 at prototype scale.

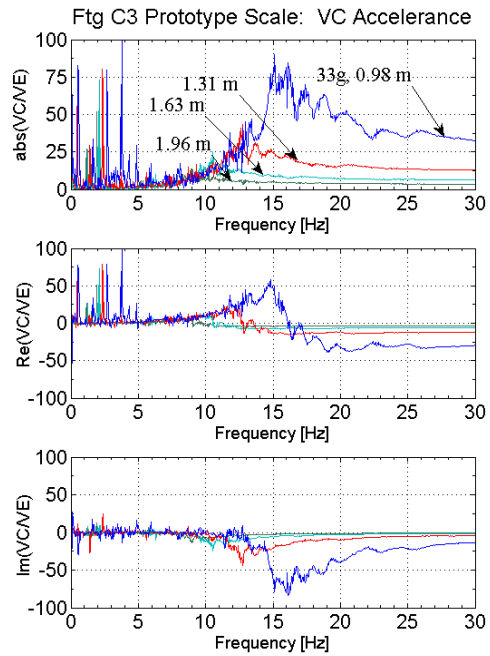


Figure 4.28: VC/VE acceleration for footing C3 at prototype scale.

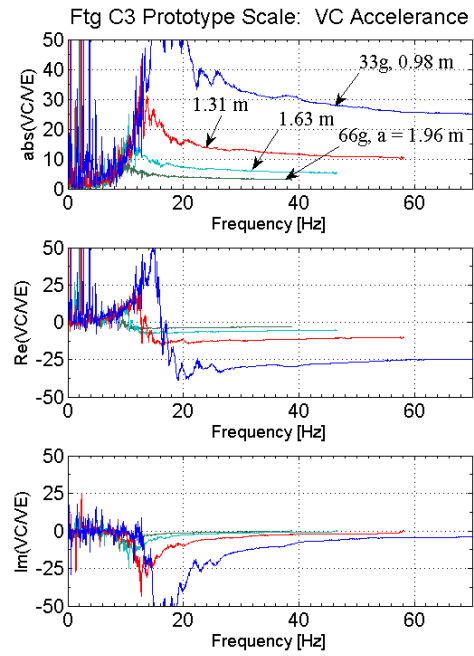


Figure 4.29: Asymptote region of the VC/VE acceleration for footing C3 at prototype scale.

One should notice that the asymptotic values are no longer matching for data collected at different g-levels as higher g-levels correspond to larger prototype foundation's size and mass. The VC/VE accelerance should approach an asymptote of $1/m$ at high frequencies. In prototype scale, these curves approach the reciprocal of the prototype footing mass (Figure 4.27). Additionally, the larger prototypes have a smaller response overall. This trend can be seen clearly in Figures 4.20 – 4.27.

There remains a clear trend relating peak frequency to g-level. In this case, it is a trend towards lower frequencies with increasing footing scaled mass and dimensions. In turn, scaled mass and length both increase with g-level. As a result, if viewed in prototype scale as opposed to model scale, the data set order will appear to be in the reversed when sorted with respect to peak frequency. This effect is demonstrated best in Figure 4.25.

All of these observations are consistent with how one would expect full size footings to behave under the given conditions. A larger more massive footing should have a lower primary resonance peak. The $1/m$ value is also smaller for larger footings, so a smaller asymptotic value is to be expected.

As previously mentioned, a total of three different footings were examined in this study. Each footing was machined with the same radius, differing only in height and number of instrumentation mount points. As a result, test in each footing and g-level combination provides data for a particular prototype soil-structure configuration. The larger and heavier footing should have a greater local effect on the soil's response whereas the smaller footing's data is closer to the free field response. In prototype scale, each footing and g-level corresponds to a different contact pressure (see Table 2.1 for pressure scaling relation). A preliminary 1g comparison plot of footings C2 and C3 is shown in Figure 4.28. An in-depth look comparing the behavior of each footing will be made after they are examined individually.

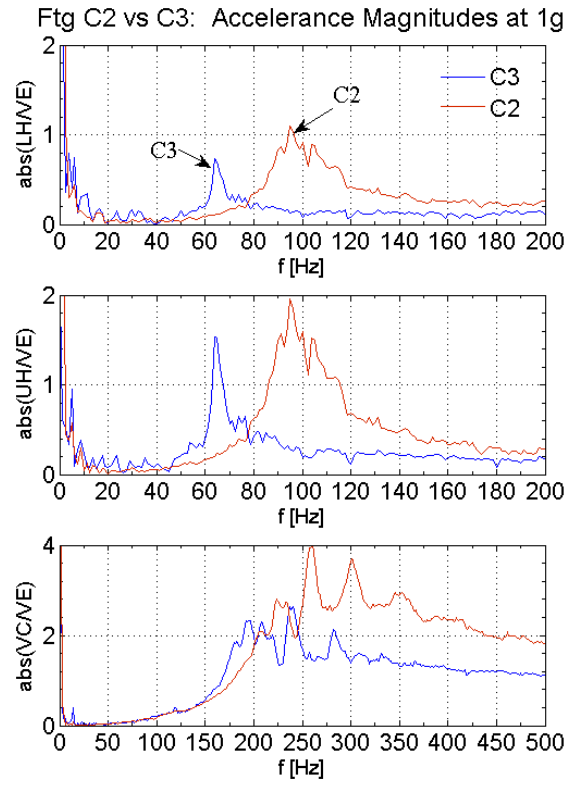


Figure 4.30: The lighter footing shows both a higher peak frequency and magnitude.

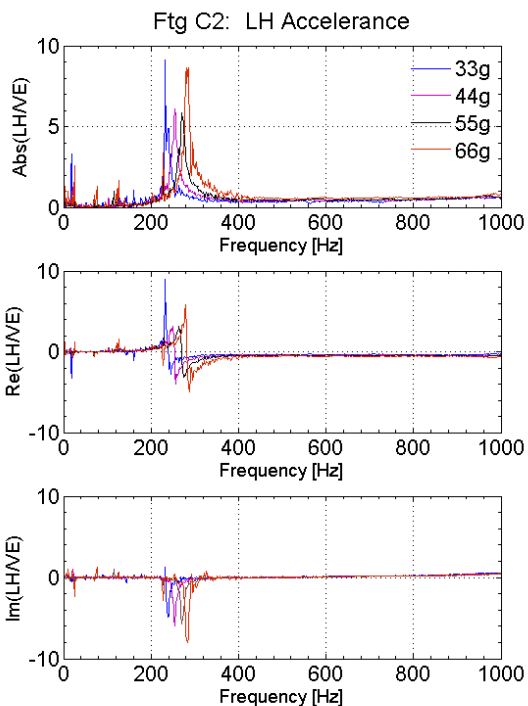


Figure 4.31: Footing C2 LH/VE acceleration at model scale.

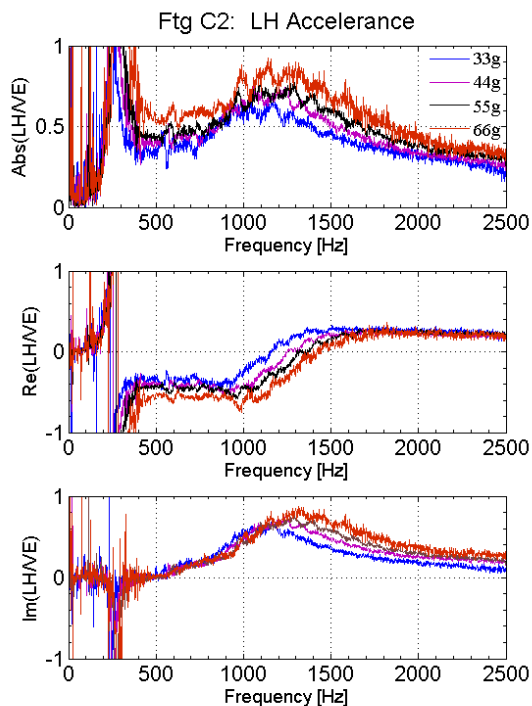


Figure 4.32: Second peak region of the LH/VE acceleration for footing C2 at model scale.

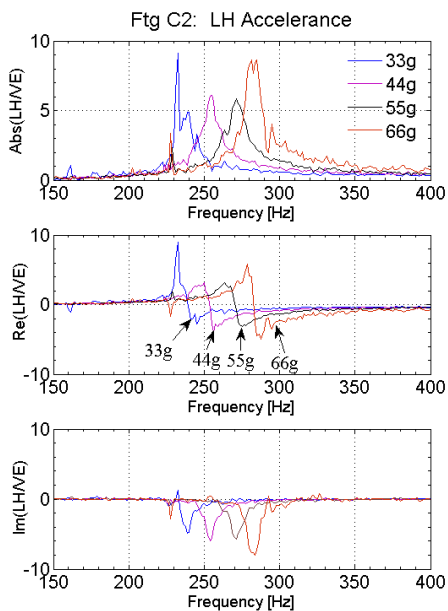


Figure 4.33: Peak frequency shift in C2 LH/VE model scale acceleration.

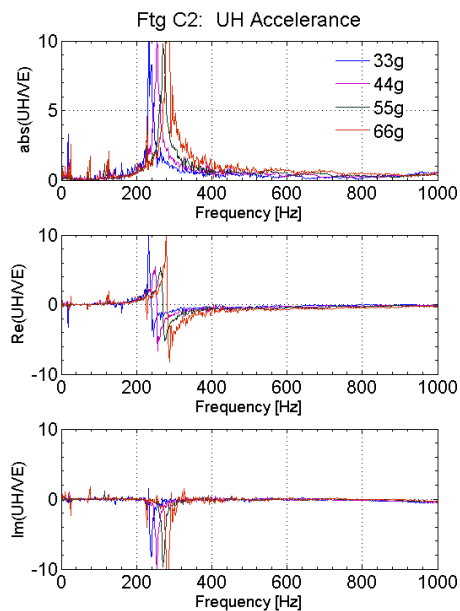


Figure 4.34: UH/VE acceleration for footing C2 at model scale.

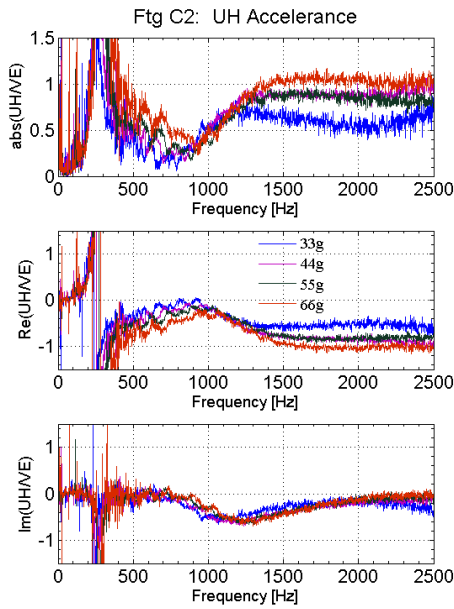


Figure 4.35: Close-up on the second peak region of the UH/VE acceleration for footing C2 at model scale.

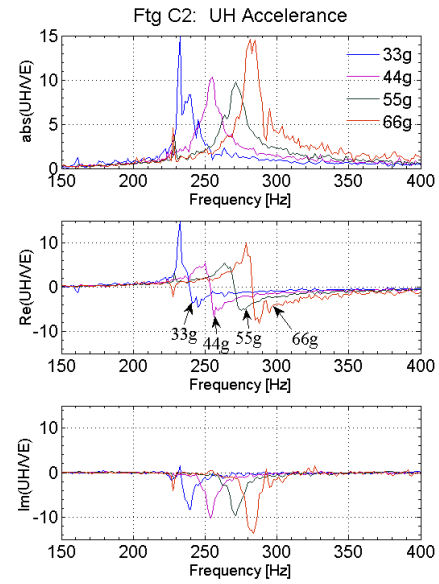


Figure 4.36: First peak (rocking peak) of the UH/VE acceleration for footing C2 at model scale.

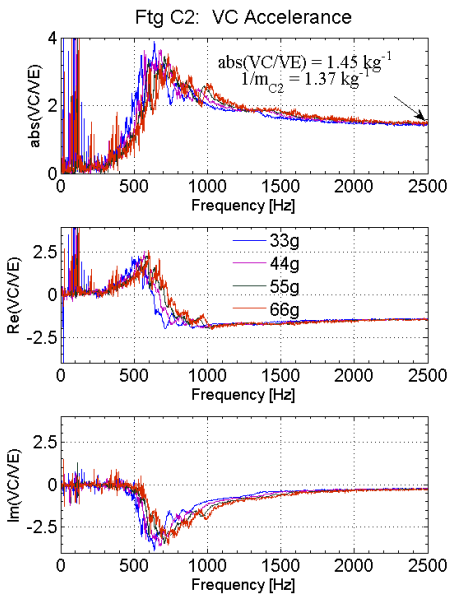


Figure 4.37: The VC/VE asymptote is in agreement for each g-level.

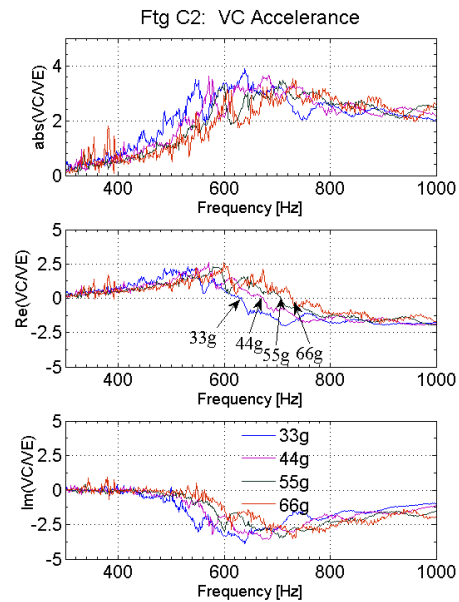


Figure 4.38: Close-up on the peak region of the VC/VE acceleration for footing C2 at model scale.

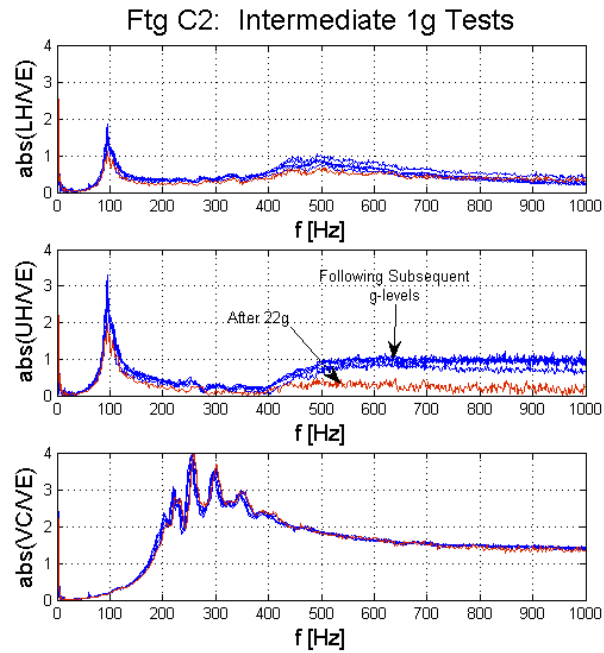


Figure 4.39: Intermediate 1g tests - possible disturbance of footing placement is shown above.

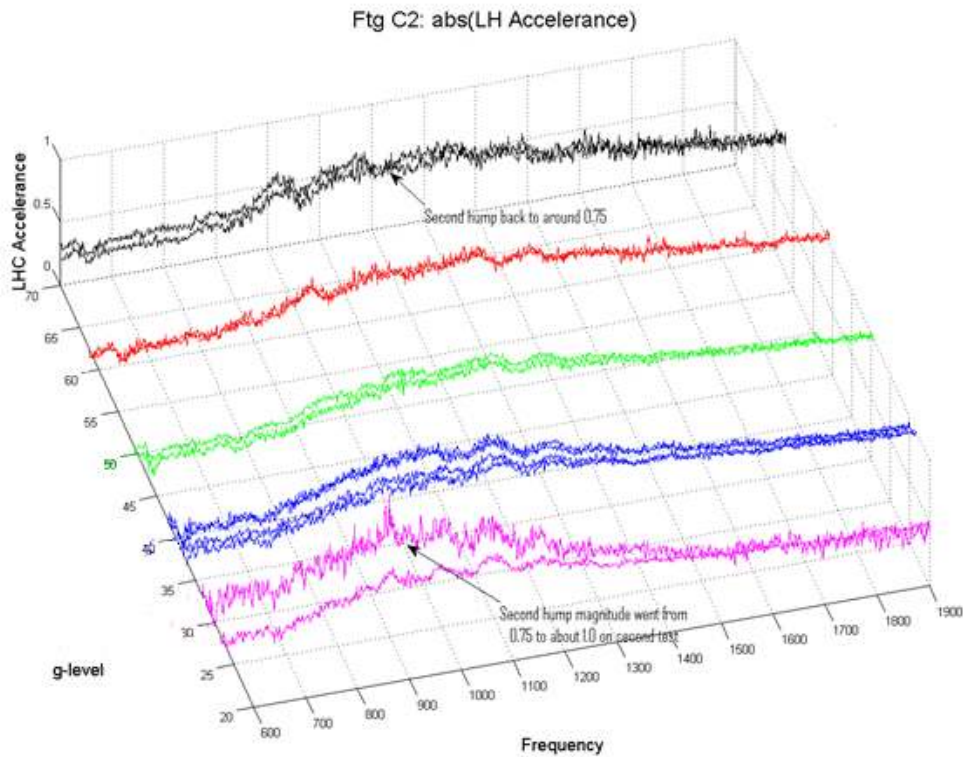


Figure 4.40: Data by g-level corresponding to Figure 4.37.

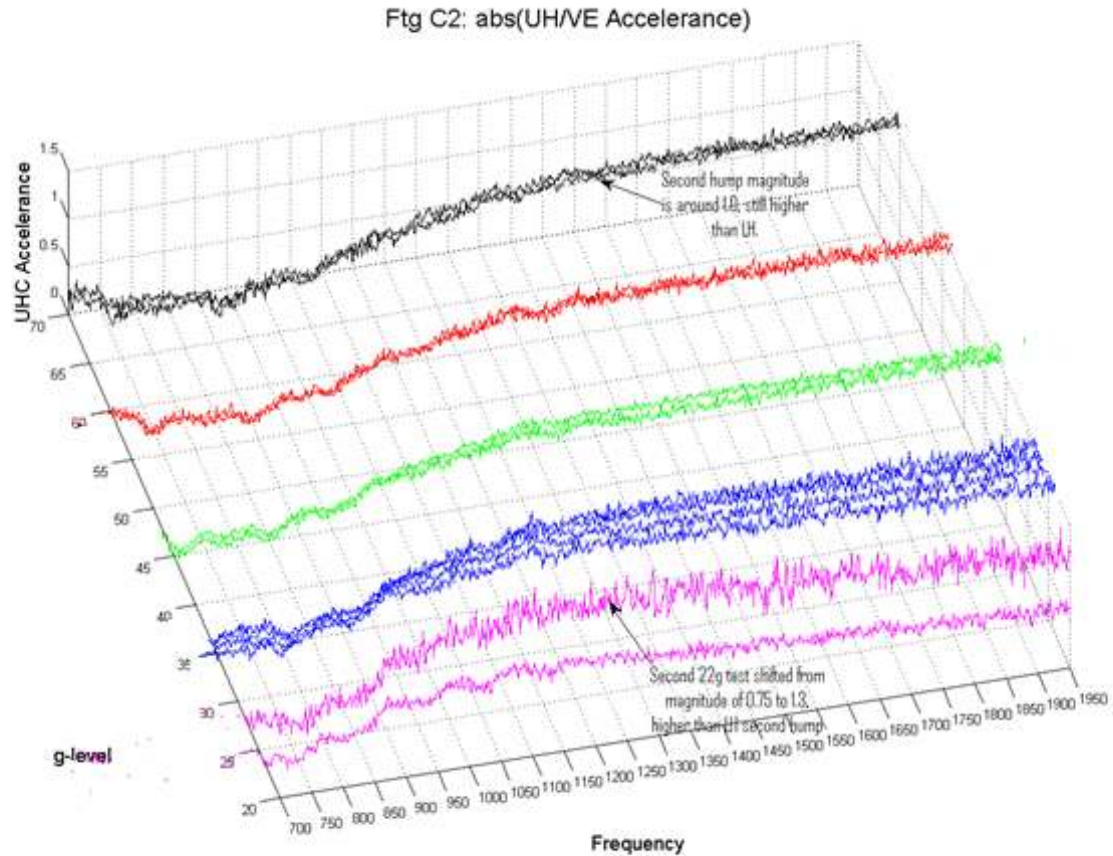


Figure 4.41: Similar to Figure 4.38 but showcasing the UH/VE acceleration.

The footing C2 model scale accelerance curves (4.29 – 4.36) contain features similar to footing C3. Trends with g-level are also comparable. Figure 4.35 demonstrates that like footing C3, the VC/VE accelerance approaches a horizontal asymptote inversely proportional to the footing mass. In contrast to footing C3 however the primary peaks of each accelerance are more discernable when different g-levels are plotted together. Comparing Figures 4.25 and 4.34 reveals the C2 data to have cleaner peaks and an overall smoother response. The frequency shift of the primary peak with respect to g-level is also larger than for footing C3 (Figure 4.29). This observation is summarized quantitatively in Table 4.1. Even if considering the larger of the two frequency shift measures in the table, the footing C2 peak still shows a peak shift that is larger by 21 Hz (from 33g to 66g).

The data for this footing at higher frequencies is drawn somewhat into question by the

inconsistency of the horizontal acceleration asymptotes at different g-levels (see Figures 4.35 through 4.37). The extent of this inconsistency depends on the viewing perspective, and is much less noticeable in the plots of the overall picture (Figures 4.29 and 4.32). The first peak value in the horizontal accelerances and the VC/VE data however are consistent judging by the intermediate 1g tests (Figure 4.35) as well as the extensive series of 1g tests conducted for footing C2 prior to centrifuge testing.

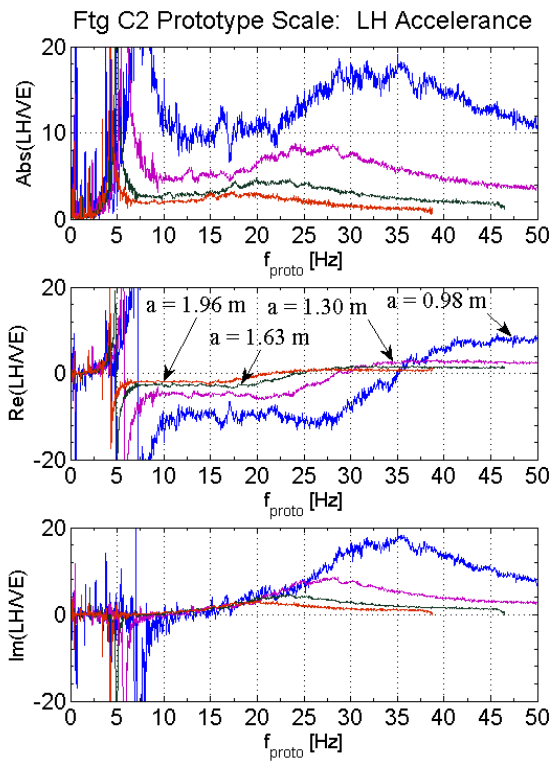


Figure 4.42: Lower horizontal acceleration for footing C2 at prototype scale.

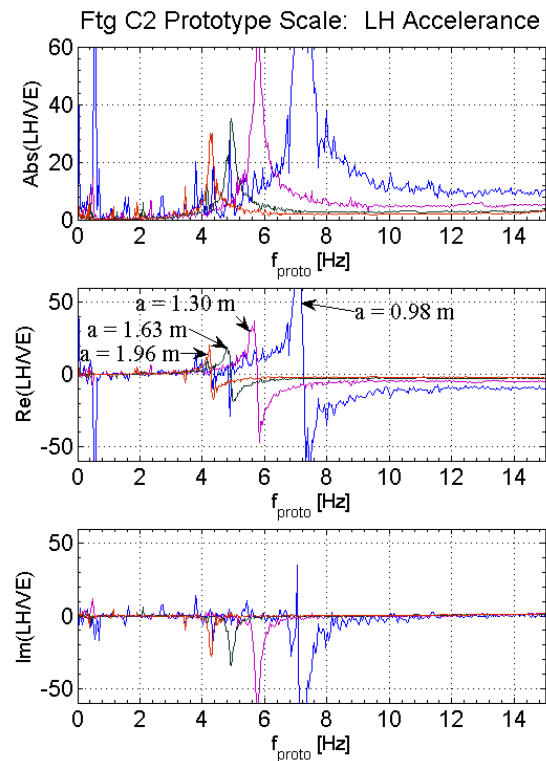


Figure 4.43: First peak region of the footing C2 lower horizontal acceleration at prototype scale.

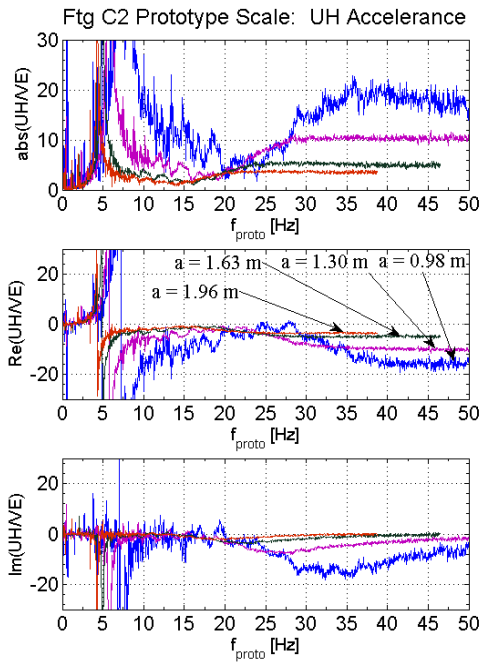


Figure 4.44: Upper horizontal acceleration for footing C2 at prototype scale.

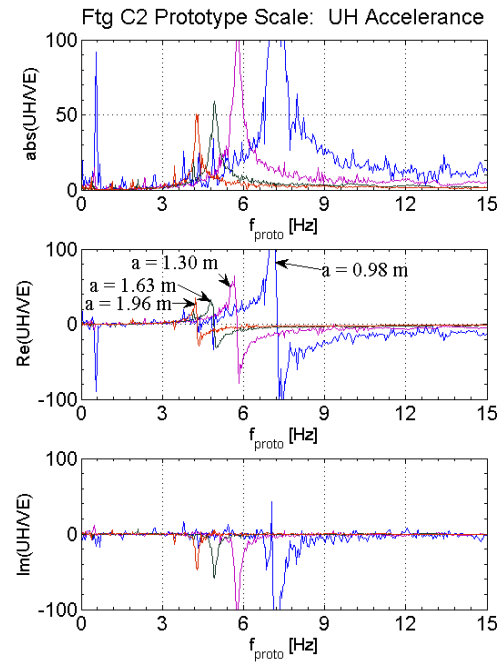


Figure 4.45: Upper horizontal acceleration for footing C2 at prototype scale.

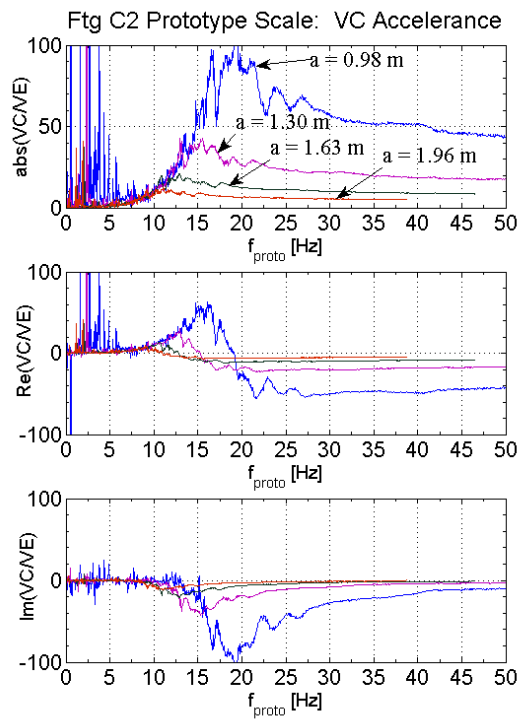


Figure 4.46: VC/VE acceleration for footing C2 at prototype scale.

Footing C1 is the smallest and lightest footing. As a result, out of the three footings it also has the smallest effect on local soil conditions, meaning the lowest stress induced increase in the soil's shear modulus in the direct vicinity of the footing. The smaller footing size, mass, and moment of inertia also imply that compared with the heavier footings, the response of C1 will be closer to that of the free field. Footing C1 model scale accelerances are plotted below in figures 4.45 – 4.50. Prototype scale figures are 4.51 – 4.53.

Horizontal rocking peaks of footing C1 behave similarly to the larger footings as demonstrated by Figures 4.45 and 4.46 but the data is not as smooth (Figure 4.47). Vertical features are also less prominent, but overarching trends are still discernable in Figure 4.50. Prototype scale, like the heavier footings shows higher frequency rocking peaks for the smaller/lighter prototypes (Figures 4.51, 4.52), as well as higher asymptotic VC/VE values (Figure 4.53).

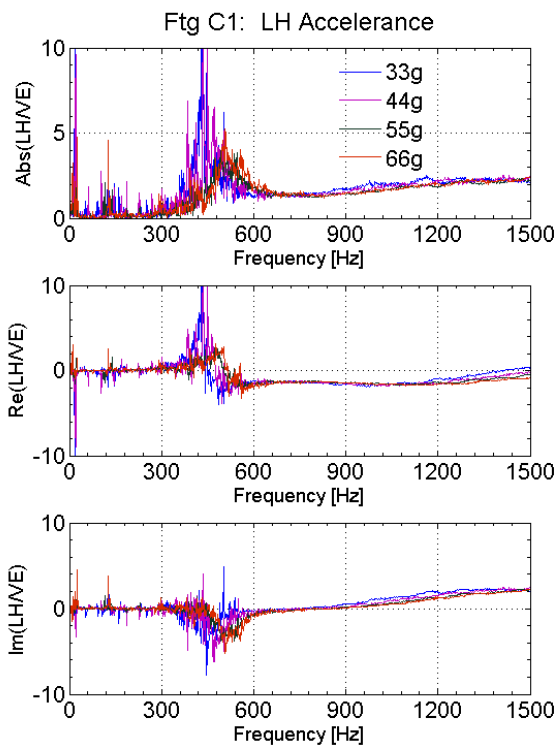


Figure 4.47: LH/VE accelerance plotted for footing C1 at model scale.

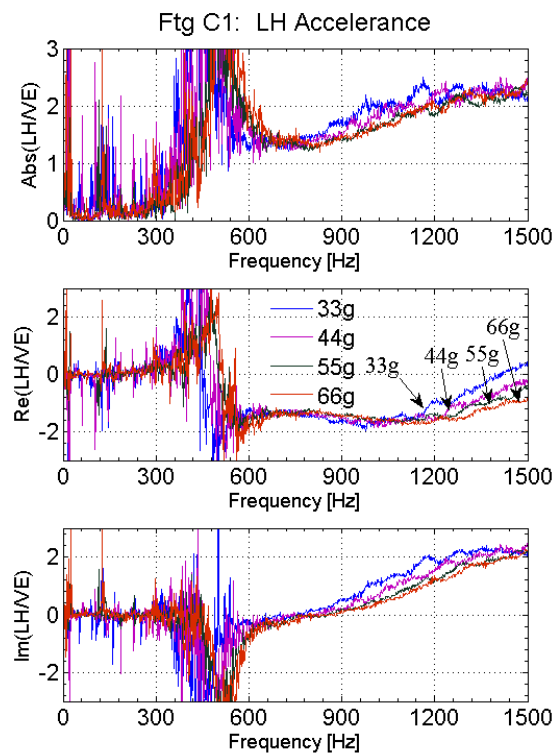


Figure 4.48: Close-up on the second peak region of the LH/VE accelerance for footing C2.

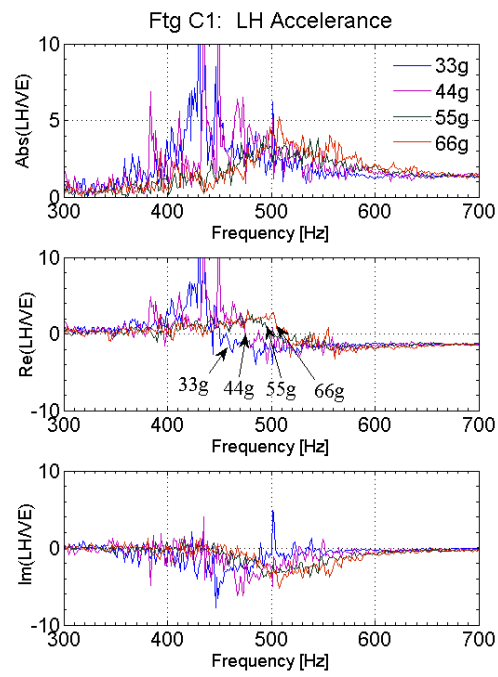


Figure 4.49: Close-up on the LH/VE rocking peak for footing C1 at model scale.

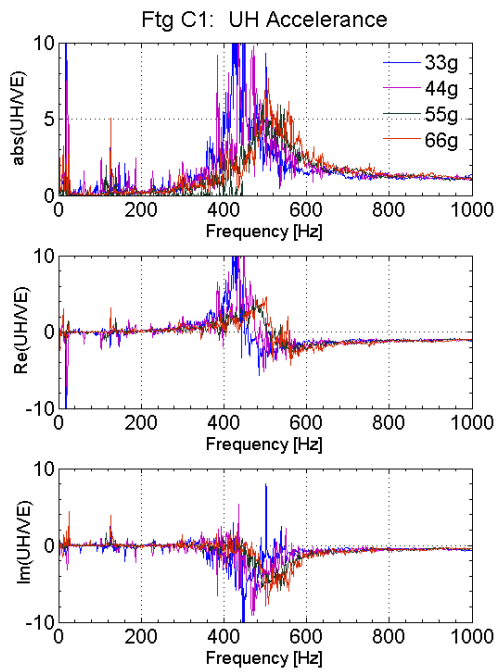


Figure 4.50: UH/VE acceleration plotted for footing C1 at model scale.

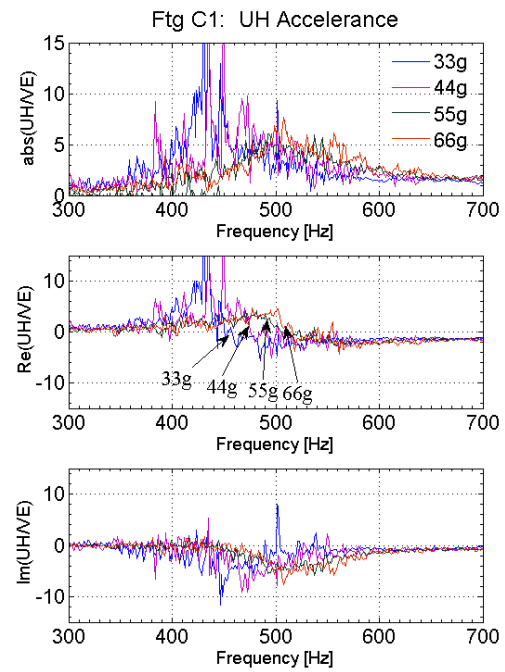


Figure 4.51: First peak close-up of the UH/VE acceleration plotted for footing C1.

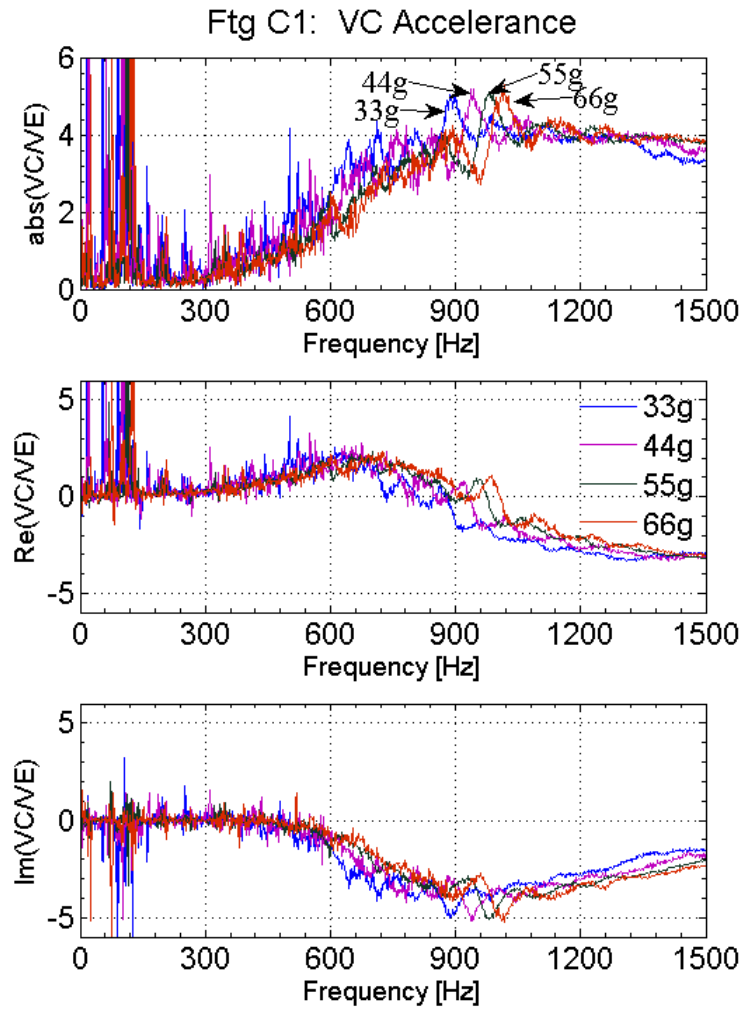


Figure 4.52: VC/VE accelerance plotted for footing C1 at model scale.

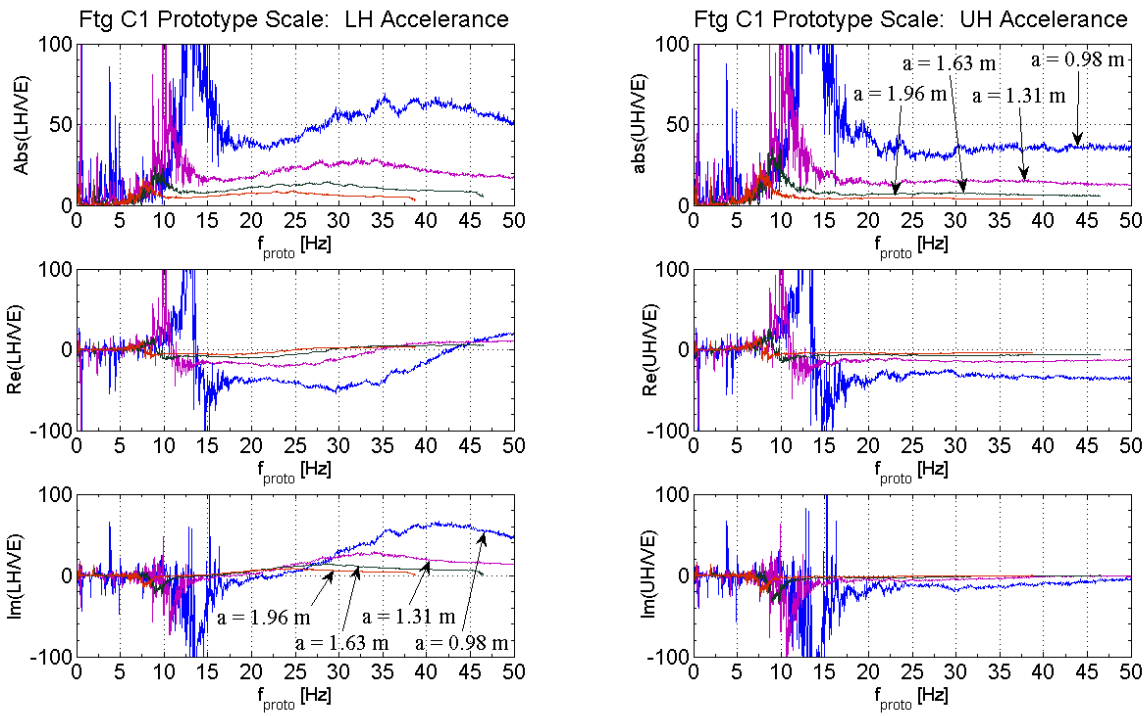


Figure 4.53: Footing C1 lower horizontal acceleration plotted at prototype scale.

Figure 4.54: Footing C1 upper horizontal acceleration plotted at prototype scale.

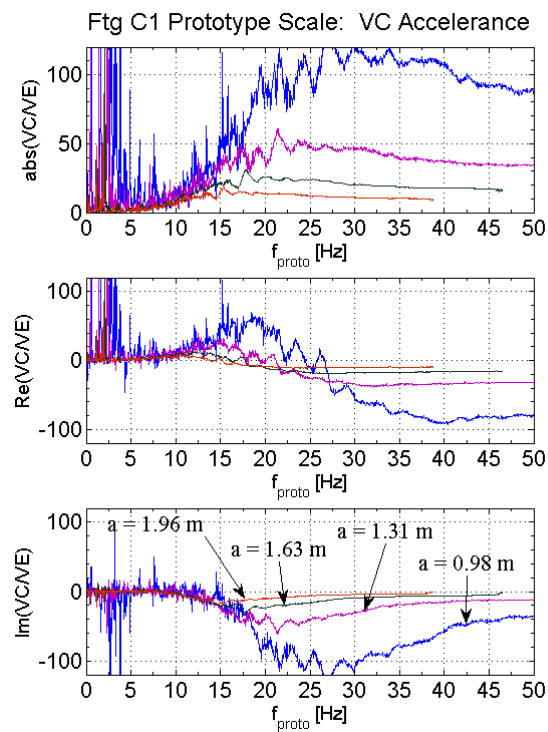


Figure 4.55: Footing C1 VC/VE accelerance plotted at prototype scale.

4.3 Footing Response Comparison

Now that each set of footing data has been plotted separately to note the distinguishing characteristics, it follows to compare the response of each footing. Once again, the noteworthy features for comparison shared by all the model footings are a primary “rocking” peak, second peak or “hump”, and asymptote in the horizontal transfer functions, as well as a peak and asymptote in the VC/VE accelerance.

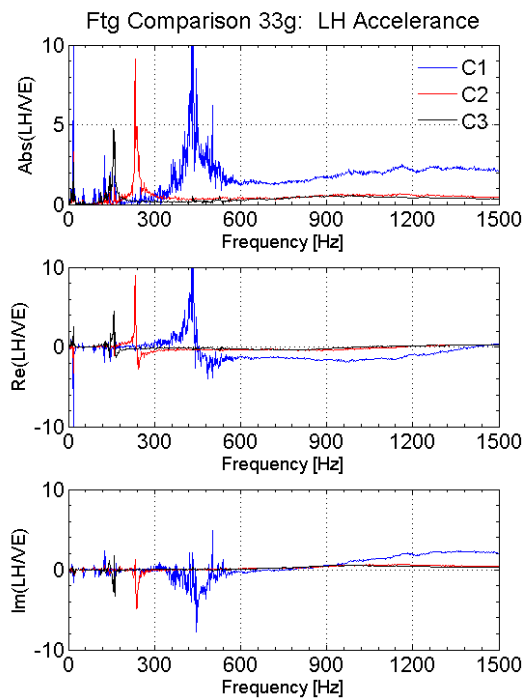


Figure 4.56: LH/VE accelerance at 33g plotted for all footings.

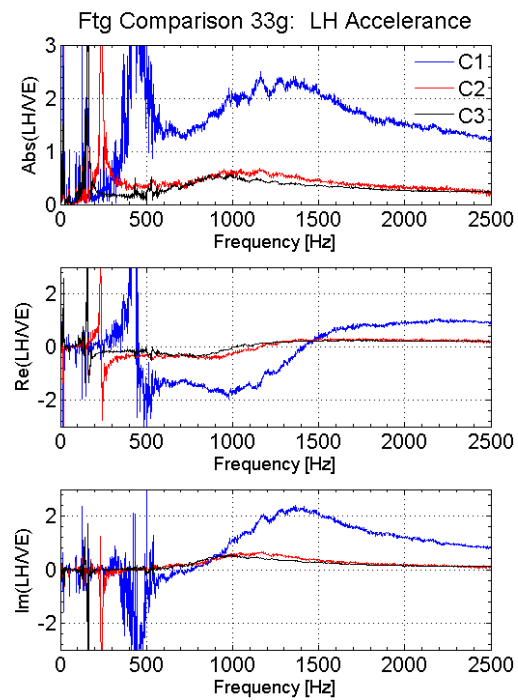


Figure 4.57: LH/VE second peak close-up for all footings at 33g.

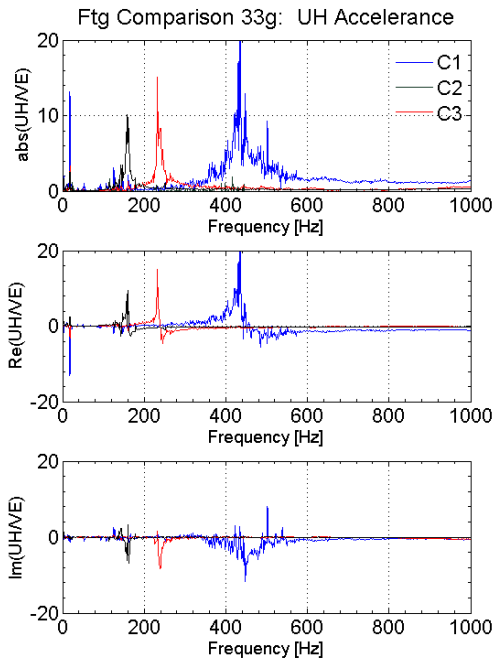


Figure 4.58: UH/VE accelerance for all footings at 33g.

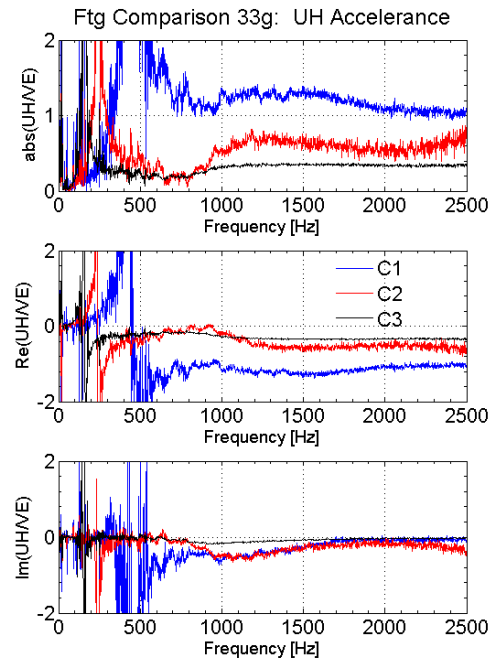


Figure 4.59: UH/VE second peak close-up for all footings at 33g.

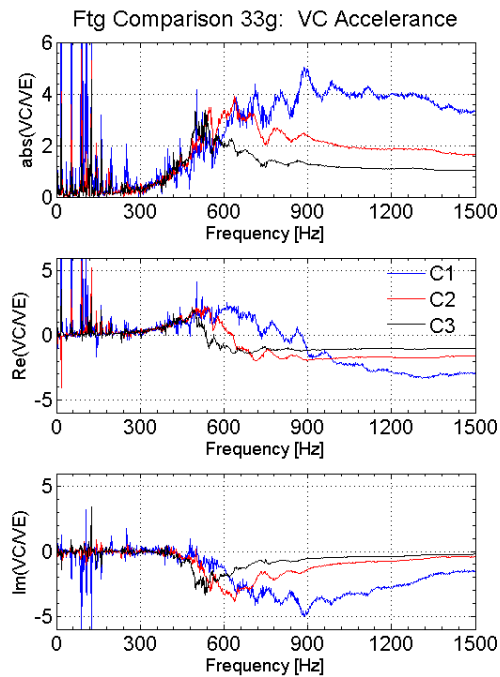


Figure 4.60: VC/VE accelerance for all footings at 33g.

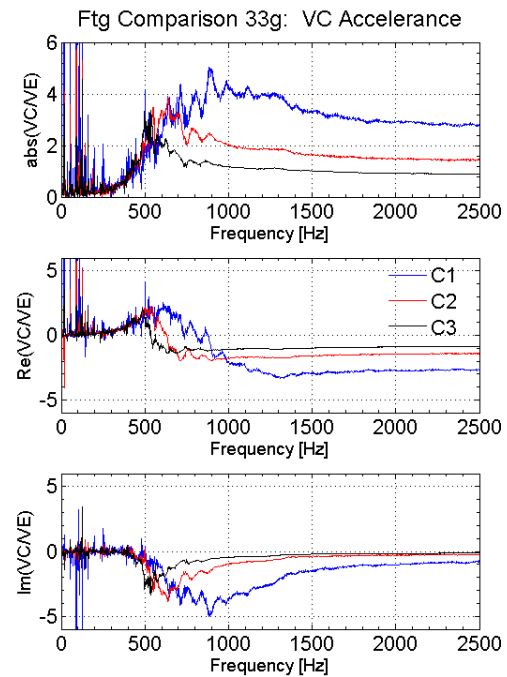


Figure 4.61: VC/VE accelerance for all footings at 33g zoomed out to show the asymptote.

Given the greater mass and mass moment of inertia values for the larger footings, one would expect the response profile to be shifted toward lower frequencies as footing size increases. This can indeed be observed in Figures 4.54 – 4.59 above. The horizontal rocking peak becomes smaller and narrower with increasing footing size (Figures 4.54 – 4.57). For the lightest footing (C1) the peak is actually somewhat wide and jagged by comparison, and it should be noted that overall the data is less clean for this footing. The smaller footings also have a higher asymptote and more prominent second peak in the horizontal transfer functions. Similar to the horizontal transfer functions, the VC/VE response features are at lower frequencies for lighter footings, as shown in Figures 4.58 and 4.59. Additionally, as footing size decreases the resonance peak becomes smoother and wider, and the asymptote is higher.

It should also be noted that in the horizontal accelerances below 50 Hz and the VC/VE accelerance below 150 Hz there is a significant degree of “noise”. Of course these specific frequencies are subject to change at different g-levels but they coincide for all footings. This is attributable to ambient effects such as air turbulence, vibrations from the centrifuge drivetrain, or electrical noise.

g-level	C1 [Hz]	C2 [Hz]	C3 [Hz]
33	435, 446	232	157
44	435, 450	255	168
55	492	271	180
66	507	281	178, 185
Range (largest):	507 – 435 = 72	281 – 232 = 49	185 – 157 = 28
Range (smallest):	507 – 446 = 61	281 – 232 = 49	178 – 157 = 21

Table 4.1: Primary rocking peak of each footing at different g-levels (model scale).

The first frequency given above in each column (Table 4.1) was chosen for largest magnitude without applying any sort of judgment or filter. If the peak was not clear or appeared to be split, the second highest spike was also included in the table separated by a comma.

4.4 Repeatability

Up to this point the plots in this chapter have been described as showing typical responses for each footing. To understand exactly what this implies it is important also to examine comparisons of multiple tests under the same conditions. An understanding of the repeatability and variation of the results can be gained accordingly. The most data was collected for footing C3 (Table 4.2). On each g-level approximately 3-4 tests were conducted at each g-level. The footing C3 plots are thus the best representation of what the error margin can look like. Had there been more data collected for the other two footings there would likely be a similar spread.

Footing	Dates
C3	10-23-2009, 10-27-2009, 10-29-2009, 11-11-2009
C2	11-19-2009
C3	12-04-2009

Table 4.2: Reference table for how many data sets are on plots below (Figures 4.6 – 4.72) corresponding to each footing.

Figures 4.60 – 4.63 demonstrate the wide band covered by footing C3 datasets, especially when compared with similar plots for footing C2 (Figures 4.64 – 4.68) and C1 (Figures 4.69 – 4.73). Because the C1 rocking peak is less smooth by nature there is still a significant band covered in this region, depicted in Figures 4.69 – 4.72. The vertical data and horizontal asymptotes are however quite consistent, as in Figures 4.70 and 4.73.

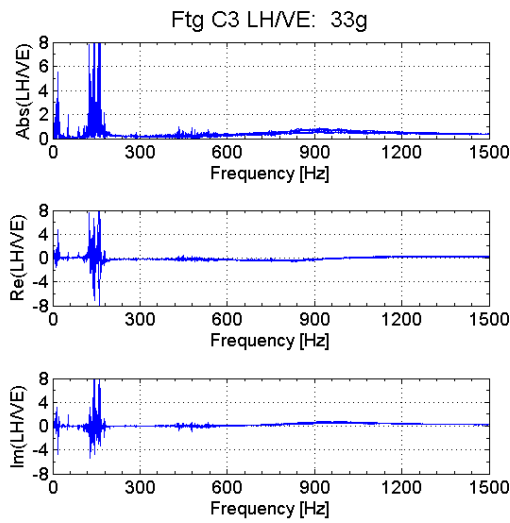


Figure 4.62: A band of data collected for the largest footing plotted at model scale.

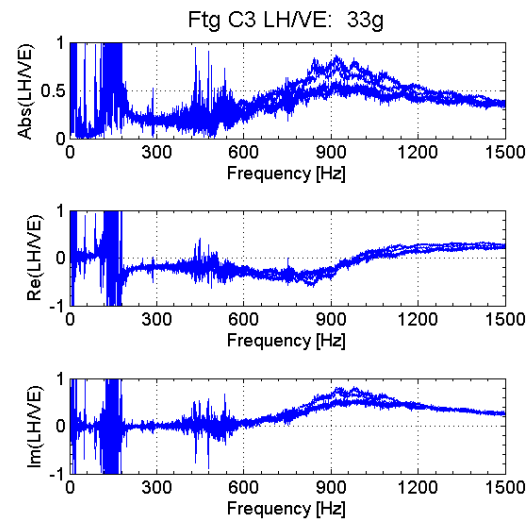


Figure 4.63: A close-up on the spread within the second peak of the UH/VE accelerance for footing C3.

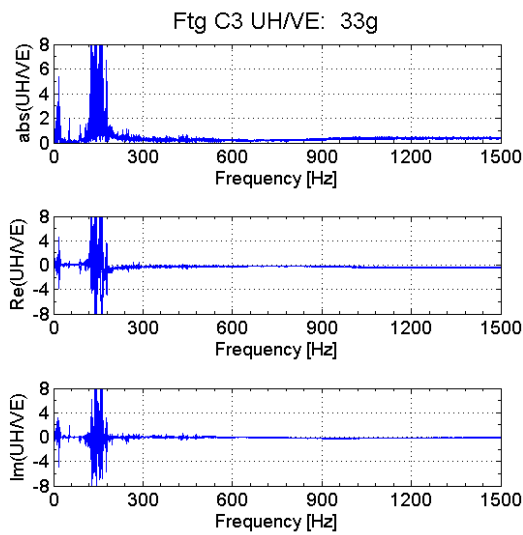


Figure 4.64: First peak frequency range for footing C3 at 33g (120-180 Hz)

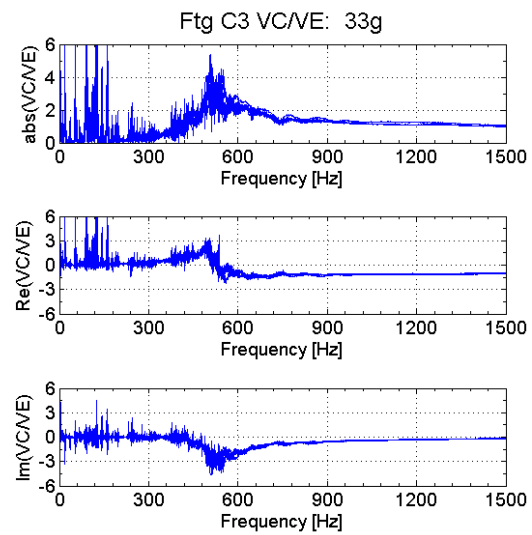


Figure 4.65: VC/VE data for footing C3 at 33g highlighting peak magnitude variation.

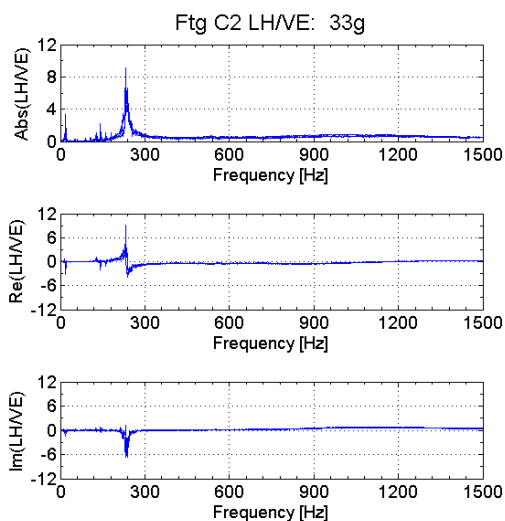


Figure 4.66: Data band for footing C2.

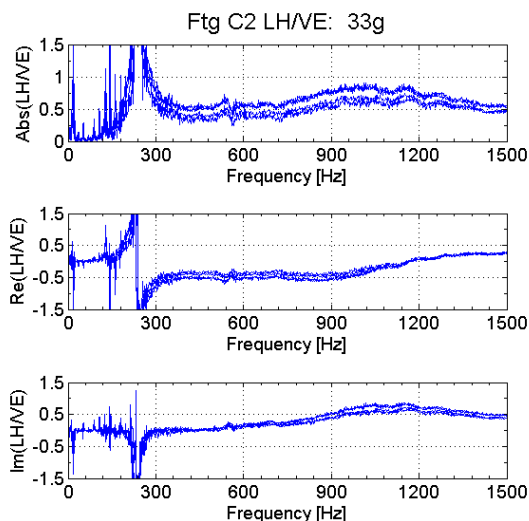


Figure 4.67: Second peak close-up, footing C2 LH/VE.

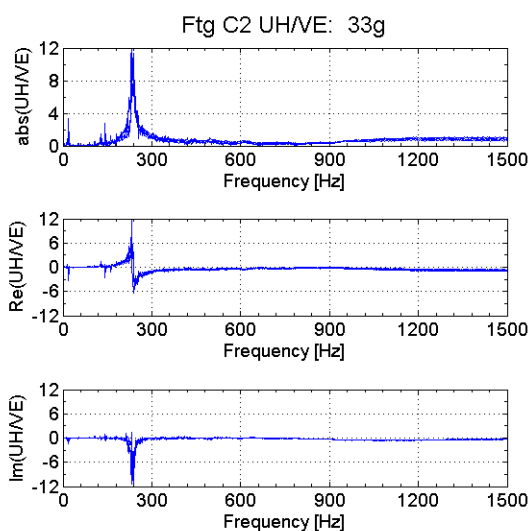


Figure 4.68: Four UH/VE acceleration data sets plotted for footing C2.

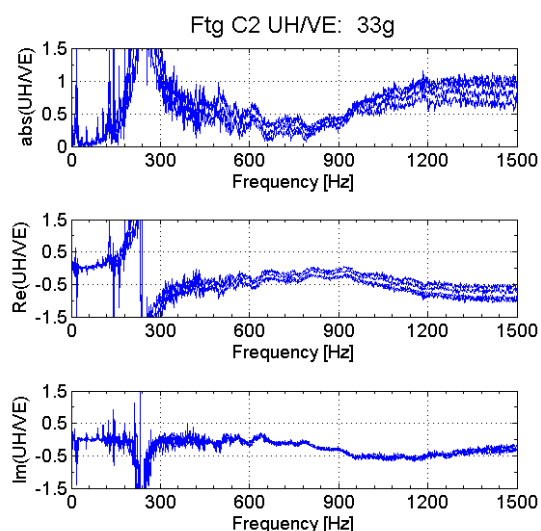


Figure 4.69: Close-up on the second peak of the UH/VE acceleration at model scale for footing C2.

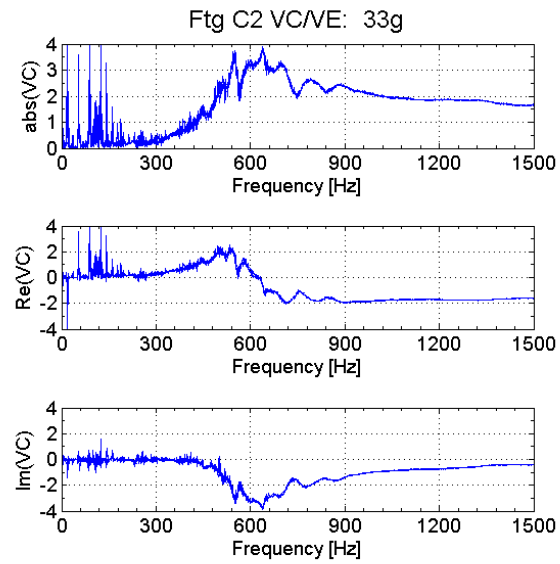


Figure 4.70: Four footing C2 VC/VE accelerance curves.

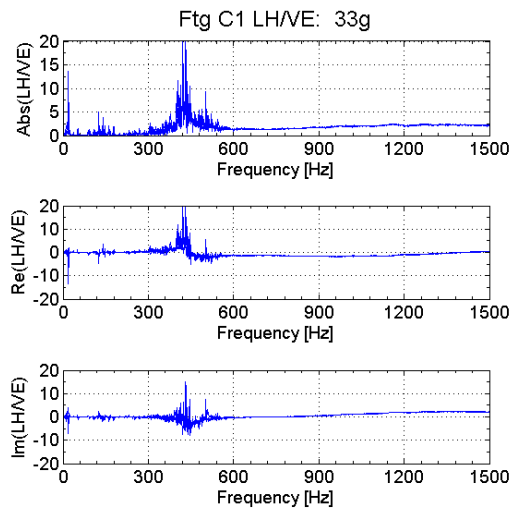


Figure 4.71: Four data sets for footing C1.

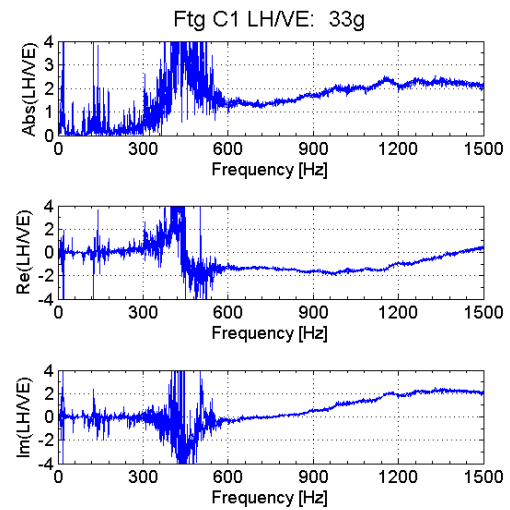


Figure 4.72: Peak region for footing C1.

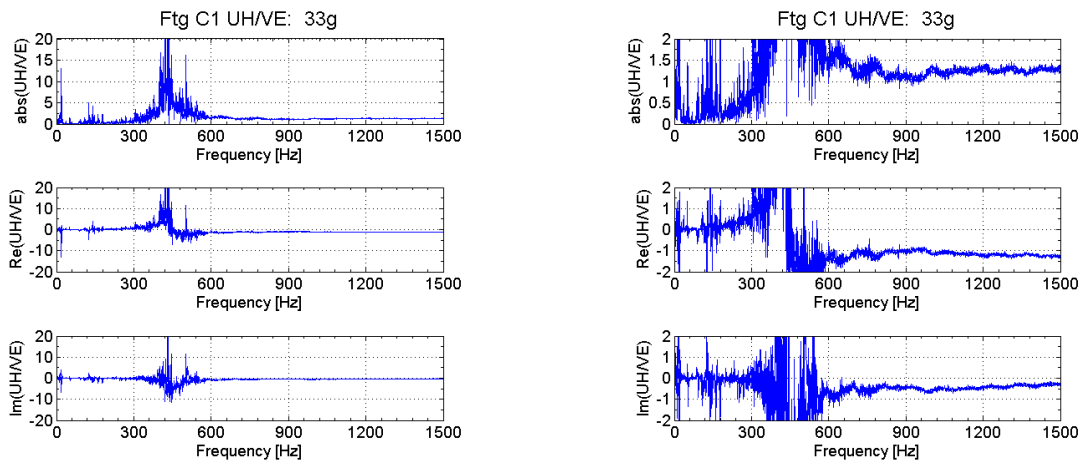


Figure 4.73: UH/VE acceleration of four different data sets collected on 12-04-2009.

Figure 4.74: Multiple data sets for footing C1 at 33g.

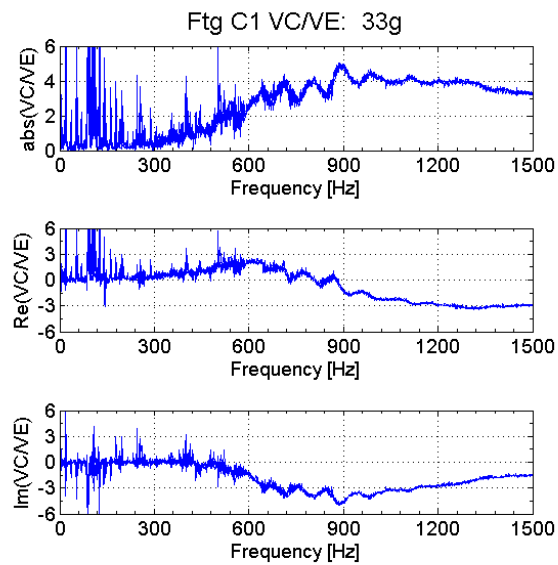


Figure 4.75: VC/VE results plotted for four different data sets corresponding to footing C1 at model scale at 33g.

Chapter 5

Experimental Results of Circular and Square Footings

5.1 Footing Properties

Because of the wealth of data available from previous studies (e.g. Ashlock 2000, Ashlock 2006, Soudkhah 2010), a comparison of the present results with them is the next logical step. The work of Soudkhah focused on the behavior of square-base surface foundations on the same stratum studied in this report. The experimental setup was also identical. The footing properties differ to varying degrees as summed up in Tables 5.1 – 5.3. Square footings listed in Table 5.1 as B1, B2, and B3, were referred to by Soudkhah as B13, B23, and B33. The change of designation has been made to draw a clearer correspondence with the circular footings. Centroid and mass moment of inertia values are in reference to the above footing coordinate system in Figure 2.9. The instrumentation locations on the square footings are also identical in every respect except for the x coordinates of the UH and LH accelerometer locations. This is summarized in Table 5.4.

Property	Footing C1	Footing B1	Percent Difference
Characteristic Length [m]	0.0297	0.0275	7.5 %
Contact Area [m ²]	0.00277	0.00302	9.2 %
Mass M [kg]	0.37216	0.39891	7.2 %
Mass Mom. Inertia J_y [kg m ²]	0.000160974	0.000182398	13.3 %
Centroid: x_c [mm]	-0.11408	-0.12805	12.2 %
Centroid: y_c [mm]	0	0	
Centroid: z_c [mm]	23.67	23.50	0.3 %
1/M [kg ⁻¹]	2.687	2.568	6.7 %

Table 5.1: Comparison of the lightest circle (C1) and square (B1) footing properties. Percent difference is relative to footing C1.

Property	Footing C2	Footing B2	Percent Difference
Characteristic Length [m]	0.0297	0.0275	7.5 %
Contact Area [m ²]	0.00277	0.00302	9.2 %
Mass M [kg]	0.72796	0.78006	7.2 %
Mass Mom. Inertia J_y [kg m ²]	0.000687434	0.000756678	10.1 %
Centroid: x_c [mm]	-0.0583	-0.0655	12.2 %
Centroid: y_c [mm]	0	0	
Centroid: z_c [mm]	46.11	46.03	0.2 %
1/M [kg ⁻¹]	1.374	1.282	6.7 %

Table 5.2: A comparison of the mid-size circle (C2) and square (B2) footing properties. Percent difference is relative to footing C2.

Property	Footing C3	Footing B3	Percent Difference
Characteristic Length [m]	0.0297	0.0275	7.5 %
Contact Area [m ²]	0.00277	0.00302	9.2 %
Mass M [kg]	1.09966	1.18228	7.5 %
Mass Mom. Inertia J_y [kg m ²]	0.00204597	0.00222275	8.6 %
Centroid: x_c [mm]	-0.0386	-0.0419	8.6 %
Centroid: y_c [mm]	0	0	
Centroid: z_c [mm]	69.73	69.68	0.07 %
1/M [kg ⁻¹]	0.909	0.846	7.0 %

Table 5.3: A comparison of the heaviest circle (C3) and square (B3) footing properties. Percent difference is relative to C3.

	C Footings	B Footings	Percent Difference
$x_{UH} = x_{LH}$ [m]	0.029225	0.027500	3.1

Table 5.4: UH and LH coordinates for circular footing versus square. All other locations are the same for respective footings (C1,B1), (C2,B2), and (C3,B3). See section 2.4 or the footing drawings in the appendix.

5.2 Comparison

Presented below in Figures 5.1 – 5.13 is a series of plots comparing accelerances for each location at 33g. Each plot highlights a comparison between a circular footing and its respective square counterpart. Both the circular and square data series exhibit the same set of features: A sharp first peak and long smooth second peak in the UH/VE and LH/VE, in addition to a single peak and asymptotic behavior in the VC/VE accelerance. In Figure 5.1, for instance, the LH/VE accelerance are plotted for footings C1 and B1 at model scale. They are the lightest circular and

square footings respectively. Despite the differences listed in Tables 5.1 – 5.4, the data agree well, except for a consistent difference in magnitude of about 0.5 kg^{-1} in the second peak/asymptote region. In the previous chapter it was observed that heavier footings with a larger mass moment of inertia exhibit a lower second peak and asymptote. Footing B1 is indeed more massive and has a greater mass moment of inertia than C1. In Figure 5.2 where VC/VE accelerances are plotted for footings C1 and B1 at model scale with a larger frequency range, however, one can see that the data points have not converged at 2500 Hz. The larger footings exhibit similar behavior in their comparisons (Figures 5.11, 5.15). This is consistent with observations made in the previous chapter concerning the lower asymptotic value of heavier footings in the VC/VE transfer function. In Figure 5.7 which is a close-up near the second peak of the LH/VE accelerance, it is difficult to say which footing has a larger second peak. The other two comparisons (C1, B1) and (C3, B3) show a smaller second LH/VE peak for the heavier square footings (Figures 5.6 and 5.13), similar to trends for the VC/VE asymptote.

Relative to the amount of noise in both data sets, the square and circular footing rocking peaks agree well, sharing large regions of overlap. This holds true for both the LH/VE and UH/VE accelerances for all three footing sets (C1, B1), (C2, B2), and (C3, B3). Peak agreement can be seen in Figures 5.5, 5.10, and 5.14 for footings 1, 2, and 3 respectively. The square footing data shown here is somewhat noisier, most notable in sharp peak regions such as the rocking peak in Figure 5.4.

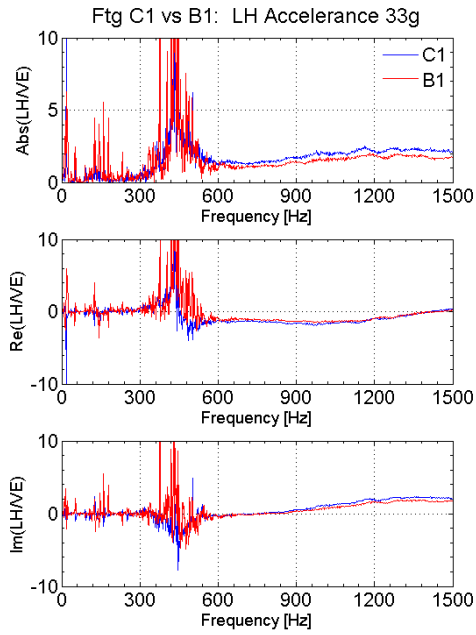


Figure 5.3: LH/VE acceleration plotted for footings C1 and B1 at model scale.

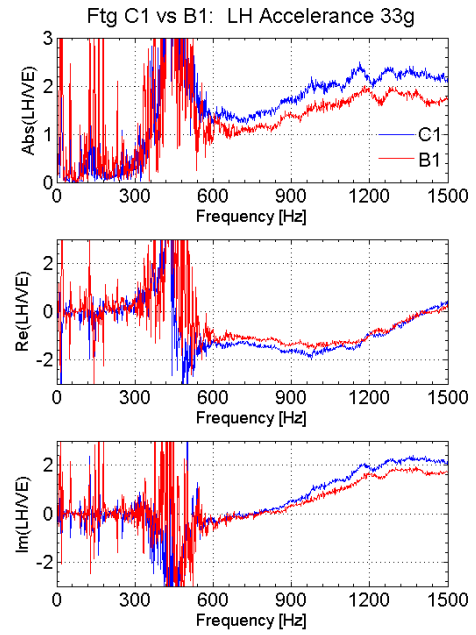


Figure 5.4: Close-up on the second peak of the LH/VE acceleration.

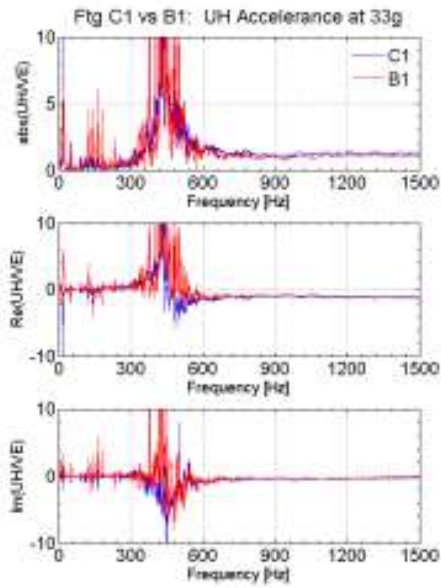


Figure 5.5: UH/VE acceleration plotted for footings C1 and B1 at model scale.

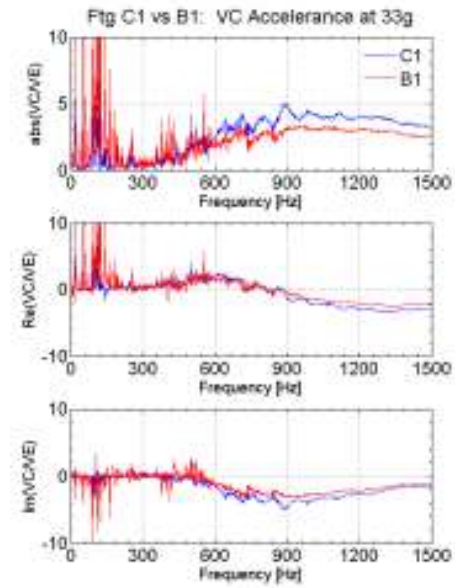


Figure 5.6: VC/VE acceleration plotted for footings C1 and B1 at model scale.

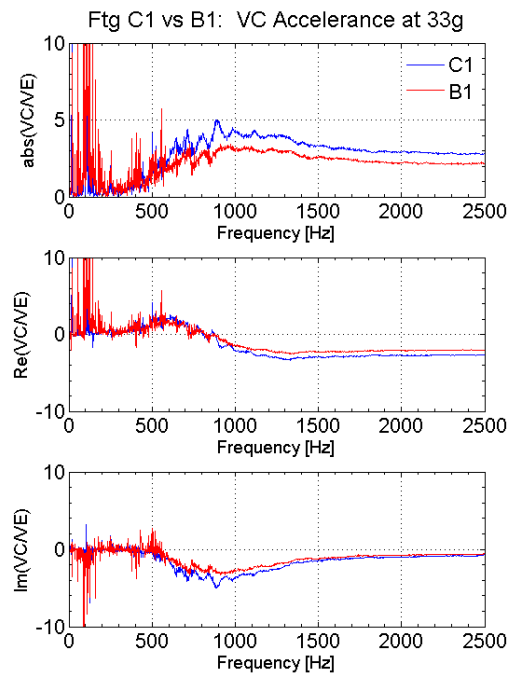


Figure 5.7: VC/VE plotted for footings C1 and B1 at model scale up to 2500 Hz

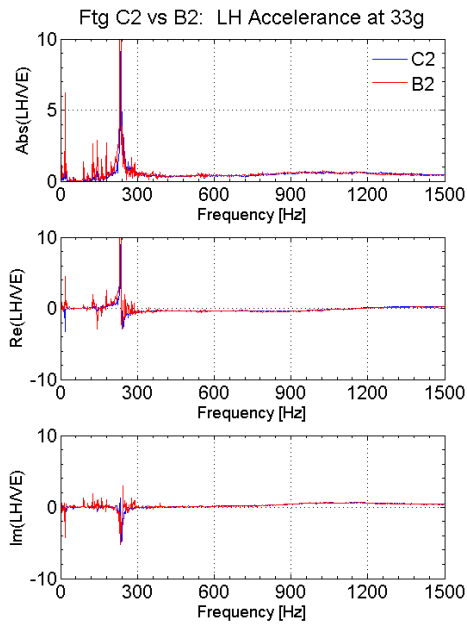


Figure 5.8: LH/VE acceleration plotted for footings C2 and B2 at model scale.

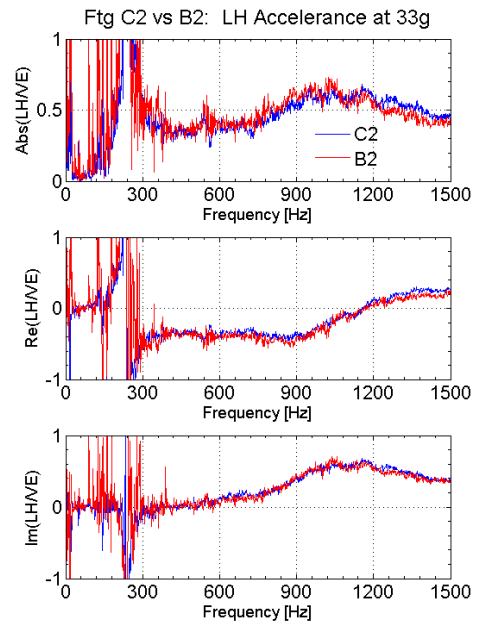


Figure 5.9: Close-up on the second peak of the LH/VE acceleration.

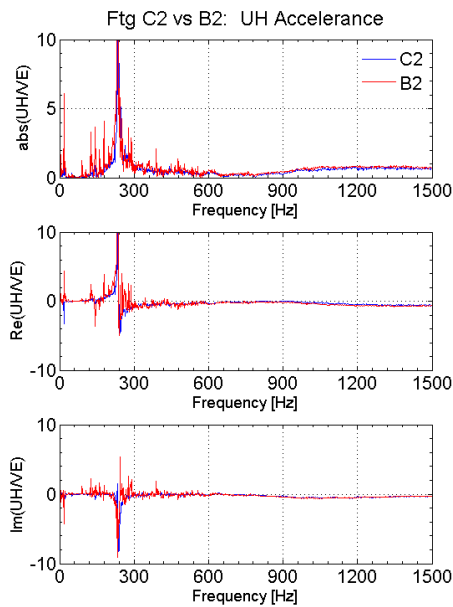


Figure 5.10: UH/VE acceleration plotted for footing C2 and B2 at model scale.

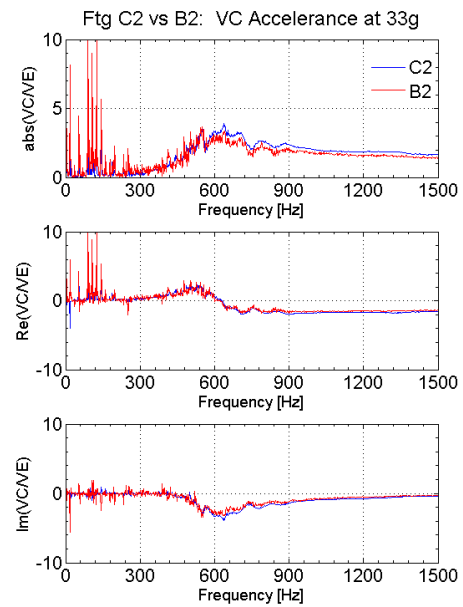


Figure 5.11: VC/VE acceleration plotted for footings C2 and B2 at model scale.

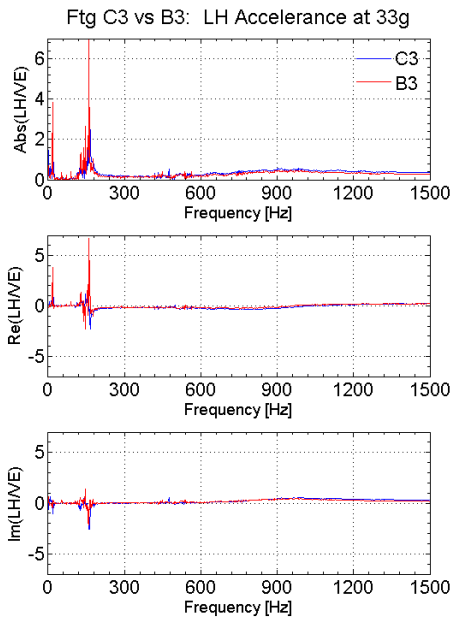


Figure 5.12: LH/VE accelerance plotted for footings C3 and B3 at model scale.

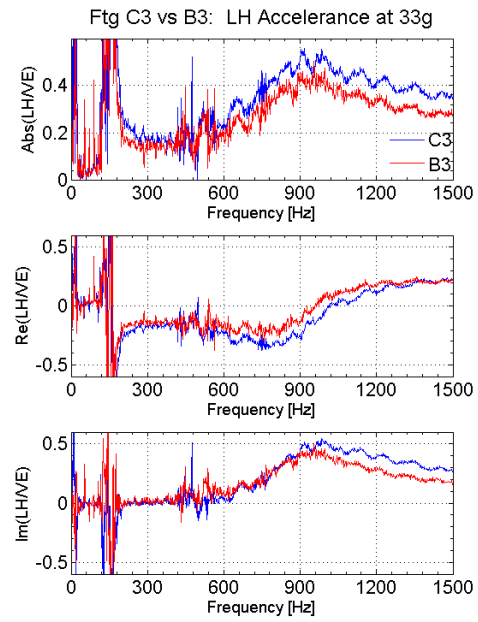


Figure 5.13: Close-up plot of the LH/VE accelerance peak.

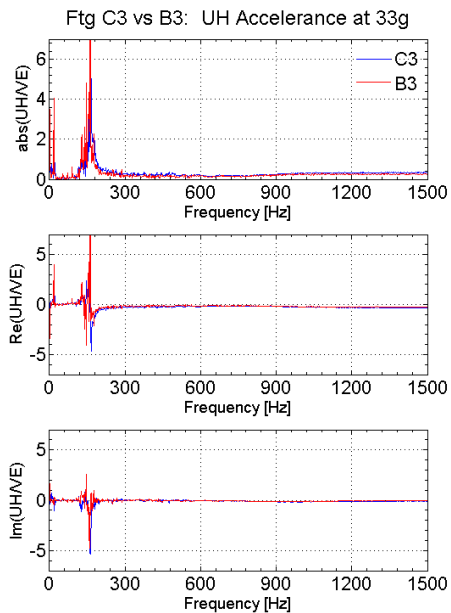


Figure 5.14: UH/VE accelerance plotted for footings C3 and B3 at model scale.

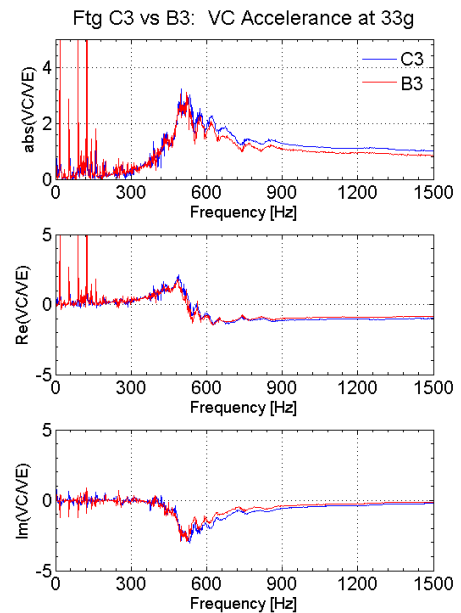


Figure 5.15: VC/VE accelerance plotted for footings C3 and B3 at model scale.

The following series of plots shows comparisons of accelerance magnitudes at all g-levels with similar results. Features are observable in both square and circle accelerances, with asymptotic values differing proportionally to their respective mass reciprocals. The brown curves correspond

to square footing data. Rocking peak agreement can be seen in horizontal acceleration plots such as 5.19 or 5.22. Data for the vertical response peak is in similar agreement, e.g. Figure 5.24. In all the Figures 5.16 – 5.24 a slight disagreement in asymptotic value can be observed, though it is more difficult to quantify in the 3D perspective.

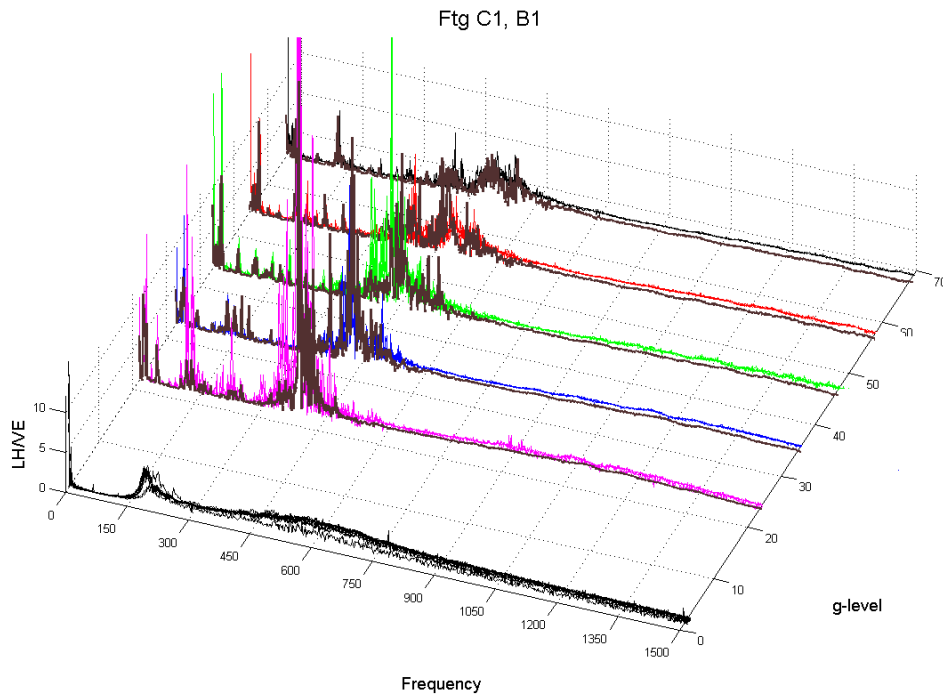


Figure 5.16: Footing C1 and B1 LH/VE acceleration magnitudes by g-level.

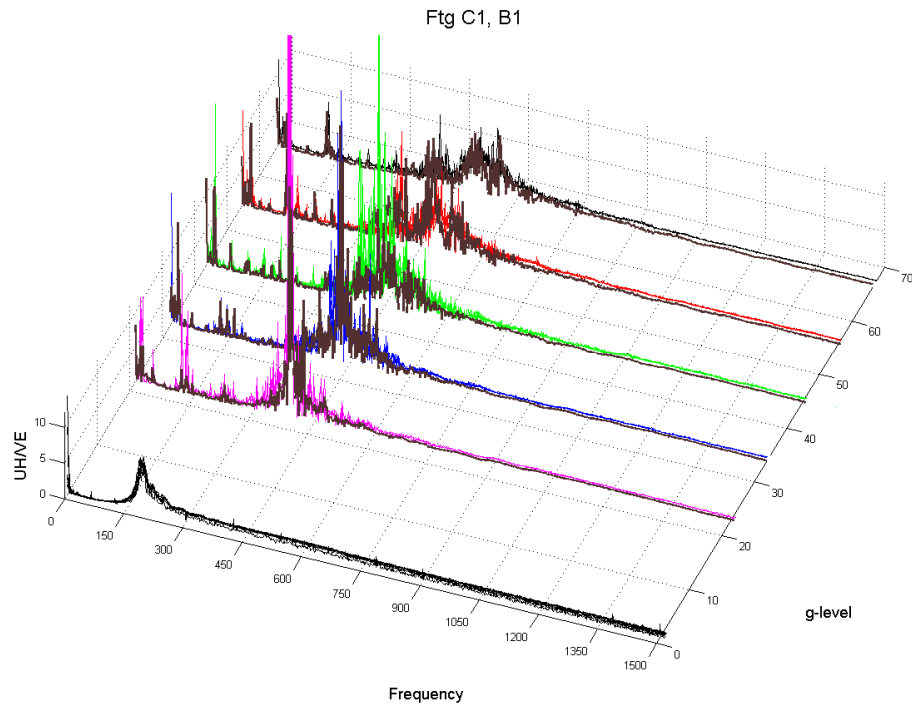


Figure 5.17: Footing C1 and B1 UH/VE accelerance magnitudes by g-level.

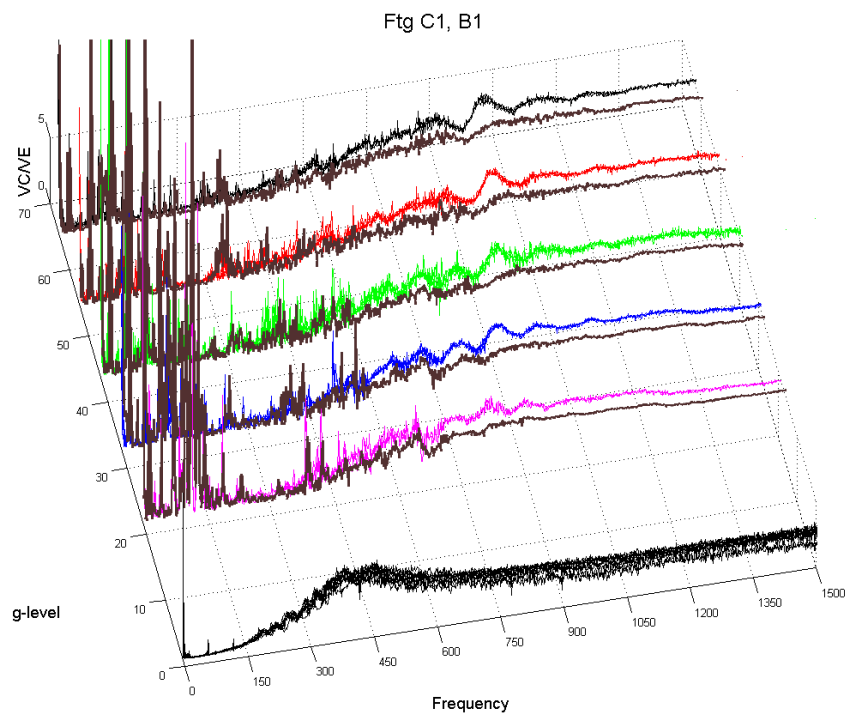


Figure 5.18: Footing C1 and B1 VC/VE accelerance magnitudes by g-level.

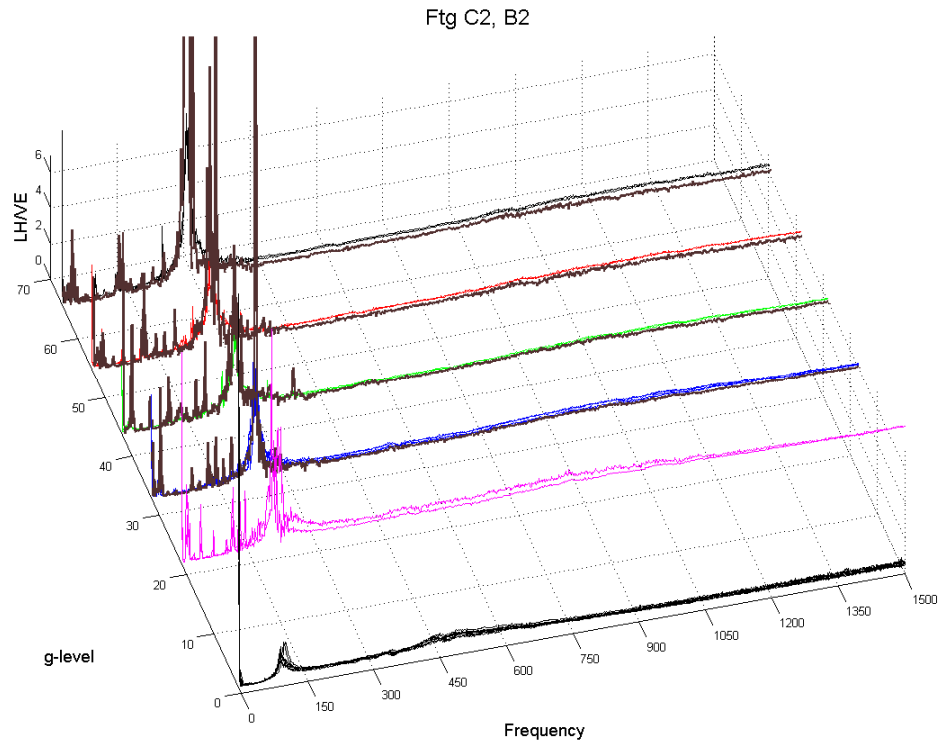


Figure 5.19: Footing C2 and B2 LH/VE accelerance magnitudes by g-level.

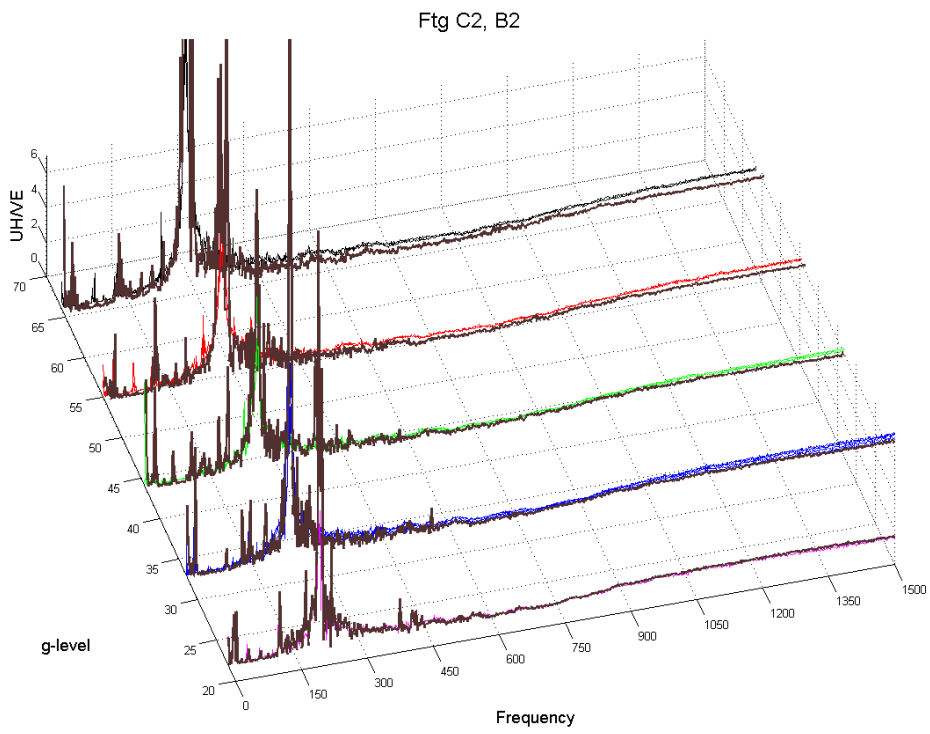


Figure 5.20: Footing C2 and B2 UH/VE accelerance magnitudes by g-level.

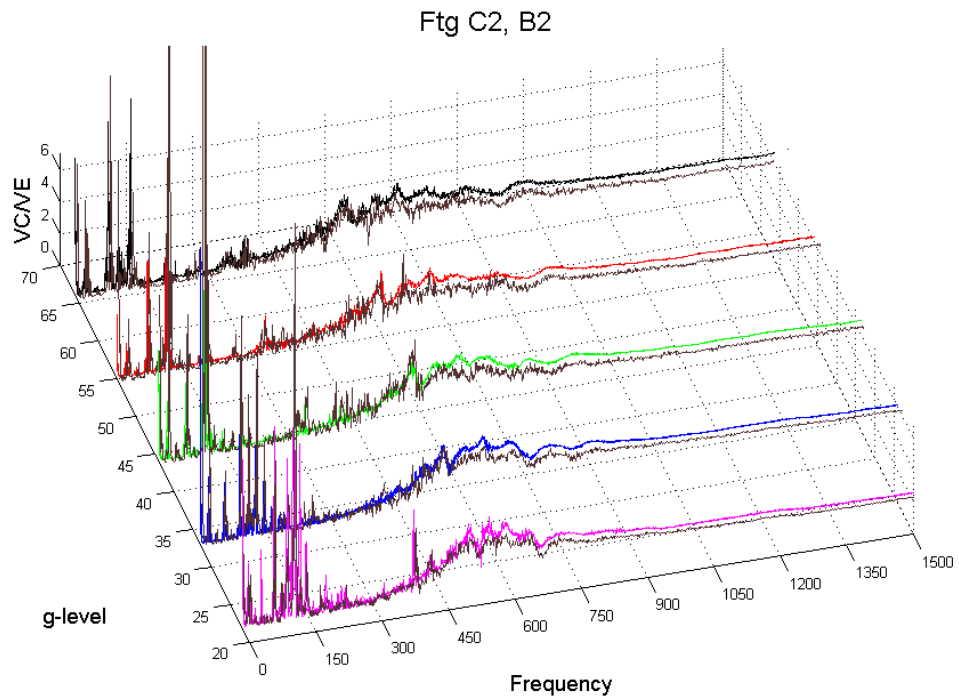


Figure 5.21: Footing C2 and B2 VC/VE accelerance magnitudes by g-level.

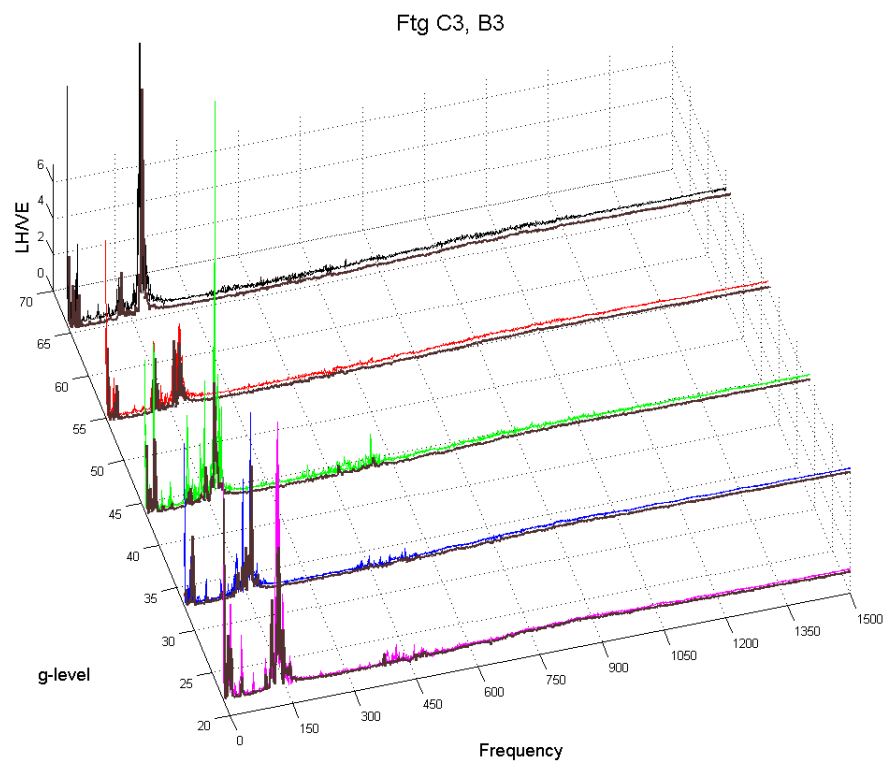


Figure 5.22: Footing C3 and B3 LH/VE accelerance magnitudes by g-level.

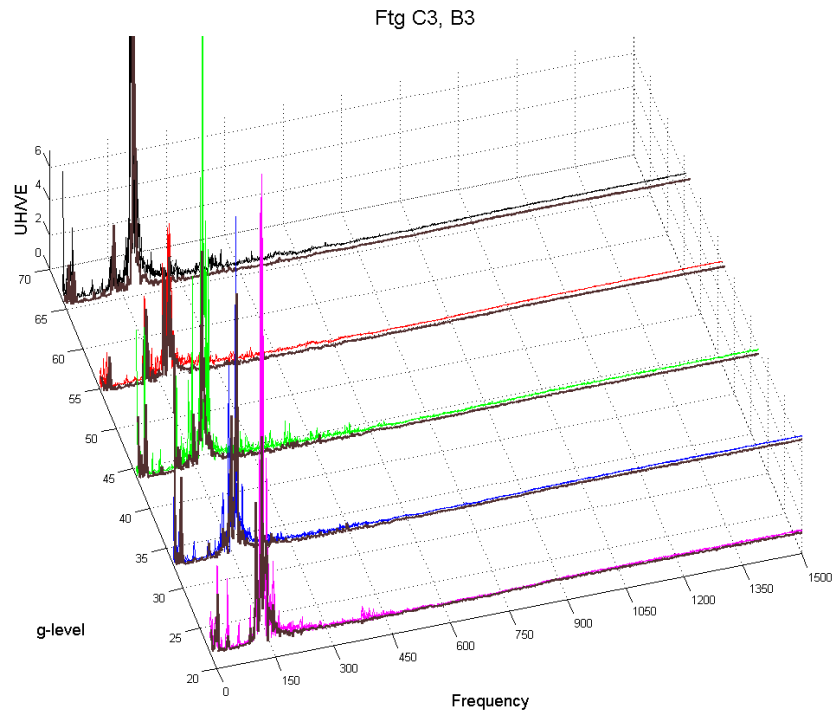


Figure 5.23: Footing C3 and B3 UH/VE acceleration magnitudes by g-level.

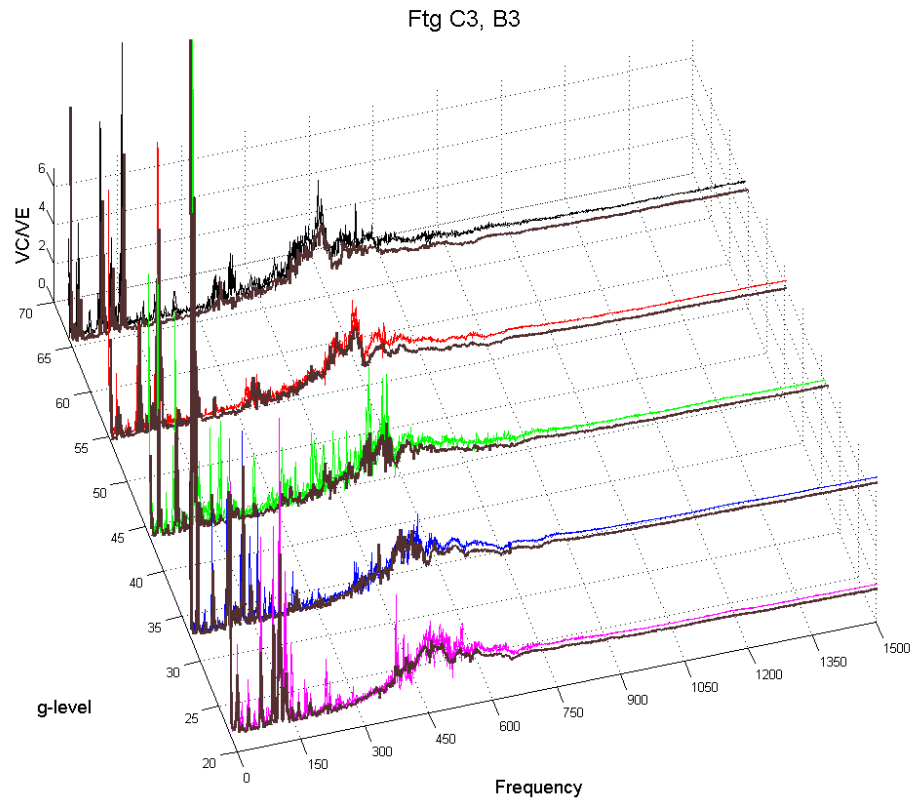


Figure 5.24: Footing C3 and B3 VC/VE accelerance magnitudes by g-level.

Chapter 6

Computational Modeling

6.1 Boundary Element Method

Because of its ability to rigorously handle infinite domains, the boundary element method (BEM) was used in this study to analyze the footing response computationally. In this study, a linear visco-elastic soil representation in the program BEASSI (Boundary Element Analysis for Soil Structure Interaction) was used as in the work of Pak, Guzina, Ashlock, and Soudkhah. The frequency domain formulation used in this synthesis is discussed in detail in Guzina (1996).

6.2 The Two-zone Model

As mentioned in the introduction, the nonlinear properties of soil even in small strain pose a considerable difficulty in analysis of soil-structure interaction problems. Due to its stress dependent nature, the soil's shear modulus near the footing may differ quite significantly from either a pure in-situ square-root (Hardin-Drnevich) profile or an equivalent homogeneous value. As will be demonstrated later, the latter two soil profile models are generally incapable of capturing the essence of footing-soil system behavior properly. This will be demonstrated in Chapter 7 where their predictions are compared with the experimental results.

A novel theoretical model that holds great promise to this class of problems is the dual-zone idea in Pak and Ashlock (2010). Their proposed idea that has been proven effective for a square footing on a half-space (Ashlock 2006), as well as a stratum (Soudkhah 2010), is to decompose the soil into two separate soil domains to balance the account of the foundation load influence and the free-field in-situ soil conditions. The influence zone was modeled as a finite soil region resembling a bulb directly underneath the footing, as depicted in Figures 6.1 and 6.2. Close-ups of the four

different meshes used for the stiffened inclusion zone are shown in Figures 6.3 – 6.10.

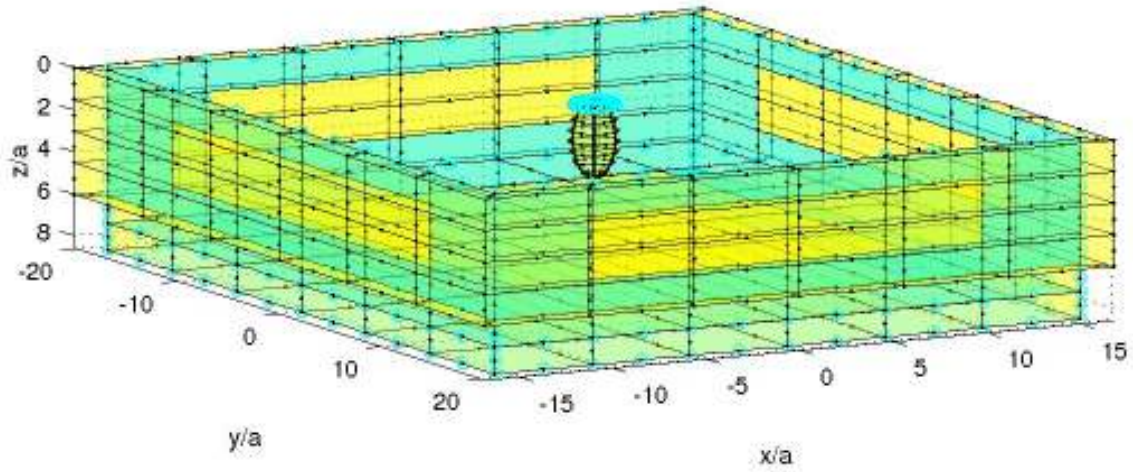


Figure 6.1: Full mesh for BEASSI input.

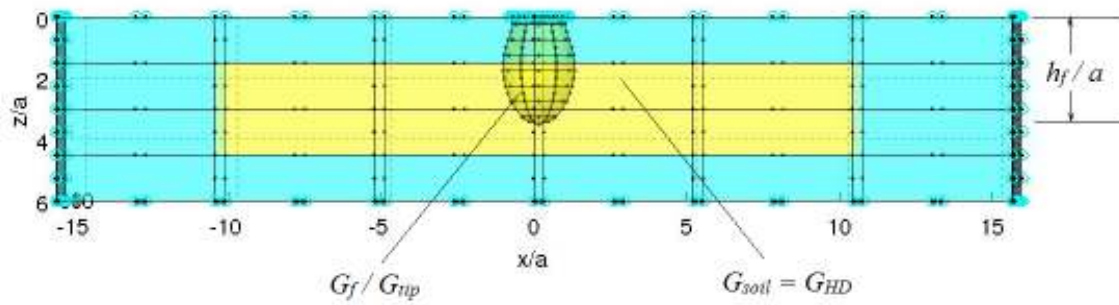


Figure 6.2: Side view showing the inclusion shape and properties.

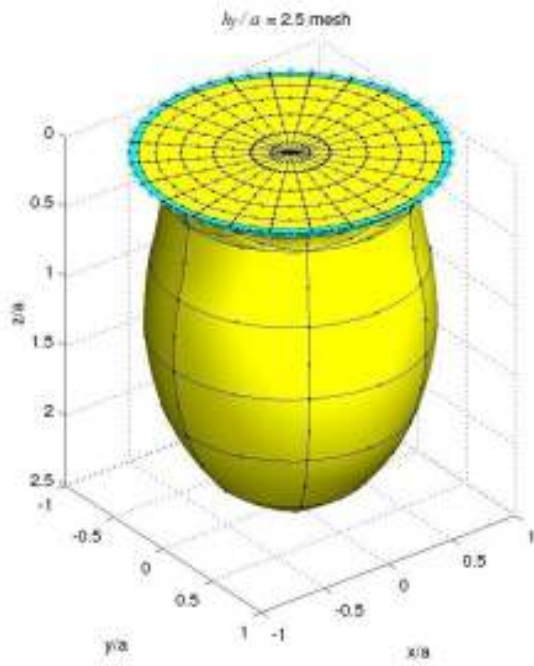


Figure 6.3

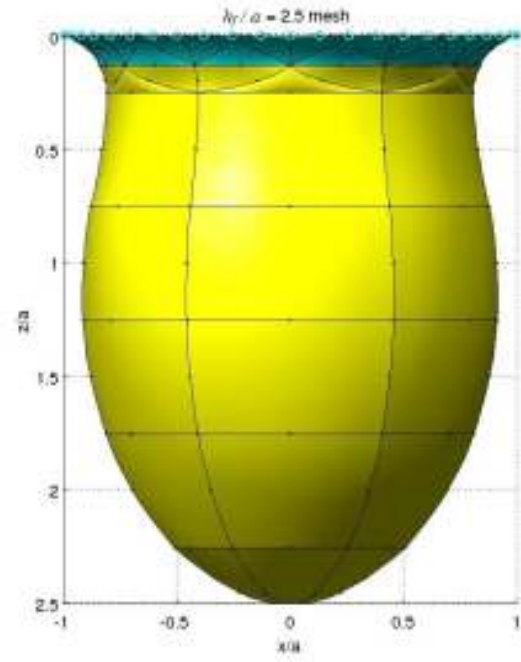


Figure 6.4

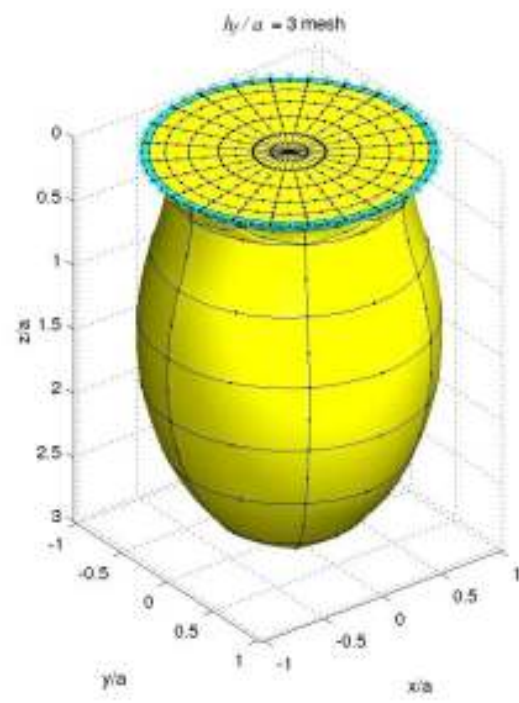


Figure 6.5

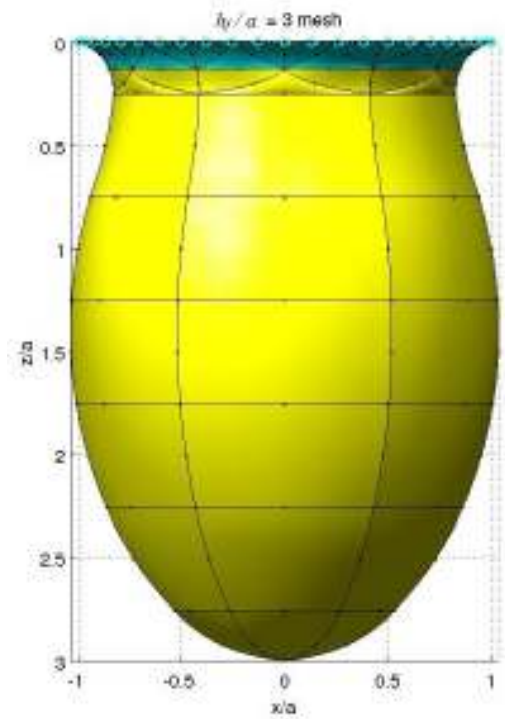


Figure 6.6

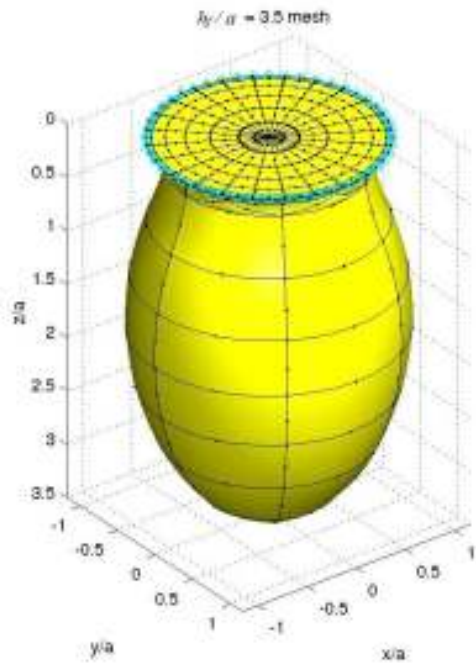


Figure 6.7

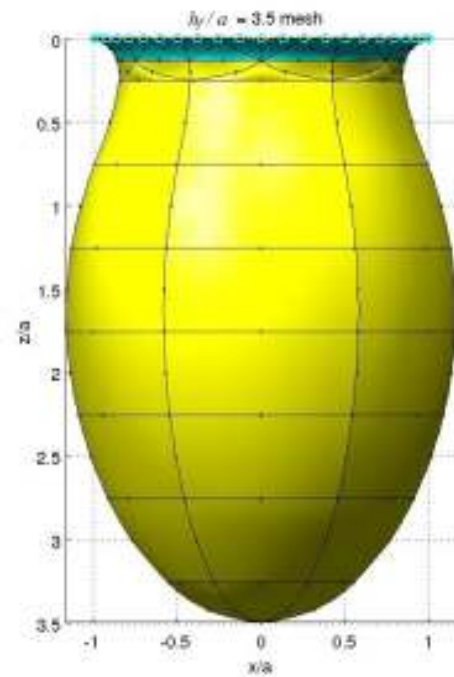


Figure 6.8

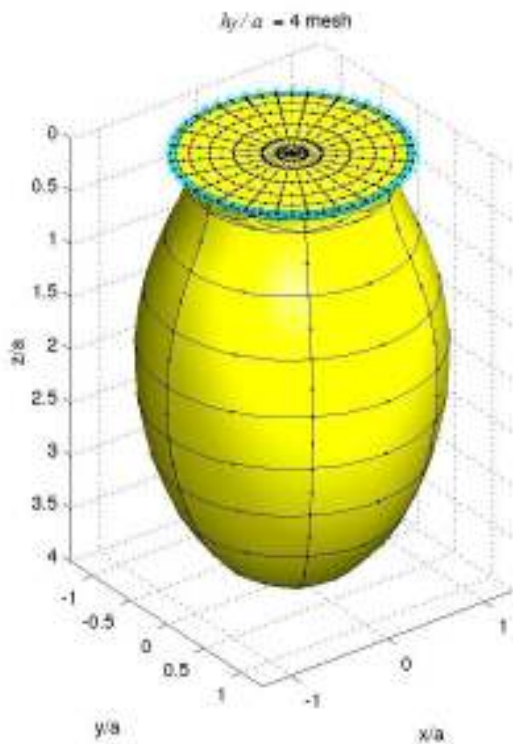


Figure 6.9

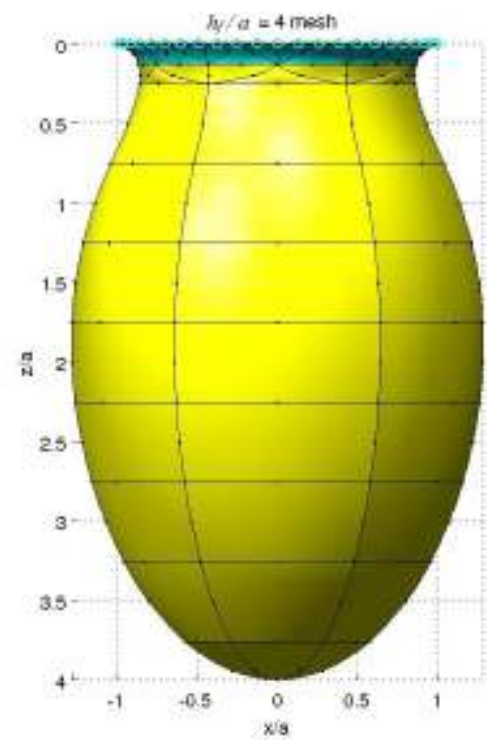


Figure 6.10

The inner/inclusion zone has a homogeneous shear modulus G_f . The soil outside of the inclusion zone is taken to follow a pure square-root-of-depth profile as appropriate for a uniform sand. The

use of this two-zone model allows for a closer representation of the actual soil without a complicated analysis of the stress and shear modulus in the footing influence region.

Intended to be adaptable to a foundation's configuration, the inclusion zone's dimension and modulus are the two key parameters of the dual zone model. Under higher contact pressure for example, a deeper and stiffer inclusion will be required although the combination of size and modulus is likely not totally unique, i.e. within a certain range, the depth may be increased if the stiffness is decreased and vice versa. To explore these aspects, impedance functions were generated for different inclusion depths and moduli to allow for more complete validation and calibration of the theory using the experimental data for all three footings. Quantities relevant to the two zone model are normalized accordingly:

$$\bar{h} = h_f / a \quad (6.1)$$

$$\bar{G} = G_f / G_{tip} \quad (6.2)$$

where G_{tip} is the in-situ shear modulus at a depth h_f which is the depth of the inclusion zone.

6.3 Material Properties

Material regions were defined according to Figure 6.11 and modeled in BEASSI using the parameters given in Table 6.1 below. The soil region is divided into two domains for the dual-zone model. The shake-table (aluminum plate) and support pads (rubber) were installed for seismic-type loading. A series of seismic test data was also collected for the circular footings; however the analysis is not included in this thesis.

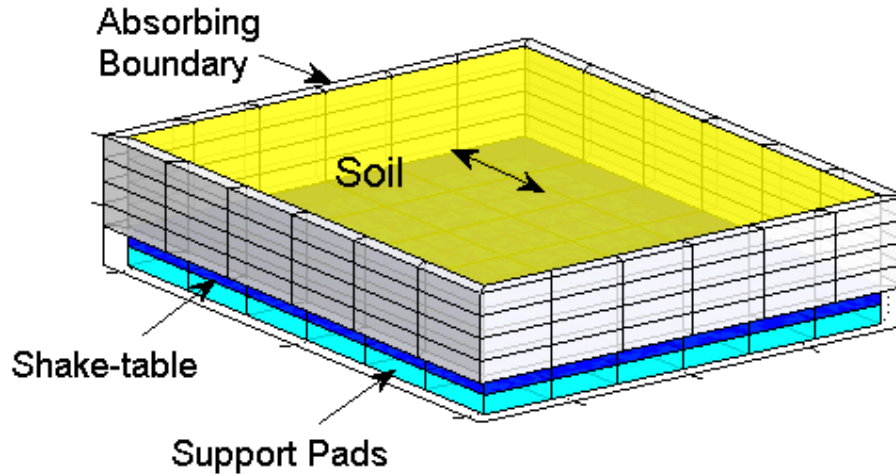


Figure 6.11: Material domains for the BEM model for centrifuge soil-container configuration

Property	Shake table	Elastomeric Pad	Duxeal	Soil
Density [kg/m^3]	2700	1800	1800	1739
Poisson's Ratio	0.35	0.45	0.45	0.25
Damping Ratio	0	10%	$0.18 - \frac{0.009 \sigma_{mean}}{30 \text{ 1KPa}}$	2%
Shear Modulus [MPa]	2.66×10^4	$1.5 \sqrt{\frac{\sigma_v}{1 \text{KPa}}}$	$2 + \frac{0.5 \sigma_{mean}}{30 \text{ 1KPa}}$	(See below)

Table 6.1: Material properties used in BEASSI computations.

As previously mentioned the soil shear modulus was given a set value for the homogeneous inclusion zone, outside of which it followed a square-root-of-depth profile consistent with the Hardin-Drnevich model (Equation 4.1). Converted for a result in Pascals, with σ_{mean} input in Pascals, one has

$$G_{HD} [Pa] = 1230 \left(6894 \left[\frac{Pa}{psi} \right] \right) \left(\frac{(2.973 - e)^2}{(1 + e)} \right) (OCR)^K \left(\frac{\sigma_{mean}}{6894 \left[\frac{Pa}{psi} \right]} \right)^{1/2} \quad (6.3)$$

Because it is a clean sand sample at near maximum density, the over-consolidation factor can be set

to be one. The void ratio was calculated from the specific gravity of the F-75 silica used and the bulk density of the soil sample as follows:

$$G_s = 2.65 \quad (6.4)$$

$$e = \frac{G_s(1000)}{\rho_{soil}} - 1 \quad (6.5)$$

The bulk density was recorded during calibration of the sand raining apparatus to be 1739 kg/m^3 .

The mean stress can be computed as follows:

$$\sigma_{mean} = \frac{(1 + 2K_0)}{3} \sigma_z \quad (6.6)$$

For the n^{th} g-level:

$$\sigma_{mean} = \frac{(1 + 2K_0)}{3} n \rho_{soil} g z \quad (6.7)$$

Because the soil is confined by the viscous Duxseal, it was reasoned in Ashlock (2006) and Soudkhah (2010) that K_0 was significantly larger than the result given by Jaky's formula $K_0 = 1 - \sin(\varphi)$. On the basis of seismic free-field experiments, it was deduced in Soudkhah (2010) that K_0 was in a range from 0.9 to 1.0, with an average of 0.95. The average value was used for computations in this thesis.

6.4 Impedance Functions

Computational results are returned by BEASSI in the form of non-dimensional impedances as a function of frequency, which relate force and displacement at the soil-structure interface in the frequency domain as

$$\begin{Bmatrix} F_z^O(\omega) \\ F_x^O(\omega) \\ M_y^O(\omega) \end{Bmatrix} = \begin{bmatrix} K_{vv}(\omega) & 0 & 0 \\ 0 & K_{hh}(\omega) & K_{hm}(\omega) \\ 0 & K_{mh}(\omega) & K_{mm}(\omega) \end{bmatrix} \begin{Bmatrix} U_z^O(\omega) \\ U_x^O(\omega) \\ \theta_y^O(\omega) \end{Bmatrix} \quad (6.8)$$

or in matrix form

$$\mathbf{F}_O = \mathbf{K}(\omega)\mathbf{U}_O(\omega) \quad (6.9)$$

The impedance functions in (6.8) are returned by BEASSI in non-dimensional form, normalized by a user-defined reference length and reference shear modulus. In the case of the cylindrical footing, the radius ‘ a ’ was used as the characteristic length. In general, the reference in-situ shear modulus is taken as the value at a depth equal to the reference length, computed using the Hardin Drnevich formula (6.3). That is

$$l_{ref} = a = \text{footing radius} \quad (6.10)$$

$$G(z) = G_f \left(\frac{z}{a} \right)^{1/2} \quad (6.11)$$

$$G_{ref} = G_{HD}(a) \quad (6.12)$$

g-level (N)	$G_{ref} = G_{HD}(a)$ [MPa]
1	8.90
11	29.44
22	41.54
33	50.91
44	58.75
55	65.71
66	72.00

Table 6.2: Reference shear modulus by g-level.

Impedances and frequency were normalized using (6.10) and (6.11) in the manner described below.

Non-dimensional quantities will be designated by an overbar.

$$c_s = \sqrt{\frac{G_{ref}}{\rho_{soil}}} \quad (6.13)$$

$$\varpi = \frac{\omega a}{c_s} \quad (6.14)$$

$$\bar{K}_{vv} = \frac{K_{vv}}{G_{ref} a} \quad (6.15)$$

$$\bar{K}_{hh} = \frac{K_{hhv}}{G_{ref} a} \quad (6.16)$$

$$\bar{K}_{hm} = \frac{K_{hm}}{G_{ref} a^2} \quad (6.17)$$

$$\bar{K}_{mm} = \frac{K_{mm}}{G_{ref} a^3} \quad (6.18)$$

$$\bar{K}_{tt} = \frac{K_{tt}}{G_{ref} a^3} \quad (6.19)$$

The last quantity \bar{K}_{tt} given in (6.19) is for torsional motions which were not investigated in this report. BEASSI however generates \bar{K}_{tt} as one of the outputs, so it will be briefly considered. To generate the impedances needed for the analysis of the experimental data, BEASSI was run for three separate loading cases: an applied unit vertical, horizontal and rocking foundation motion. Coupling terms \bar{K}_{hm} and \bar{K}_{mh} will be generated for both the horizontal force and moment case. Theoretically these should be equal but computationally there is usually a minor difference. This is accounted for by averaging the coupling terms:

$$\bar{K}_{hm} = \bar{K}_{mh} = \left(\frac{1}{2}\right)(\bar{K}_{hm} + \bar{K}_{mh}) \quad (6.20)$$

For a more detailed explanation refer Ashlock 2006. As illustrations, Figures 6.12 – 6.14 are a typical set of the frequency-dependent normalized impedance functions as a function of \bar{h} and \bar{G} .

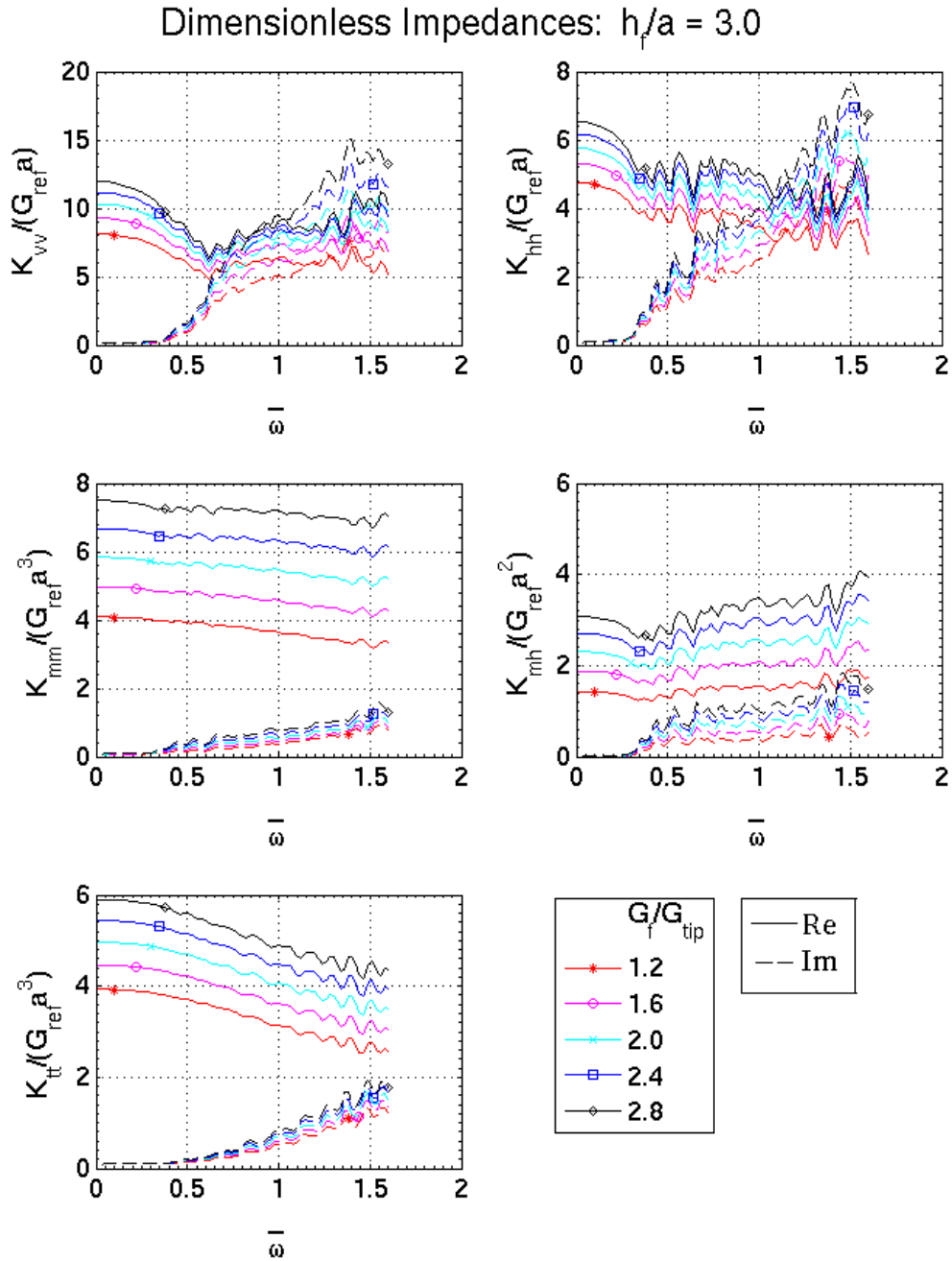


Figure 6.12: Impedance results from BEASSI for a family of dual-zone models of $\bar{h} = 3.0$

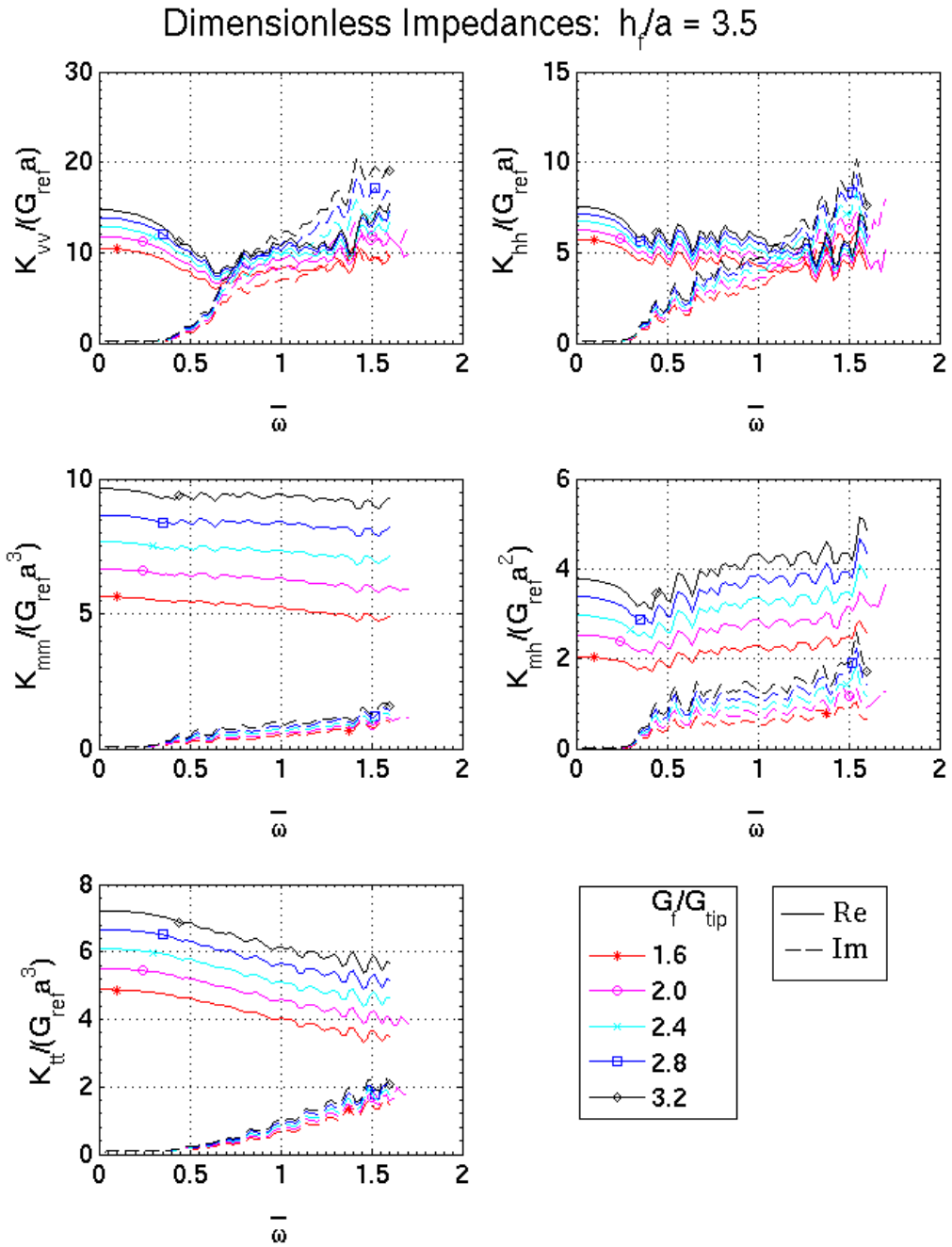


Figure 6.13: Impedance results from BEASSI for a family of dual-zone models of $\bar{h} = 3.5$

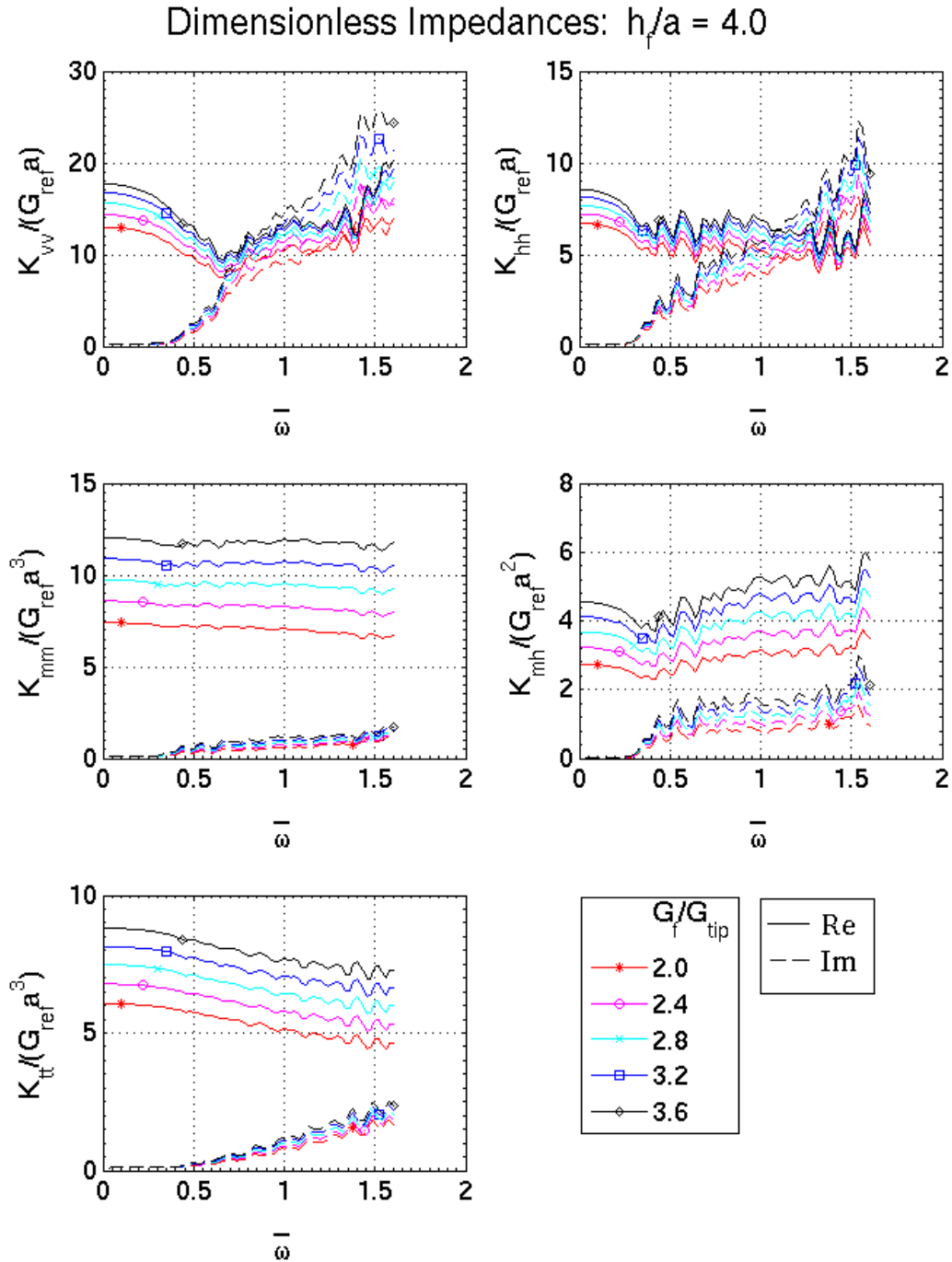


Figure 6.14 Impedance results from BEASSI for a family of dual-zone models of $\bar{h} = 4.0$

Larger \bar{h} and \bar{G} correspond to a deeper and stiffer inclusion zone, as one would expect to be reasonable in the case of a heavier foundation. Both the real and imaginary parts are plotted on

the same set of axes. The results at $\varpi = 0.05$ can be interpreted as a static solution as one may notice that the imaginary part of each impedance function is basically zero here. One can also see that the static values of \bar{K}_{ij} increase with both \bar{h} and \bar{G} . Making the analogy to a mechanical spring-dashpot model, the imaginary part of $\bar{K}_{ij}(\varpi)$ can represent damping effects. The real parts intersect the y-axis at higher locations with increasing \bar{G} , and this order is generally maintained throughout the frequency range shown. The smaller impedances of a softer inclusion zone mean a smaller reaction force from the soil per unit footing displacement. Looking at the numerical results, it can also be concluded that for the range of \bar{h} shown, a deeper inclusion of equal stiffness gives a stiffening trend. This is summarized in Tables 6.3 and 6.4 below.

	$\bar{h} = 3.0, \bar{G} = 2.0$	$\bar{h} = 3.5, \bar{G} = 2.0$	$\bar{h} = 4.0, \bar{G} = 2.0$
$\text{Re}(\bar{K}_{vv}) _{\varpi=0}$	10.5	11.7	13.0
$\text{Re}(\bar{K}_{hh}) _{\varpi=0}$	5.7	6.3	6.7
$\text{Re}(\bar{K}_{mh}) _{\varpi=0}$	2.3	2.5	2.7
$\text{Re}(\bar{K}_{mm}) _{\varpi=0}$	5.9	6.6	7.5
$\text{Re}(\bar{K}_{tt}) _{\varpi=0}$	5.0	5.5	6.1

Table 6.3: Effect of inclusion depth on static impedance.

	$\bar{G} = 1.6, \bar{h} = 3.5$	$\bar{G} = 2.0, \bar{h} = 3.5$	$\bar{G} = 2.4, \bar{h} = 3.5$	$\bar{G} = 2.8, \bar{h} = 3.5$	$\bar{G} = 3.2, \bar{h} = 3.5$
$\text{Re}(\bar{K}_{vv}) _{\varpi=0}$	10.5	11.7	12.9	13.9	14.8
$\text{Re}(\bar{K}_{hh}) _{\varpi=0}$	5.7	6.3	6.7	7.1	7.5
$\text{Re}(\bar{K}_{mh}) _{\varpi=0}$	2.0	2.5	2.9	3.4	3.8
$\text{Re}(\bar{K}_{mm}) _{\varpi=0}$	5.6	6.6	7.6	8.6	9.6
$\text{Re}(\bar{K}_{tt}) _{\varpi=0}$	4.9	5.5	6.1	6.6	7.2

Table 6.4: Effect of inclusion stiffness on static impedance

Similarly, the imaginary parts are larger for stiffer inclusions. A larger \bar{h} or \bar{G} will therefore also result in wider resonance peaks due to the increased radiation damping.

Up to about $\varpi = 3.5$, the impedance functions for the finite-depth soil model are generally smooth in the real part and have an imaginary part that is small by comparison. As frequency increases, the translational impedances (\bar{K}_{vv} and \bar{K}_{hh}) exhibit larger oscillations in both the real and imaginary. One can also see that the imaginary part may be higher than the real part at sufficiently high frequency. The rotational and coupling impedance functions are smoother by comparison and have a larger real component than imaginary for all frequencies shown.

6.5 Impedance Comparison: Circular vs. Square Foundations

Before using these results to compute the accelerances for comparing with the experimental data, it would be meaningful to plot the circular footing's impedances against the impedance results for the corresponding square footing problem in Soudkiah (2010) for the same finite domain soil model. A superscript or subscript 'a' will designate values corresponding to the circular footing. Square footing values will be denoted with a superscript or subscript 'b', representing the half-width b of the footing base.

As we saw in Chapter 5, the experimental data of both the square and circular cases compare quite well in terms of type, location, and magnitude of each response feature. The impedances will therefore be compared to gain some preliminary insight on the BEASSI results. To reconcile the different reference parameters used in computation, the square results will first be scaled for a footing of equivalent area to the circular footing (termed 'equivalent square' from this point on), and then renormalized with respect to the circular footing's properties.

The equivalent square will be denoted by its half width b^* . First, we define the requirement that the areas of the circle and equivalent square should be equal:

$$(2b^*)^2 = \pi a^2 \quad (6.21)$$

$$b^* = a \sqrt{\frac{\pi}{4}} \quad (6.22)$$

Both footings are also resting in the same soil, so both cases must match the same soil profile despite the difference in choice of normalization lengths, i.e.,

$$G(z) = G_{ref}^a \sqrt{\frac{z}{a}} \quad (6.23)$$

$$G(z) = G_{ref}^{b^*} \sqrt{\frac{z}{b^*}}$$

$$G_{ref}^a \sqrt{\frac{z}{a}} = G_{ref}^{b^*} \sqrt{\frac{z}{b^*}} \quad (6.24)$$

$$G_{ref}^{b^*} = G_{ref}^a \sqrt{\frac{b^*}{a}} \quad (6.25)$$

The result (6.25) can be written purely in terms of G_{ref}^a by making use of (6.22):

$$G_{ref}^{b^*} = G_{ref}^a \left(\frac{\pi}{4} \right)^{1/4} \quad (6.26)$$

The dimensional impedances for the equivalent square can now be written in terms of circular footing properties using the appropriate factors (6.22) and (6.26):

$$K_{vv}^{b^*} = G_{ref}^{b^*} \overline{K}_{vv}^b(\varpi_b) \quad (6.27)$$

$$K_{vv}^{b^*} = \left(\frac{\pi}{4} \right)^{3/4} a G_{ref}^a \overline{K}_{vv}^b \quad (6.28)$$

Similarly,

$$K_{hh}^{b*} = \left(\frac{\pi}{4}\right)^{3/4} a G_{ref}^a \overline{K}_{hh}^b \quad (6.29)$$

$$K_{hm}^{b*} = \left(\frac{\pi}{4}\right)^{5/4} a^2 G_{ref}^a \overline{K}_{hm}^b \quad (6.30)$$

$$K_{mm}^{b*} = \left(\frac{\pi}{4}\right)^{7/4} a^3 G_{ref}^a \overline{K}_{mm}^b \quad (6.31)$$

The process for scaling the frequency is similar. Although like the soil profile the dimensional frequency should be the same for all footings, the actual frequency vectors computed by BEASSI may have different lengths and discrete values. For this reason the subscript will be retained to specify the source of the computation.

$$\omega_{b*} = \frac{\overline{\omega}_b c_s^{b*}}{b^*} \quad (6.32)$$

$$\omega_{b*} = \left(\frac{\pi}{4}\right)^{-3/8} \frac{\overline{\omega}_b c_s^a}{a} \quad (6.33)$$

Now, for a dimensionless comparison, we can normalize the results (6.28) – (6.31) and (6.33) with respect to the cylindrical footing's properties. It is in this fashion that the dimensionless results can be measured and compared in the same diagram meaningfully. To clarify the conversion process from circle to equivalent square using impedances generated for a square footing, the notation b^*/a will be utilized to denote square footing results scaled to a half width of b^* and then normalized with respect to a circular base footing of radius a , *i.e.*,

$$\overline{K}_{vv}^{b*/a} = \frac{K_{vv}^{b*}}{G_{ref}^a a} \quad (6.34)$$

Making use of (6.28), one may write

$$\overline{K}_{vv}^{b*/a} = \left(\frac{\pi}{4}\right)^{3/4} \overline{K}_{vv}^b \quad (6.35)$$

Similarly:

$$\overline{K}_{hh}^{b*/a} = \left(\frac{\pi}{4}\right)^{3/4} \overline{K}_{hh}^b \quad (6.36)$$

$$\overline{K}_{hm}^{b*/a} = \left(\frac{\pi}{4}\right)^{5/4} \overline{K}_{hm}^b \quad (6.37)$$

$$\overline{K}_{mm}^{b*/a} = \left(\frac{\pi}{4}\right)^{7/4} \overline{K}_{mm}^b \quad (6.38)$$

$$\varpi_{b*/a} = \left(\frac{\pi}{4}\right)^{-3/8} \varpi_b \quad (6.39)$$

Using these results, the impedances can now be compared on the same non-dimensional scale. Figures 6.15 – 6.18 show the dimensionless impedance plots comparing the circle, equivalent square, and original square impedances. Both the equivalent square and circular impedances are normalized using a and G_{ref}^a and plotted versus ϖ_a for a direct comparison. The square impedances are normalized by b and G_{ref}^b , and plotted versus ϖ_b . This plotting scheme makes it possible to also observe the effects of the equivalent square conversion process.

Among Figures 6.15 – 6.18, the largest disagreement between the circle and equivalent square is observable in the mid-frequency range ($\varpi_a > 0.6$) of the real part of \overline{K}_{vv} in Figure 6.15. The impedances relate force to displacement through Equation (6.9). When considered as force per displacement factors, it implies that a smaller vertical footing displacement produces a larger soil reaction force in this frequency range, when computing the response using the circular impedances versus the equivalent square's impedances. In the comparison with the original square impedances, the equivalent square conversion is closer to the circular case for \overline{K}_{hh} according to Figure 6.15. As with \overline{K}_{hh} , the equivalent square conversion for \overline{K}_{hm} can be seen in Figure 6.17 to be closer to the circular case than the original square case.

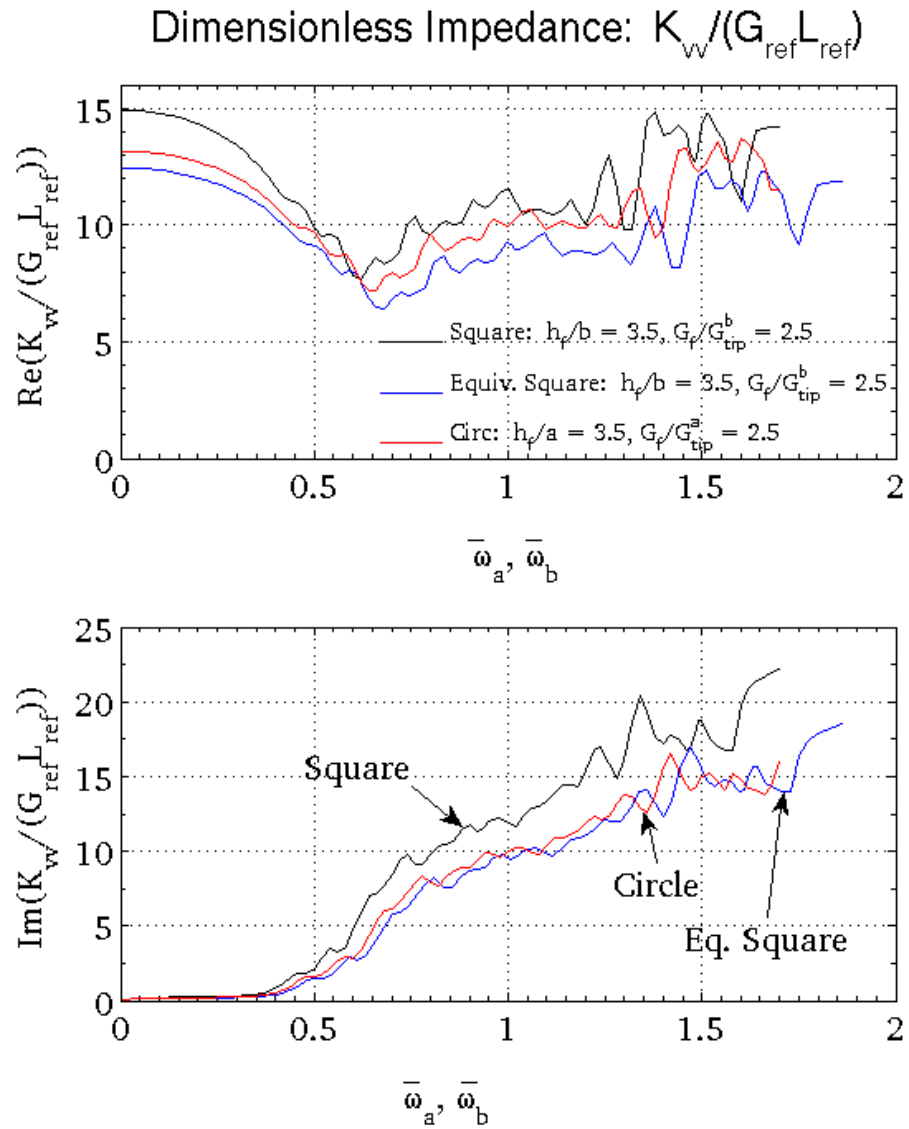


Figure 6.16: Dimensionless impedance \bar{K}_w comparison between square, equivalent square and circular footings.

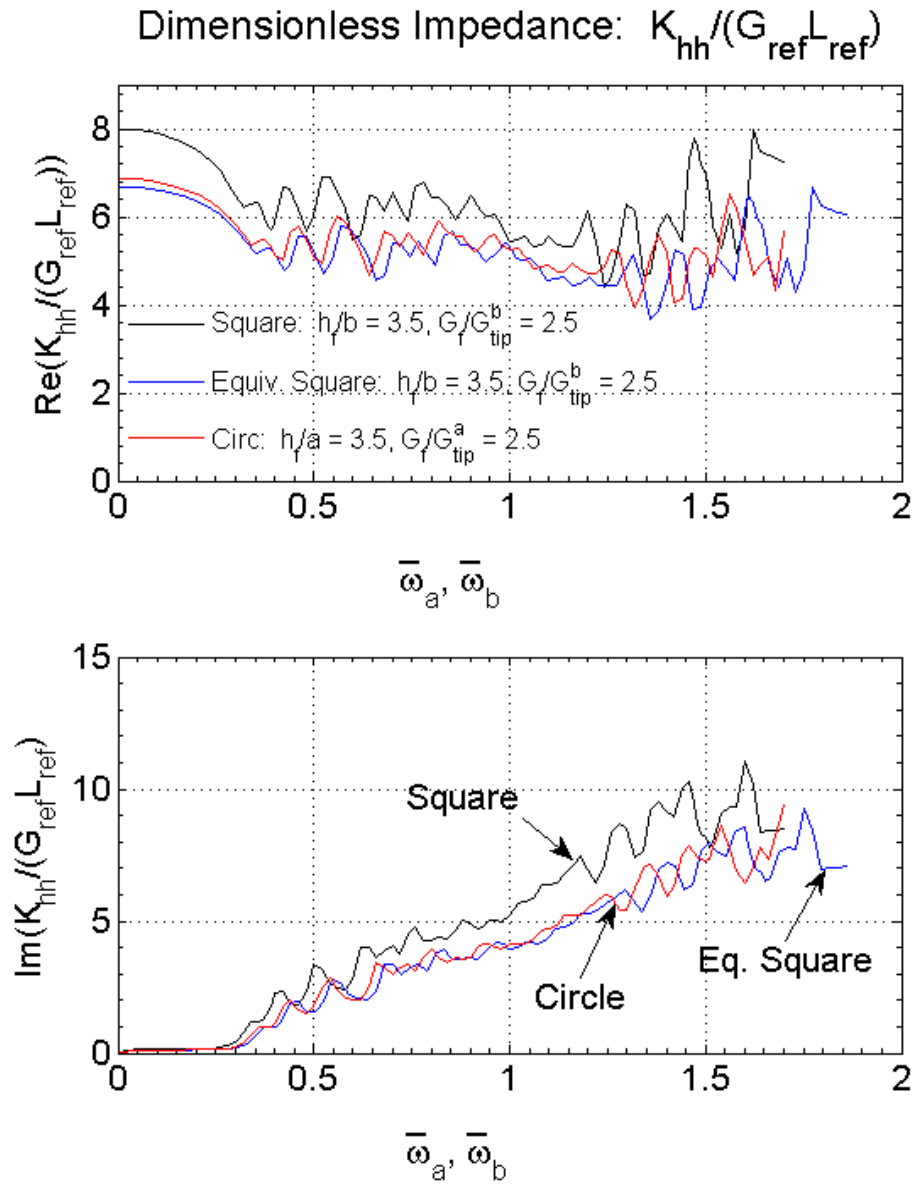


Figure 6.17: Dimensionless impedance \bar{K}_{hh} comparison between square, equivalent square, and circle.

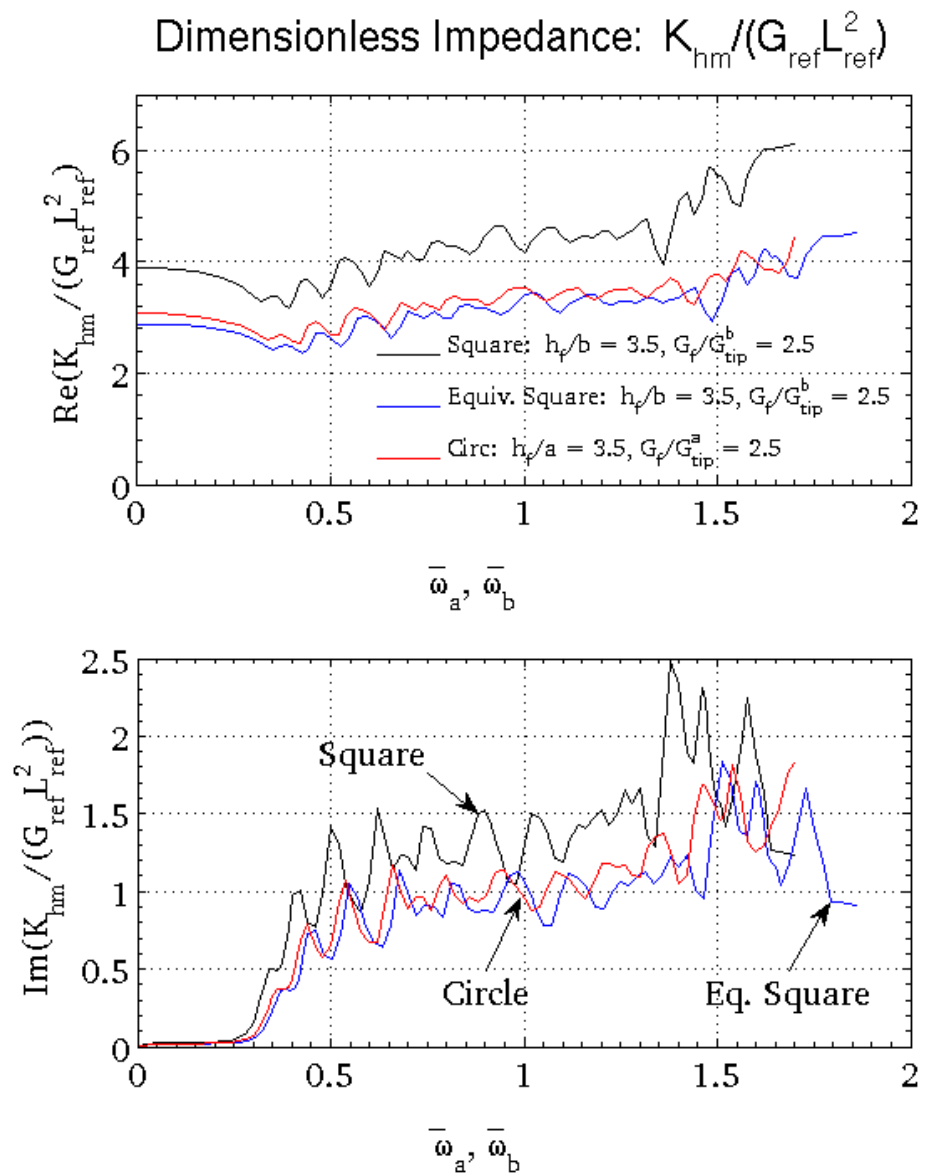


Figure 6.18: Dimensionless impedance \bar{K}_{hm} comparison for a square, equivalent square, and circle.

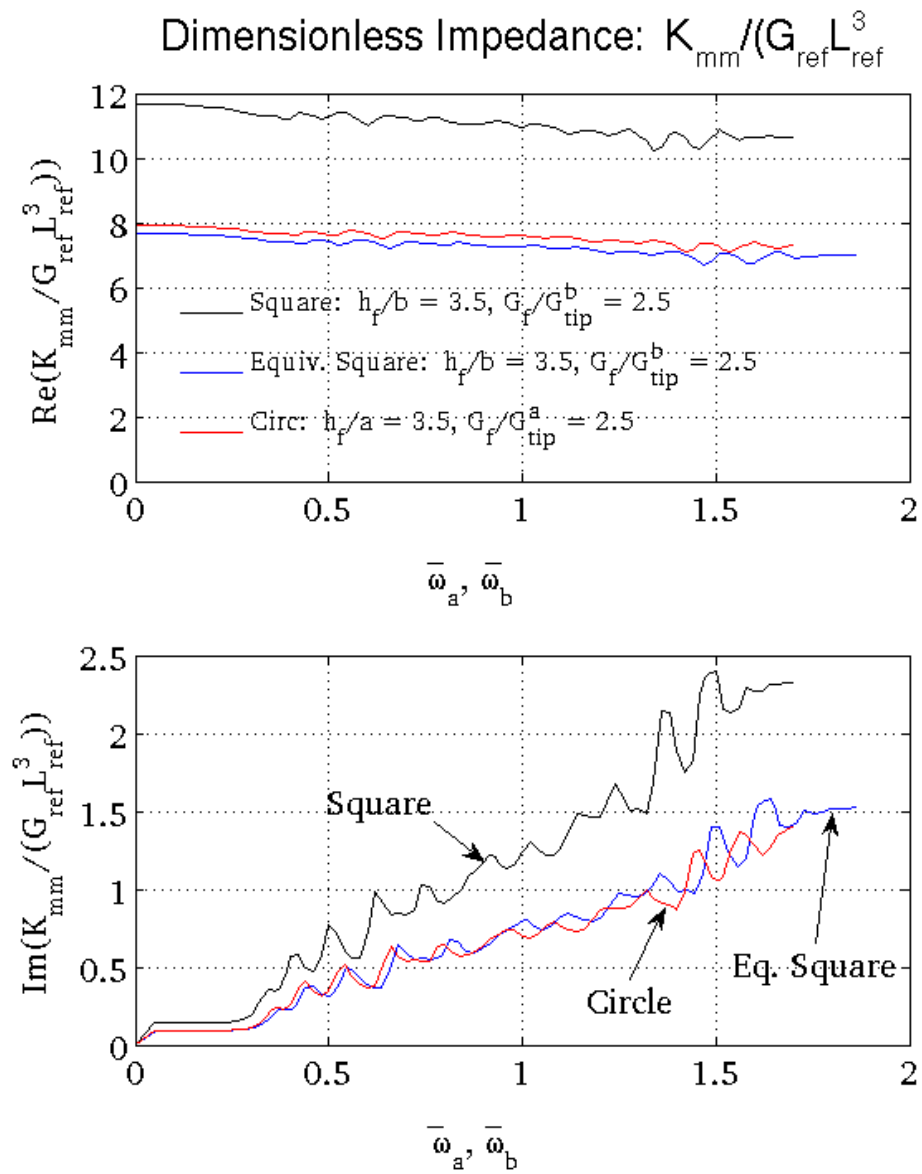


Figure 6.19: Dimensionless impedance \bar{K}_{mm} comparison for the square, equivalent square, and circular cases.

6.6 Theoretical Accelerance Functions

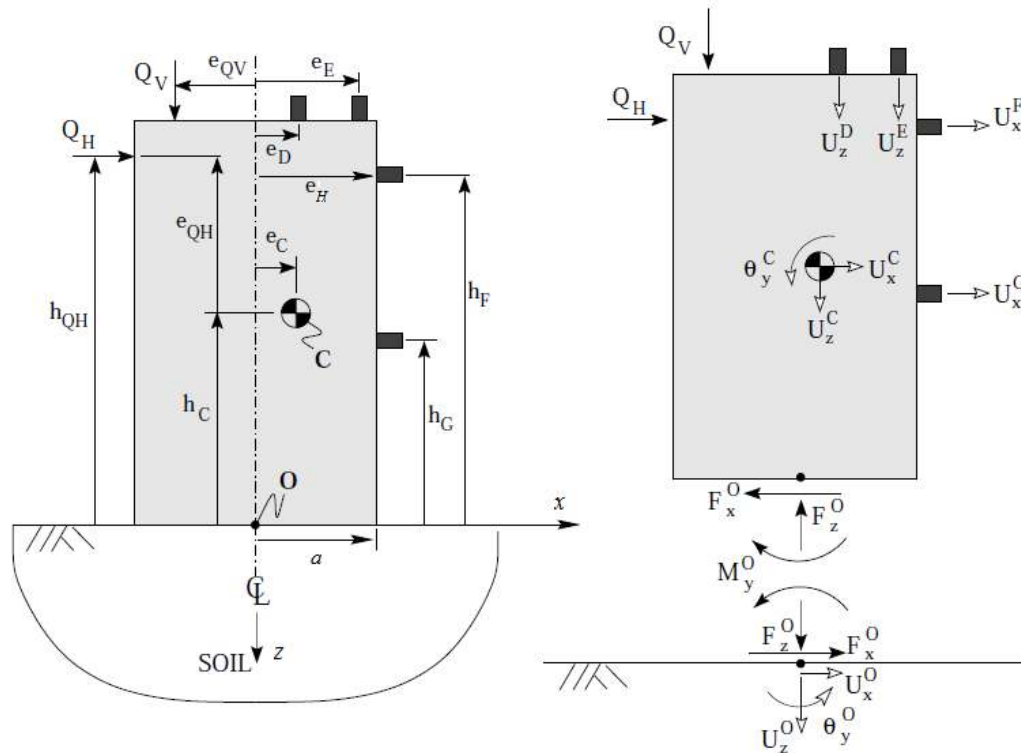


Figure 6.20: Diagram showing possible load cell and accelerometer locations, as well as forces, moments, and points of interest.

In order to utilize the impedances in characterizing the footing motions, accelerance functions can be generated for the response measurement locations of interest through a straightforward load analysis and kinematic transformation, as in Ashlock (2006). With the notation and sign convention in Figure 6.19 as in Ashlock (2006), the equations of motion for a rigid footing can be written in the frequency domain (6.41) - (6.43) as

$$Q_M = Q_V(e_{QV} + e_c) - Q_H(e_{QH}) \quad (6.40)$$

$$Q_V(\omega) - F_z^O(\omega) + m_f \omega^2 U_z^C(\omega) = 0 \quad (6.41)$$

$$Q_H(\omega) - F_x^O(\omega) + m_f \omega^2 U_x^C(\omega) = 0 \quad (6.42)$$

$$Q_M(\omega) - F_x^O(\omega)h_c - F_z^O(\omega)e_c - M_y^O(\omega) + J_y^C \omega^2 \theta_y^C(\omega) = 0 \quad (6.43)$$

Rewriting (6.41) – (6.43) in matrix form, one has

$$\begin{bmatrix} 1 & 0 & 0 \\ 0 & 1 & 0 \\ e_c & h_c & 1 \end{bmatrix} \begin{Bmatrix} F_z^O(\omega) \\ F_x^O(\omega) \\ M_y^O(\omega) \end{Bmatrix} - \omega^2 \begin{bmatrix} m_f & 0 & 0 \\ 0 & m_f & 0 \\ 0 & 0 & J_y^C \end{bmatrix} \begin{Bmatrix} U_z^C(\omega) \\ U_x^C(\omega) \\ \theta_y^C(\omega) \end{Bmatrix} = \begin{Bmatrix} Q_V(\omega) \\ Q_H(\omega) \\ Q_M(\omega) \end{Bmatrix} \quad (6.44)$$

In terms of the matrix and vector notation

$$\mathbf{C} = \begin{bmatrix} 1 & 0 & 0 \\ 0 & 1 & 0 \\ e_c & h_c & 1 \end{bmatrix} \quad (6.45)$$

$$\mathbf{M} = \begin{bmatrix} m_f & 0 & 0 \\ 0 & m_f & 0 \\ 0 & 0 & J_y^C \end{bmatrix} \quad (6.46)$$

$$\mathbf{U}_C(\omega) = \begin{Bmatrix} U_z^C(\omega) \\ U_x^C(\omega) \\ \theta_y^C(\omega) \end{Bmatrix} \quad (6.47)$$

$$\mathbf{Q}(\omega) = \begin{Bmatrix} Q_V(\omega) \\ Q_H(\omega) \\ Q_M(\omega) \end{Bmatrix} \quad (6.48)$$

the equations of motion can be rewritten in a compact form as

$$\mathbf{CK}(\omega)\mathbf{U}_O(\omega) - \omega^2\mathbf{MU}_C(\omega) = \mathbf{Q}(\omega) \quad (6.49)$$

Figure 6.19 is for the general case of either horizontal or vertical loading with a number of possible

accelerometer configurations. The case of interest in this study is for vertical eccentric loading with one accelerometer measurement location on top of the footing and two on the side. The kinematic transformation is therefore

$$\begin{Bmatrix} U_z^D(\omega) \\ U_x^F(\omega) \\ U_x^G(\omega) \end{Bmatrix} = \begin{bmatrix} 1 & 0 & -(e_D - e_C) \\ 0 & 1 & -(h_F - h_C) \\ 0 & 1 & -(h_G - h_C) \end{bmatrix} \begin{Bmatrix} U_z^C(\omega) \\ U_x^C(\omega) \\ \theta_x^C(\omega) \end{Bmatrix} \quad (6.50)$$

Taking the inverse, one can write

$$\begin{Bmatrix} U_z^C(\omega) \\ U_x^C(\omega) \\ \theta_x^C(\omega) \end{Bmatrix} = \begin{bmatrix} 1 & \frac{-(e_D - e_C)}{(h_F - h_G)} & \frac{(e_D - e_C)}{(h_F - h_G)} \\ 0 & \frac{-(h_G - h_C)}{(h_F - h_G)} & \frac{(h_F - h_C)}{(h_F - h_G)} \\ 0 & \frac{-1}{(h_F - h_G)} & \frac{1}{(h_F - h_G)} \end{bmatrix} \begin{Bmatrix} U_z^D(\omega) \\ U_x^F(\omega) \\ U_x^G(\omega) \end{Bmatrix} = \mathbf{TU}_{DFG}(\omega) \quad (6.51)$$

The kinematic transformation from \mathbf{U}_C to \mathbf{U}_O is

$$\begin{Bmatrix} U_z^O(\omega) \\ U_x^O(\omega) \\ \theta_y^O(\omega) \end{Bmatrix} = \begin{bmatrix} 1 & 0 & e_C \\ 0 & 1 & h_C \\ 0 & 0 & 1 \end{bmatrix} \begin{Bmatrix} U_z^C(\omega) \\ U_x^C(\omega) \\ \theta_y^C(\omega) \end{Bmatrix} = \mathbf{C}^T \mathbf{U}_C(\omega) = \mathbf{C}^T \mathbf{TU}_{DFG}(\omega) \quad (6.52)$$

Substituting equations (6.51) and (6.52) into (6.49) gives the result

$$\mathbf{CK}(\omega) \mathbf{C}^T \mathbf{TU}_{DFG}(\omega) - \omega^2 \mathbf{MTU}_{DFG}(\omega) = \mathbf{Q}(\omega) \quad (6.53)$$

$$[\mathbf{CK}(\omega) \mathbf{C}^T \mathbf{T} - \omega^2 \mathbf{MT}] \mathbf{U}_{DFG}(\omega) = \mathbf{Q}(\omega) \quad (6.54)$$

By means of (6.54), one can compute the accelerance function as:

$$A_i^j(\omega) = \frac{\ddot{U}_i^j(\omega)}{Q_N(\omega)} = \frac{-\omega^2 U_i^j(\omega)}{Q_N(\omega)} \quad (6.55)$$

$$\mathbf{A}_{DFG}(\omega) = \begin{Bmatrix} A_z^D(\omega) \\ A_x^F(\omega) \\ A_x^G(\omega) \end{Bmatrix} = -\omega^2 [\mathbf{CK}(\omega)\mathbf{C}^T\mathbf{T} - \omega^2\mathbf{MT}]^{-1} \begin{Bmatrix} Q_v(\omega) \\ Q_N(\omega) \\ Q_H(\omega) \\ Q_N(\omega) \\ Q_M(\omega) \\ Q_N(\omega) \end{Bmatrix} \quad (6.56)$$

In the case of vertical excitation, $Q_N(\omega)$ is set to be $Q_v(\omega)$.

6.7 Theoretical Accelerance Behavior

Using the result from (6.56), it is now possible to generate theoretical accelerance curves for any g-level or footing size. Continuing from the impedance comparison with the equivalent square, a further analysis can be conducted by plotting the corresponding accelerances. The model scale comparisons are shown for footing C2 at 33g in Figures 6.20 – 6.22 as illustrations. The match between the circular result and equivalent-square is very close other than a slight disagreement of 0.5 kg^{-1} in the VC/VE peak magnitude and small high-frequency fluctuations in all three accelerance curves.

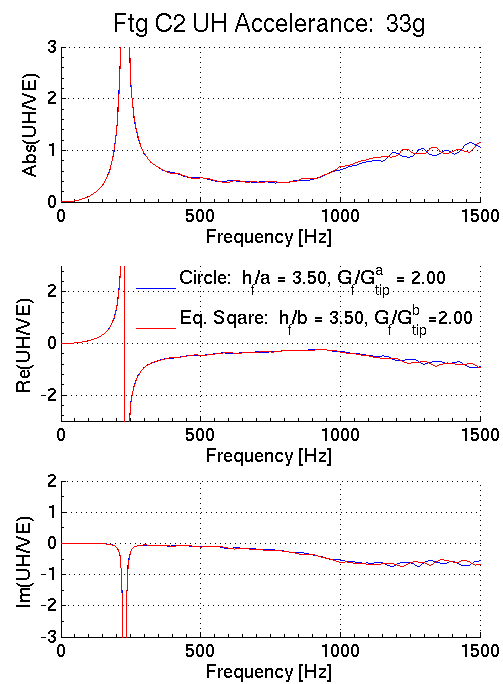
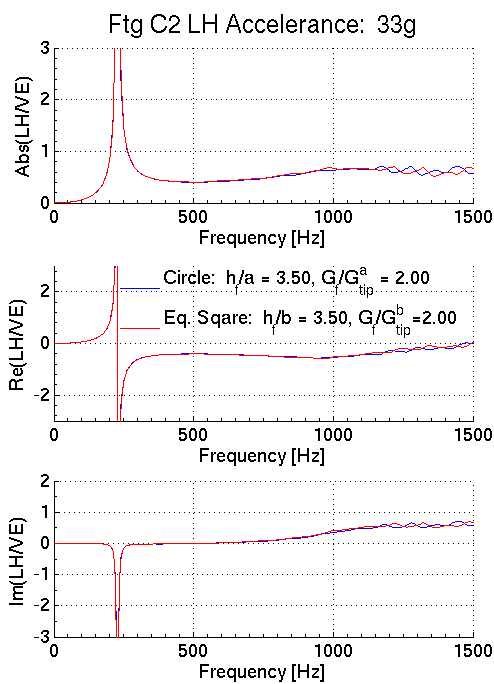


Figure 6.21: LH/VE theoretical accelerances plotted for footing C2 at 33g.

Figure 6.22: UH/VE theoretical accelerances plotted for footing C2 at 33g.

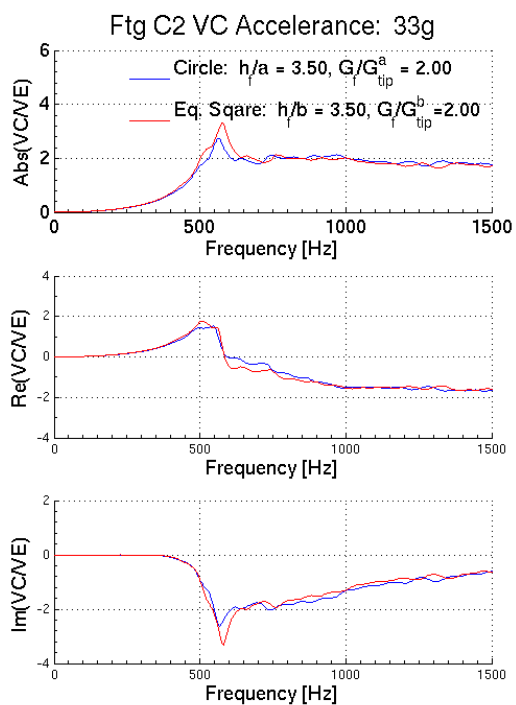


Figure 6.23: VC/VE theoretical accelerance plotted for footing C2 at 33g.

Plotted in Figures 6.23 – 6.40 as well as Figures 6.41 – 6.47 are arrays of accelerances for each model footing that demonstrate the effects of footing size, as well as inclusion depth and stiffness. This type analysis reveals the effective nature of the dual-zone continuum theory prior to comparison with the data.

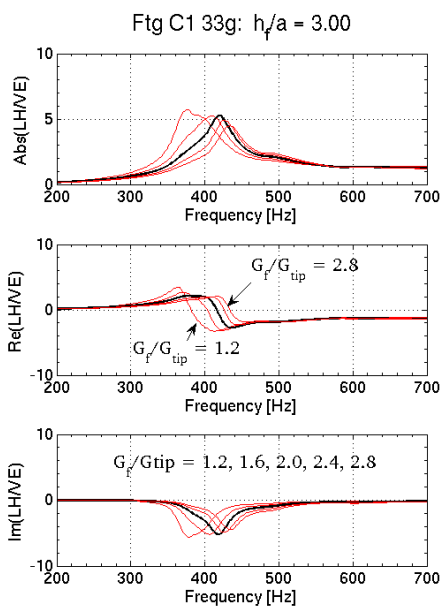


Figure 6.24: Footing C1 LH/VE theoretical acceleration, rocking peak region.

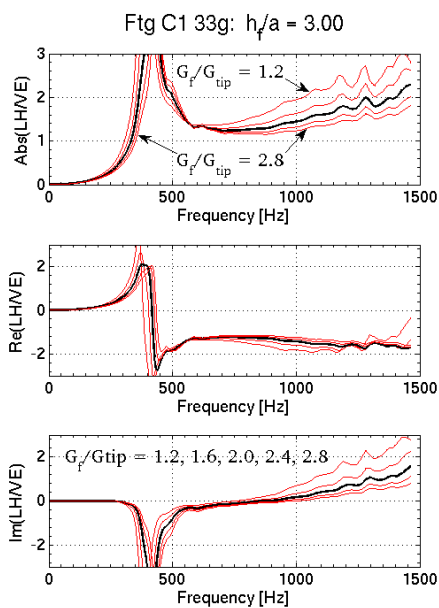


Figure 6.25: Footing C1 LH/VE theoretical acceleration, second peak.

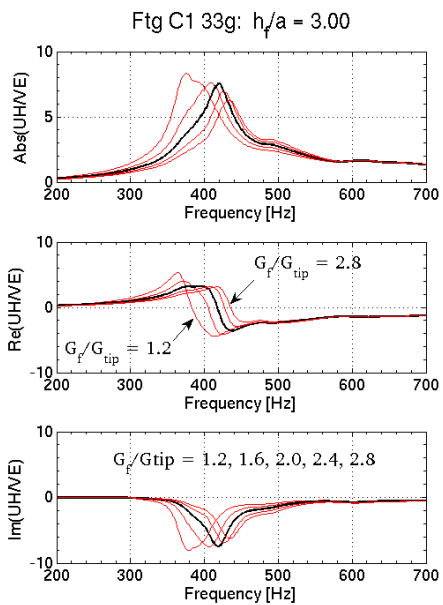


Figure 6.26: Footing C1 UH/VE theoretical rocking peak.

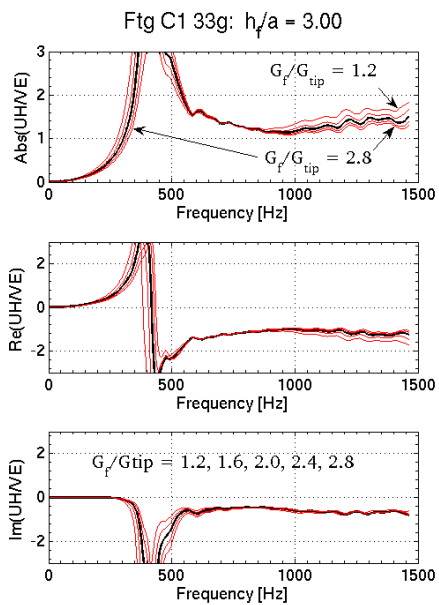


Figure 6.27: Footing C1 UH/VE theoretical second peak.

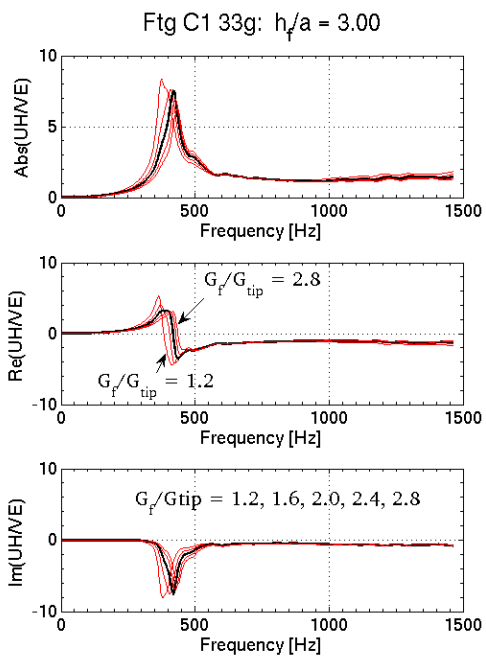


Figure 6.28: Footing C1 UH/VE theoretical acceleration, entire range.

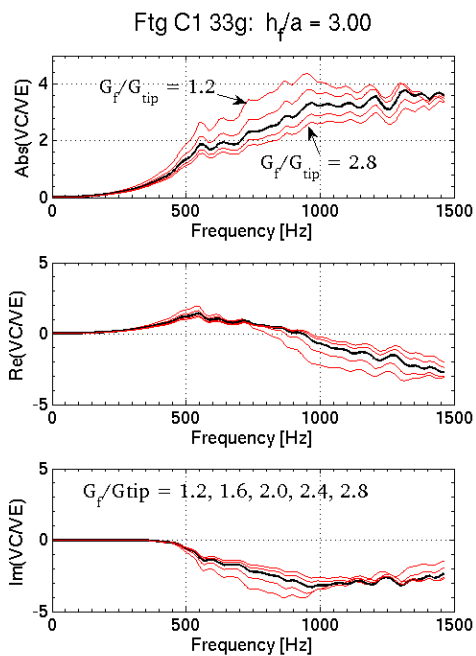


Figure 6.29: Footing C1 VC/VE theoretical acceleration.

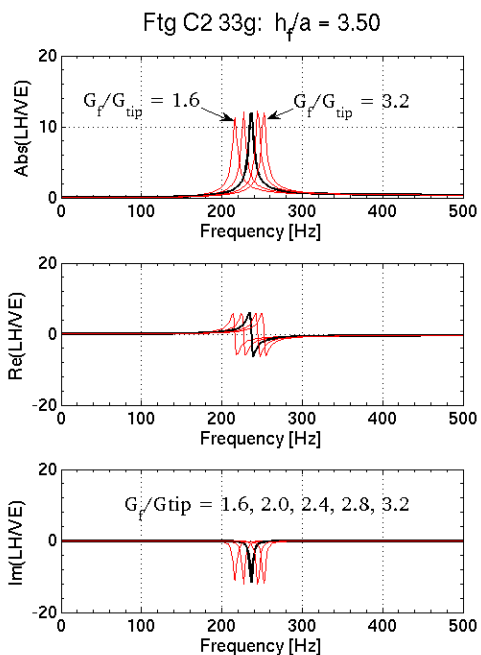


Figure 6.30: Footing C2 LH/VE theoretical rocking peak.

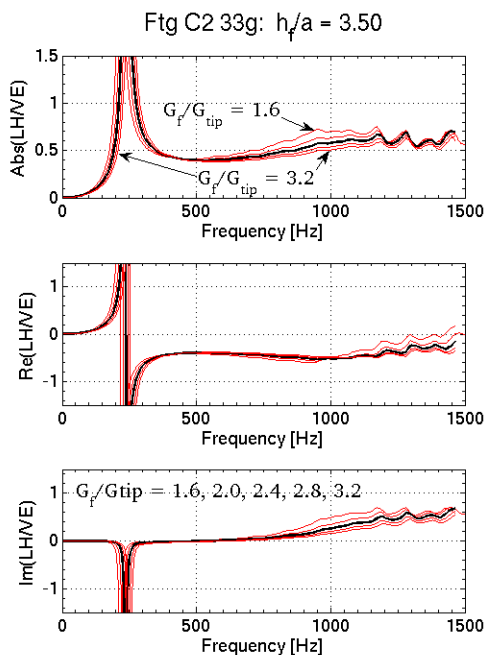


Figure 6.31: Footing C2 LH/VE theoretical second peak.

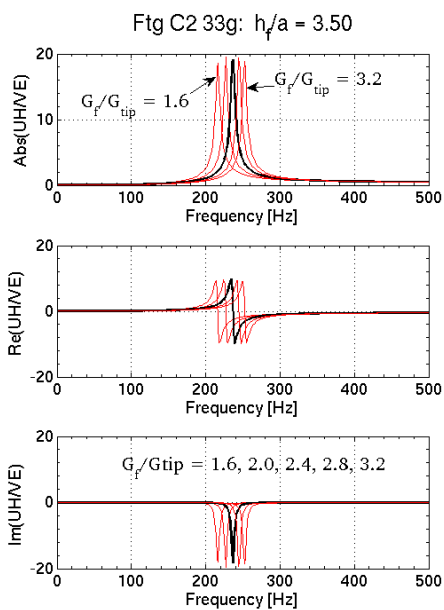


Figure 6.32: Footing C2 UH/VE theoretical rocking peak.

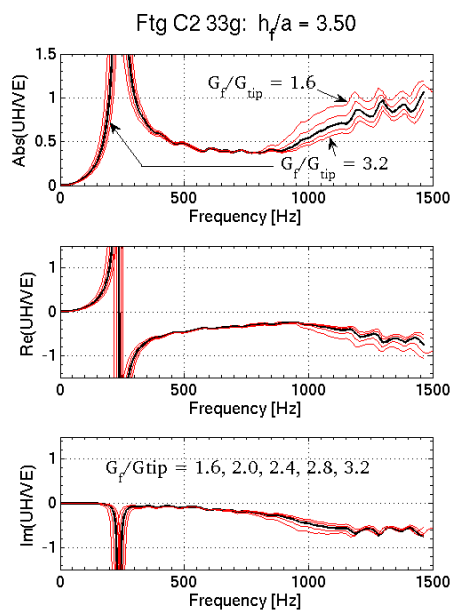


Figure 6.33: Footing C2 UH/VE theoretical second peak.

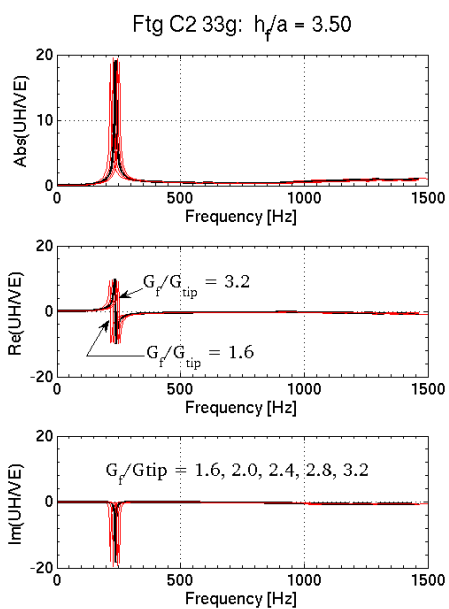


Figure 6.34: Footing C2 UH/VE theoretical accelerances.

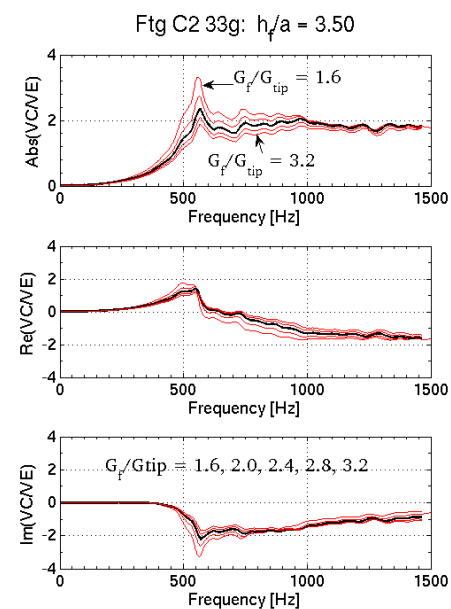


Figure 6.35: Footing C2 VC/VE theoretical accelerances.

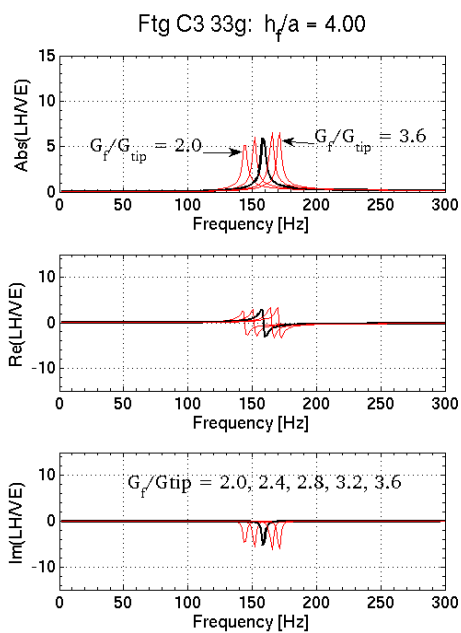


Figure 6.36: Footing C3 LH/VE theoretical rocking peak.

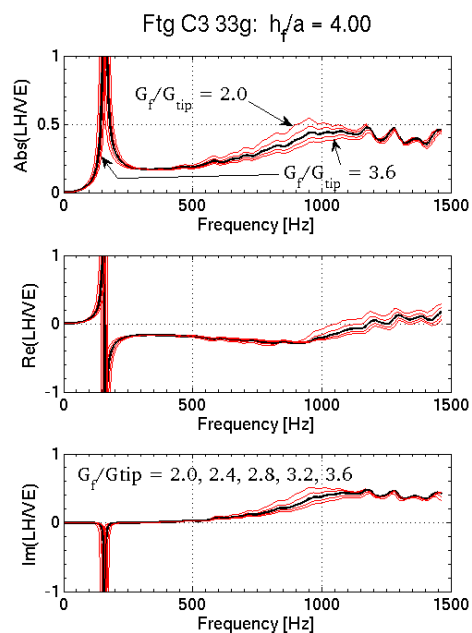


Figure 6.37: Footing C3 LH/VE theoretical second peak.

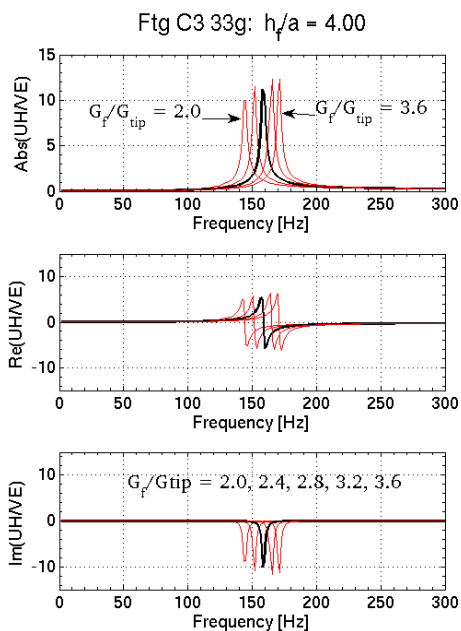


Figure 6.38: Footing C3 UH/VE theoretical rocking peak.

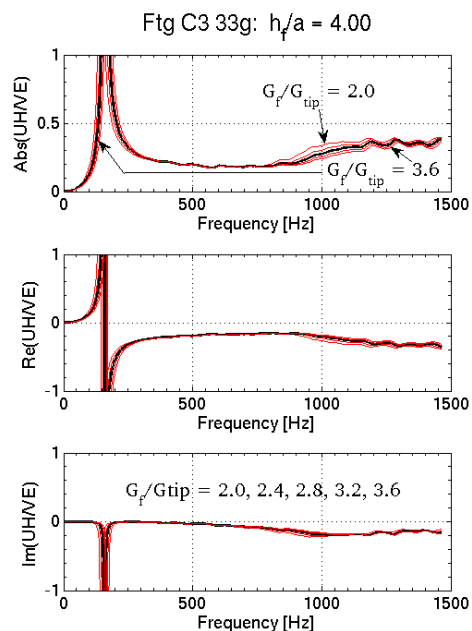


Figure 6.39: Footing C3 UH/VE theoretical second peak.

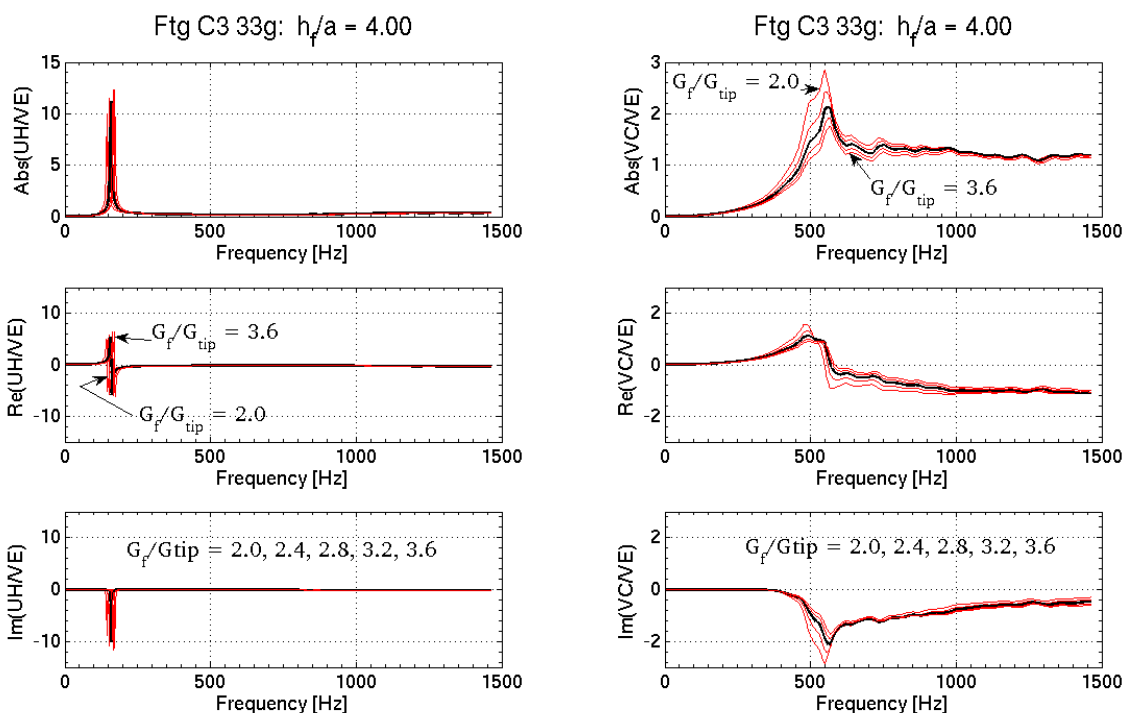


Figure 6.40: Footing C3 UH/VE theoretical accelerances

Figure 6.41: Footing C3 VC/VE theoretical accelerances

The similar key features are observable in Figures 6.23 – 6.40 as in the experimental data: A sharp resonance peak and a longer smoother peak in both horizontal accelerances, in addition to a VC/VE resonance peak. Utilizing the insights from the impedance functions by recalling how the imaginary component is initially zero and increases with frequency, one can observe how the presence of damping affects the response. The lowest frequency peaks are the sharpest, for example, in the UH/VE accelerance, associated with the rocking resonance peak for footing C3. Corresponding peaks for C2 and C1 are at higher frequencies, as well as wider and smoother by comparison. The VC/VE peaks are also progressively wider in these cases, respectively.

The inner zone's modulus and size play a significant role in both the vertical and horizontal response profile. For footing C1, a deeper/stiffer inclusion zone in the soil usually gives a higher frequency but smaller first resonance peak in the horizontal transfer functions (Figures 6.23 – 6.27). For footings C2 and C3 with the use of deeper inclusions, the rocking peak can be seen to increase

in frequency as well as magnitude in model scale (see Figures 6.29 – 6.33, and 6.35 – 6.39). The second peak shows a similar shift toward higher frequencies for larger \bar{G} values for each footing; however the magnitude decreases in all cases in Figures 6.24 and 6.26. The VC/VE accelerance again follows the same trend, but with a smaller frequency shift. The vertical accelerance peak magnitude is in fact more sensitive than the resonant frequency itself (see Figures 6.28, 6.34, and 6.40).

Plotted in Figures 6.41 – 6.46 are theoretical accelerances for different inclusion depths with the modulus held constant. The effect is to a certain extent similar to increasing modulus with the depth held constant. The rocking peak in the accelerance function increases in both magnitude and frequency (Figures 6.41, 6.43, 6.45), and the vertical and second horizontal peaks increase in frequency yet decrease in magnitude (Figures 6.42, 6.46).

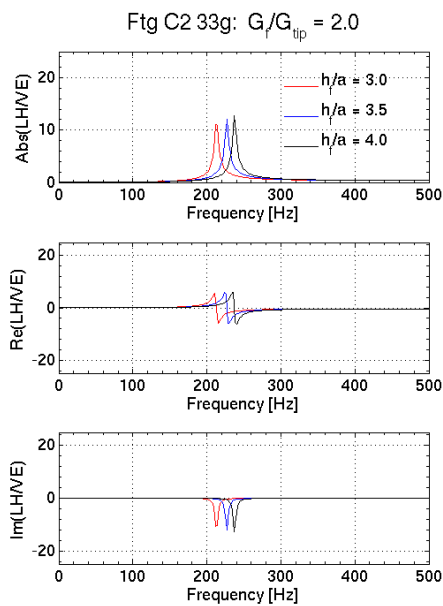


Figure 6.42: Footing C2 LH/VE rocking peak.

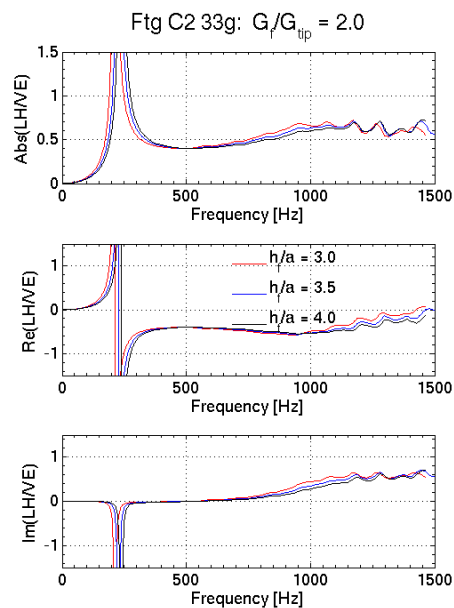


Figure 6.43: Footing C2 LH/VE second peak.

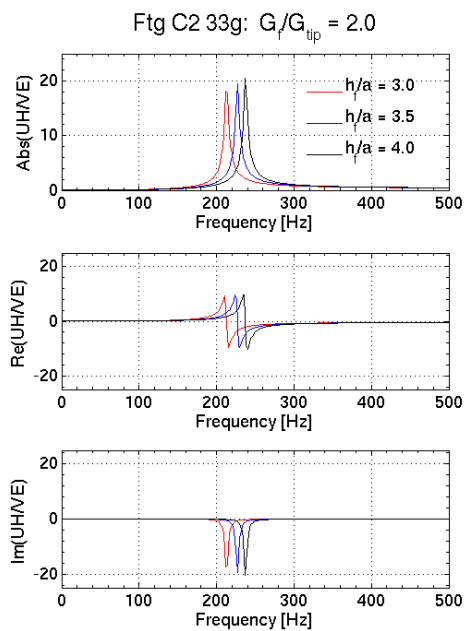


Figure 6.44: Footing C2 UH/VE rocking peak.

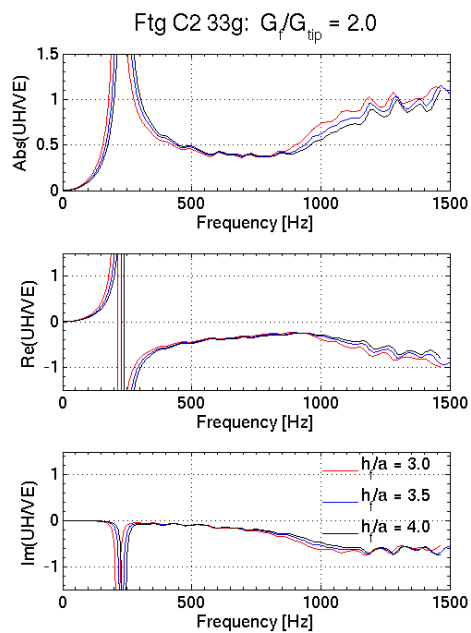


Figure 6.45: Footing C2 UH/VE second peak.

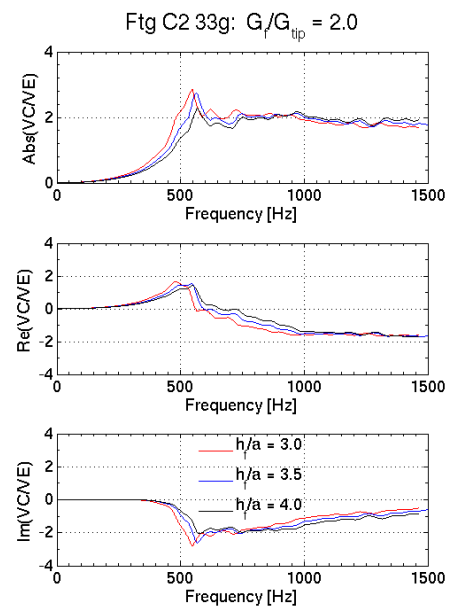
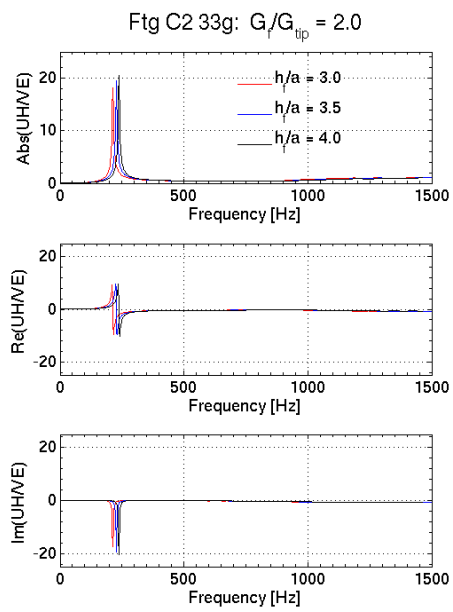


Figure 6.46: Footing C2 UH/VE acceleration.

Figure 6.47: Footing C2 VC/VE acceleration.

Chapter 7

Synthesis of Data and Theory

7.1 Equivalent Homogeneous Shear Modulus

To get an idea of the performance of some of the current engineering approaches in practice for the physical problem, BEASSI was also used to compute the theoretical footing response on a finite stratum which has a homogeneous shear modulus. As mentioned in the Introduction, the approach has been shown to result in some significant discrepancies between theory and experimental data, even in the case of a specially prepared soil of uniform shear wave velocity (Erden, 1974). The related idea of an equivalent or representative shear modulus was also found as recently as in Ashlock (2006) and Soudkhah (2010) to be unable to capture all features of a square footing's response undergoing simultaneous vertical-horizontal-rocking motions in both thick or thin models of a uniform sand.

To explore the issues related to the homogeneous soil model in the context of the present problem, the theoretical impedances for the circular footing on a finite homogeneous-modulus model setting were generated using BEASSI for the case of 33g. The circular foundation results are plotted in Figure 7.1, including a comparison with the square and areal-equivalent square footing solutions. Real and imaginary parts are plotted on the same set of axes (see 6.1, 6.2, and 6.13-6.20 for normalization scheme). Similar to the two-zone model, the static values of the circular and equivalent square impedances are quite close as summarized quantitatively in Table 7.1. The imaginary parts of each impedance increase from zero at low frequencies as expected. At higher frequencies, however, the behavior of the circular results becomes highly oscillatory, crossing over into the negative for both the real and imaginary parts of \bar{K}_{vv} , as well as for the imaginary part of \bar{K}_{mh} . Both the square and equivalent square show similar such behavior in \bar{K}_{mh} .

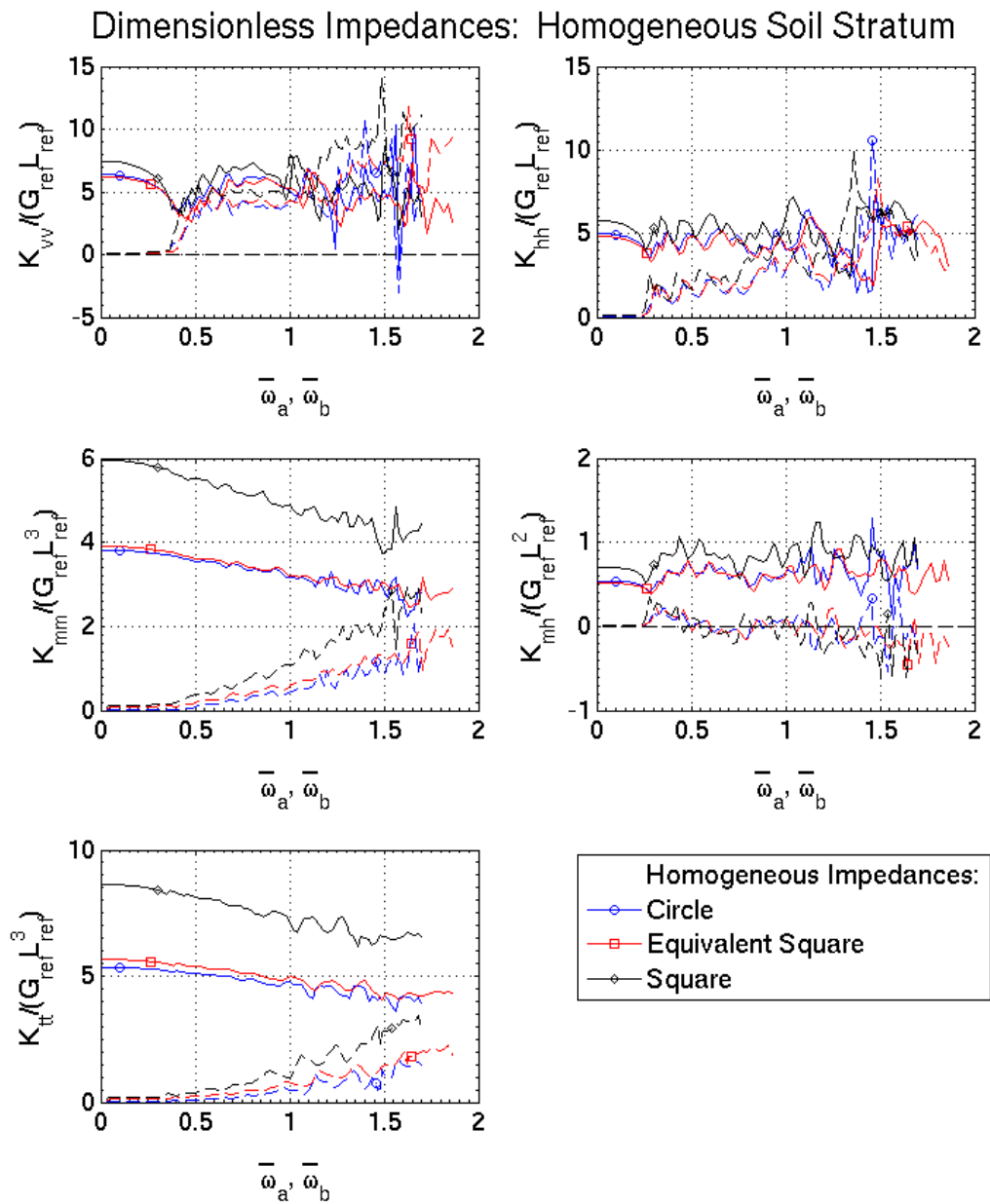


Figure 7.1: Foundation impedances for finite stratum with homogeneous shear modulus G_{eq-hom}

$\text{Re}(\bar{K}_{ij})$	Circle	Equivalent Square
$\text{Re}(\bar{K}_{vv})$	6.4	6.2
$\text{Re}(\bar{K}_{hh})$	5.0	4.8
$\text{Re}(\bar{K}_{mm})$	3.9	3.8
$\text{Re}(\bar{K}_{mh})$	0.5	0.5
$\text{Re}(\bar{K}_{tt})$	5.6	5.3

Table 7.1: Static impedance comparison between the circle results and equivalent square.

To compare with the data, the homogeneous soil stratum model requires a choice of the shear modulus G_{eq-hom} . This is done by requiring the theoretical solution to match the experimental data in a suitable manner. To enhance the engineering interpretation, the process will be presented in prototype scale to establish a more direct connection with engineering application. As in Chapter 4, all prototype scale accelerances are in units of $(mm/s^2)/kN$, which can also be written directly in terms mass units as kt^{-1} (kilotonne⁻¹ or Gg^{-1}). Prototype-scale frequency units are Hz . Unlike the two-zone results, the equivalent homogeneous cases were re-run for each g-level to maintain the correct relative material properties of the soil-Duxseal system and the normalization used for each subdomain. Owing to the limit of time, only comparisons at 33g will be given, where the corresponding footing radius in prototype scale is 0.98 m (Table 2.8) although results at other g-levels, e.g., 66g may have data that is more consistent and corresponds to heavier footing prototypes.

Figures 7.2 – 7.21 highlight the process of matching different critical features of the experimental accelerance results. In Figure 7.2 for example, a comparison of the homogeneous theory with the experimental data is given for footing C1 with $a_{proto} = 0.98$ m and $p_{proto} = 41.1$ kPa. There, the theoretical LH accelerance is made to match the rocking resonant frequency. Figure 7.3 shows the comparison of the homogeneous theory with the experimental UH/VE data for footing C1. One can see that the peak can be matched closely in both real and imaginary parts. Figure 7.4 show the comparison of the homogeneous theory with the experimental VC/VE data for footing C1

$a_{\text{proto}} = 0.98 \text{ m}$, $p_{\text{proto}} = 41.1 \text{ kPa}$. The result using a rocking peak match appears to compare well with the VC/VE accelerance as well. However, if one chooses to change $G_{\text{eq-hom}}$ to better match the VC/VE response, one will find a slightly higher $G_{\text{eq-hom}}$ is required as can be seen in Figure 7.5. Using this new vertical response match, the LH/VE and UH/VE rocking frequency is higher than the measured one but still acceptable as indicated in Figures 7.6 and 7.7. Prototype radii for each footing and g-level shown below are summarized in Table 7.2.

Footing	g-level	a_{proto} [m]	p_{proto} [kPa]
C1	33	0.98	41.1
C2	33	0.98	82.5
C3	33	0.98	125.8

Table 7.2: Contact pressures for prototype footings in Figures 7.2 – 7.21.

In many of the figures the theory does not always approach the asymptote without additional peaks not observed in the data (Figures 7.2, 7.6, 7.13). Approximating the soil domain with a homogeneous shear modulus theory has the effect of artificially stiffening soil near the surface, and softening soil at the bottom of the container. The theoretical footing response is affected by boundary effects in the container, and the closest boundary is on the soil surface. It is possible that the zone artificially stiffened on the soil surface by the homogeneous theory is in fact what produces these peaks that are not present in the data.

To fit all key distinct features of the experimental curves as discussed earlier in both the horizontal and vertical accelerance curves, the use of two separate homogeneous shear modulus values was found to be necessary. The dilemma will be elaborated upon in the ensuing analysis.

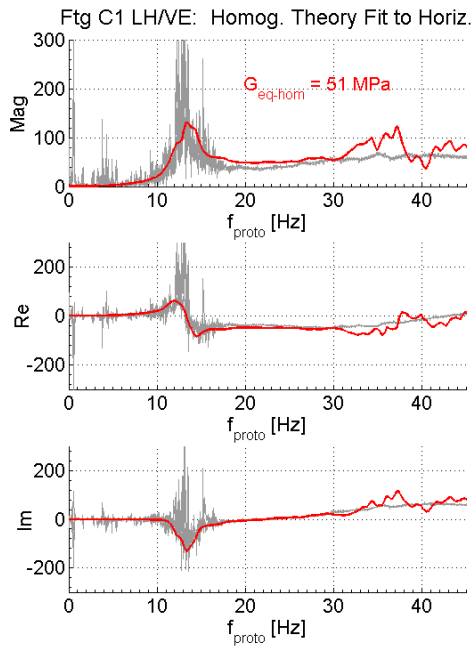


Figure 7.2: Comparison of homogeneous theory with experimental LH/VE data for footing C1 by matching rocking frequency.

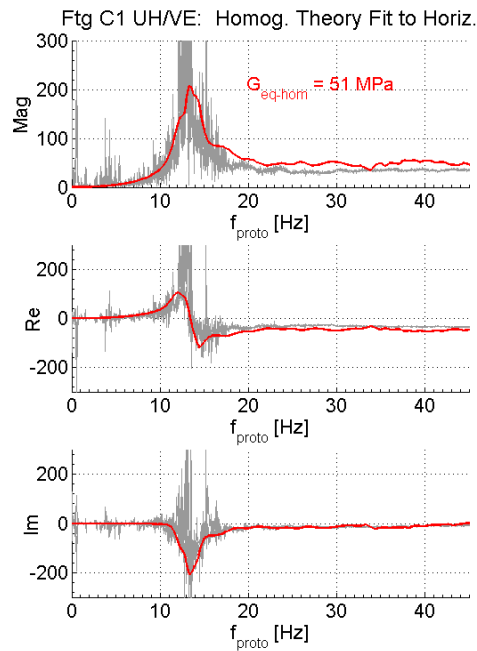


Figure 7.3: Comparison of homogeneous theory with experimental UH/VE data for footing C1 by matching rocking frequency.

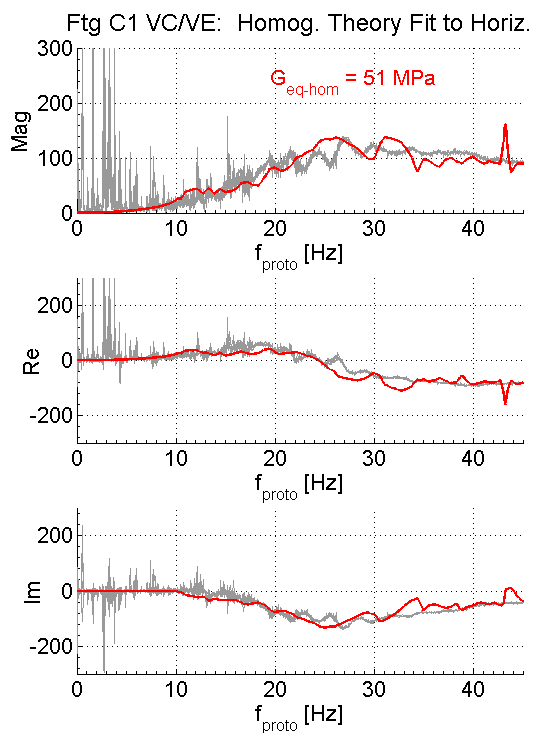


Figure 7.4: Comparison of homogeneous theory with experimental VC/VE data for footing C1 by matching rocking frequency.

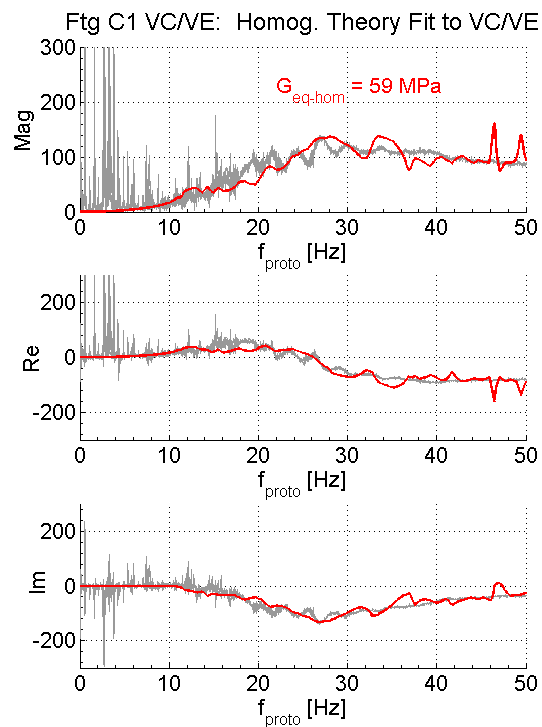


Figure 7.5: Comparison of homogeneous theory with experimental VC/VE data for footing C1 by matching VC response.

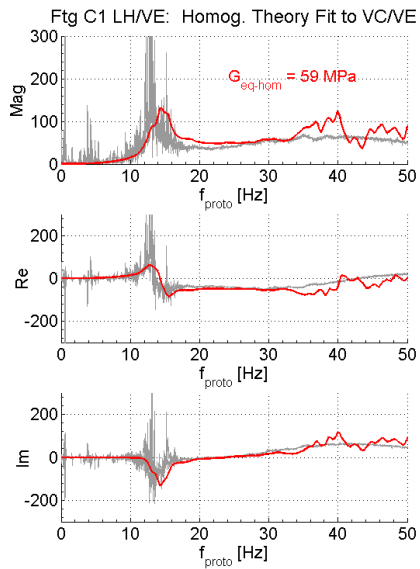


Figure 7.6: Comparison of homogeneous theory with experimental VC/VE data for footing C1 by matching VC response.

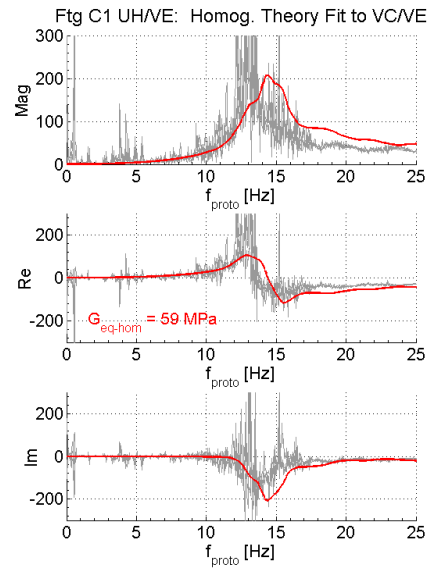


Figure 7.7: $a_{\text{proto}} = 0.98 \text{ m}$, $p_{\text{proto}} = 41.1 \text{ kPa}$. Close-up of the rocking peak using the value from the VC match.

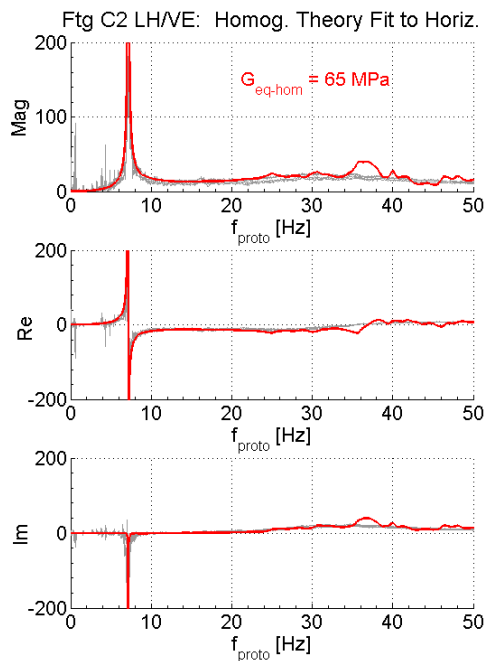


Figure 7.8: Comparison of homogeneous theory with experimental LH/VE data for footing C2 by matching rocking frequency.

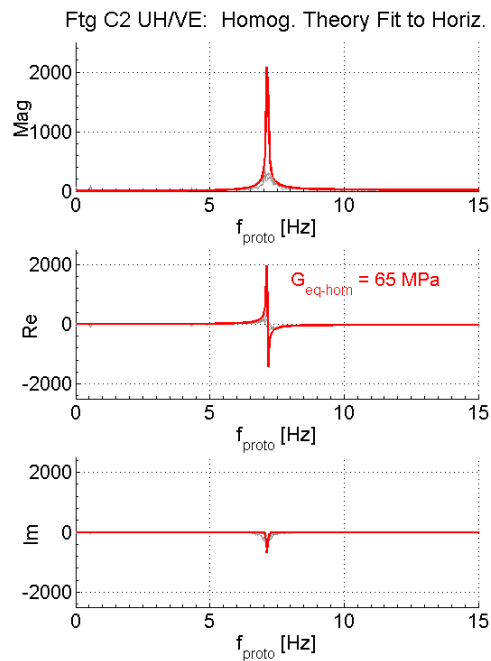


Figure 7.9: Comparison of homogeneous theory with experimental UH/VE data for footing C2 by matching rocking frequency.

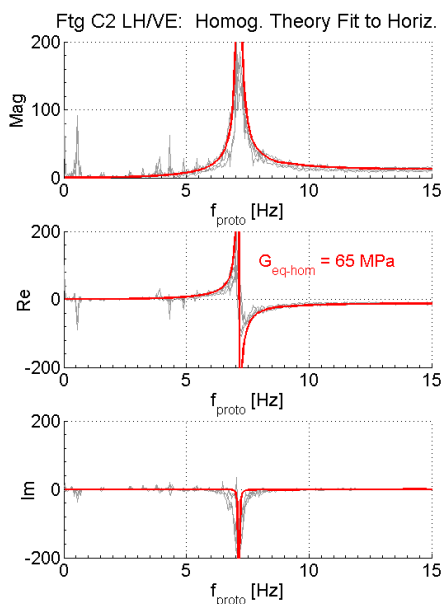


Figure 7.10: Comparison of homogeneous theory with experimental LH/VE data for footing C1 by matching rocking frequency.

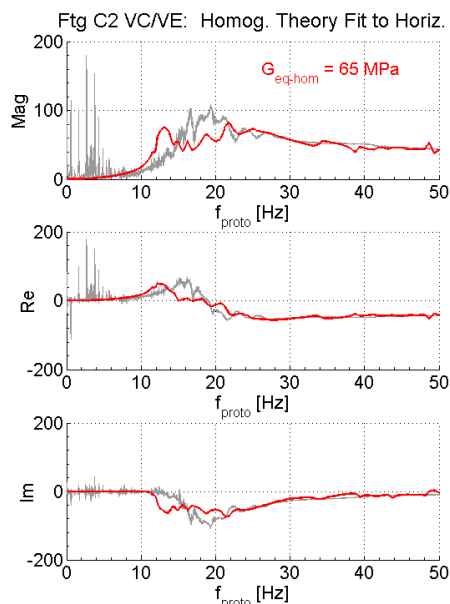


Figure 7.11: Comparison of homogeneous theory with experimental VC/VE data for footing C2 by matching rocking frequency.

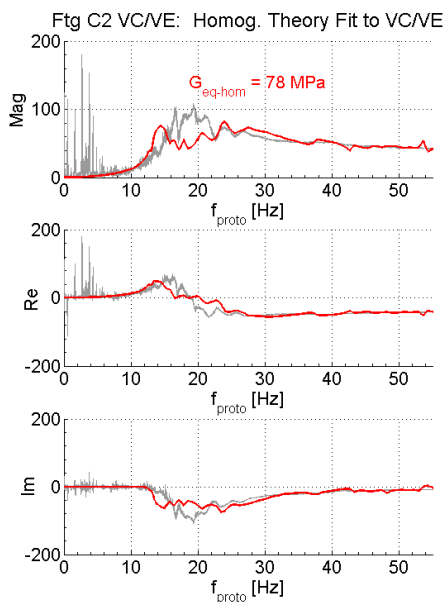


Figure 7.12: Comparison of homogeneous theory with experimental VC/VE data for footing C2 by matching VC response.

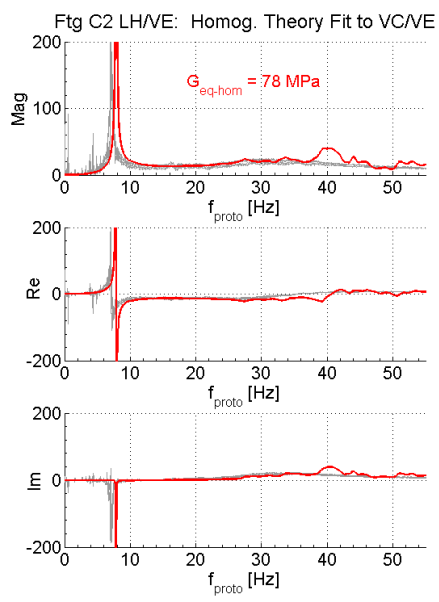


Figure 7.13: Comparison of homogeneous theory with experimental LH/VE data for footing C2 by matching VC response.

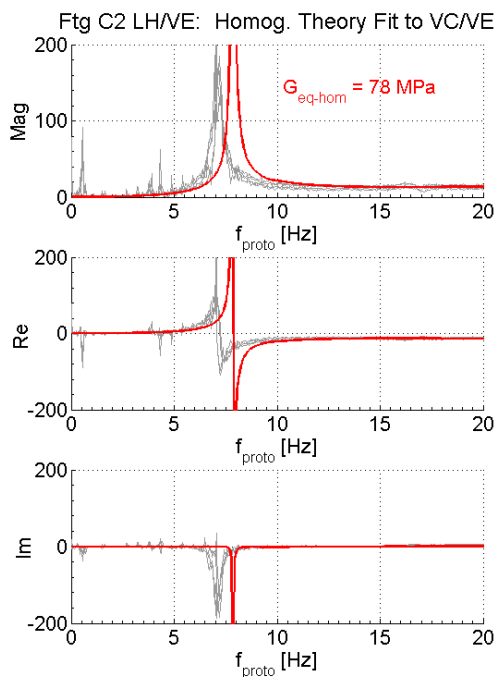


Figure 7.14: Comparison of homogeneous theory with experimental LH/VE data for footing C2 by matching VC response.

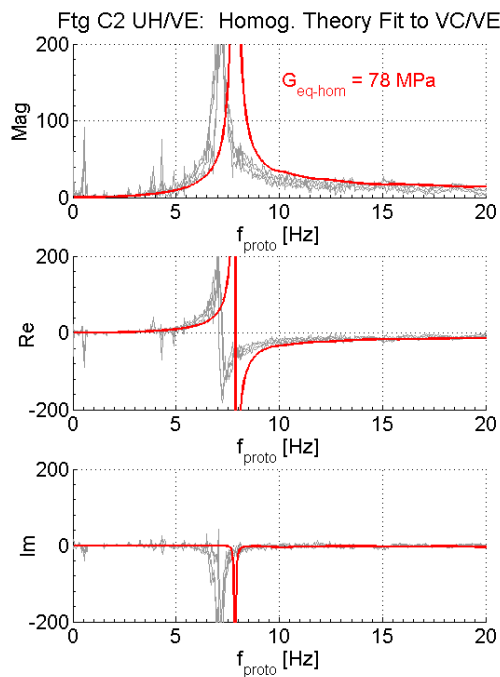


Figure 7.15: Comparison of homogeneous theory with experimental UH/VE data for footing C2 by matching VC response.

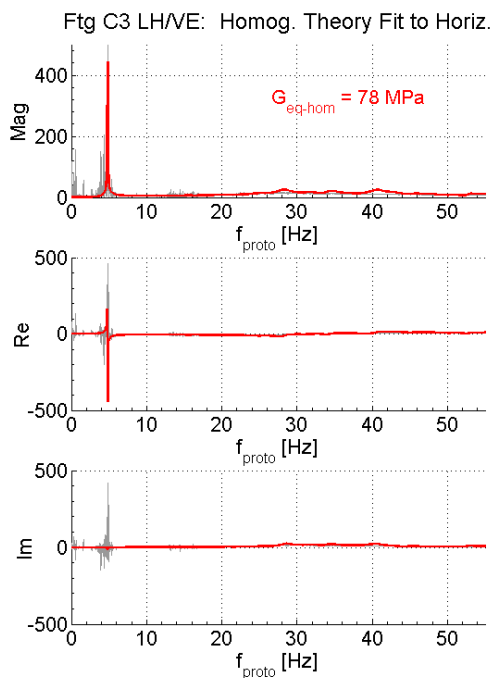


Figure 7.16: Comparison of homogeneous theory with experimental LH/VE data for footing C3 by matching rocking frequency.

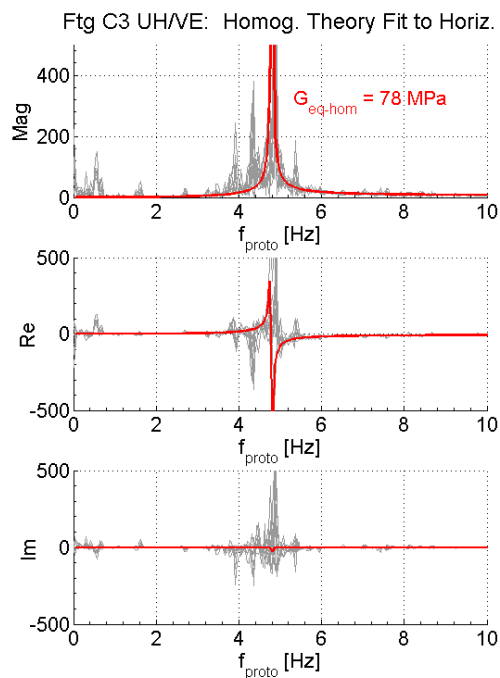


Figure 7.17: Comparison of homogeneous theory with experimental UH/VE data for footing C3 by matching rocking frequency.

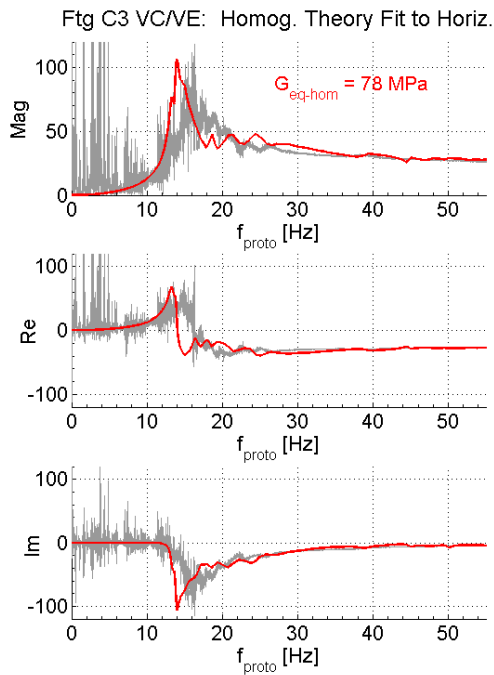


Figure 7.18: Comparison of homogeneous theory with experimental VC/VE data for footing C3 by matching rocking frequency.

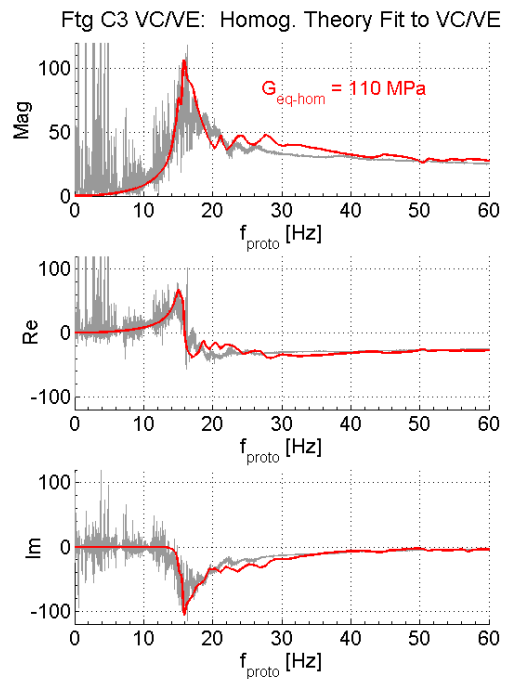


Figure 7.19: Comparison of homogeneous theory with experimental VC/VE data for footing C3 by matching vertical response

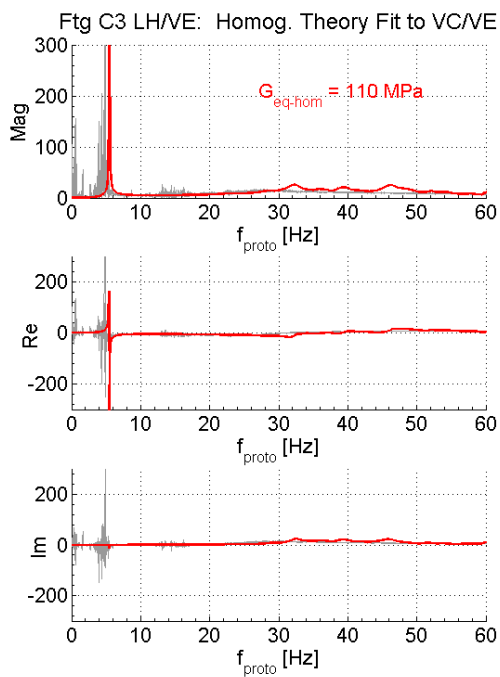


Figure 7.20: Comparison of homogeneous theory with experimental LH/VE data for footing C3 by matching vertical response.

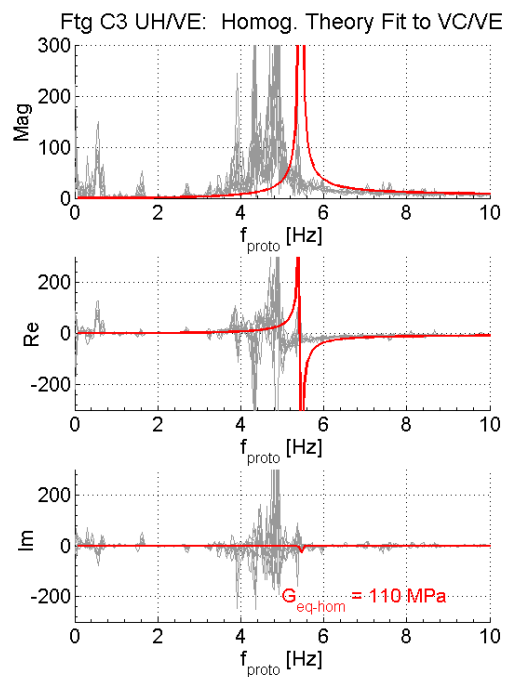


Figure 7.21: Comparison of homogeneous theory with experimental UH/VE data for footing C3 by matching vertical response.

Footing	Rocking Peak	VC/VE	Percent Difference
C1	$G_{eq-hom} = 50$ [MPa]	$G_{eq-hom} = 59$ [MPa]	18 %
C2	$G_{eq-hom} = 65$ [MPa]	$G_{eq-hom} = 78$ [MPa]	20 %
C3	$G_{eq-hom} = 78$ [MPa]	$G_{eq-hom} = 110$ [MPa]	41 %

Table 7.3: Comparison of G_{eq-hom} values needed to match the rocking peak and VC/VE peak for each circular footing.

As summarized in Table 7.3, the discrepancy between theory and experiment becomes larger as contact pressure increases. This corresponds to larger disagreement between local stress conditions and far-field values which is difficult to reconcile using an equivalent homogeneous soil model. The results of Soudkhah (2010) showed similar disagreement between G_{eq-hom} values necessary to fit each feature, in addition to a large discrepancy in the VC/VE peak magnitude for footing B33. This disagreement was not observable in the circular footing results, however application of the equivalent square model showed that the results are similar to Soudkhah (2010), as in Figures 7.22 and 7.33.

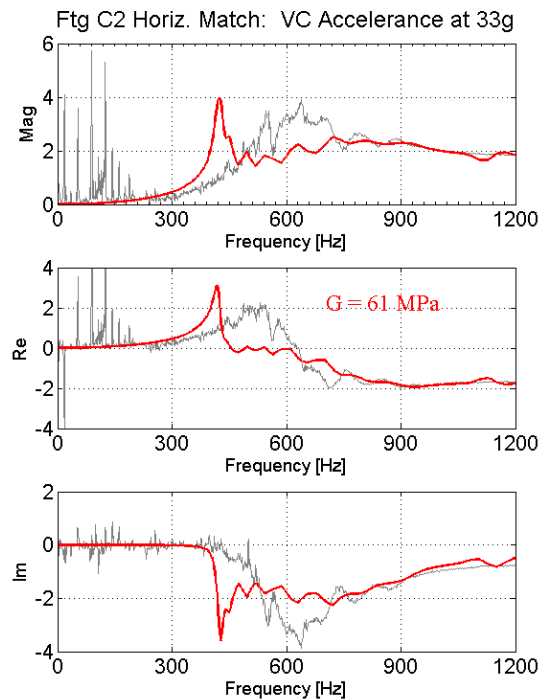


Figure 7.22: Homogeneous soil model using the equivalent square impedances.

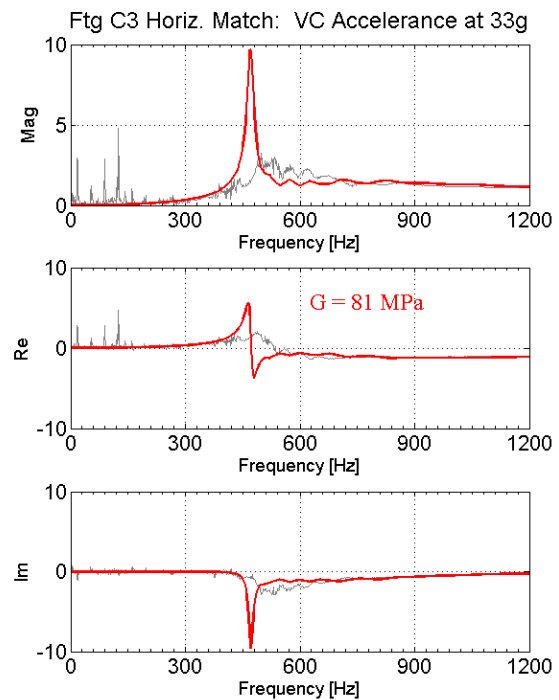


Figure 7.23: Similar to figure 7.22 but for footing C3.

Ignoring the large theoretical fluctuations at higher frequencies in the LH/VE ($f_{proto} > 30$ Hz), and spikes in the VC/VE at 45 Hz, the homogeneous theory is quite good for the smallest circular footing C1, as well as the smallest square footing B1 (Soudkhah 2010). For footing C2, it is somewhat more difficult to match the vertical response, as the peak shape could arguably be described as two separate humps. This VC/VE peak behavior affects the choice of G_{eq-hom} value in trying to fit the vertical response of footing C2, not encountered in dealing with footings C1 and C3. For footing C3, the homogeneous theory produces responses with distinct and easily identifiable features that correspond with those found in the experimental results, which makes it easier in deciding on an equivalent homogeneous shear modulus to fit either the rocking peak or the vertical resonance peak. For this footing, the apparent need of two very different G_{eq-hom} s of the order of 40% to fit the vertical and lateral responses is obvious.(see Table 7.3).

7.2 Calibration of the Two-zone Continuum Model

Using the two-zone model to match the experimental data requires the choice of two parameters (\bar{h} , \bar{G}). To this end, the approach in Ashlock (2006) was utilized to define a weighted error measure that can be tailored to find the optimal values of \bar{h} and \bar{G} for agreement with the experimental data. This allows the synthesis process to be systematic and reproducible. Measured and theoretical accelerances will be designated with superscripts ‘*m*’ and ‘*th*’, respectively. Vertical and horizontal acceleration will be denoted with subscripts ‘*V*’ and ‘*H*’ respectively.

To proceed, an error measure relevant to the vertical acceleration is defined as

$$\varepsilon_V = \int_{f_1}^{f_2} \sqrt{(\operatorname{Re}(A_V^m) - \operatorname{Re}(A_V^{th}))^2 + (\operatorname{Im}(A_V^m) - \operatorname{Im}(A_V^{th}))^2} df \quad (7.1)$$

The frequency range for the integral (7.1) was chosen to include the entire response, with a lower bound defined to eliminate the usual centrifuge ambient vibrations without omitting critical response features. This value was set specifically for each g-level to cut out the large low frequency spikes that can be seen in the data plots from noise in Chapter 5. This did not overlap into the vertical resonance peak band which is at higher frequencies in all cases.

It was important also to define a measure specifically to weight the rocking peak frequency value, as it is one of the most prominent features and of critical importance from a design standpoint. Although in the measured data the peaks are sometimes choppy or contain spikes, in the interest of being objective, the frequency point within the peak frequency range with the largest magnitude was chosen for this value. In contrast, the theoretical curves were considerably smooth in the frequency band with clearly definable rocking peak frequencies. The peak error measure was therefore defined as

$$\varepsilon_{pk} = |f_{th} - f_m| \quad (7.2)$$

An area error measure similar to Eq. (7.1) was also implemented for the horizontal accelerances. The frequency range for the integral could be chosen to include everything but low

frequency centrifuge noise or to capture the second horizontal peak only. In this thesis, a frequency range was chosen for each footing, at each g-level, that included the rocking peak in the error measure but omitted low frequency centrifuge vibrations observed to be present during ambient tests (thus labeled as ‘ambient’ noise). This is a little different from Ashlock (2006) where the frequency range was defined to focus on the broad second horizontal peak. It was explored to see if it would be beneficial to include the first peak region to allow for more flexibility in capturing the lobes of the rocking peak, in the case where the peak frequency is not easily discernable. The horizontal area error measure is thus defined as

$$\varepsilon_H = \int_{f_1}^{f_2} \sqrt{(\operatorname{Re}(A_H^m) - \operatorname{Re}(A_H^{th}))^2 + (\operatorname{Im}(A_H^m) - \operatorname{Im}(A_H^{th}))^2} df \quad (7.3)$$

Finally, a normalized weighted error measure will be introduced to combine suitably the error measures in recognition of the differences in magnitude of the terms introduced in (7.1) – (7.3). This total error measure is defined as

$$\varepsilon = w_V \frac{\varepsilon_V}{\int_{f_1}^{f_2} |A_V^m| df} + w_{pk} \frac{\varepsilon_{pk}}{f_m} + w_H \frac{\varepsilon_H}{\int_{f_1}^{f_2} |A_H^m| df} \quad (7.4)$$

A curve fitting program was written to compute the error measures (7.1) – (7.3) for each data set using every available combination of \bar{h} and \bar{G} . The weights in (7.4) were chosen such that the contribution of the peak, as well as vertical and horizontal error measures were approximately equal. The resulting weights are listed in Table 7.4 with the label ‘ w ’, along with those used by Ashlock (2006), labeled as ‘ a ’, and a scheme to match only the horizontal peak, labeled ‘ p ’. Bear in mind that Ashlock defined the horizontal area error measure so as to only include the second peak region, and an appropriate frequency range was chosen for the implementation of this weighting scheme. It was also observed that these weights in Scheme a gave relatively a heavier emphasis on the vertical response in the case of the circular footing data, as will be demonstrated in the remainder of this section.

Weighting Scheme	w_V	w_H	w_{pk}
w	1/7	1/7	5/7
a	0.3	0.3	0.4
p	0.0	0.5	0.5

Table 7.4: Definition of error-weighting schemes used for the figures in this section.

A few examples error analysis results are shown in Figures 7.22 and 7.33. A more complete picture will be shown after the accelerance comparison plots are presented.

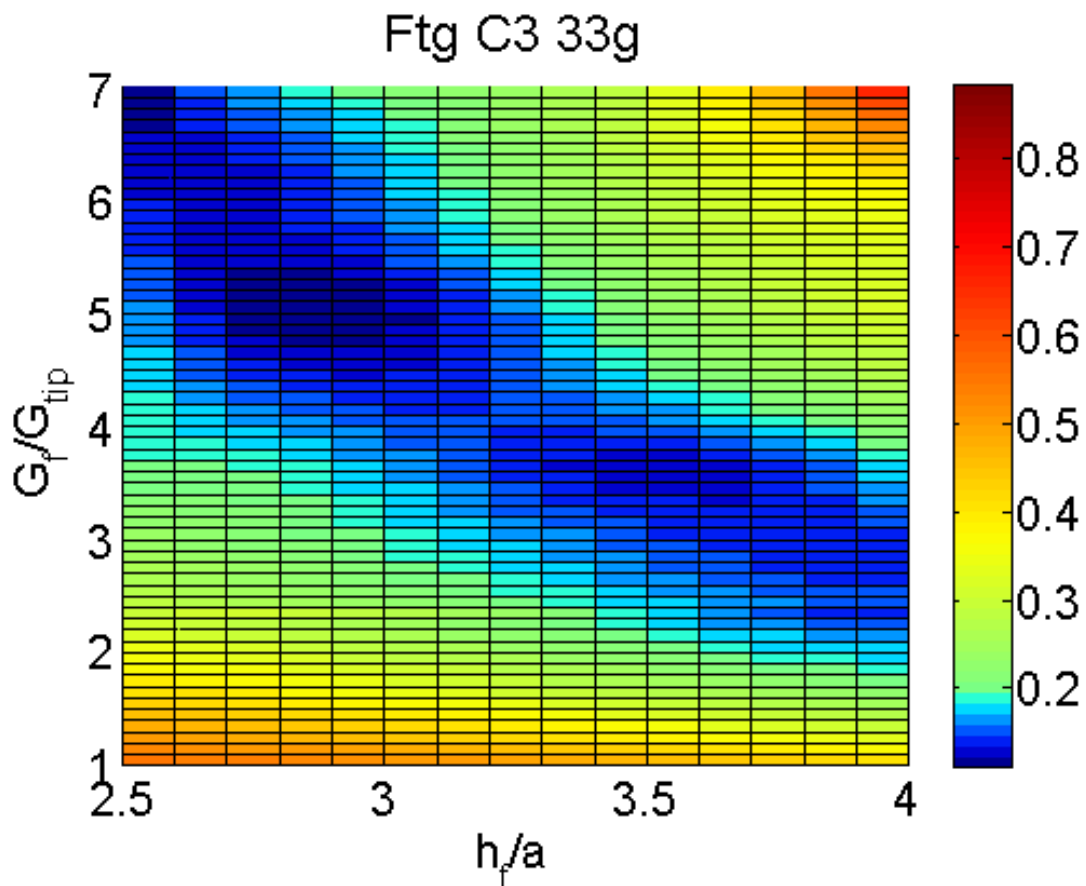


Figure 7.24: Example of the total error measure for footing C3 at 33g using scheme 'w'. A band representing the minimum error is designated by the dark blue color.

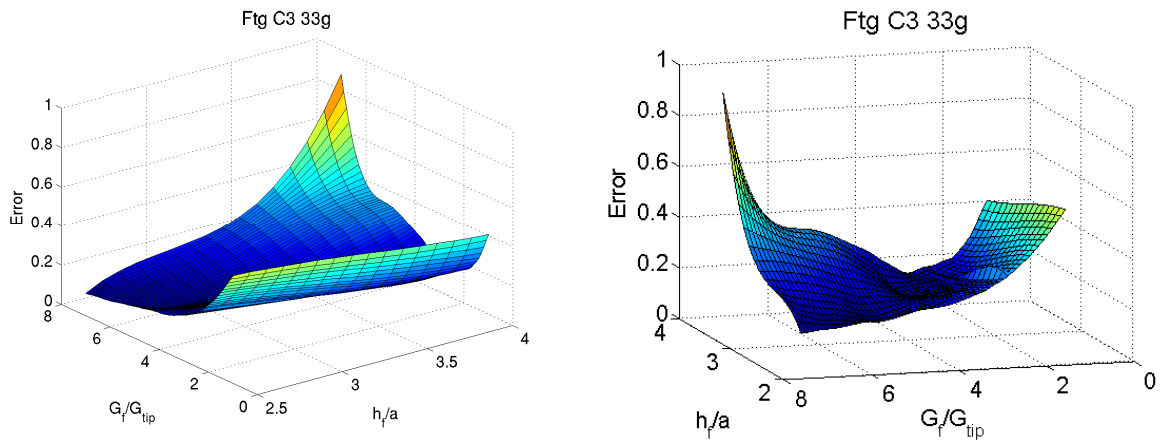


Figure 7.25: The same error measure as Figure 7.22 (w) but plotted in the form of a 3D surface.

Results of the weighted error analysis are shown in the following series of figures. Each combination of weights from Table 7.4 was used to find an optimal set of \bar{h} and \bar{G} for every footing at each g-level. For the sake of saving space only 33g and 66g are shown; the complete results will be summarized later. The g-levels 33 and 66 have corresponding prototype footing radii of 0.98 m and 1.96 m respectively (see Table 2.8).

As can be seen in the figures, each scheme has its strengths. Observable in Figures 7.29, 7.33, 7.36, or 7.41, Scheme *a* matches the vertical response quite well, however does not always match the horizontal, e.g. Figures 7.32 or 7.34. Scheme *p* in turn matches the horizontal peaks (Figures 7.26, 7.27, etc.); however it is a poor choice for fitting the vertical response, as can be seen in Figures 7.29 or 7.33. Scheme *w* is proposed as a compromise, and its effectiveness in capturing prominent aspects of each response is observable in Figures 7.27, 7.29, 7.31, or 7.33 as a few examples.

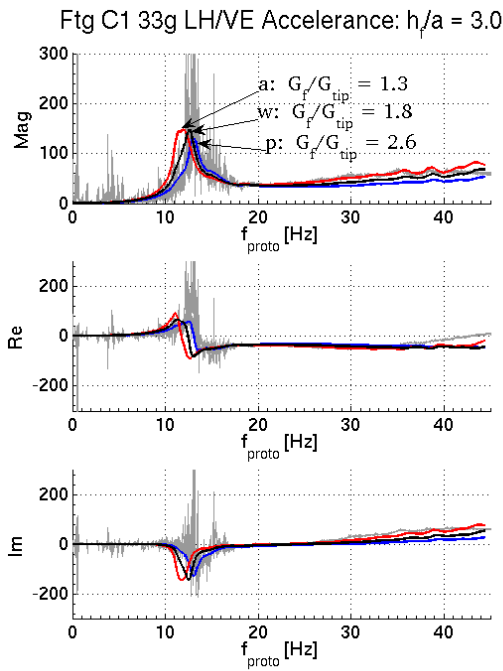


Figure 7.26: LH/VE accelerance of Footing C1 at 33g: 2-zone theory with $a_{proto} = 0.98$ m, $p_{proto} = 41.1$ kPa.

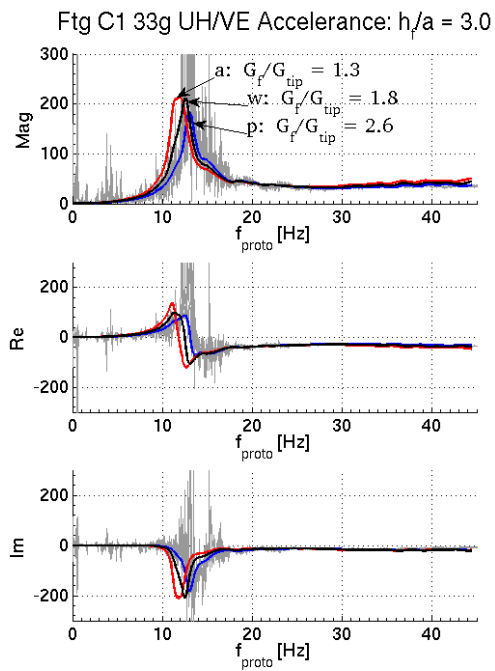


Figure 7.27: UH/VE accelerance of Footing C1 at 33g: 2-zone theory with $a_{proto} = 0.98$ m, $p_{proto} = 41.1$ kPa.

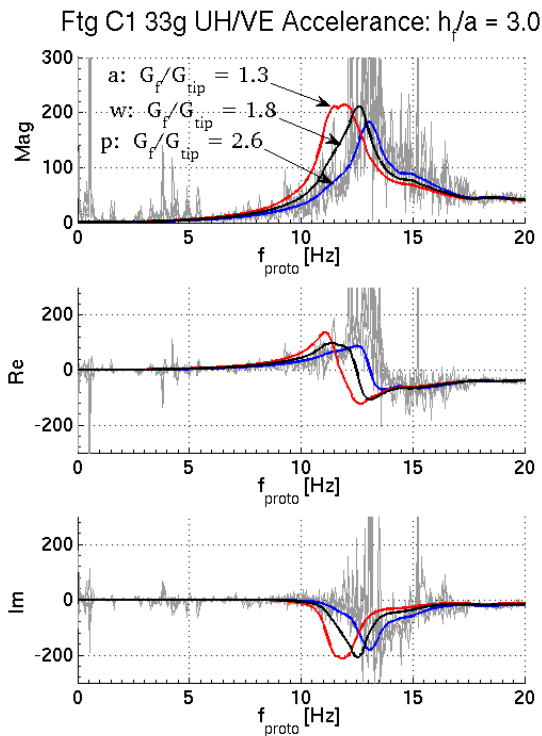


Figure 7.28: UH/VE accelerance of Footing C1 at 33g: 2-zone theory with $a_{proto} = 0.98$ m, $p_{proto} = 41.1$ kPa.

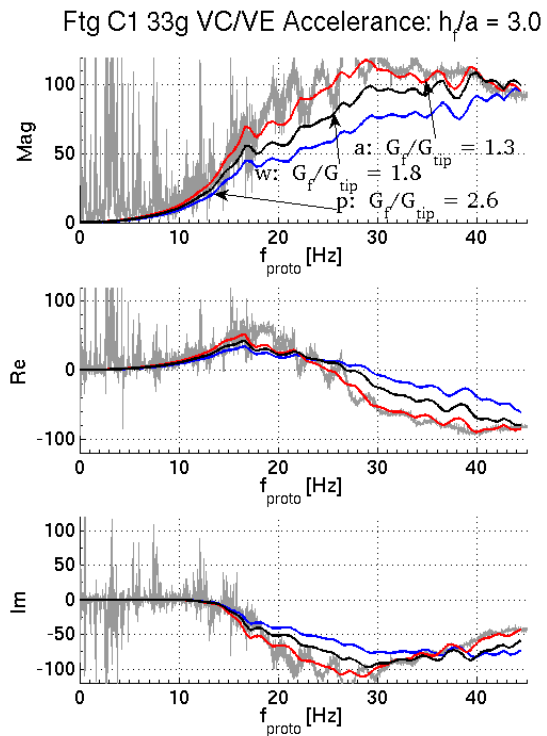


Figure 7.29: VC/VE accelerance of Footing C1 at 33g: 2-zone theory with $a_{proto} = 0.98$ m, $p_{proto} = 41.1$ kPa.

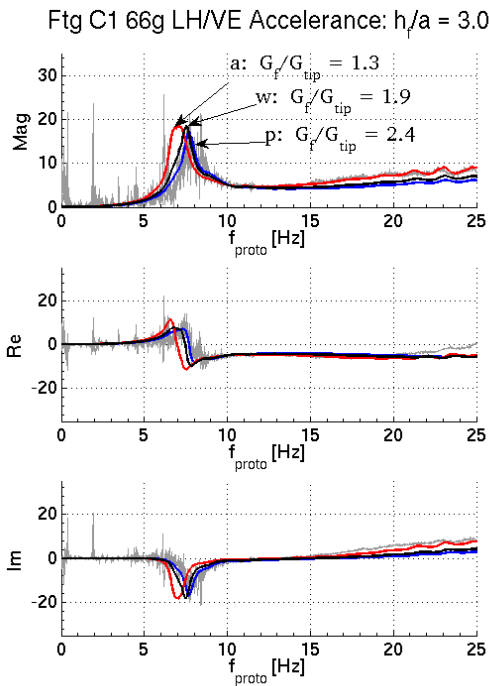


Figure 7.30: LH/VE accelerance of Footing C1 at 66g: 2-zone theory with $a_{proto} = 1.96$ m, $p_{proto} = 82.1$ kPa.

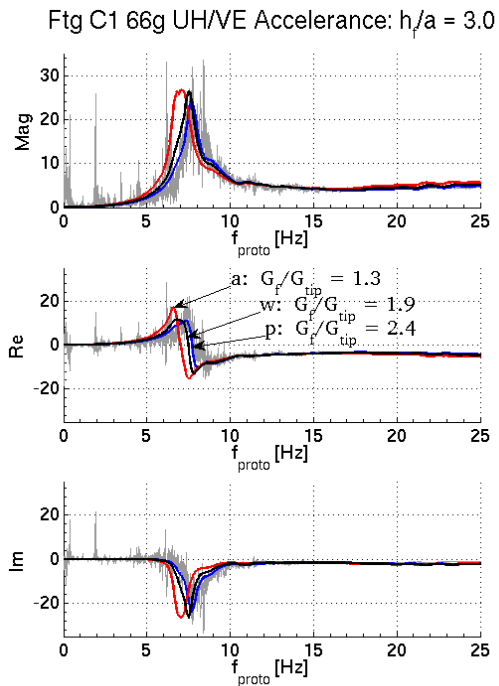


Figure 7.31: UH/VE accelerance of Footing C1 at 66g: 2-zone theory with $a_{proto} = 1.96$ m, $p_{proto} = 82.1$ kPa.

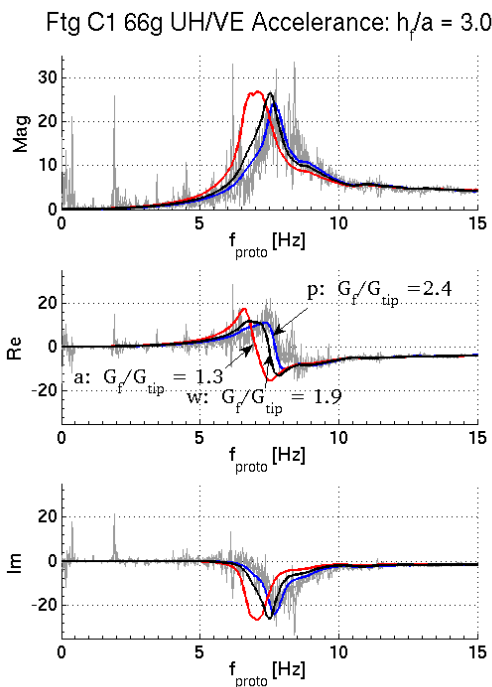


Figure 7.32: UH/VE accelerance of Footing C1 at 66g: 2-zone theory with $a_{proto} = 1.96$ m, $p_{proto} = 82.1$ kPa.

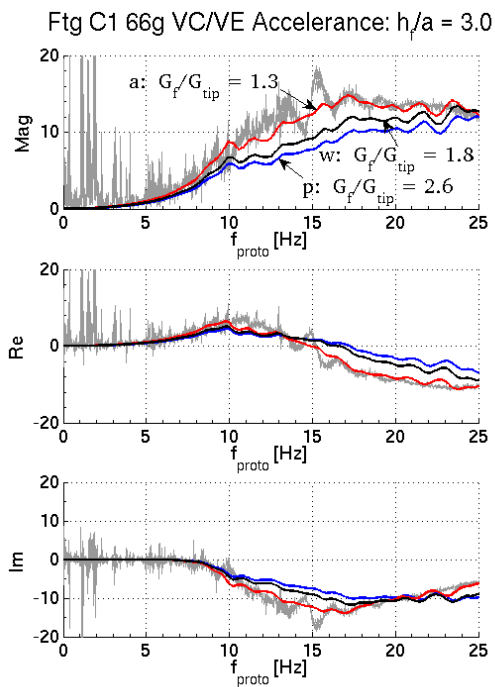


Figure 7.33: VC/VE accelerance of Footing C1 at 66g: 2-zone theory with $a_{proto} = 1.96$ m, $p_{proto} = 82.1$ kPa.

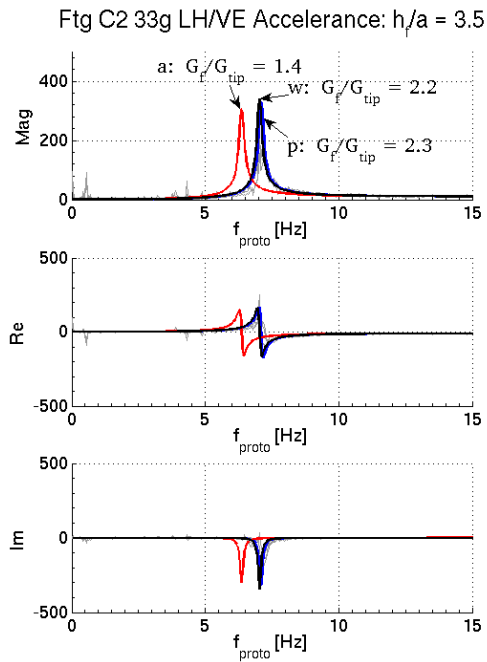


Figure 7.34: LH/VE accelerance of Footing C2 at 33g: 2-zone theory with $a_{proto} = 0.98$ m, $p_{proto} = 82.5$ kPa.

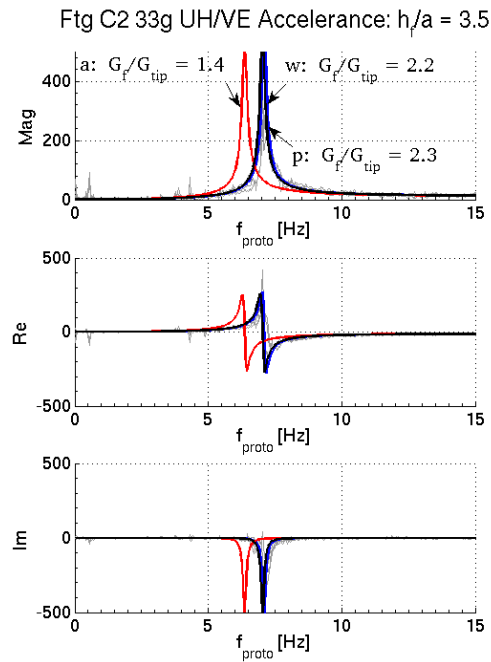


Figure 7.35: LH/VE accelerance of Footing C2 at 33g: 2-zone theory with $a_{proto} = 0.98$ m, $p_{proto} = 82.5$ kPa.

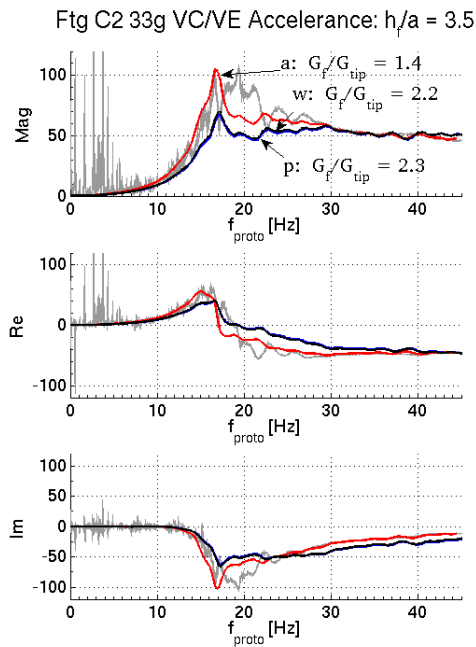


Figure 7.36: VC/VE accelerance of Footing C2 at 33g: 2-zone theory with $a_{proto} = 0.98$ m, $p_{proto} = 82.5$ kPa.

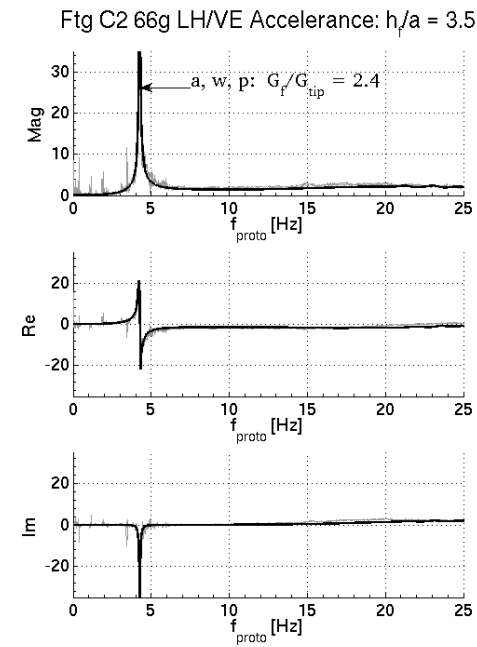


Figure 7.37: LH/VE accelerance of Footing C2 at 66g: 2-zone theory with $a_{proto} = 1.96$ m, $p_{proto} = 165.0$ kPa.

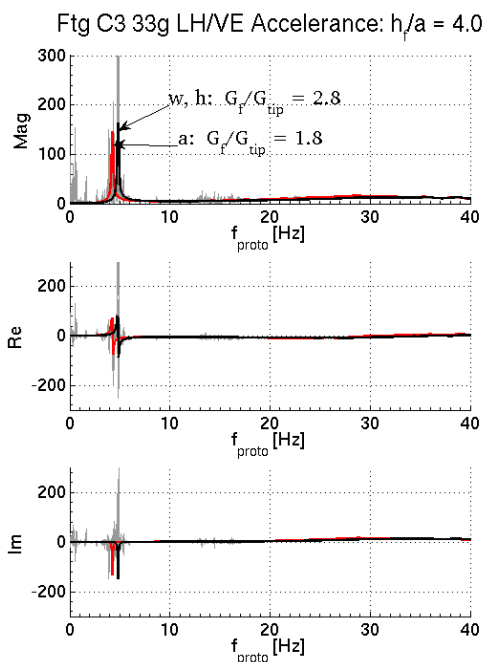


Figure 7.38: LH/VE acceleration of Footing C3 at 33g: 2-zone theory with $a_{proto} = 0.98$ m, $p_{proto} = 125.8$ kPa.

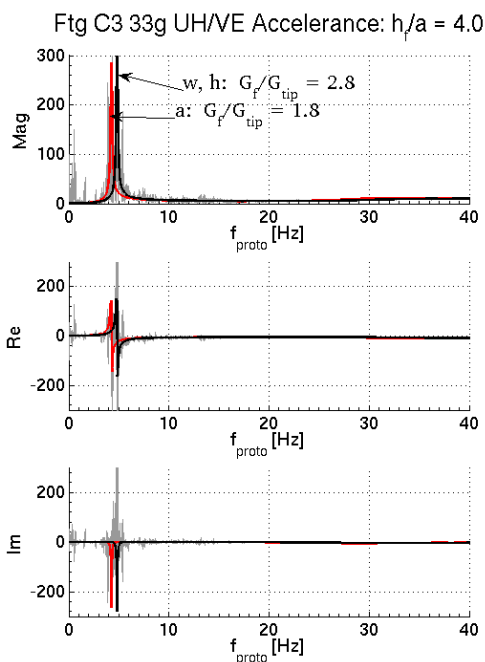


Figure 7.39: UH/VE acceleration of Footing C3 at 33g: 2-zone theory with $a_{proto} = 0.98$ m, $p_{proto} = 125.8$ kPa.

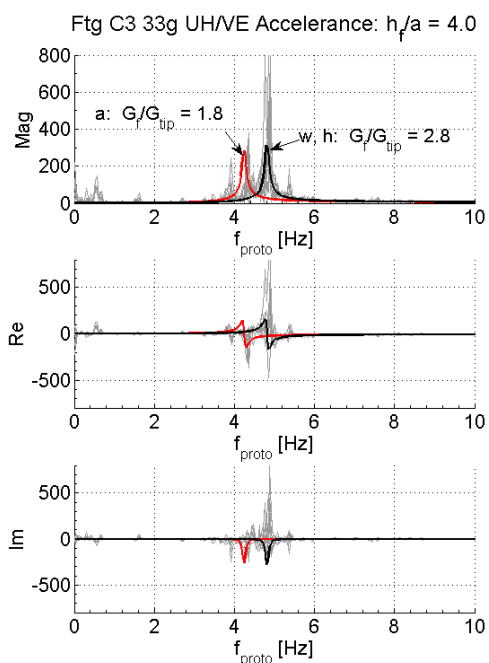


Figure 7.40: UH/VE acceleration of Footing C3 at 33g: 2-zone theory with $a_{proto} = 0.98$ m, $p_{proto} = 125.8$ kPa.

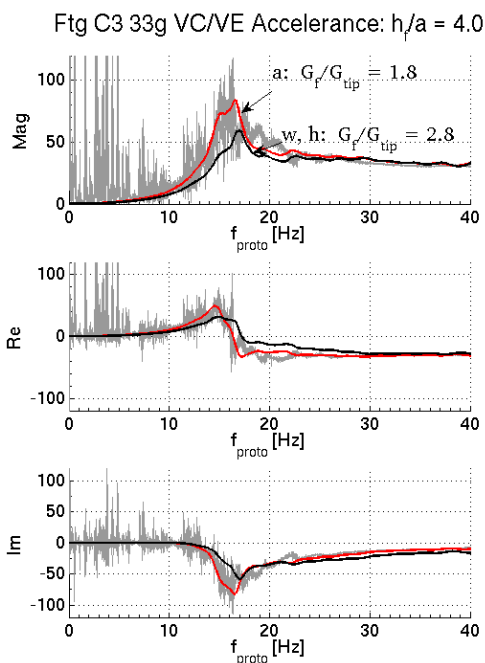


Figure 7.41: VC/VE acceleration of Footing C3 at 33g: 2-zone theory with $a_{proto} = 0.98$ m, $p_{proto} = 125.8$ kPa.

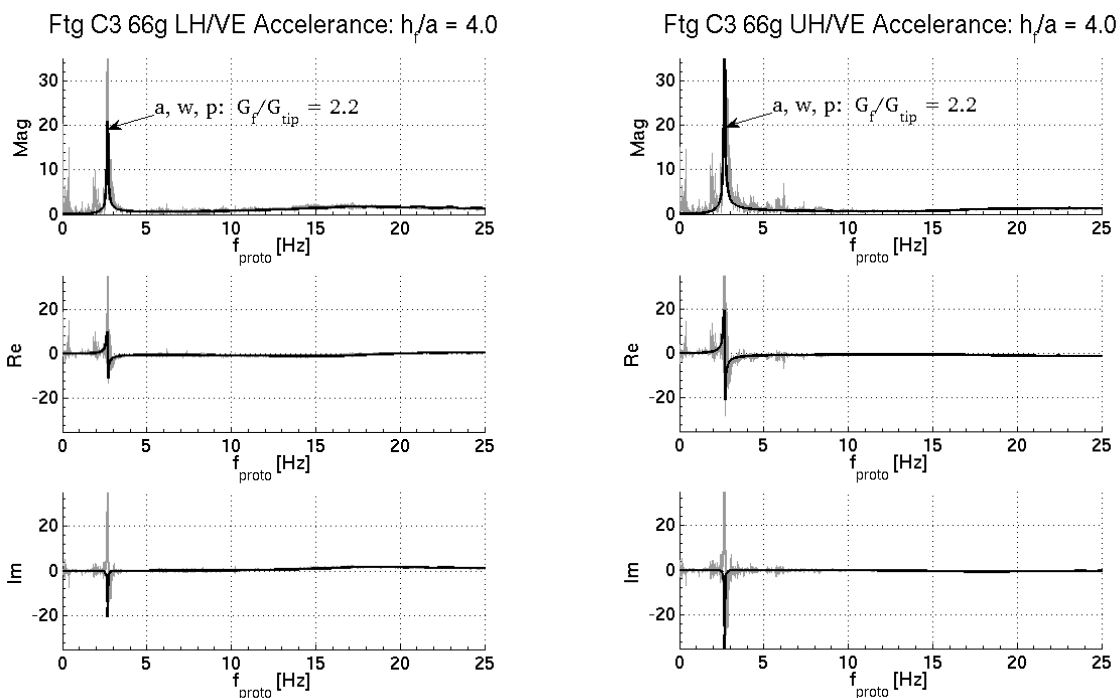


Figure 7.42: LH/VE accelerance of Footing C3 at 66g: 2-zone theory with $a_{proto} = 1.96$ m, $p_{proto} = 251.6$ kPa.

Figure 7.43: UH/VE accelerance of Footing C3 at 66g: 2-zone theory with $a_{proto} = 1.96$ m, $p_{proto} = 251.6$ kPa.

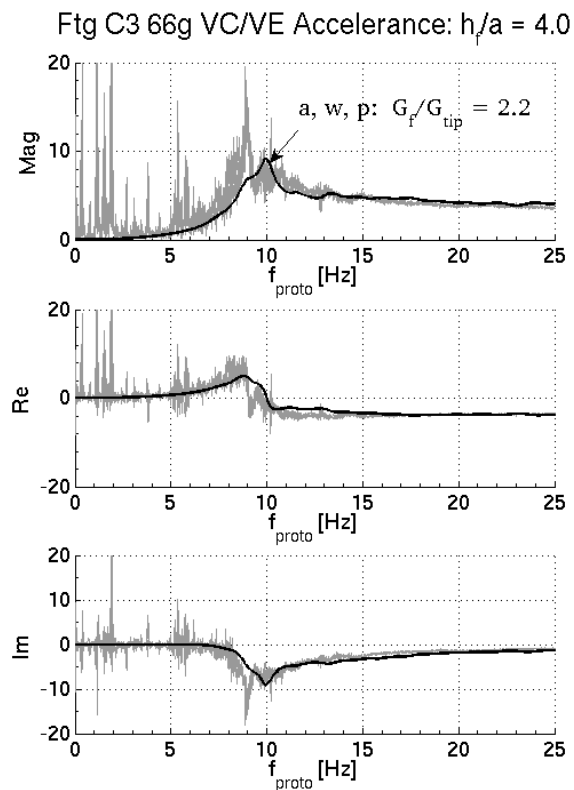


Figure 7.44: VC/VE accelerance of Footing C3 at 66g: 2-zone theory with $a_{proto} = 1.96$ m, $p_{proto} =$

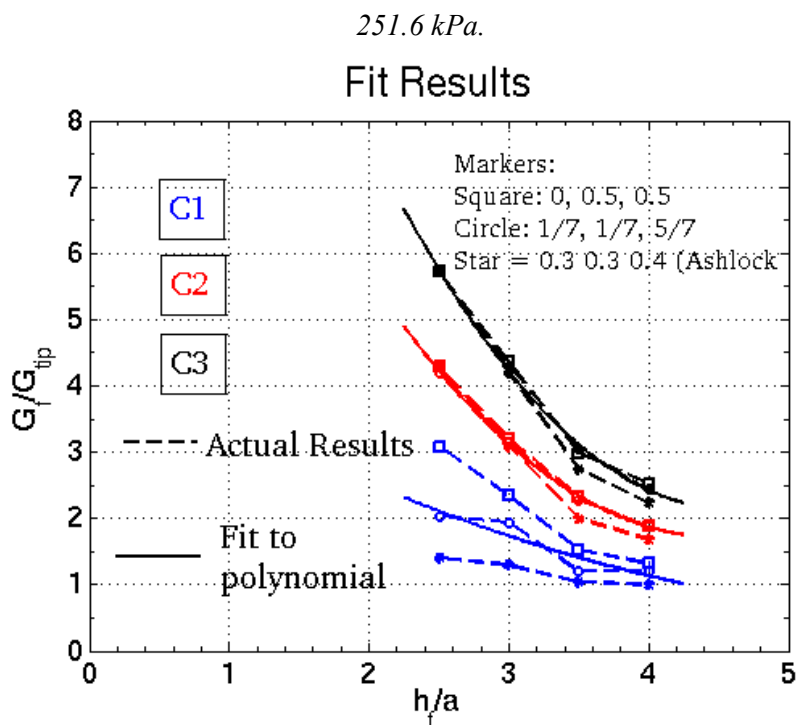


Figure 7.45: Fit results for all three weighting schemes, showing the average results of all g-levels.

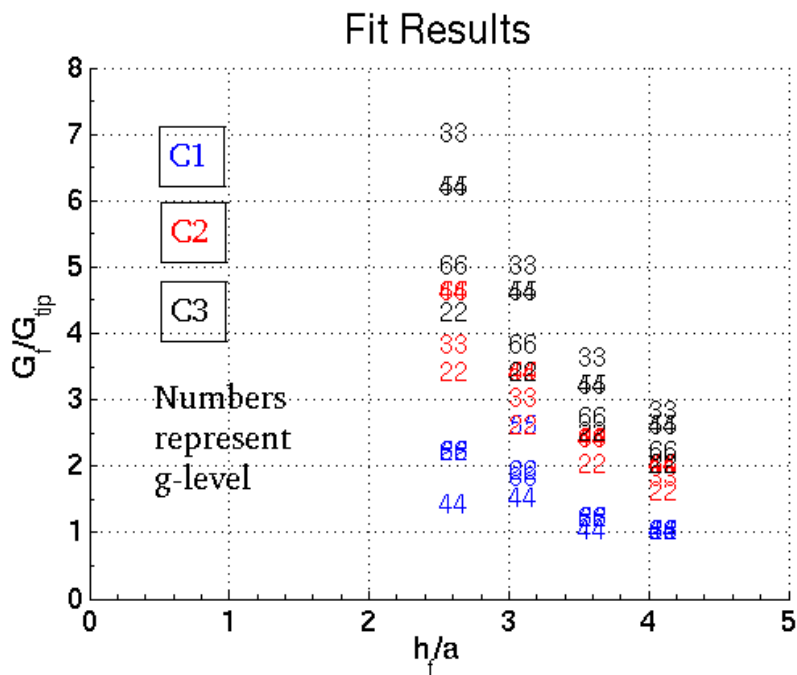


Figure 7.46: Weighting scheme fit results by g-level.

Figures 7.45 and 7.46 summarize the results from each weighting scheme. The weights corresponding to each marker are listed on the plot. For the heavier footings C2 and C3, all three

schemes are in close agreement. The lightest footing C1 has a larger band of suggested inclusion depth and stiffness, and depends on which of the three weighting schemes is used. The results at each g-level using the scheme 'w' appear to define more of a band of usable inclusion parameters rather than a clear optimal choice.

7.3 Homogeneous Shear Modulus vs. the Two-zone Model

The results for the homogeneous soil model were plotted earlier (Figures 7.2 – 7.21) by fitting either the horizontal rocking peak or the vertical response. Since the error weighting schemes (other than 'p') used for the two-zone model were intended to give a balance to the relative importance of each response feature, the fairest form of comparison would include a similar compromise measure for the homogeneous theory instead of either extreme. This is attempted by finding an equivalent homogeneous shear modulus to match the rocking peak of the two-zone theory, determined with a strong emphasis toward matching the rocking peak by using the weighting scheme 'w'. Any sort of resulting disagreements between the two theories in other areas of the horizontal and vertical response are then apparent.

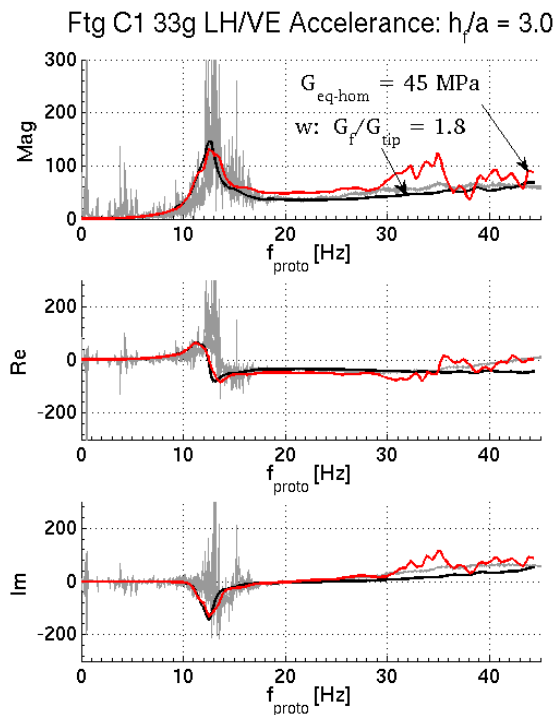


Figure 7.47: LH/VE acceleration of Footing C1 at 33g: $a_{proto} = 0.98 \text{ m}$, $p_{proto} = 41.1 \text{ kPa}$.

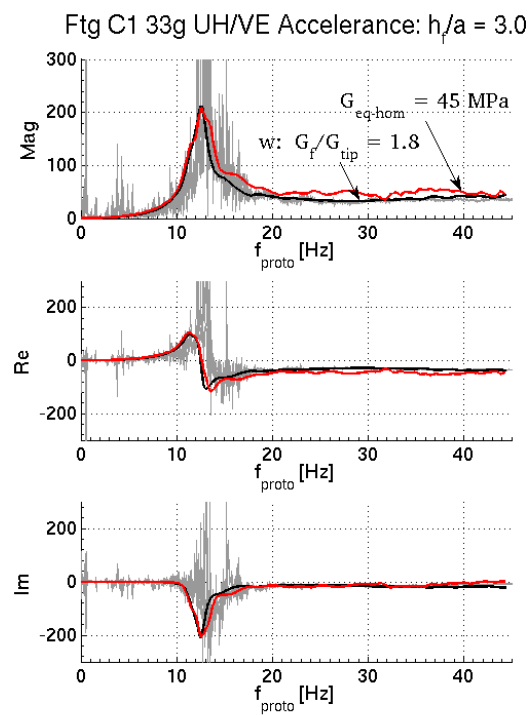


Figure 7.48: UH/VE acceleration of Footing C1 at 33g: $a_{proto} = 0.98 \text{ m}$, $p_{proto} = 41.1 \text{ kPa}$.

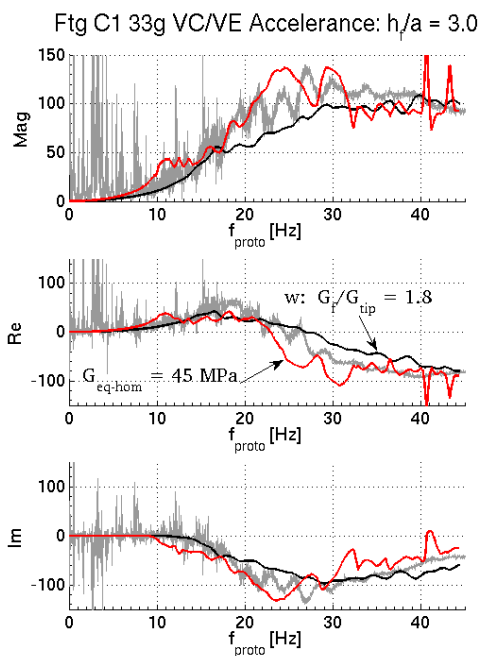


Figure 7.49: VC/VE acceleration of Footing C1 at 33g: $a_{proto} = 0.98$ m, $p_{proto} = 41.1$ kPa.

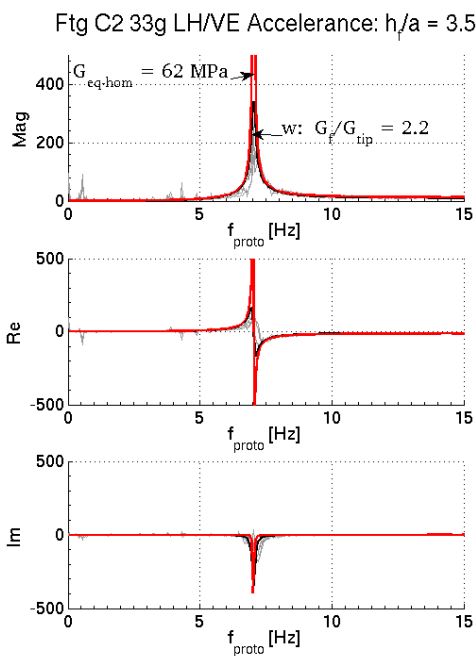


Figure 7.50: LH/VE acceleration of Footing C2 at 33g: $a_{proto} = 0.98$ m, $p_{proto} = 82.5$ kPa.

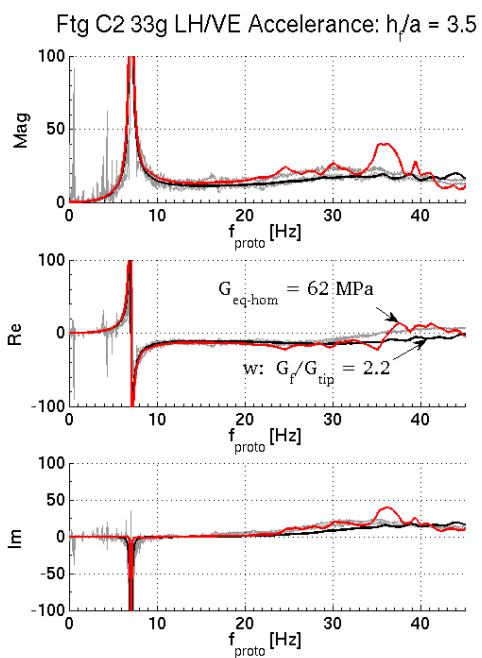


Figure 7.51: LH/VE acceleration of Footing C2 at 33g: $a_{proto} = 0.98$ m, $p_{proto} = 82.5$ kPa.

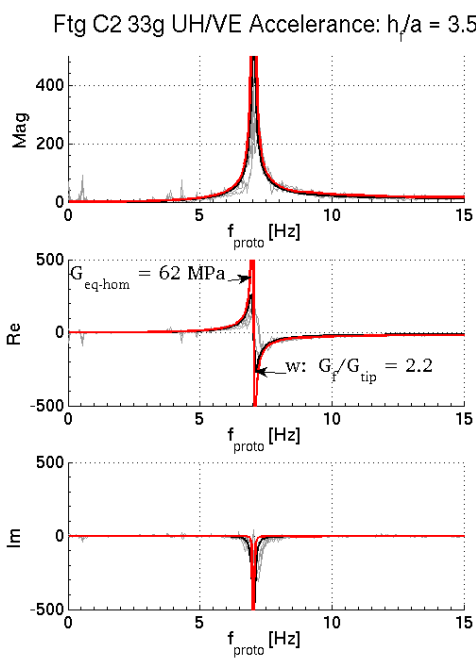


Figure 7.52: UH/VE acceleration of Footing C2 at 33g: $a_{proto} = 0.98$ m, $p_{proto} = 82.5$ kPa.

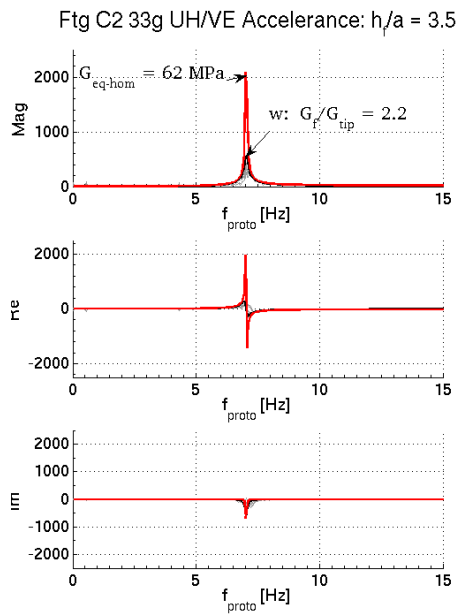


Figure 7.53: UH/VE accelerance of Footing C2 at 33g: $a_{proto} = 0.98 \text{ m}$, $p_{proto} = 82.5 \text{ kPa}$.

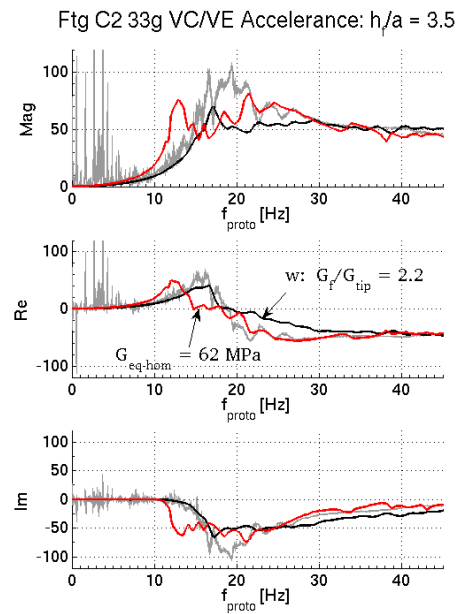


Figure 7.54: VC/VE accelerance of Footing C2 at 33g: $a_{proto} = 0.98 \text{ m}$, $p_{proto} = 82.5 \text{ kPa}$.

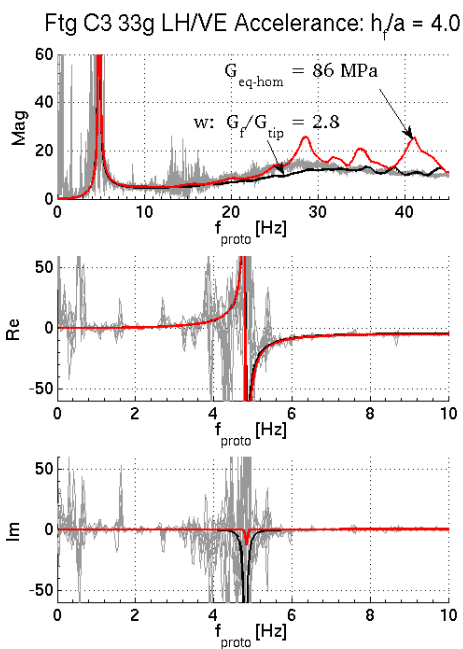


Figure 7.55: LH/VE accelerance of Footing C3 at 33g: $a_{proto} = 0.98 \text{ m}$, $p_{proto} = 125.8 \text{ kPa}$.

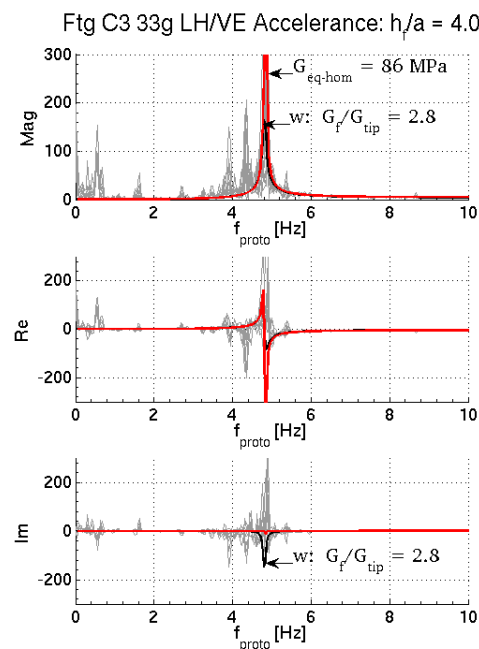


Figure 7.56: LH/VE accelerance of Footing C3 at 33g: $a_{proto} = 0.98 \text{ m}$, $p_{proto} = 125.8 \text{ kPa}$.

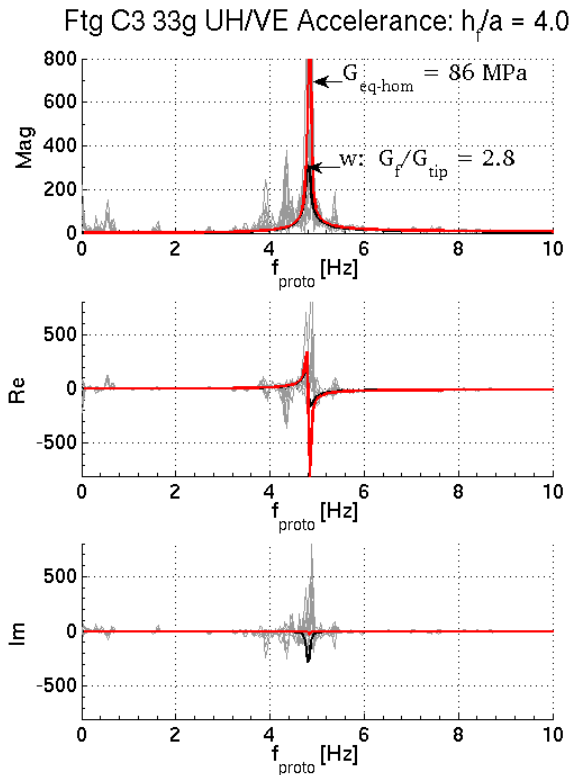


Figure 7.57: UH/VE acceleration of Footing C3 at 33g: $a_{proto} = 0.98$ m, $p_{proto} = 125.8$ kPa.

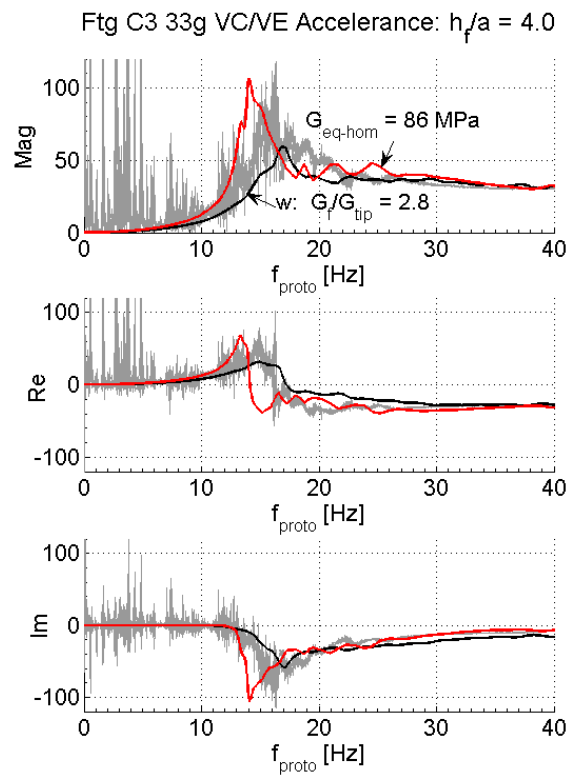


Figure 7.58: VC/VE acceleration of Footing C3 at 33g: $a_{proto} = 0.98$ m, $p_{proto} = 125.8$ kPa.

Beginning with footing C1 (Figures 7.47 – 7.49), the largest difference between the two models is the smoothness of the curves. The continuum theory is also smooth like the data at higher frequencies in the horizontal where the equivalent homogeneous theory is not (Figure 7.47). For footings C2 and C3, the vertical response of the homogeneous theory becomes increasingly shifted from that of the data (Figures 7.54, 7.58). The continuum theory maintains a balanced match with the choice of the 2 parameters according to the weighting scheme.

Each of the two theories plotted in Figures 7.47 – 7.58 have their advantages and disadvantages. The homogeneous soil model is simple, straightforward, and involves only one parameter in matching measured accelerances. Other than the second peak in the LH/VE acceleration, it is capable of reproducing the key features in the footing C1 response using only one value for G_{eq-hom} . Without the data as a guide, however, it may be difficult to interpret the vertical

response, as its behavior is erratic, especially at higher frequencies ($f_{proto} > 25$). The vertical response for footing C2 using a G_{eq-hom} is smoother; however, the peak itself is not clear, and is even split into multiple humps, making it more difficult to match with the measured data (e.g. Figure 7.54). The rocking peak magnitudes are also significantly (7X) times larger than their measured counterparts. Footing C3's result is the most difficult for the homogeneous soil model to explain. Matching the horizontal peak produces a VC/VE resonance peak that is off by 18%, taking the largest measured value within the peak lobes as the resonance peak location. Doing the same with the two-zone model results in a difference of only 2%. Admittedly, the degree-of-fit is subjective. From the above plots (Figures 7.47 – 7.58), it is arguable that at a certain depth of analysis, the homogeneous soil model is sufficient to characterize the experimental data collected in this project. The disadvantage is that despite the fact that it works in some cases, the G_{eq-hom} value is difficult to derive from a mechanics standpoint; in the end, it becomes merely a fudge parameter. This theory may also not be applicable to footings with lesser contact pressures than C1, or greater than C3. The work of Ashlock (2000, 2006) and Soudkhah (2010) also suggested as much.

The two-zone model is an attempt at a next-order approximation beyond the homogeneous soil model. The incorporation of a stiffened zone and square root soil profile are intended to acknowledge the stress-dependent nature of the soil's shear modulus, and utilize current insights and theories in mechanics in a practical, albeit being still an approximate, model.

The two-zone and homogeneous soil model accelerances are close when applied to the lightest footing C1, the main differences being smoothness, and the two-zone model results in a slightly stiffer vertical accelerance. Differences in response characteristics are further revealed in Figures 7.50 – 7.58, for footings C2 and C3. In each case where the rocking peak frequencies of both theories are matched to each other and the data, the two-zone vertical response is stiffer, i.e. response features shift to higher frequencies. It is through this shift that the two-zone model is better able to capture the frequency location of each response feature for the two heavier footings. For the most part, these features are also better matched in terms of magnitude and response profile,

most observable for footing C2 (see Figures 7.50 – 7.54).

Another method of comparison is to examine the two-zone result against the homogeneous theory with a modulus chosen to match the vertical response. Because the homogeneous theory can actually fit both the horizontal and vertical response for footing C1, it will be omitted in the following. Figures 7.15 and 7.21 demonstrate however that if the VC/VE response is captured, the rocking peak will be off significantly. This is plotted along with the two-zone model in Figures 7.59 – 7.66. For the case of footing C2 where the homogeneous response does not seem to have a clear vertical resonance peak, the effort was concentrated on matching the lobes of the peak in the measured data.

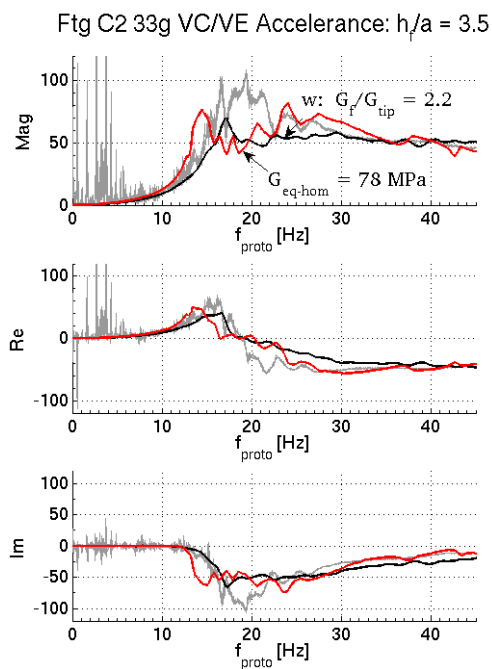


Figure 7.59: VC/VE accelerance of Footing C2 at 33g: homogeneous vs 2-zone theory with $a_{proto} = 0.98$ m, $p_{proto} = 82.5$ kPa.

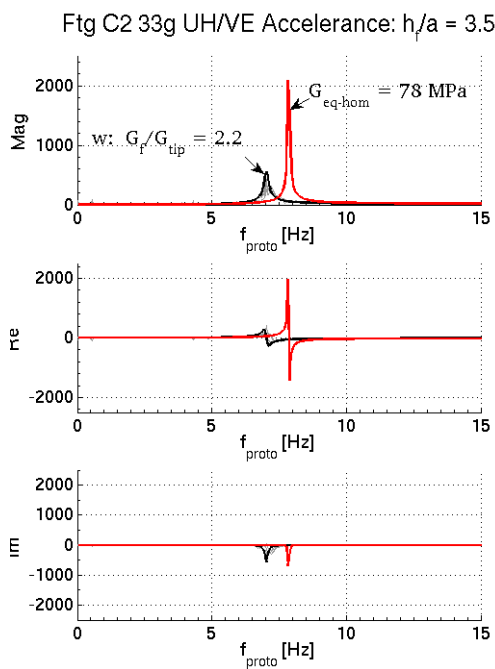


Figure 7.60: UH/VE accelerance of Footing C2 at 33g: homogeneous vs 2-zone theory with $a_{proto} = 0.98$ m, $p_{proto} = 82.5$ kPa.

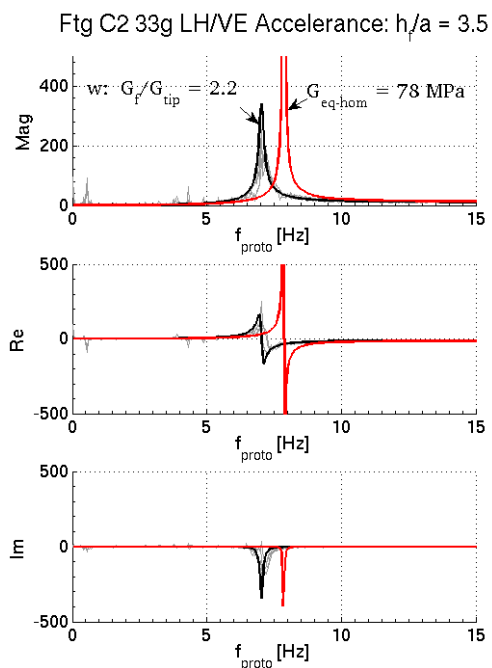


Figure 7.61: LH/VE accelerance of Footing C2 at 33g: homogeneous vs 2-zone theory with $a_{proto} = 0.98$ m, $p_{proto} = 82.5$ kPa.

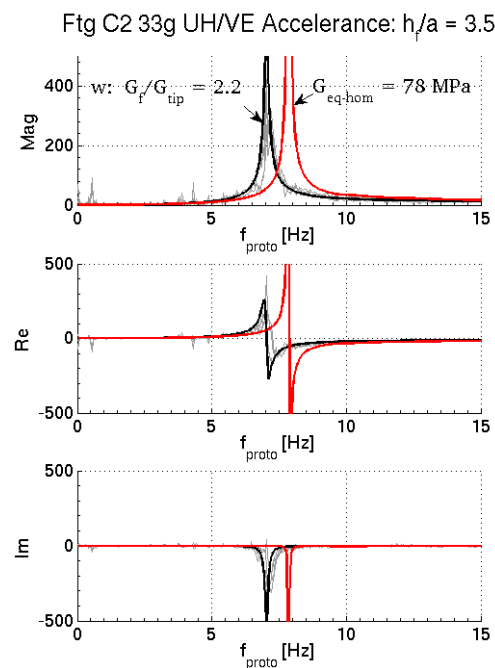


Figure 7.62: UH/VE accelerance of Footing C2 at 33g: homogeneous vs 2-zone theory with $a_{proto} = 0.98$ m, $p_{proto} = 82.5$ kPa.

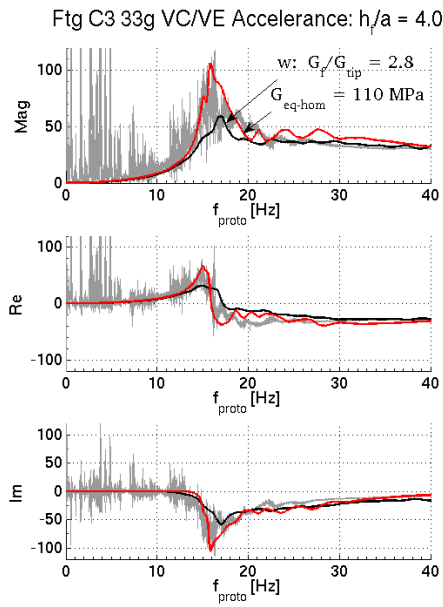


Figure 7.63: VC/VE acceleration of Footing C3 at 33g: homogeneous vs 2-zone theory with $a_{proto} = 0.98$ m, $p_{proto} = 125.8$ kPa.

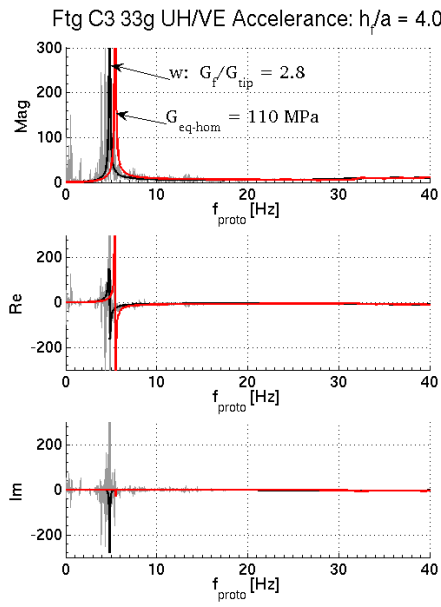


Figure 7.64: UH/VE acceleration of Footing C3 at 33g: homogeneous vs 2-zone theory with $a_{proto} = 0.98$ m, $p_{proto} = 125.8$ kPa.

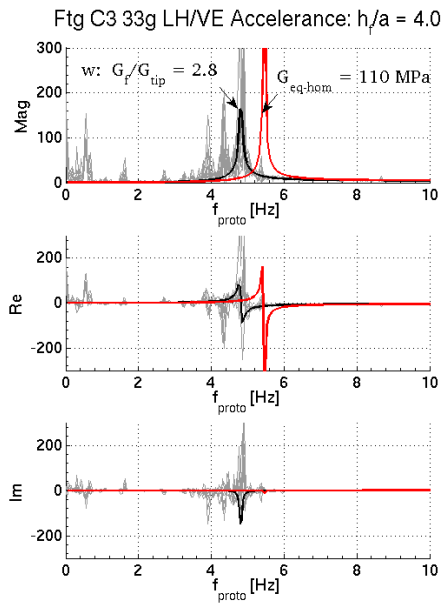


Figure 7.65: LH/VE acceleration of Footing C3 at 33g: homogeneous vs 2-zone theory with $a_{proto} = 0.98$ m, $p_{proto} = 125.8$ kPa.

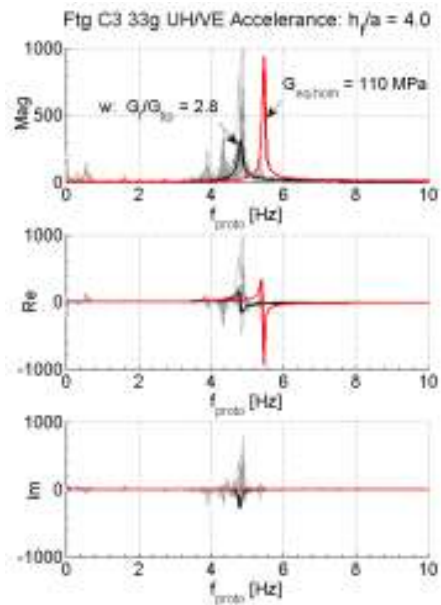


Figure 7.66: UH/VE acceleration of Footing C3 at 33g: homogeneous vs 2-zone theory with $a_{proto} = 0.98$ m, $p_{proto} = 125.8$ kPa.

It is evident from Figures 7.59 – 7.66 that although using an equivalent homogeneous shear modulus can produce the correct response curve profile for both vertical and horizontal accelerances, a single value cannot be chosen such that the locations of each key feature in the frequency domain are captured. Matching the VC/VE accelerance results in a rocking peak with too high of a frequency (Figures 7.60 and 7.66). Due to the variation in rocking peak magnitude between measured data at different g-levels, matching the magnitude of the sharp peak is of lower priority. However, the homogeneous theory seems to be somewhat sensitive with regard to peak magnitude (Figure 7.60). The two-zone model, on the other hand, has two model parameters and richer physical basis to capture the experimental behavior.

Chapter 8

Conclusions

In this study the response of a cylindrical footing under vertically eccentric loading on a dry soil stratum was investigated by means of centrifuge experimental modeling as well as analytical modeling via boundary element methods. Experimentally, the circular foundation results were found to compare well with prior results for square footings. Theoretically, the use of a homogeneous-modulus (or equivalent homogeneous-modulus) model was found to be unable to capture all but one basic resonance feature and requires a change in the homogeneous shear modulus of the entire soil region for each change in the foundation configuration or vibration mode of interest. This lack of flexibility became more of a hindrance as footing-soil contact pressure increased. The best demonstration of this obstacle was made by fitting the vertical response with a homogeneous shear modulus, and making the observation that theoretical horizontal accelerances generated using the same shear modulus value could not capture the rocking peak.

In contrast, using the two-zone soil model which is composed of a square root shear modulus profile for the far field and a homogeneous stiffened inner zone, it was found that it can reproduce multiple response features with only a logical change of the inner zone's modulus and dimension. Applied to the light, medium and heavy footings in the experiment, the two-zone model was found to perform generally well. While it is still an approximate solution, it offers sound reasoning on the basis of mechanics principles and known material behavior of soils. The sufficiency of varying both the depth and stiffness of the stiffened zone via merely two parameters to match the variety of behavior of the three different footings is the most attractive feature of the 2-zone continuum model.

Bibliography

- [1] J. C. Ashlock. Experimental and Theoretical Modeling of Dynamically Loaded Surface Foundations on Granular Soils. Master's thesis, University of Colorado at Boulder, 2000.
- [2] J. C. Ashlock. Computational and Experimental Modeling of Dynamic Foundation Interaction With Sand. PhD thesis, University of Colorado at Boulder, 2006.
- [3] J. S. Bendat and A. G. Piersol. Random Data. *Wiley-Interscience Publications*, New York, 1993.
- [4] G. N. Bycroft. Forced vibrations of a rigid circular footing on a semi-infinite elastic space and on a elastic stratum. *Phil. Trans. Roy. Soc. Lond.*, 248, A, (948), 327 – 368, 1956.
- [5] C. J. Coe, J. H. Prevost, and R. H. Scanlan. Dynamic stress wave reflections/attenuation: earthquake simulation in centrifuge soil models. *Earthquake Eng. & Struct. Dyn.*, 13(1), 109-128, 1985.
- [6] C. B. Crouse and B. Hushmand. Soil-structure interaction at CDMG and USGS accelerograph stations. *Bull. Seismol. Soc. Am.*, (USA) 79(1), 1-14, (1989)
- [7] C. B. Crouse, B. Hushmand, J. E. Luco, and H. L. Wong. Foundation Impedance functions: Theory versus experiment. *J. Geotech. Eng.* 116(3), 432-449, 1990.
- [8] R. Dobry and G. Gazetas. Dynamic response of arbitrarily shaped foundations. *J. Geotech. Eng.* 112(2), 109-135, 1986.
- [9] S. M. Erden. Influence of shape and embedment on dynamic foundation response. PhD thesis, U Mass Amherst, 1974.
- [10] Z. B. Fry. Development and evaluation of soil bearing capacity, foundations of structures; field vibratory tests data. *Waterways Experiments Station*, Technical Report No. 3-632 Vol 1, 1963.
- [11] G. Gazetas and K. H. Stokoe. Free vibration of embedded foundations, theory versus experiment. *J. Geotech Eng.* 117(9), 1382-1401, 1991.
- [12] G. M. L. Gladwell. Forced tangential and rotator vibration of a rigid circular disc on a semi-infinite solid. *Int. J. Engrg. Sci.*, 6, 592 – 607, 1962.
- [13] G. G. Gillmor. Centrifuge modeling of surface foundations subject to dynamic loads. Masters's thesis, University of Colorado at Boulder, 1999.
- [14] B. B. Guzina. Dynamic behavior of surface foundations on heterogeneous soils. Master's thesis, University of Colorado at Boulder, 1992.
- [15] B. B. Guzina. Seismic Response of Foundations and Structures in Multilayered Media. PhD thesis, University of Colorado at Boulder, 1996.

- [16] B. O. Hardin and V. P. Drnevich. Shear modulus and damping in soils: Design equations and curves. *Journal of the Soil Mechanics and Foundations Division, Proceedings of the American Society of Civil Engineers*, 98(SM7):667:692, July 1972.
- [17] B. Hushmand. Experimental Studies of Dynamic Response of Foundations. PhD thesis, California Institute of Technology, Pasadena CA, 1983.
- [18] H.-Y Ko. The Colorado centrifuge facility. In Corte, ed., *Centrifuge 88*, Balkema, Rotterdam, pages 73-75, 1988.
- [19] T. Kobori, R. Minai, and T. Suzuki. Dynamical ground compliance of rectangular foundations on a viscoelastic stratum, in *Disaster Prev. Res. Inst., Mar 1971, Kyoto Univ.*, Vol. 20, pages 289 – 329, 1971.
- [20] L. R. Lenke, R. Y. S. Pak, and H.-Y. Ko. Boundary effects in modeling of foundations subjected to vertical excitation. In H.-Y Ko, editor, *Centrifuge 91*, pages 473-480. Balkema, Rotterdam, 1991.
- [21] A. N. Lin and P. C. Jennings. Effects of embendment on foundation-soil impedances. *J. Eng. Mech.* 110(7), 1060 – 1075, 1984
- [22] J. E. Luco and R. A. Westmann. Dynamic response of circular footings. *J. Eng Mech. Div.*, ASCE 97, 1381 – 1395, 1971.
- [23] J. Lysmer. Vertical Motions of Rigid Footings. PhD thesis, University of Michigan Ann Arbor, 1965.
- [24] P. J. Moore., ed. Analysis and design of foundations for vibrations. A. A. Balkema, Rotterdam, 1985.
- [25] M. Novak and Y. O. Beredugo. Vertical vibration of embedded footings. *J. Soil Mech. Found Div.* ASCE 98 (SM12), 1291 – 131, 1972.
- [26] R. Y. S. Pak and J. C. Ashlock. Fundamental dynamic behavior of foundations on sand. In R. Y. S. Pak and J. Yamamura, eds, *Soil Dynamics and Liquefaction 2000, GSP*, 107, ASCE, Denver CO, pages 10-19, 2000.
- [27] R. Y. S. Pak and J. C. Ashlock. A fundamental dual-zone continuum theory for dynamic soil-structure interaction. *International Journal of Earthquake Engineering and Structural dynamics*, DOI: 10. 1002/eqe.1075, 2010 .
- [28] R. Y. S. Pak, J. C. Ashlock, S. Kurahashi, and F. Abedzadeh. Parametric Gmax sounding of granular soils by vibration methods. *Geotechnique*, ICE 58(7), 571-580. URL: <http://dx.doi.org/10.1680/geot.2007.00203>. 2008.
- [29] R. Y. S. Pak, J. C. Ashlock, S. Kurahashi, and M. Soudkhah. Physical characteristics of dynamic vertical-horizontal-rocking response of surface foundations on cohesionless soils. *Geotechnique*, 2010 (in press).
- [30] R. Y. S. Pak and A. T. Gobert. On the axisymmetric interaction of a rigid disc embedded in a semi-infinite solid. *Z. Agnew. Math. Phys.*, 41, 684 – 700, 1990.

- [31] R. Y. S. Pak and B. B. Guzina. Dynamic characterization of vertically loaded foundations on granular soils. *Journal of Geotechnical Engineering*, 121(3):274-286, March 1995.
- [32] R. Y. S. Pak and B. B. Guzina. Seismic soil-structure interaction analysis by direct boundary element methods. *International Journal of Solids and Structures*, 36:4743-4766, May 1998.
- [33] E. Reissner. Stationäre axialsymmetrische durch eine elastische halbe Ebene. *Ingenieur Archiv* 7(6) 381 – 396, 1936.
- [34] E. Reissner and H. F. Sagoci. Forced torsional oscillations of an elastic half-space, I. *J. App. Phys.*, 15(9), 652-654, 1944.
- [35] Richart, Hall and Woods. *Vibrations of soils and foundations*, Prentice-Hall, Englewood Cliffs NJ, 1970.
- [36] I. A. Robertson. Forced vertical vibration of a rigid circular disc on a semi-infinite elastic solid. *Proc. Cambridge Phil. Soc.* 62, 547 – 553, 1966.
- [37] H. B. Seed and I. M. Idriss. Moduli and damping factors for dynamic analyses of cohesionless soils. *Journal of Geotechnical Engineering*, 112:1016-1032, 1986.
- [38] M. Soudkhah. Development of engineering continuum models for seismic soil-foundation interaction. PhD thesis, University of Colorado at Boulder, 2010.
- [39] K. H. Stokoe and F. E. Richart Jr. Dynamic response of embedded machine foundations. *ASCE J. Geotech Eng. Div.* 100(GT4), 427 – 447, 1974.
- [40] J. P. Wolf. *Dynamic Soil-Structure Interaction*, Prentice-Hall, Englewood Cliffs NJ, 1985.
- [41] J. P. Wolf and J. W. Meek. Insight on 2d- versus 3d-modelling of surface foundations via strength-of-materials solutions for soil dynamics. *Earthquake Engineering and Structural Dynamics*, 23(1), 91-112, 1994.
- [42] H. L. Wong, J. E. Luco, and M. D. Trifunac. Contact stresses and ground motion generated by soil-structure interaction. *Earthq. Eng Struct. Dyn.* 5(1), 67-79, 1977.

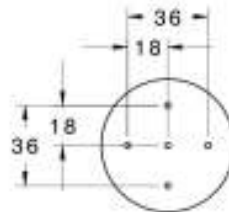
Appendix A

Footing Drawings

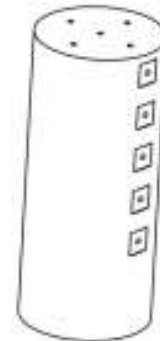
C09 (B): 06-25-2009

Dimensions in mm unless noted

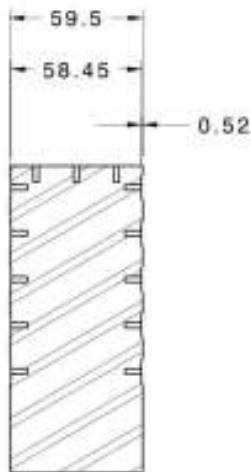
Holes:
 Hole Depth = 0.2915 in
 Thread Depth = 0.2835 in
 5-40 UNC Threads
 (use .101 in drill bit)



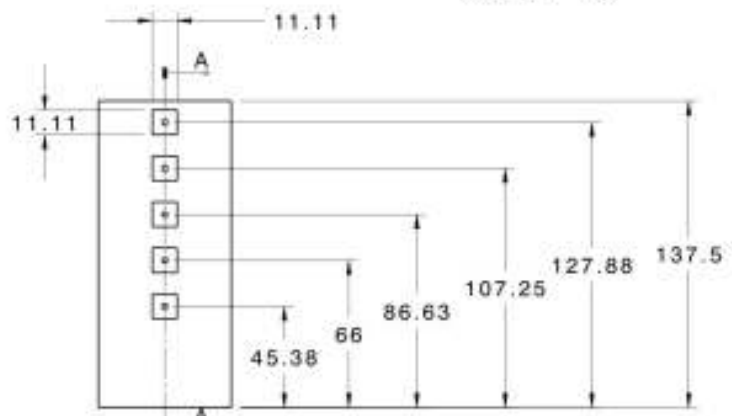
Top view
 Scale: 1:2



Isometric view
 Scale: 1:2



Section view A-A
 Scale: 1:2

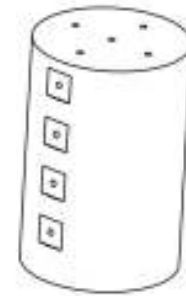
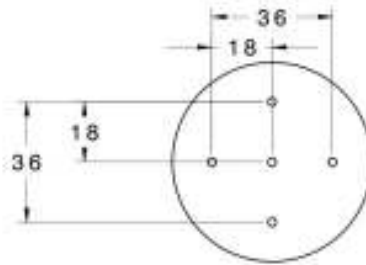


Front view
 Scale: 1:2

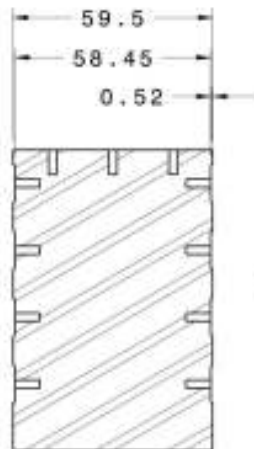
C2309 (B23): 06-25-2009

Dimensions in mm unless
otherwise noted.

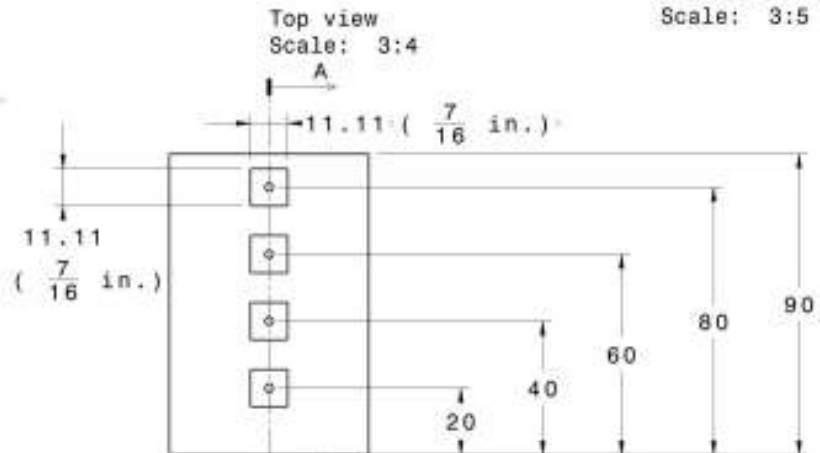
Holes:
Hole Depth = 7.4 mm
Thread Depth = 7.2 mm
5-40 UNC Threads
(use .101 in drill bit)



Isometric view
Scale: 3:5



Section view A-A
Scale: 3:4

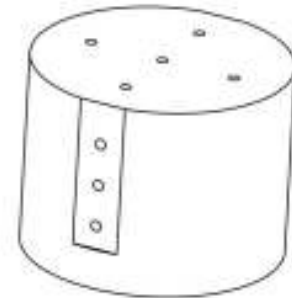
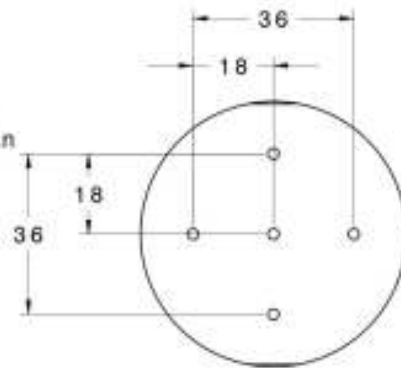


Front view
Scale: 3:4

C1309 (B13) 06-25-2009

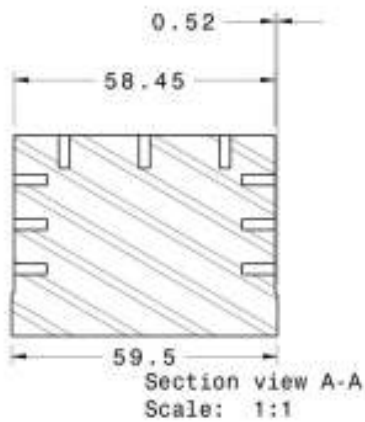
All Dimensions in mm
unless noted

Holes:
Hole Depth = 0.2915 in
Thread Depth = 0.2835 in
5-40 UNC Threads
(use .101 in drill bit)

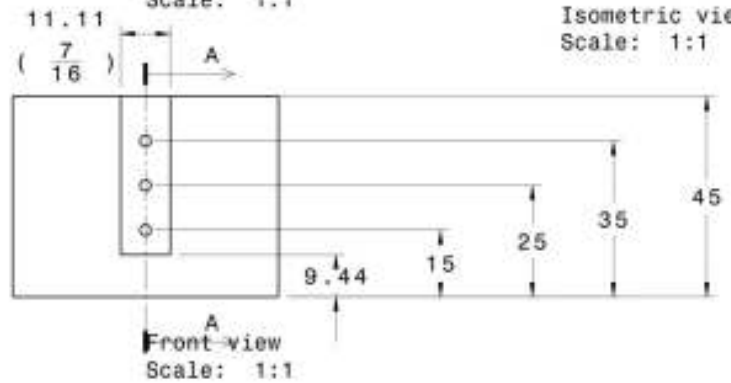


Top view
Scale: 1:1

Isometric view
Scale: 1:1



Section view A-A
Scale: 1:1



Front view
Scale: 1:1

Appendix B

Data Records and Test Dates

Test Number	Footing	g-level	File Name
1	C1	1	C1312042009_01g_001
2	C1	22	C1312042009_22g_001
3	C1	22	C1312042009_22g_002
4	C1	22	C1312042009_22g_003
5	C1	1	C1312042009_01g_011
6	C1	1	C1312042009_01g_012
7	C1	33	C1312042009_33g_amb
8	C1	33	C1312042009_33g_001
9	C1	33	C1312042009_33g_002
10	C1	33	C1312042009_33g_003
11	C1	1	C1312042009_01g_021
12	C1	1	C1312042009_01g_022
13	C1	1	C1312042009_01g_023
14	C1	44	C1312042009_44g_amb
15	C1	44	C1312042009_44g_001
16	C1	44	C1312042009_44g_002
17	C1	44	C1312042009_44g_003
18	C1	44	C1312042009_44g_004
19	C1	1	C1312042009_01g_031
20	C1	1	C1312042009_01g_032
21	C1	55	C1312042009_55g_amb
22	C1	55	C1312042009_55g_001
23	C1	55	C1312042009_55g_002
24	C1	55	C1312042009_55g_003
25	C1	55	C1312042009_55g_004
26	C1	1	C1312042009_01g_041
27	C1	1	C1312042009_01g_042
28	C1	66	C1311242009_66g_amb
29	C1	66	C1311242009_66g_001
30	C1	66	C1311242009_66g_ambS
31	C1	66	C1311242009_66g_002
32	C1	66	C1311242009_66g_003
33	C1	1	C1312042009_01g_041
34	C1	33	C1312042009_33g_amb1
35	C1	33	C1312042009_33g_011

Test Number	Footing	g-level	File Name
1	C2	1	C2311192009_01g_001
2	C2	1	C2311192009_01g_002
3	C2	22	C2311192009_22g_001
4	C2	1	C2311192009_01g_001
5	C2	1	C2311192009_01g_002
6	C2	1	C2311192009_01g_011
7	C2	33	C2311192009_33g_amb
8	C2	33	C2311192009_33g_001
9	C2	33	C2311192009_33g_002
10	C2	1	C2311192009_01g_021
11	C2	1	C2311192009_01g_022
12	C2	44	C2311192009_44g_amb
13	C2	44	C2311192009_44g_001
14	C2	44	C2311192009_44g_002
15	C2	1	C2311192009_01g_031
16	C2	55	C2311192009_55g_amb
17	C2	55	C2311192009_55g_001
18	C2	55	C2311192009_55g_002
19	C2	1	C2311192009_01g_041
20	C2	66	C2311192009_66g_amb
21	C2	66	C2311192009_66g_001
22	C2	66	C2311192009_66g_002
23	C2	1	C2311192009_01g_051
24	C2	33	C2311192009_33g_amb1
25	C2	33	C2311192009_33g_011
26	C2	33	C2311192009_33g_012
27	C2	1	C2311192009_01g_061

Test Number	Footing	g-level	File Name
1	C3	1	C10232009_01g_021
2	C3	1	C10232009_01g_022
3	C3	1	C10232009_01g_023
4	C3	33	C10232009_33g_001
5	C3	33	C10232009_33g_002
6	C3	1	C10232009_01g_031
7	C3	44	C10232009_44g_001
8	C3	44	C10232009_44g_002
9	C3	1	C10232009_01g_041
10	C3	55	C10232009_55g_001
11	C3	55	C10232009_55g_002
12	C3	1	C10232009_01g_051
13	C3	66	C10232009_66g_001
14	C3	66	C10232009_66g_002
15	C3	33	C10232009_33g_011
16	C3	33	C10232009_33g_012
17	C3	33	C10232009_33g_013

Test Number	Footing	g-level	File Name
1	C3	1	C10272009_01g_001
2	C3	22	C10272009_22g_amb
3	C3	22	C10272009_22g_001
4	C3	22	C10272009_22g_002
5	C3	22	C10272009_22g_003
6	C3	1	C10272009_01g_011
7	C3	1	C10272009_01g_012
8	C3	33	C10272009_33g_amb
9	C3	33	C10272009_33g_001
10	C3	33	C10272009_33g_002
11	C3	33	C10272009_33g_003
12	C3	33	C10272009_33g_004
13	C3	1	C10272009_01g_021
14	C3	44	C10272009_44g_amb
15	C3	44	C10272009_44g_001
16	C3	44	C10272009_44g_002
17	C3	44	C10272009_44g_003
18	C3	1	C10272009_01g_031
19	C3	55	C10272009_55g_amb
20	C3	55	C10272009_55g_001
21	C3	55	C10272009_55g_002
22	C3	55	C10272009_55g_003
23	C3	55	C10272009_55g_004
24	C3	1	C10272009_01g_41
25	C3	1	C10272009_01g_42
26	C3	1	C10272009_01g_43
27	C3	66	C10272009_66g_amb
28	C3	66	C10272009_66g_001
29	C3	66	C10272009_66g_002
30	C3	1	C10272009_01g_51
31	C3	1	C10272009_01g_52
32	C3	1	C10272009_01g_53
33	C3	33	C10272009_33g_011
34	C3	33	C10272009_33g_012
35	C3	1	C10272009_01g_61
36	C3	1	C10272009_01g_62

Test Number	Footing	g-level	File Name
1	C3	1	C10292009_01g_001
2	C3	1	C10292009_01g_002
3	C3	22	C10292009_22g_amb
4	C3	22	C10292009_22g_001
5	C3	22	C10292009_22g_002
6	C3	22	C10292009_22g_003
7	C3	1	C10292009_01g_011
8	C3	1	C10292009_01g_012
9	C3	1	C10292009_01g_013
10	C3	33	C10292009_33g_amb
11	C3	33	C10292009_33g_001
12	C3	33	C10292009_33g_002
13	C3	1	C10292009_01g_021
14	C3	44	C10292009_44g_amb
15	C3	44	C10292009_44g_001
16	C3	44	C10292009_44g_002
17	C3	44	C10292009_44g_003
18	C3	1	C10292009_01g_031
19	C3	1	C10292009_01g_032
20	C3	55	C10292009_55g_amb
21	C3	55	C10292009_55g_001
22	C3	55	C10292009_55g_002
23	C3	1	C10292009_01g_041
24	C3	1	C10292009_01g_042
25	C3	66	C10292009_66g_amb
26	C3	66	C10292009_66g_001
27	C3	66	C10292009_66g_002
28	C3	1	C10292009_01g_051
29	C3	33	C10292009_33g_011

Test Number	Footing	g-level	File Name
3	C3	1	C11112009_01g_003
4	C3	22	C11112009_22g_001
5	C3	22	C11112009_22g_002
6	C3	1	C11112009_01g_011
7	C3	33	C11112009_33g_001
8	C3	33	C11112009_33g_002
9	C3	1	C11112009_01g_021
10	C3	44	C11112009_44g_001
11	C3	44	C11112009_44g_002
12	C3	1	C11112009_01g_031
13	C3	55	C11112009_55g_001
14	C3	55	C11112009_55g_002
15	C3	1	C11112009_01g_041
16	C3	66	C11112009_66g_001
17	C3	66	C11112009_66g_002